MATERIAL CHARACTERIZATION OF DIRECTED ENERGY DEPOSITION OF H13 TOOL STEEL AND FUNCTIONALLY GRADED H13-COPPER

by

Owen H. Craig

Submitted in partial fulfillment of the requirements
for the degree of Doctor of Philosophy

at

Dalhousie University
Halifax, Nova Scotia,
August 2022

DEDICATION PAGE

I'd like to dedicate this work to my late granddad (1948 - 2020), Jerry Craig, who passed from Idiopathic Pulmonary Fibrosis (IPF). He provided lots of love and instilled a strong desire to learn. I know he would have loved to read the findings of this work. To Camper who was one of the best dogs I had growing up.

TABLE OF CONTENTS

LIST OF TABLES

LIST OF FIGURES

ABSTRACT

The aim of this study is to determine the laser directed energy deposition (DED) parameters for an H13-Cu functionally graded material (FGM). Monolithic steel tools have poor thermal conductivity, reducing the cycle times. This could be improved with the high thermal conductivity of Cu in a FGM structure. Research began with wrought H13 heat-treated at varying tempering temperatures to examine the influence on the microstructure and mechanical properties. DED H13 samples were produced by varying the scanning speed and powder feed rates to examine geometrical and microstructural influences. Several techniques were employed to characterize the materials which included surface roughness, optical and scanning electron microscopy, hardness, X-ray diffraction, energy dispersive X-ray spectroscopy, and scratch hardness. The top surface roughness of the samples was found to be greater than the side surface roughness. The addition of a draft angle to a vertical surface was shown to reduce the side surface roughness. The deposited material undergoes rapid solidification, producing a highly refined microstructure with near-theoretical density (99.7%). The as-printed multi-layer samples show a cellular dendritic structure with tempered martensite and alloy carbides in the lower layers. The top layers consist of fine lath martensite and retained austenite. Tempering the multi-layer samples results in a homogenized microstructure of tempered martensite and alloy carbides. There was variation in the Vickers hardness of the as-processed samples due to the cyclic heating. Applying a heat treatment to the DED-processed materials reduced the hardness and variation. Scratch hardness was highest in the as-printed condition with a heat treatment reducing the scratch resistance. No trend was observed in the scratch response with changing the scanning speed, powder feed rate, or number of layers.

Varying H13-Cu blends were printed on wrought H13 as well as a multi-layered FGM. Single layer and 3-layer tracks resulted in detrimental porosity and vertical cracking characteristic of solidification cracking. The multi-layered FGM samples showed transverse cracking and porosity. The microstructure consisted of tempered martensite, martensite, alloy carbides, retained austenite, and a Cu-rich matrix with scattered H13 particles. There is clear separation of the H13- and Cu-rich liquids due to the miscibility gap, aided with differential scanning calorimetry analysis. Printing onto C110 was unsuccessful using varied laser powers resulting in inconsistent beads.

LIST OF ABBREVIATIONS AND SYMBOLS USED

AM	Additive manufacturing
AR	As-received
CLSM	Confocal laser scanning microscope
COF	Coefficient of friction
D_{10}	10% of the total particles are smaller than size reported
D_{50}	50% of the total particles are smaller than size reported
D_{90}	90% of the total particles are smaller than size reported
DED	Directed energy deposition
DSC	Differential scanning calorimetry
EDS	Electron dispersive X-ray spectroscopy
FE-SEM	Field emission scanning electron microscope
FGM	Functionally graded material
HAZ	Heat affected zone
ICP-OES	Inductively coupled plasma – optical emission spectroscopy
M_s	Martensite start temperature
PSD	Particle size distribution
S_a	Surface area roughness
SDAS	Secondary dendrite arm spacing
T_m	Melting point
WDS	Wavelength-dispersive spectroscopy
wt%	Weight percent
XRD	X-ray diffraction
α	Ferrite
α’	Martensite
γ	Austenite
ε	Copper

ACKNOWLEDGEMENTS

Firstly, I'd like to acknowledge the funding support provided from the National Sciences and Engineering Research Council of Canada (NSERC) for the network entitled "NSERC Network for Holistic Innovation in Additive Manufacturing (HI-AM)" under the grant NETGP 494158-16. This funding allowed me to attend conferences across Canada and conduct my research at the Centre de métallurgie du Québec (CMQ) and at the Navajo Technical University (NTU) in New Mexico – which graciously offered to help me with my work at no charge and welcomed me with open arms.

I would not have been able to complete this work without the support of my supervisor Dr. Kevin Plucknett who allowed me to conduct my research as I see fit. He provided much needed guidance and inspiration over the years and made sure I was on track. I will carry on his values and high standard of work in the next chapter of my professional career. My committee members Dr. Ghada Koleilat and Dr. Zoheir Farhat should be thanked for their time and commitment in supervising my thesis. I want to profoundly thank my loving family and the support they provide; to my supportive dad who would help with random writing or presentation questions and to my mom who may not understand what I do but still enjoyed hearing about my research.

As my time at Dalhousie comes to an end, I would not have envisaged myself receiving a Ph.D. when I first enrolled. The people I have met along the way are one of the main reasons I have stayed for so long. This work sparked my realization that I enjoy research and my desire to continuously learn. I want to thank Jon Hierlihy who I met in my undergrad but became good friends when we started our (long) journey in graduate school. He would always answer my questions about basic material science knowledge,

expanding my understanding of difficult concepts, always being up to chat about whatever, and getting me out of my comfort zone and going outside to go fishing. I would like to express my sincerest gratitude to Zhila Russell – who helped me navigate the lab as a fresh graduate student and was there to answer questions I had, to Greg Sweet and Mark Amegadzie – who I pestered with questions about general life as a graduate student and showing me the tips and tricks to be successful in the lab. I would also like to thank my friends Paria Siah Pour and Samer Omar - they would provide thoughtful insights, would answer questions I had, and exposed me to their cultural traditions and customs. I wish them the best of luck with their future endeavors. I can't forget all the other individuals that have helped me over the years starting with Randy Cooke – who would help set up equipment, show me proper practices, or assist without question, Patricia Scallion – for providing solutions and endless help when operating the SEM, Eric Moreau – who took over my difficult-to-polish samples and ran my DSC analyses, Scott Halliday, Joshua Toddy, Nylana Murphy – who invited me to their lab at NTU to print my samples and help run the equipment. To Peter Jones and the machinists Mark, Albert, Colin, Graham, and Gregory who had to decipher my crude drawings but managed to get there in the end. I owe them several drinks for the many headaches I likely caused them. My sincerest apologizes to anyone else I forgot but who is deserving of a thank you. To my good friends, Arden, Derek, Sarah, and Roman who always have my back, let me forget about my work, and would coax me to find a little more celebration and silliness in life.

Lastly, I want to wish the next group of graduate students to continue producing excellent research and find joy in their work.

1 INTRODUCTION

1.1 Research Significance and Aims

Current literature has provided several parameter settings for directed energy deposition (DED) systems to successfully print defect free samples of H13 tool steel using pre-alloyed powder. Since process parameters are highly dependent upon the material system, successful system parameters need to be tailored to accommodate the different physical properties, with the settings for printing homogenous H13 being insufficient to transfer to a functionally graded material (FGM). The main objective of this research is to determine printing parameters of a DED-processed, compositionally FGM of H13-copper (H13-Cu), without defects onto a wrought H13 substrate. Secondly, the research aimed to print an H13-Cu FGM onto a highly pure Cu substrate. The intent of developing an advanced material of H13-Cu is for use in the tool and die industry as it would be advantageous to increase cycling times of tools where they are typically monolithic steel tools with poor thermal conductivity. To overcome this issue, it is theorized that these tools can be improved with the increased thermal conductivity from Cu, graded with a high strength and wearing surface of H13 tool steel. The advantage of using a DED system to manufacture an FGM is it allows for multi-material deposition and freeform building for added design flexibility. DED technology is not constrained by a proprietary substrate, so material can be deposited onto an existing surface or to repair a worn part.

1.2 Anticipated Outcomes

The present issue for this material system is that Cu poses a significant challenge when processing using a laser, due to the high reflectivity at the near infrared wavelengths used in the lasers of commercially available additive manufacturing machines. In addition, Cu is known to cause cracking in steels in large amounts. To overcome this issue, the wavelength of the laser must be reduced, or back-reflection technology must be implemented in the laser system to allow Cu to be processed effectively. The challenge of the solidification behavior of the iron (Fe) and Cu will be difficult to overcome, with large amounts of cracking and porosity anticipated. To alleviate this issue, it is suggested that a nickel (Ni) buffer layer be added between the H13 tool steel and Cu. Even with these remedies, the varying compositions of H13-Cu will likely require their own respective system processing conditions for successful printing to occur with increasing laser required with increasing Cu content.

As mentioned previously, the reflectivity of copper poses a major obstacle. Printing onto a copper substrate would be in the correct orientation for the compositional gradient for a tool and die scenario. This method will result in the surface (*i.e.,* last printed layers) comprising of the wear resistant H13 tool steel while the core will consist of the thermally conductive copper. Ultimately, the goal is verifying the viability of printing an FGM H13-Cu homogenous part for the intended use in the forming industry (*i.e.,* forging, dies, and molds) where a high wear resistant material is needed on the face of the tool and can conduct the heat away quickly to increase cycling time between workpieces.

1.3 Chapter Organization

This work began with the characterization of the wrought material to have a baseline understanding of how the traditionally manufactured tool steel behaves so that it can be compared to the additively manufactured equivalent and FGM processed material using DED. This involved purchasing round feedstock and applying various double temper heat treatments to the wrought material. The wrought heat-treated samples were then characterized using a variety of techniques which included optical microscopy, hardness, scratch hardness, field emission scanning electron microscopy (FE-SEM), energy-dispersive X-ray spectroscopy (EDS), and X-ray diffraction (XRD).

After characterization of the wrought H13 tool steel, additive manufactured DED H13 tool steel samples were printed under varying printing parameters to determine successful settings for depositing homogenous DED H13 samples. For the deposition of H13, changing system parameters, namely, the powder feed rate and scanning speed, were investigated to examine the influence on the final as-printed surface roughness, mechanical properties, and microstructure. The DED samples were characterized using the same techniques as mentioned for the wrought material.

Finally, single and 3-layer clad tracks with varying blends of H13-Cu were printed on an H13 and Cu substrate with the laser power and scanning speed being varied. Two H13-Cu FGM rectangular samples were printed into one homogenous part with six different compositional changes in the build direction (+z). The printed FGM H13-Cu samples were evaluated using, CLSM, XRD, EDS, and FE-SEM. Differential scanning calorimetry (DSC) consisting of a full and interrupted melt with vary blends of loose H13

and Cu powder were used to aid with the thermodynamic and solidification behavior of the material system.

Additional work included pack boriding of wrought and DED H13 tool steel. The aim of this study was to examine if there were any differences in mechanical properties and the formation of the dual-phase boride layer between the two manufacturing methods. There has been extensive work conducted on boriding wrought H13 tool steel but there appears to be a gap in research on boriding additively manufactured H13 tool steel using DED. Characterization of this material included CSLM, XRD, EDS, FE-SEM, and wavelength-dispersive spectroscopy (WDS).

Chapter 1 provides an outline of the thesis chapters and how the document is structured. As well, it includes the objectives, significance, and contributions made by the author to the research of DED additively manufactured H13-Cu functionally graded material. The main contributing information to this field of research is providing system parameters using relevant DED equipment and laser technology to print a functionally graded material of H13-Cu.

Chapter 2 presents a literature review of pertinent background information. The first section of this chapter explains the additive manufacturing process, specifically the DED process. It provides details about the various process parameters and their influence on the deposited material (material properties and microstructure). The second section provides a background knowledge for tool steel, copper, and functionally graded materials. It goes into details about the influence alloying has on the microstructure and mechanical properties.

Chapter 3 is the material characterization of the wrought H13 tool steel material system. This was conducted to gain a preliminary understanding of the material and have a better understanding of the behavior of the alloy before printing. There were no published journal papers for this work as this alloy has been extensively studied and data collected was primarily used for a baseline. The wrought material was studied in various tempering conditions to examine how the microstructure and mechanical properties changed. Heat treatment involved austenitizing at 1032°C with a 30 mins hold followed by an air quench. This was followed by double tempering at varying temperatures ranging from 300 – 700°C with 100°C for two-hour intervals. A quenched sample was produced with the same austenitizing temperature (1032°C) and hold time but did not receive a tempering heat treatment. This resulted in the wrought in three different conditions: as-receievd (annealed), quenched, and tempered totaling seven samples. These experiments were conducted in-house.

Chapter 4 is the characterization of the DED printed H13 samples by varying scanning speed and powder feed rate. It provides a justification for the purpose and a schematic of each sample. The first set of samples were printed using the Optomec LENS 450XL system at CMQ. Any remaining samples printed were printed in-house using the Optomec LENS 500 MTS-Ca system. Characterization began with the virgin H13 powder using the Hall flow test for the flowability characteristics and microscopy to examine the morphology of the powder. Next, the as-printed geometry, as-printed surface roughness, wear response, as-printed and heat-treated microstructure was investigated when the scanning speed and powder feed rate were varied. From this work, there has been a published journal paper and two that require submission.

Chapter 5 presents the characterization of the FGM of H13-Cu and DSC work conducted on H13 and pure Cu powder. Six different powder blends of varying Cu-content were studied. Two temperature conditions were used: a full melt and a partial melt that was slightly above the melting point of copper. Printing the FGM of H13-Cu was conducted at the Navajo Technical University on an Optomec LENS 500 Hybrid Controlled Atmosphere System using a laser with back-reflection technology to process pure Cu. Printing on a pure Cu substrate was also attempted to find successful printing parameters. From this study, a journal paper on the system parameters and microstructural development of an FGM H13-Cu will be submitted.

Chapter 6 is on surface treatment of pack borided DED-processed H13 compared to wrought equivalent. Data collection and running heat treatments was assisted by Riley Roache. It appears the findings from this study were novel in the field of study of boriding steels. Findings will be presented at the 61st Conference of Metallurgists.

Chapter 7 presents the major conclusions of printing H13 tool steel and an FGM of H13-Cu using a DED system along with future suggestions for the research.

Finally, an appendix is also provided listing the author's dissemination contributions, in the form of journal papers, conference papers and presentations, as well as reports from the research presented in this study.

The research presented in this thesis was conducted from September 2018 to May 2022. All the data collection, sample preparation, or material characterization was completed by the author unless otherwise stated with contributions from others gratefully acknowledged. Writing was completed but the author with assistance from Dr. Plucknett.

Construction of the G-code and preparing the DED system was performed by the relevant technicians at QMC, Dalhousie, and NTU. ICP-OES was conducted by the Minerals Engineering Centre (MEC) staff at Dalhousie University. All DSC testing was conducted by Dr. Eric Moreau with analysis assistance from Dr. Corbin in the High Temperature Thermal Analysis Laboratory (HTTAL). WDS testing was conducted by Danny Macdonald in the Earth and Environmental Sciences Department at Dalhousie University. Any major metal working was performed by the machinists at Dalhousie University and NTU to produce samples.

2 LITERATURE REVIEW

2.1 General Additive Manufacturing Process and Information

Parts intended to be manufactured using additive manufacturing (AM) begin with the operator designing a part using parametric computer-aided design (CAD) software to create a 3D model of the part. The part is then "sliced" into layers using a slicing software. The data from the slicing software is converted to a STL file and transferred to the machine which informs it of the build parameters such as layer thickness, hatch spacing, and energy power, which are selected by the operator based on several design and material factors. Once the information has been received, the machine is set up with the correct feedstock and the construction of the part can begin. AM differs from traditional subtractive methods of manufacturing such as Computerized Numerical Control (CNC) machining, in that material is added to the part as opposed to subtracting material from wrought material. This technology enables material to be deposited or fused in precise locations allowing for complex geometries that subtractive methods cannot produce. Once the printing is complete, the part is removed, and any post-processing is completed. AM is not limited to metal but also includes polymer, ceramics, and bio-organic materials. In industry, AM is commonly referred to as 3D printing, however there are many different AM technologies each with their own benefits and drawbacks. The prominent metal AM technologies today are listed in Table 2.1. This report will focus on ferrous-based AM for DED.

Table 2.1: List of other AM technologies and nomenclature used [1].

Bed Technologies	Free-form Technologies
Laser Powder Bed (L-PBF)	Directed Energy Deposition (DED)
Selective Laser Sintering (SLS)	Laser Powder Fusion (LPF)
Selective Laser Melting (SLM)	Laser Metal Deposition (LMD)
Direct Metal Laser Sintering (DMLS)	Direct Metal Deposition (DMD)
Electron Beam Melting (EBM)	Laser Cladding

ASTM F2792-10 is the standard that governs additive manufacturing and states that it is a layer by layer build process instead of a subtractive process [1]. The ASTM standard F3187-16 is the guide for DED of materials [2]. The flexibility of AM allows it to adapt to a variety of applications that include various industries and material research. One drawback is, AM requires higher system parameter control and materials must be specifically tuned to fit the equipment conditions. This results in more time researching new chemistries and optimizing system parameters for materials. On the other hand, materials that are not suited for traditional manufacturing methods may be suited for AM.

2.2 Laser Technology: Theory and Operating Principles

A laser is the most common power source found on AM systems and they have been extensively studied for welding applications. Lasers are an excellent choice for AM because they are non-contact joining tools that can accurately irradiate specific spots with very minimal heating to the surrounding materials and they are widely available [3]. Lasers deliver a monochromatic beam capable of producing high intensity light energy at very precise locations. Due to this combination of precision and energy input, they are well-suited for AM processes. The different types of lasers commonly employed in AM systems are covered in more detail in the following section. The first requirement of a

laser is to have a gain medium (solid, liquid or gas) that has a specific frequency. The gain medium determines the operating wavelength [3]. Another necessity for laser function, is the use of a pump (power source), which will excite electrons to the required energy level. A simplified set up of a laser is shown in Figure 2.1. When a photon interacts with an electron that has been pumped to a higher energy level, the electron will emit a photon when returning to the ground state. This is known as stimulated emission [4]. The electron is unstable at the higher energy levels and falls to the ground state. This releases a second photon of the same frequency, phase, and polarization [3], [4]. The pump will continuously input energy for the electron to reach a higher energy state. However, for laser operation, the electron is not always at the highest energy level, but at a metastable state just below that higher state. With energy input from the pump, more electrons will be in the metastable region known as population inversion [4]. By having the population of electrons at the metastable energy level, they will all have the same emitted photon energy, frequency, and polarization. When a photon interacts with the first electron releasing a photon, it creates a cascading effect as those photons encounter other electrons, which causes the release of more photons. Finally, a mirror and a partial mirror on the other side of the tube causes constructive interference, called light amplification [4].

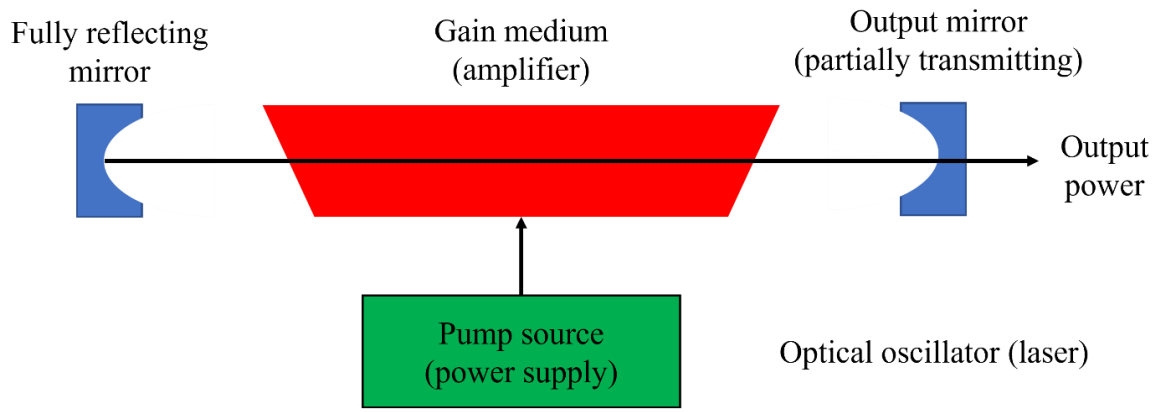

Figure 2.1: Simplified diagram of a laser set up, adapted from [4].

The pump source can operate continuously or in a pulsed mode [4], [5]. In the continuous mode, the pump is supplied with constant power; whereas, in the pulsed mode, it will emit power in short durations [5]. Some lasers used in AM can operate in either state (continuous or pulsed); however, it may be beneficial to operate in the pulsed mode because it allows for a higher peak power than continuous and rapid cooling and heating. In addition, the pulsed mode almost instantly heats the particles with minimal thermal energy dissipation to the surrounding particles [5]; whereas, in the continuous mode, the same average power will be dissipated to the surrounding area [5].

2.2.1 Types of Lasers Employed in AM Systems

The most common lasers include the CO_2 laser, neodymium doped yttrium aluminum garnet (Nd: YAG) laser and the ytterbium fiber (Yb – fiber) laser with Table 2.2 listing the specifications of each laser [5].

Table 2.2: Comparison of the three main laser types currently employed in AM [5].

Laser	CO_2	Nd: YAG	Yb–Fiber
Application	SLM, SLS, DED	SLM, SLS, DED	SLM, SLS, DED
Operation wavelength	9.4 & 10.6 μm	1.06 μm	1.07 μm
Efficiency	5 – 20%	Lamp Pump: 1–3% Diode Pump: 10-20%	10-30%
Output power (CW)	Up to 20 kW	Up to 16 kW	Up to 10 kW
Pump source	Electrical discharge	Flash lamp or laser diode	Laser diode
Operation mode	Continuous or pulsed	Continuous or pulsed	Continuous or pulsed
Pulse duration	Hundreds ns-ten μs	Few ns-ten ms	Tens ns-tens ms
Fiber delivery	Not possible	Possible	Possible
Maintenance period	2000 hrs	200 hrs (lamp life) 10 000 hrs (diode life)	Maintenance free (25 000 hrs)

Each laser has a different gain medium, which in turn dictates the wavelength of the laser. Even though the lasers have high output powers, they typically do not operate at these levels. Operating at such high-power requires cooling systems to avoid damage to the laser system and reduces the electrical energy needed to run the machine. In general, the maximum operating powers reach a maximum of 5 – 6 kW, but this rarely occurs because such high powers are not required to melt the particles for AM-associated processes.

2.2.2 CO_2 Laser

This laser consists of a discharge tube, an electric pump and optics (mirrors, windows and lenses) [5]. CO_2 gas is the gain medium used to fill the discharge tube and is pumped with either AC or DC current to initiate population inversion [5]. A schematic of a CO_2 laser is shown in Figure 2.2. The pump is positioned between a highly reflective mirror and a partial mirror. The entire device is then encased in a water jacket for cooling [5].

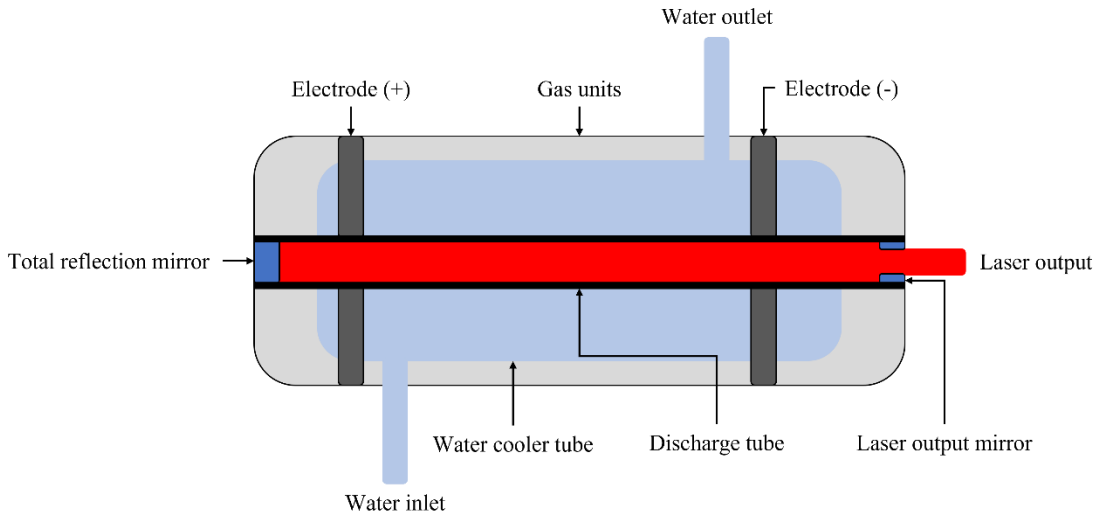

Figure 2.2: A cross-section schematic of a CO_2 laser highlighting the major components, adapted from [5].

These lasers have high efficiency and output power. In addition to being an economical choice these lasers have a simple design that is reliable and compact [3], [5]. However, due to thermal expansion from heating the gas or from gas turbulences, the output power can become unstable [5]. Since the output wavelength is in the infrared region, it suffers from low light absorption. This in turn reduces the amount of materials, especially metals, that can be processed [5]. Fiber lasers are used more frequently due to this limitation.

2.2.3 Nd: YAG Laser

The gain medium for this laser is a solid comprised of a rod-shaped Nd: YAG crystal [5]. The Nd: YAG and the CO_2 lasers are the two most prevalent power sources in AM [5]. A schematic of the laser is shown in Figure 2.3. If a flash (xenon) lamp pump is used, it is optically pumped in the radial direction. Whereas if a laser diode with a wavelength of 808 nm is used, it is pumped in the axial direction [3], [5]. Nd: YAG lasers operate in the

near infrared region, with a wavelength of 1.06 μm for either type of pump source [3], [5]. This allows the light beam to be transmitted through flexible fibers. Using fibers to deliver the beam reduces the overall size of the system and improves the efficiency compared to the CO_2 laser.

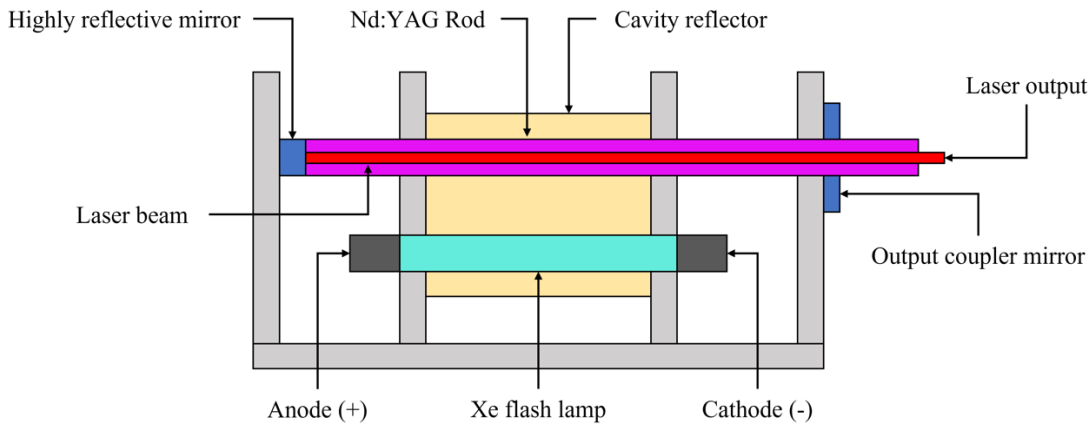

Figure 2.3: A cross-section schematic of a Nd: YAG laser with the major components highlighted, adapted from [5].

To operate continuously, crystals are doped with low concentrations and are capable of output powers of a few kW. Whereas, operating in the pulsed mode, crystals are doped with high concentrations and are capable of reaching 20 kW [5]. If using a xenon flash lamp, the beam quality can suffer. Unabsorbed energy is dissipated as thermal energy (from the pump), resulting in a low electrical to optical power conversion due to thermal lensing and birefringence effects [3], [5]; thus lowering the overall beam quality. In addition, the xenon bulbs have a short life span. A better alternative is to employ diode lasers known as diode-pumped solid-state lasers (DPSS), as the pump source [5]. This pump source allows for selective excitation and has a higher electrical to optical power conversion with a gain in efficiency of ~ 5 times compared to the flash lamp pump [5].

Even with the benefits that Nd: YAG has over the CO_2 laser, they are being replaced with the Yb – fiber laser [5].

2.2.4 Yb – Fiber Laser

Similar to the Nd: YAG laser, the gain medium is a ytterbium (Yb) doped optical fiber [5]. A diagram of a fiber laser set up is shown in Figure 2.4. Ytterbium is selected over other rare elements because it has the highest quantum efficiency [3], [5]. The pumping system consists of laser diodes with a wavelength of 950 – 980 nm, producing an operating beam wavelength of 1.03 – 1.07 μm [3], [5]. The advantages of using this laser include a gain medium with a high electrical to optical efficiency (30%), a compact system, and a system that is robust to environmental disturbances [3], [5].

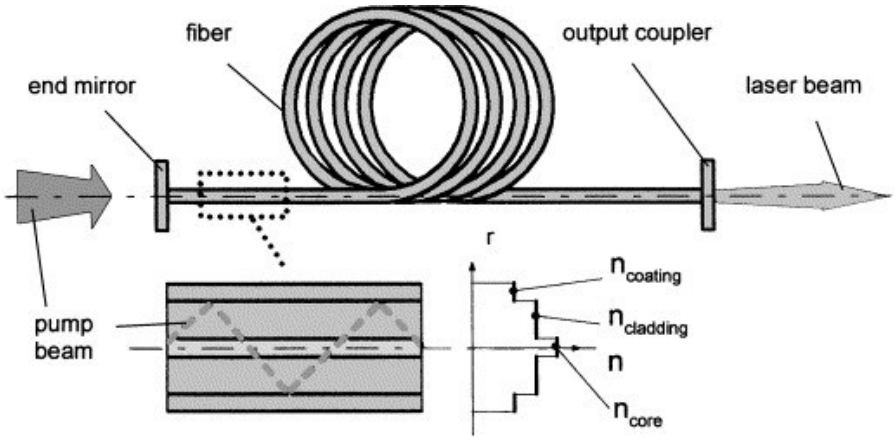

Figure 2.4: A side view of a fiber laser set up with highlighted components, with permission from[6].

Even with these benefits, light travelling through an optical fiber is strongly influenced by the fiber. When operating at maximum power, the beam can self-focus or have self-phase modulation due to optical nonlinear effects. In addition, unpredicted polarization

from bends in the fiber, vibrations or temperature changes will lower the beam quality [5]. Polarization of the fibers is needed to alleviate this problem [5].

2.3 Laser Material Absorptance and Interaction

The interaction between the laser beam and the material being joined is critical to a successful bond. When a beam of light is incident on a material, the beam will be partially reflected and scattered with the remaining being absorbed [3]. There are four main criteria that govern the material interaction including the laser beam wavelength, power, spatial, and temporal characteristics [3]. As a material is being processed, it will absorb photons from the laser beam, exciting electrons to a higher energy state [3]. At the higher state, the electron must remove this excess energy. When the electron is excited, it will be scattered by dislocations or grain boundaries in the lattice, converting electronic energy from the beam into heat [3]. Photon interactions with matter occur between the infrared and ultraviolet region. This leads to an absorption band for metals between 0.2 – 10 μm [3]. In metals, the electron-photon conversion energy is almost instantaneous due to excitation of valence electrons also known as conduction band electrons [3]. The oscillating electrons will interact with other electrons due to the high free electron density. This results in an absorption time of 10^{-16} s from the laser energy [3], [7]. This energy is transferred through the lattice by electron-photon collisions within ≈ 1 ps [3]. As the wavelength of the beam shortens, it will have higher energy than a beam of a longer wavelength. This shorter wavelength will have more energetic photons that can be absorbed by more electrons in the material. This results in reflectivity decreasing and absorptivity increasing [7]. The amount of the reflected incident light beam can be calculated using Equation 1 [7]:

$$R = [(1-n)^2 + k^2]/[(1+n)^2 + k^2]$$

Equation 1: The amount of reflected incident light [7].

Where *n,* is the reflection coefficient and *k,* is the extinction coefficient. Knowing the amount of reflected light (R), the absorptivity can be calculated using Equation 2 [7]:

$$A = 1 - R$$

$$A = 4n/[(n+1)^2 + k^2]$$

Equation 2: The absorptivity based off the amount of reflected light (R) [7].

When the temperature of the material increases, there is an increase in phonon population resulting in more phonon-electron energy exchanges [7]. This causes the electrons to interact with the structure, rather than oscillate, decreasing the reflectivity and increasing absorption, with Figure 2.5 showing the % reflectivity as a function of temperature of common elements [7]. Surface films such as oxide films will also have an effect on the absorption [7]. Another consideration for processing reflective materials is the reflectivity. Metals such as copper can reflect the beam back into the system causing damage [8]. A surface modification can be applied to the substrate to avoid unwanted reflection and can help with absorbance [7]. Tilting the substrate surface or roughening the surface to scatter the laser beam are some of ways of mitigating this problem.

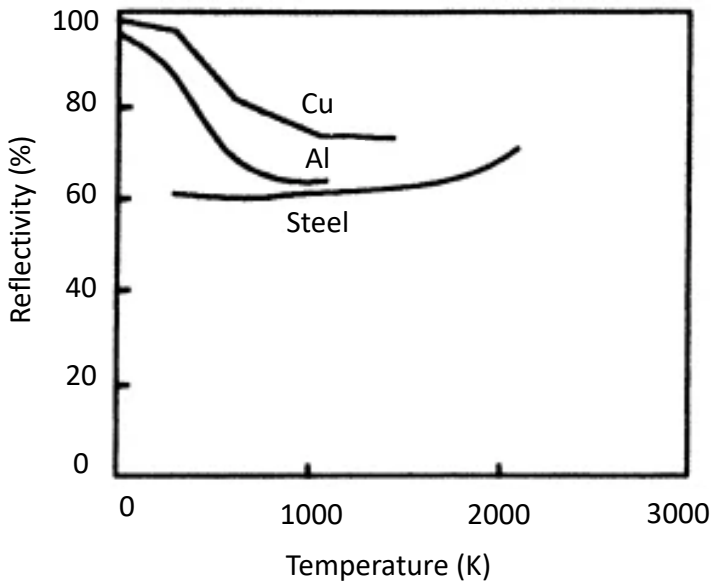

Figure 2.5: Percent reflectivity (%) of Al, Cu, and steel as a function temperature for a 1.06 μm wavelength, adapted from [7].

Table 2.3 shows different surface modifications and how it affects the reflectivity percentage of a 10.6 μm wavelength [7]. However, if the surface roughness is less than the wavelength, the surface will be perceived as flat [7].

Table 2.3: Reflectivity of 10.6 μm wavelength at a normal angle of incidence [7].

Surface Type	**Reflectivity (%) Direct**	**Diffuse**	**Total**
Sandpaper-roughened (1 μm)	90.0	2.7	92.7
Sandblasted (19μm)	17.3	14.5	31.8
Sandblasted (50μm)	1.8	20	21.8
Oxidized	1.4	9.1	10.5
Graphite	19.1	3.6	22.7
MoS_2	5.5	4.5	10.0

Certain operating wavelengths work better for different materials. For example, manufacturing a ceramic, a CO_2 laser would be advantageous because less of the light beam is reflected. On the other hand, if a metal is being fabricated, a shorter wavelength

from the Nd: YAG laser or fiber laser would be better. For AM, a high material absorption is desired because less energy is needed to melt the particles [5]. Since shorter wavelengths have a higher energy density, it is well-suited for metals because it will fully melt the powder which is achieved with either a Nd: YAG or Yb – fiber laser [5], [9]. Table 2.4 highlights the differences in absorption between materials using two different wavelengths.

Table 2.4: Absorptivity of various materials under 1.06 μm and 10.6 μm wavelengths [10].

Material	**Nd:YAG Laser (1.06 μm)**	**CO_2 Laser (10.6 μm)**
	Reflectivity (%)	
Cu	59	26
Fe	64	45
Sn	66	23
Ti	77	59
Pb	79	-
ZnO	2	94
Al_2O_3	3	96
SiO_2	4	96
SnO	5	95
CuO	11	76
SiC	78	66
Cr_3C_2	81	70
TiC	82	46
WC	82	48

2.4 Powder Production

DED technology typically employs pre-alloyed powders, but has the ability to use a wide range of materials, including combining elemental powders to make alloys or using ceramics for cladding surfaces [10].There are many processes that can manufacture powders. However, not every method is suitable for the DED process. Materials suitable for welding, such as metals, make good candidates for material selection; whereas, ceramics become increasingly more difficult due to the higher melting points [11], [12].

There are three main categories in which powder falls: atomization processes, mechanical milling/alloying, and chemical reactions. For this research, the feedstock of concern uses gas-atomized powders for both H13 tool steel and copper.

2.4.1 Atomization Processes

This production method is commonly used as it is cost effective and has a high production output. Typical atomization units are vertical with the melt heated in a resistive furnace in a graphite crucible [13]. In the case of using gas, the melt is enclosed within an inert environment. Tubes are connected to the crucible and delivers the molten metal to converging compressed gas jets [14]. The gas jets disturb the molten metal causing the metal to spheroidize. As the superheat increases, the viscosity and surface tension decreases, resulting in a smaller D_{50} [14]. Powder is then collected at the bottom of the vessel. Gas atomization is capable of manufacturing reactive metals and reduces the oxide layer. This process can be performed with water jets to spheroidize the powder. However, there is a higher amount of contaminates and oxides. The powders produced by gas atomization will have a spherical morphology whereas water atomized powders have an irregular rounded morphology [14]. Both methods allow for a large production volume. For DED technology, gas-atomized powders are favored because they have better rheological properties (improved flowability characteristics) over processes that produce more irregular particles. The PSD and desirable powder characteristics are listed in sections (2.5.2.1) and (2.14.2) respectively.

2.5 Major Additive Manufacturing Technologies

Laser Powder Bed Fusion (L-PBF) and Laser Powder Fusion (LPF) are the two dominant styles of metal additive manufacturing techniques that builds layers in different manners. Each style presents its own benefits and drawbacks. The most popular type of technology currently employed and researched is L-PBF, where a layer of material is spread across a print bed and consolidated with a high-power heat source. Powder bed allows for precise builds but is a slower process. The counterpart to powder bed technology is LPF, where a build plate is not required. LPF allows for the deposition of material to be placed in specific spots directly onto an existing part that needs fixing, or an entirely new part can be built on a substrate. However, this technology is not as well researched, so benefits and drawbacks are still being discovered. For both technologies, new material combinations are constantly being developed for AM, as it does not follow conventional methods of manufacturing practices.

2.5.1 Laser Powder Bed Fusion (L-PBF)

This technology involves depositing powder metal, smoothing it to create a uniform layer, then selectively sintering or fusing the particles to produce a part [11], [15]. A general layout of L-PBF process is shown in Figure 2.6. The heat source is either a laser or an electron beam that is directed towards the powder bed causing a precise location of powder to melt, forming a thin layer. Once that layer is completed, the build plate is lowered by one-layer thickness and a new layer of powder is deposited [11], [16].

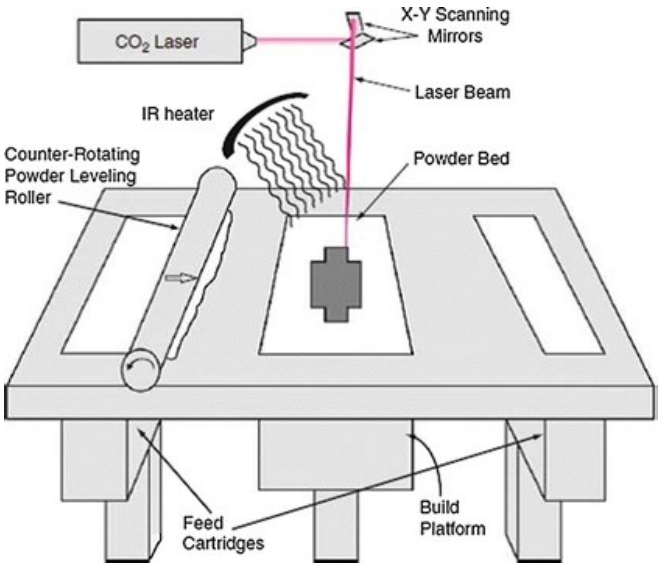

Figure 2.6: Schematic of a L-PBF machine with highlighted components, with permission from [11].

An inert gas is pumped into an enclosed chamber across the build plate to create an inert atmosphere to reduce the amount of oxidation during building [11], [16]. The build platform is heated to below the melting point of the material using heaters. The powder is then heated in the feed cartridges concurrently before being spread across the build platform using a counter rotating roller or blade to level the powder [11]. Pre-heating the powder and built platform has two major benefits. By pre-heating the powder near the melting temperature, the power needed for the laser to melt is reduced [11]. This also helps to create a smoother transition between layers due to the smaller temperature gradient [16]. For L-PBF processes, the build platform is typically heated to 473K [17]. In general, pre-heating reduces warping, internal stresses between layers, and nonuniform expansion and contraction [11], [16]. After a layer has been sintered, the build platform is lowered, and the process repeats itself. Any loose powder that has not been fused remains on the platform and acts as supports for the consolidated powder, removing the need for

secondary supports in certain cases [11]. In addition, loose powder can be recycled for future use [16]. Once the process is completed, the part is allowed to cool for safe handling and post-processing can be completed [11].

EBM follows a similar process to L-PBF in that a thin layer of powder is spread across the build platform and selectively fused to create layers. However, this process takes place in a vacuum with an electron beam that is controlled by electromagnetic coils [1], [15]. Another difference is that the build platform is pre-heated to above 923K [17]. For L-PBF, the feed is usually coated powders; whereas, for EBM it uses uncoated pre-alloyed powders [15]. L-PBF requires a particle size of ~ 35 μm diameter on average and EBM requires an average diameter of ~ 77 μm [18].

2.5.2 Directed Energy Deposition (DED)

This style of AM technology does not require a build platform and is capable of depositing material onto an existing part or onto a platform (substrate). DED, also commonly reported as LPF, systems consist of a heat source, positioner, feedstock feed mechanism, and a control system [2]. This technology uses a focused energy source (typically a laser, electron beam, or plasma arc) that melts depositing powder onto the substrate melt pool [1], [11], [12], [15], [19]. The material feedstock is deposited directly onto the substrate. Since this process does not require a build platform and has the capability of printing onto an existing part it, enhances the flexibility of the technology [11]. Pre-heating is possible to help with residual stresses but since these print on a larger scale, this becomes difficult. The most common energy source is a laser. The types of lasers used will be covered later in the report.

2.5.3 DED – Feedstock Delivery Mechanism

The delivery system for a powder DED system involves hoppers for storage, tubing for transport, , a carrier gas or ultrasonic vibration in some cases [2]. For improved flow, the powder is either fluidized with a gas or ultrasonically vibrated [2], [11]. Since the kinetic energy of the carrier gas is greater than gravitational forces, nonvertical deposition is possible [11]. Simpler systems employ a gravity feed [2]. An auger is used for moving the powder from the hopper(s) and is accompanied by a carrier gas that can accurately delivery the correct amount of powder [2]. Powder size ranges from 5-150 μm, but commonly 50 – 150 μm is used as smaller particles have poor flowability [2], [20]. The main benefit of the shielding/carrier gas is to reduce oxidation [2]. Care must be taken to avoid distorting the melt pool when using a carrier gas. A balance between driving the air away and introducing the shielding gas must be taken into consideration [10]. The carrier gas serves to reduce the amount of sputter and fumes from hitting the nozzle, which helps keep the optics clean.

2.5.4 DED – Nozzle Head

The nozzle head contains the laser optics, powder nozzle(s), shielding gas tubing, and in newer editions, sensors [9], [11]. An example of a co-axial (Figure 2.7(A)) and single (Figure 2.7(B)) feed nozzle is shown in the figure below. For a single feed nozzle, the powder is blown directly into the laser. On the other hand, for a co-axial feed nozzle there can be feed arrangements of triple (120°), quad (90°), or concentric annular feed ports around the nozzle [2].The tip of the nozzle operates within a few centimeters; therefore the nozzle material needs to be able to withstand high temperatures and reflected energy [2]. If operating with a fiber laser, the beam is delivered through a fiber to the nozzle

along with a collimator, so the beam will pass through the focusing lens [2]. Operating at higher powers requires the lenses to be cooled [2]. The focal length will range from 150 - 200mm [2]. Finally, the beam passes through a cover glass intended to protect the sensitive focusing lens and will require cleaning if it becomes too dirty because it can distort the beam quality [2]. The collimated beam is commonly focused with a transmissive lens, but a reflective lens can be used for higher temperatures [2]. If the system is using a CO_2 laser, the beam comes directly from the laser [2]. Lately, sensors such as thermal imaging cameras and closed-looped systems are being added to the tip of the nozzle to monitor the melt pool in real time in order to make adjustments if needed [2].

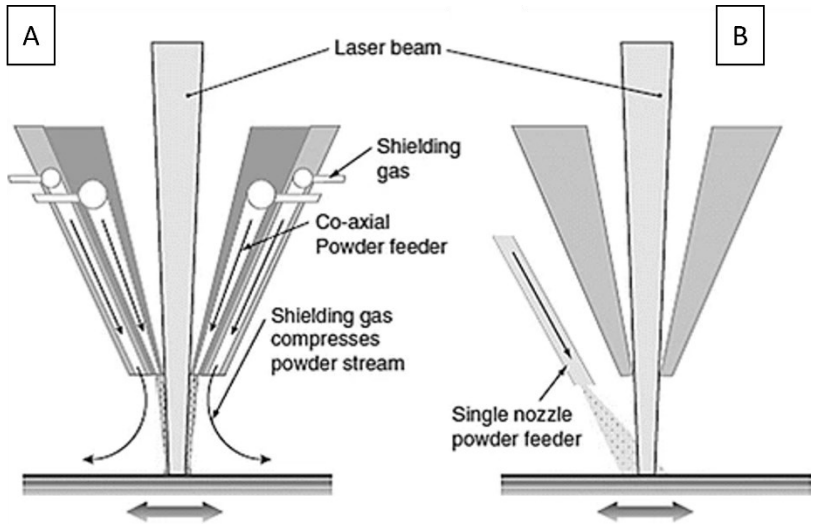

Figure 2.7: A cross-section view of a DED nozzle system: (A) a co-axial powder feed system and (B) a single-powder feed system with components highlighted, with permission from [11].

2.5.5 DED - Movement Mechanisms

The movement for a DED system can be complex because the process is not limited to printing on a flat surface, instead it allows for deposition onto an existing part with changing topography. If the part has an irregular surface, it will require multiple movement directions. With the combination of nozzle and substrate movement, operators have increased flexibility of material deposition. Motion commonly occurs in one of three orthogonal directions including the nozzle moving over a stationary component, or moving the component relative to a stationary nozzle, or a combination of the two [1], [2], [11], [12], [20]. If the part is large, it is more convenient to move the nozzle head. Whereas, if the part is small or flat, the nozzle is fixed and the substrate moves [11]. Linear movement is accomplished by either a ball screw, toothed belt, rack and pinion, or another system [2]. Robotic 4- to 6-axis systems can be employed for even greater design freedom [11], [12]. This allows for rotation, tipping, and titling of the part, nozzle, or both, but this can also influence the melt pool shape, potentially requiring a limit to what can be implemented on extreme angles [2].

2.5.6 Enclosure Atmosphere and Shielding

Due to the reactive nature of most metals with oxygen, nitrogen, and water, care must be taken to reduce the concentration of these gases as they will promote defects such as unwanted carbide formation and entrapped gases in the final build. The most common atmosphere is a vacuum with an inert gas purge [2]. The next layer will have difficulty fusing and may cause porosity if oxygen is present in the atmosphere, as the previous layer has formed an oxide layer. A common threshold for oxygen content is 100 parts per million (ppm) [2]. When using a powder feedstock, a vacuum is not recommended

because there is already an inert carrier gas that adds to the vacuum pumping load [2]. Argon and helium are the most common inert gases used with a powder feedstock. Care must be taken not to have an excessive carrier gas flow rate as it will cause air turbulence, entrapping air and blowing powder away [2].

2.5.7 Post-Processing

After a build has been completed, the deposited material will have internal thermally induced stresses. An effective way to remove these stresses is to apply a stress relieving heat treatment [2]. In addition to a stress relieving heat treatment, tempering can be applied as well. Since the resolution of DED is not as fine as L-PBF, surface finishes such as machining, grinding, or any other required finish must be done [2]. Lastly, to increase the density and reduce the amount of internal porosity of the final part, hot isostatic pressing (HIP) may be applied [2].

2.5.8 Applications of DED

With the flexibility that DED offers, it can be applied to unique cases where other AM technologies are not well-suited or are not capable. Since the substrate can be an existing part or a traditional flat substrate, it is used to clad, build 3D parts, and deliver multiple different materials which opens a wider application potential. An area that is well-suited for DED is repairing and remanufacturing worn parts instead of purchasing new components where fixing expensive turbine blades/vanes is possible [10]. An advantage of using DED technology is that it can form significantly thicker coatings than other hard facing technologies such as physical vapor deposition (PVD) and chemical vapor deposition (CVD) [21]. Cladding of ferrous-based alloys has the benefit of reduced cost and are heavily researched. DED creates a metallic bond instead of a mechanical bond

created by a spray process [10]. Cladding and hard facing of molds, dies, and other components is another major application of DED because not only can it deposit tool steel, but it has the ability to deposit hard ceramics [10], [22]. The microstructure and composition can be tailored by changing the system parameters [11]. This offers the possibility of FGMs and other new material combinations. The major industries for this technology include manufacturing, aerospace, defense, energy, and automotive where it is more economical to repair or make near-net shape parts by reducing the number of parts in a component [20].

2.6 Printing Characteristics

Due to the interconnected system parameters, the molten material will experience vastly different conditions compared to traditional casting methods. For this reason, analyzing the melt pool is important because it can be tailored to obtain preferred phases. Since AM is a layer by layer process the previously deposited layers will experience cyclic heating that will change the microstructure and properties. To combat this uncertainty, there is research into real time process monitoring and thermodynamic modelling of non-equilibrium systems.

2.7 Melt Pool Characteristics

In DED processes, a small melt pool is generated (0.25 – 1 mm in diameter and 0.1 – 0.5 mm in depth) on the substrate as a precise amount of material is being deposited at the same time [10], [11]. Since this process melts the depositing feedstock, layers attain a high density [11]. Once the laser beam moves away, the material rapidly solidifies. With the rapid scan speeds, solidification rates can reach 10^3 – 10^5 °C/s, depending on process parameters and material properties [11]. With such extreme cooling rates, unique phases,

and microstructures are possible which were previously not obtainable under normal manufacturing methods [11]. If the scan rate is reduced or energy power increased (*i.e.,* slower cooling rates), the microstructure will begin to resemble that of a cast structure [11]. Under certain conditions, material undergoes melting during flight; however, this is abnormal and the process parameters try to keep this from occurring [11].

Using new sensing and monitoring equipment, the melt pool can be dynamically controlled. This ability to control the melt pool in real time allows for consistency between parts, which reduces the amount defects and material wastage. The delivery of the feed is the main concern for maintaining a consistent melt pool shape and size [10]. By maintaining a dimensionally stable melt pool, it reduces the size of the heat affect zone (HAZ) [10]. Since the melt pool stability is highly dependent on other process parameters such as laser power, spot size, feed rate, and scan speed, they will be covered in further detail in the next section.

2.8 Thermal History

During printing, complex thermal histories will develop that closely resemble that of multiple pass welds [10], [11]. When the nozzle makes passes, changes in the cooling rates and heat build-up can occur especially in thin-walled sections. If the wall is too thin, the heat cannot be dissipated fast enough, and the desired result may not be obtained. As well, depositing new layers will affect previous layers, thus inducing different microstructures, melting of previous layers, and phase transformations [10], [11]. The same part can contain a variety of these changes in a single part generating anisotropic properties [11].

Due to the rapid solidification of this process, the microstructure exhibits a layer structure with an extremely fine solidified region. The interface typically displays no visible porosity, with a narrow HAZ [11]. Due to the complicated thermal history, residual stresses will build in the part resulting in potential warping and crack formation [10]. This limited control of the microstructure/phase transformations and residual stresses is a major hurdle for this technology. Understanding how these problems develop will help with improving the quality and consistency of DED leading to wider adoption in industrial applications [11].

2.9 Dynamic Process Monitoring

To improve the quality and reproducibility of prints, a major area of AM includes in-situ monitoring [23]–[25], with this list not being exhaustive. This is a closed loop system that dynamically monitors the conditions during printing and helps maintain consistency [11]. For DED processes, melt pool size, temperature, and layer height are the parameters most commonly monitored [11], [26]. High-speed cameras and photodiodes measure the electromagnetic radiation from the melt pool. With a closed-looped system, the melt pool can be kept within a certain range helping reduce porosity or over-melted zones [26]. Pyrometers have been studied for DED to help determine the melt pool temperature, solidification, and layer geometry. As well, closed-looped systems have been developed to select areas for the next deposition path to avoid pre-set temperature thresholds [26].

2.10 Thermodynamic Modelling

As thermodynamic models improve in accuracy and complexity, the ability to predict the material compositions, non-equilibrium phases, and microstructures will assist in narrowing down the optimal process parameters. This area will help manufacturers

understand what problems may happen in the print before the process has started and can suggest new solutions. It will allow for a better understanding of the physical metallurgical phenomena [27]–[30]. When modelling this type of non-equilibrium process, many thermodynamic assumptions are made based on existing knowledge. However, mesoscale modelling has been considered as it offers a flexible method of investigating the thermodynamics of the melt pool based on the powder scale [30].

2.11 DED Process Parameters

DED printing is comprised of five critical process parameters that will influence the quality of the print, with several of these parameters being interconnected. The five major parameters that influence the print quality and time are listed in Table 2.5. There is a subset of parameters for each major parameter. Values for each parameter will not be listed as settings will change for different material systems and machines. As well, the geometry of the part will affect how the material will be printed. This section is intended to give a general description of the different parameters in the DED process and how they will impact the overall print quality and time. By optimizing the parameters, the desired shape, microstructure, and quality of the print can be achieved.

Table 2.5: Critical process parameters subdivided into specific system settings for a DED system.

Parameter	Subsection
Laser	Power, spot size, surface tension and wettability
Scanning	Scan speed, scan patterns, hatch spacing
Powder	Layer height, particle morphology & characteristics
Environment	Pre-heating, atmosphere and shielding gas

2.12 Laser Parameters

2.12.1 Laser Power

This is arguably the most important parameter in the system as a laser is an excellent choice for melting powder because it is contactless and has localized heating. The power input determines if you will have full fusion of the particles or if you sinter the particles. To reiterate, the power requirements will depend strongly on the chemistry of the feedstock. A common measurement to calculate the power of the laser beam for DED uses Equation 3, referred to as the energy density [16], [31].

$$E = \frac{P}{vd}$$

Equation 3: Laser beam energy density [16], [31].

Where P is the laser power (W), v is the scan speed (mm/s), and d is the spot size (mm). According to this equation, if the power of the laser increases, or the scan speed decreases the energy density will increase. Generally, the spot size is a fixed value. If the energy density is too low, there will be a lack of fusion and if the energy density is too high there will be excessive dilution [12]. As laser power increases, the width of the depositing layer increases which is caused by more powder being fused during melting leading to a rougher finish [12]. The power input greatly affects the surface finish of the part; if the surface finish is poor, the fatigue life of the part is reduced. The amount of energy input into the powder will be a major factor in the cooling rate, with scanning parameters contributing to this as well. Along with power, the laser mode type (continuous or pulsed) should be considered. On the other hand, in the pulsed mode, the

laser is turned on and off causing rapid heating and cooling of the powder, thus resulting in a more refined microstructure [32]. However, changing the frequency of the pulse may only lead to a minimal increase in hardness when power remains constant [32]. When operating at higher powers (above 1 kW), cooling is considered and using powers beyond 4 kW cooling systems are required [2]. At these high temperatures, powder can begin to clog the nozzle and optics can be damaged or become distorted [2].

2.12.2 Spot Size

The spot size is the area the beam covers on the substrate given by a diameter measurement. The laser beam is focused onto the substrate using lenses and mirrors. Thermal lensing which causes the shape of the beam to change can occur when operating with higher powers; therefore, a cooling system is required to help mitigate this effect. The depth of focus is the distance over which the focused beam has approximately the same intensity. This is defined by the distance over which the spot size changes by ± 5% [7]. The diameter of the spot size will determine the quality of the part, with a larger diameter generating a rougher surface finish, and lowering the resolution of the part [5].

2.12.3 Surface Tension and Wettability

This phenomenon governs the capillary and wetting forces that occur in the melt pool. Currently, this process is documented heavily for pure metals. Other alloy systems have not been evaluated as extensively; therefore, there exists only thermodynamic approximations [31]. When surface tension forces overcome the combination of fluid, gravitational, and adhesion forces the molten melt will form a ball. This can lead to balling on the surface, which is undesirable [11]. Balling is influenced by laser power and scanning speed. If laser power is held constant and the speed increases, balling will be

more likely to occur. For the DED process, wetting involves the molten material and the previously solidified layer [9]. Wetting of a liquid to a solid is related to the surface tension of solid-liquid γ_{sl}, solid-vapor γ_{sv}, and liquid-vapor γ_{lv} interfaces with the wettability defined by the contact angle θ, using Equation 4:

$$\cos\theta = \frac{\gamma_{sv} - \gamma_{sl}}{\gamma_{lv}}$$

Equation 4: Wettability contact angle [9].

As cos θ goes to 1, the liquid will wet the solid [9]. Additionally, the spreading of the liquid (*S*) has been defined as:

$$S = \gamma_{sv} - \gamma_{sl} - \gamma_{lv}$$

Equation 5: Spreading coefficient of a liquid [9].

A large *S* value is preferred as it will favor spreading of the liquid. If $\gamma_{sl} > \gamma_{sv}$ and $\theta > 90°$, the liquid will spheroidize, reducing its surface energy and will not wet the substrate [9]. Any oxide on the previously solidified layer will impede the wettability of the new deposit and will likely cause balling [9]. The viscosity of the melt will determine its ability to spread on the previous layer. The viscosity of the melt will decrease with increasing temperature and improve the rheological properties of the melt pool, thus leading to better densification [9].

2.13 Scanning Parameters

2.13.1 Scanning Speed

The speed of the beam, as previously mentioned, will affect the energy density, ultimately determining if the powder will melt or remain as individual particles. As the speed increases the energy density will decrease. This causes the melt pool to shrink but will increase the cooling rates [11]. There is a tradeoff for trying to decrease the print time (*i.e.,* faster scanning speeds) while producing mechanically sound parts as faster scanning speeds will distort the melt pool, risking porosity and dimensional issues from melt pool instability. In addition, if the scan speed is reduced there will be a build-up of heat causing more tempering and further changing of the microstructure of the lower layers [12]. Since DED creates a melt pool, the speed will influence its shape. Increasing the speed of the process will cause the shape of the melt pool to change from an elliptical shape to a narrower pear or tear drop shape [33]. This will create large temperature gradients which will influence the direction of the growth. The increased speed and changing melt pool shape will contribute to cracking and unwanted microstructures [12]. Furthermore, the increased speed may cause higher residual stresses perpendicular to the deposition axis [34].

2.13.2 Scanning Patterns

The purpose of designing specific beam paths is to alleviate the build of residual stresses in the part. Subsequent layers are placed in specific patterns of multiples of 30°, 45°, 90°, or are randomized [11]. Anisotropic properties caused by preferential grain growth from previous layers are alleviated by changing the layer orientation. Another benefit of

changing the layer orientation is that excess powder will dynamically level, thus improving the surface finish [11], [16].

2.13.3 Hatch Spacing

The tool path is comprised of multiple lines that are separated by a hatch spacing [31]. For a sound bonding and densification, there must be overlapping of lines [10], [16]. Often, the hatch spacing is less than the diameter of the beam [16]. Shown in Figure 2.8, ideal hatch spacing occurs when the negative space (A1) above the overlap (A2) is equal to each other with the excess powder expected to fill in the negative space [34]. The scanning strategy also helps reduce the negative space. Since an ideal hatch spacing is unrealistic because the melt pool may grow or change in shape, the hatch spacing is dynamically changing [34]. To achieve high density parts, the hatch spacing can either be small with a low energy density or a large spacing with a higher energy density [31].

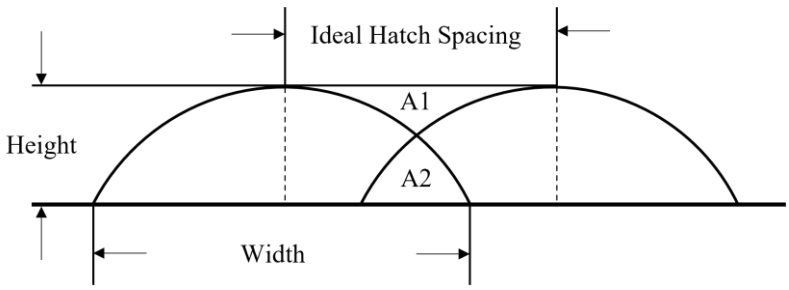

Figure 2.8: Ideal hatch spacing for the DED process, adapted from [22].

2.14 Powder Parameters

2.14.1 Layer Height

Like most parameters in DED, the layer thickness is influenced by laser power, powder feed rate, scanning speed, spot size, and is critical to ensure that bonding to the previous layer occurs [11], [12]. For example, if the powder feed rate is increased, the layer height will increase. Similarly, if the laser power is increased and scanning speed is reduced, the deposit height increases [11]. On the other hand, if the scanning speed is increased the height will decrease [5], [12]. In addition, the thickness of the layer will affect the build time and surface finish, with thicker layers having faster build times but may lead to under-building because the nozzle head raises faster than the consolidated material. The opposite is true for thin layers, which are likely to consolidate more material leading to a larger programmed layer thickness.

2.14.2 Powder Morphology and Characteristics

This parameter is strongly related to the powder feed rate and layer height. Powders should exhibit good flow properties so even layers can be produced. Spherical particles are the preferred shape as they exhibit the best flow characteristics. The particle size distribution should not be fine because flowability issues will be encountered, potentially resulting in the inability to flow [2],[35]. The shape of the particle has an influence on the layer height and melt pool temperature. As the powder feed rate increases, the number of spherical gas-atomized particles is greater than water atomized particles. This is because the water atomized particles are more irregularly shaped, locking together and reducing the flowability, which is the opposite of gas-atomized powders. The second effect of the irregular water atomized powders is that they scatter more of the laser energy which

results in more melting [36]. Figure 2.9 shows the melt pool temperature of gas and water atomized 316L and H13 with increasing powder flow rates [36].

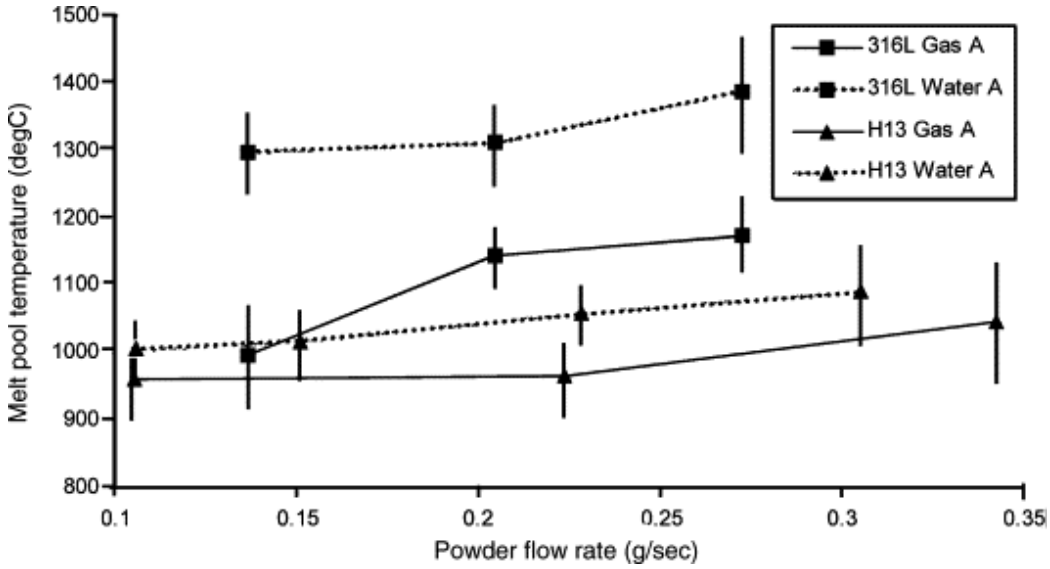

Figure 2.9: Melt pool temperature during deposition of straight walls for varying flow rates of gas and water atomized, 316L and H13 powders [36].

The greater likelihood of fully melting will improve the surface finish of the part by filling in dips. Depending on the production method, the oxide layer is thinner on the gas-atomized powder than the water atomized powder. The gas-atomized powder has a higher reflectivity, with 82% reflected versus 69% when using a CO_2 laser wavelength (10.6 μm) [37]. In addition, the composition of the powder must be known to determine laser power requirements [2].

2.15 Substrate Temperature Parameters

2.15.1 Pre-heating

The substrate and powder may be pre-heated, depending on the system, but offers two main benefits. First, it will reduce the amount of laser power necessary for melting the powder as less energy is required for fusion. Secondly, pre-heating the substrate will reduce the amount of warping and residual stresses [11]. In addition, pre-heating the substrate allowed for better bonding in some cases as previous attempts were unsuccessful on a cold substrate due to the formation of cracks [38]. The cooling rate of the deposited material will change depending on the severity of the substrate pre-heating. Furthermore, powder feedstock is pre-heated in the beam and then reabsorbed into the melt pool [39].

2.15.2 Atmosphere and Shielding Gas

The enclosure atmosphere is precisely controlled, especially when printing reactive materials. This is done to help reduce the amount of oxidation which can lead to poor bonding and defects. The enclosure commonly consists of an inert gas purge in a vacuum with an oxygen threshold around 100 ppm. In addition, the inert gas has the ability to fluidize the powder for delivery, thus increasing the convection and lowering the solidification time. However, if the shielding gas flow rate is high it can blow powder away or entrap gases both resulting in porosity.

2.16 Summary of System Parameters

Material reflectivity and absorptance are important material characteristics that need to be considered and if it not accounted for, beam reflection can damage equipment. The wavelength of the laser will also determine the amount of absorptance. For metals and

carbides, as the wavelength decreases, the absorptance increases. It is the opposite for oxide absorptance [9]. The correct PSD should be used because as the particle size decreases, the powder flowability decreases, and the incorrect amount of powder will be dispensed. *Hentschel et al.* reported that an addition of 0.5 wt.% carbon nanoparticles to gas atomized H11 tool steel powder was no longer capable of flow and could not be used [40]. The part complexity will influence the cooling rate and dimensional accuracy of the final build. Another important characteristic to consider is the wetting of the deposit material. If improper wetting occurs, the deposited material will not form a metallurgical bond and the part will have porosity or will completely fail. Pre-heating is another consideration as it will influence the cooling rate and the formation of phases leading to a coarser structure. Pre-heating has an added benefit of reducing residual stresses especially at the deposit substrate interface [38], [41].

2.17 Benefits and Limitations of DED Compared to L-PBF

AM technology is becoming increasingly more popular as the price of machines and powders are reducing in cost. Even though more research is required for larger implementation, the benefits of this technology for novel parts and complex geometries are nearly unmatched. This technology allows for cladding applications and manufacturing of three-dimensional parts with the laser as a contactless joining device. This technology allows for in-situ part repair and cladding where high wear resistant materials can be deposited [11]. Deposition of material onto irregular surfaces is a major advantage over L-PBF systems which require a proprietary build plate of fixed area to remain level and contained within an enclosure, whereas DED is not limited to the part size where open atmosphere systems are available. Since the beam interacts with the

surface for a very short period of time, there is minimal part distortion and a small HAZ [7]. FGM's are possible with a multi-hopper feeding system with an added benefit of reducing system down time between switching materials.

This technology also suffers from certain limitations including poor resolution compared to L-PBF due to the larger powder sizes (*i.e.,* larger PSD). The increased particle size means that intricate parts are not possible and will require extra post-processing. During DED, residual stresses will inherently develop in the print. To remove these residual stresses or to create the desired microstructure, post heat treatments are commonly used [11]. Furthermore, printing will cause the part to have anisotropic properties because of the thermal cycling. Lastly, there is a high initial investment for this technology which may deter companies from purchasing, thus reducing the amount of research being conducted in this field. Table 2.6 contrasts the differences between laser powder bed fusion and DED technologies, since these are similar laser-based AM styles that build layer-by-layer but have their respective advantages and disadvantages. This is a simplified comparison where the user must determine the correct processing route depending on the parts application and engineering requirements.

Table 2.6: Comparison between laser-based powder bed and blown powder technologies where "↑", "↓", and "=" indicates more advantageous, less advantageous, and equal respectively.

Parameter	Laser-based AM Style	
	Laser Powder Bed Fusion	DED
As-printed resolution	↑	↓
Deposited Volume/Time	↓	↑
Material Selection	=	=
Feedstock Flexibility	↓	↑[a]
Print Volume	↓	↑
Design Flexibility	=[b]	=[c]
Power Source	=	=
Safety	↓	↑[d]
Atmosphere	↓	↑

[a] Allows for powder and wire feedstocks.

[b] Ongoing research for multi-material FGM powder technologies [42].

[c] Cladding, repair, 5-axis, and multi-hopper capabilities.

[d] Coarser particle size distribution.

2.18 Heat Treatments

For tool steels to be effectively employed, a heat treatment is applied before the tool enters service. Typically for tool steels this involves heating the sample to the austenite (γ) region as seen in Figure 2.10, known as austenitizing, and the sample soaks in this region for a certain amount of time depending on the chemistry and to allow for diffusion of carbon and alloying elements to enter austenite [43]. Then the sample is quenched from the austenite region to room temperature in a cooling medium (air, water, or oil) creating a new non-equilibrium phase called martensite (α'). A simplified quench and double temper heat treatment cycle is illustrated in Figure 2.11. The sample then undergoes tempering, which is when the sample is heated to a temperature below the annealing temperature (critical temperature, A_1) to improve toughness, precipitate alloy carbides, and temper the martensite. Depending on the chemistry the tempering temperature will vary and generally takes several hours at a selected temperature. This tempering process can be repeated for a second or third time according to the steel type. The temperature at which tempering will influence what type of carbides that will form and cause them to grow in size. Research into the specific heat treatment of the tool steel must be done as austenitizing temperature, quench medium, and tempering temperature and time will vary.

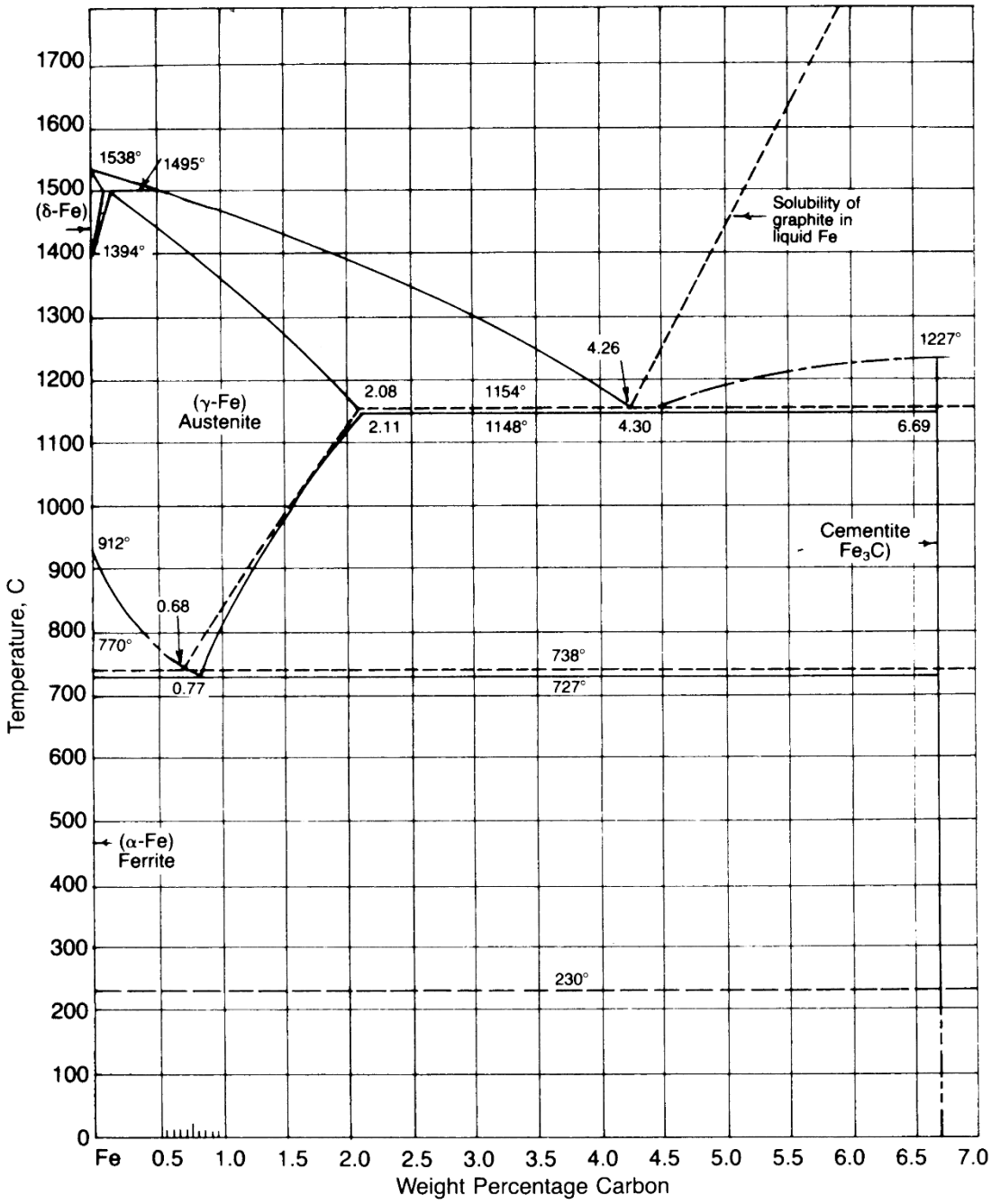

Figure 2.10: Fe-C phase diagram, with permission from [44].

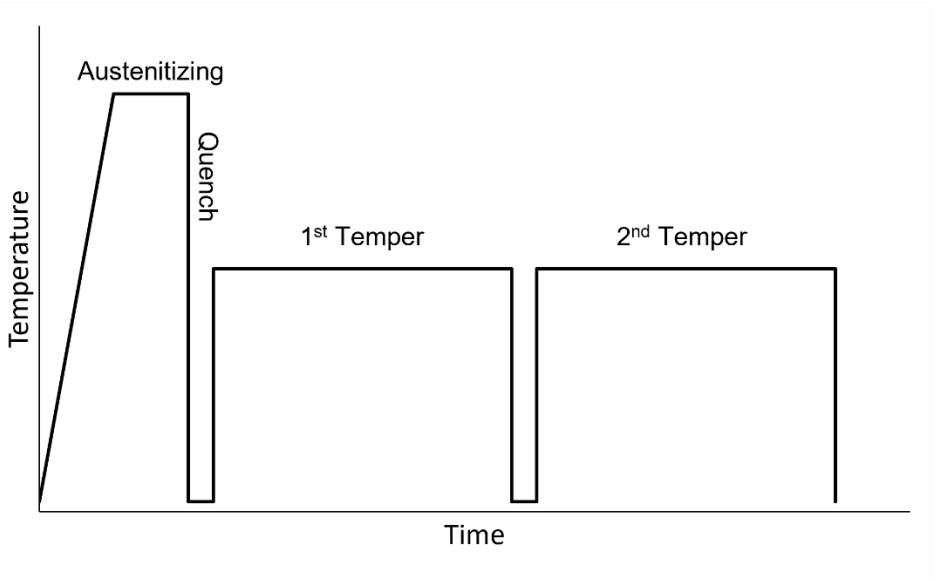

Figure 2.11: Common heat treatment cycle applied to tool steels involving a quench and double temper.

2.18.1 Austenitizing

The first step to heat treating a tool steel involves heating the component to a certain temperature in the austenite region. When the sample passes the eutectoid temperature (A_1), it undergoes an allotropic phase transformation from α-iron to γ-iron. This phase change causes the crystal lattice to change from a body-centered cubic (BCC) to a face-centered cubic (FCC) crystal structure. Austenite is a stable equilibrium phase that has a FCC structure that exists at elevated temperatures and can be retained depending on the alloying contents and cooling rate [45]–[47]. This phase is important because in order to form martensite in steel, it must first be austenitized; whereas, if cooling occurs under equilibrium conditions it will form ferrite and cementite. As in ferrite, the carbon atoms are in the octahedral interstitial sites and with increasing temperature, the solubility increases, austenite has even higher carbon solubility because of the FCC structure [45],

[48]. Austenite can be retained at room temperature if sufficient quantities of austenite-stabilizing elements, such as Ni and Mn, are added which lower the M_s transformation temperature [45], [49]. As the alloying content increases, it will lower the M_s temperature allowing for more austenite to be retained at room temperature [48]. Tempering the retained austenite will cause it to transform into ferrite and cementite between the martensite plates and laths [48]. If the prior condition of the steel contains evenly distributed carbides, austenite will form at a faster rate above the subcritical annealing temperature [46]. Lower austenitizing temperatures in the intercritical range will result in an inhomogeneous austenite, promoting spheroidal carbide formation [46].

2.18.2 Quench and Tempering

During quenching, it is possible to obtain metastable phases not predicted by an equilibrium phase diagram and allows for extended solid solubilities [33]. This rapid quench will result in a finer grain structure and finer secondary dendrite arm spacing [9], [33], [50]–[52]. Quenching will induce significant residual stresses because of the different cooling rates on the surface and the core [43]. Carbide precipitation can be rapid if the cooling rate is relatively high [43]. The purpose of tempering the material is to improve the mechanical properties, namely ductility, toughness, and hardness, after quenching [33], [46], [48]. Quench and tempering will inherently occur in AM parts due to the thermal cycling. This heat treatment involves heating the material below the austenitizing temperature and is used to improve mechanical properties caused by quenching [33], [46]. Martensite provides excellent hardness and strength; however, the material's toughness and ductility are greatly reduced. In tool steels, the microstructure generally consists of untempered martensite, retained austenite, and carbides [43], [46].

When a martensitic structure is tempered (as the laser makes subsequent passes), different reactions will occur. The temperature ranges listed are time and temperature dependent, so some reactions may not be encountered during printing. In the temperature ranges between 100 – 200°C, precipitation of iron carbides occur [33], [48]. Temperatures between 200 – 350°C results in tempered martensite and causes the retained austenite to transform into ferrite and cementite [33], [48]. Tempering temperature between 250 – 750°C causes greater formation of ferrite and cementite, as well as spheroidized carbides [48]. When the steel is re-heated, carbon atoms begin to diffuse and start to react with the iron to form cementite [46]. Tempering between 500 – 700°C causes alloy carbides to begin to form with Cr, Mo, V, and W, with the composition of the carbides changing if held for extended periods of time [48]. Since tool steels have more alloying additions that form carbides, tempering between 400 – 600°C will result in more stable carbides containing Cr, Mo, V, or W than cementite [45], [46]. These alloy carbides are capable of secondary hardening where the matrix becomes even harder due to tempering [45], [46].The formation of these alloy carbides with carbon are determined by the activation energy provided, the diffusivity of the element, time and temperature [43], [45]. These alloy carbides have a low diffusivity which results in a finer carbide and will take longer to coarsen, along with maintaining hardness at elevated temperatures [43], [45], [46]. The strong carbide formers such as Cr, W, V, and Mo that undergo secondary hardening must first be dissolved in the austenite and trapped in the martensite during quenching [43]. The secondary carbides that form will begin to form as needles or plates. The carbides with multiple alloying elements will resist coarsening and have high stability [43]. However, before ferrite is formed, fine carbides will develop in

the tempered martensite due to the slow kinetics at lower temperatures [43]. If the tempering temperature remains between 375 – 575°C there can be a loss of toughness known as temper embrittlement [48]. It is known that the impurity phosphorus is a major element linked to temper embrittlement along with silicon [48], [53]. In addition, retained austenite can transform back into martensite on subsequent tempers. This is a prevalent issue in AM part even though during thermal cycling the part will not remain at this temperature for extended periods of time. The fine grains from the faster cooling rate are a major reason why there is lower toughness compared to a wrought equivalent. Tempering the martensite even further will release carbon from the martensite matrix, reducing the tetragonality and leads to a more cubic structure [43], [54]. Even though this is considered ferrite, it is still referred to as martensite because it retains its lath or plate shape [43]. *Telasang* [32], experimented with post-cladding tempering using laser re-heating. This method of heat treatment will result in a fine super-saturated martensite and carbides microstructure. The re-heating leads to the dissolution of precipitates in the grain boundaries and the formation of martensite on cooling. Compared to the conventional tempering of 550°C for 2 hours, there is a drop in hardness due to martensite tempering as seen in Figure 2.12. However, the as-clad conventional tempered sample will still have higher hardness than the wrought quench and tempered substrate.

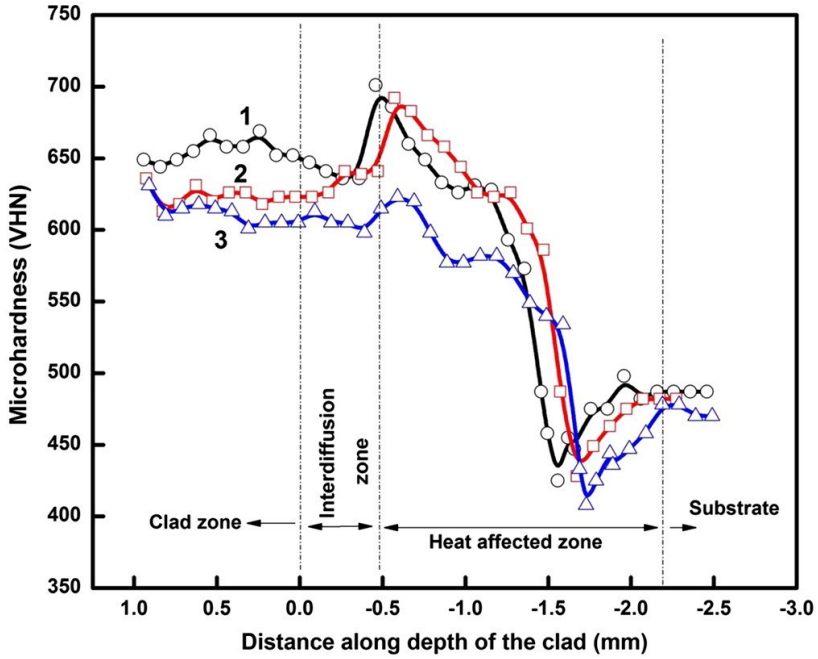

Figure 2.12: Vickers microhardness of H13 processed with laser energy density of 133 J/mm^2 and powder density of 13.3 x 10^{-3}g/mm^2 (plot 1), conventional tempering of post-cladding at 550°C for 2 hr (plot 2), laser assisted re-heating with a power density of 67 J/mm^2 and laser assisted surface re-heating with laser energy density of 67 J/mm^2 (plot 3), with permission from [32].

2.19 Tool Steels

With AM on the rise, pre-alloyed tool steel powder has been used for building parts and cladding applications. This category of steel alloys has been developed with complex compositions to operate in severe working conditions. They contain relatively large amounts of chromium (Cr), tungsten (W), molybdenum (Mo), vanadium (V), and manganese (Mn) that help control dimensional accuracy and resist cracking during heat treatments [48]. Tool steels also exhibit good wear resistance, even at elevated operating temperatures [48]. To obtain the desired properties for the application, tool steels must be heat-treated as mentioned previously using a quench and temper heat treatment [48]. Multiple tempering heat treatments are typically required to obtain the desired property

such as hardness, toughness, or a combination of both. Tool steels can either be in wrought form or manufactured using powder metallurgy (P/M). P/M is used for compositions that are difficult to manufacture or cannot be cast. The P/M method also allows for more uniform distribution of carbides [48]. However, due to the amount of expensive alloying additions and the difficulty of manufacturing tool steel, it results in a higher cost. Tool steels are used in die forging, extrusion dies, drawing dies, and many other applications that require high hardness and toughness [48].

2.20 Classification of Tool Steels

There are several different classes of tool steels that have been researched for AM including molybdenum high-speed steels (M-series), chromium hot work steels (H-series), high carbon and chromium cold-work steels (D-series), low-carbon mold steels (P-series), and crucible particle metallurgy steels (CPM-series) [48]. A significant area of research has been conducted on the H-series tool steels, specifically H13 [55]. This tool steel is well researched due to its optimal combination of wear, thermal resistance, and acceptable amount of alloying additions for maintaining hardness at elevated temperatures [55]. Ferrous-based AM research is well developed but obtaining fully dense parts is still a problem, so system optimizing is a critical step towards improvement [9]. Processing steel becomes a problem because the main constituent iron and other alloying elements are reactive with oxygen which results in oxides, balling, and inclusions in the final build [9].

American Iron and Steel Institute (AISI) H13 is classified as a chromium-containing, hot work tool steel for applications which require high wear resistance and toughness, with the ‘H’ designating it for use at elevated temperatures [48]. To achieve high hardness, it

is heavily alloyed to produce carbides during subsequent heat treatment cycles. Common applications for H13 tool steel include dies for hot-forging, casting, and other hot-forming processes with temperatures ranging from 215 – 600°C [43], [45], [48].

2.21 Wrought Tool Steel Microstructure and Phases

Compared to an AM manufactured tool steel, the wrought tool steel will have a more homogenous microstructure. Common phases that are encountered in tool steels are martensite, tempered martensite, ferrite, bainite, retained austenite, and carbides. A general description of each phase is given below. These phases will be present in ferrous AM builds; however, from thermal cycling, the microstructure will be inhomogeneous depending on how many layers there are and what system parameters have been chosen.

2.21.1 Martensite

Before, any surface treatments are performed, martensite is the hardest and strongest phase produced by steels [48]. Martensite is a metastable structure that is comprised of a super-saturated solid solution of carbon in α-iron [45]. Before martensite can be formed, the steel must go through austenitization, where the final element partitioning between the austenite matrix and retained carbide occurs [46]. To do this, the steel is heated to the austenite region of the respective phase diagram, based on instructions from the supplier or handbook. Next, the piece is rapidly quenched from the austenite region. This rapid cooling does not allow the carbon atoms to segregate from the matrix which creates a super-saturated metastable phase that will change to a stable equilibrium phase with additional thermal energy input [45]. Quenching causes rapid cooling and residual tensile forces on the surface, potentially causing surface cracking and the core to come under compression [43], [46], [48]. Cracking occurs when the localized strain exceeds the

materials failure strain with cracks following the austenite grains. If the substrate is not pre-heated, high thermal gradients will create high thermal stresses as the cooler sections contract. The ability to remove some of the stresses is diminished when martensite is formed because of the low ductility [46]. The formation of martensite is diffusionless, which gives the atoms no time to mix and form other phases [45], [48]. Martensitic embryos will nucleate at grain boundaries, incoherent twin boundaries, and inclusion particles [45]. The martensite start temperature (M_s) is a specific temperature and it is influenced by the composition of the austenite. As the austenitizing temperature is increased, more alloying elements go into solution, and the M_s temperature drops, resulting in more retained austenite [46]. As well, increasing the carbon content will lower the M_s temperature resulting in more retained austenite [45], [48]. As the M_s temperature increases, the tendency to crack will typically reduce [46]. A graph depicting the M_s temperature as a function of carbon content is shown in Figure 2.13. The carbon content in the steel will determine the type of martensite of which there are two main types: lath or plate or a combination of both [45], [48]. By alloying the steel, this will help stop the diffusion-controlled transformations, making martensitic formation easier [48]. When the carbon content is low, around 0.2 wt%, well defined laths of martensite form and if the carbon content is too low, martensite will not form. If the carbon content reaches around 0.6 wt%, it will begin to form a mix of plate and lath martensite. Once the carbon content starts to exceed 1.2 wt%, well defined plates of martensite form [45]. Instead of the matrix forming a BCC ferrite as it transitions under equilibrium from austenite which has a FCC, martensite will transform into a body-centered tetragonal (BCT) structure [45].

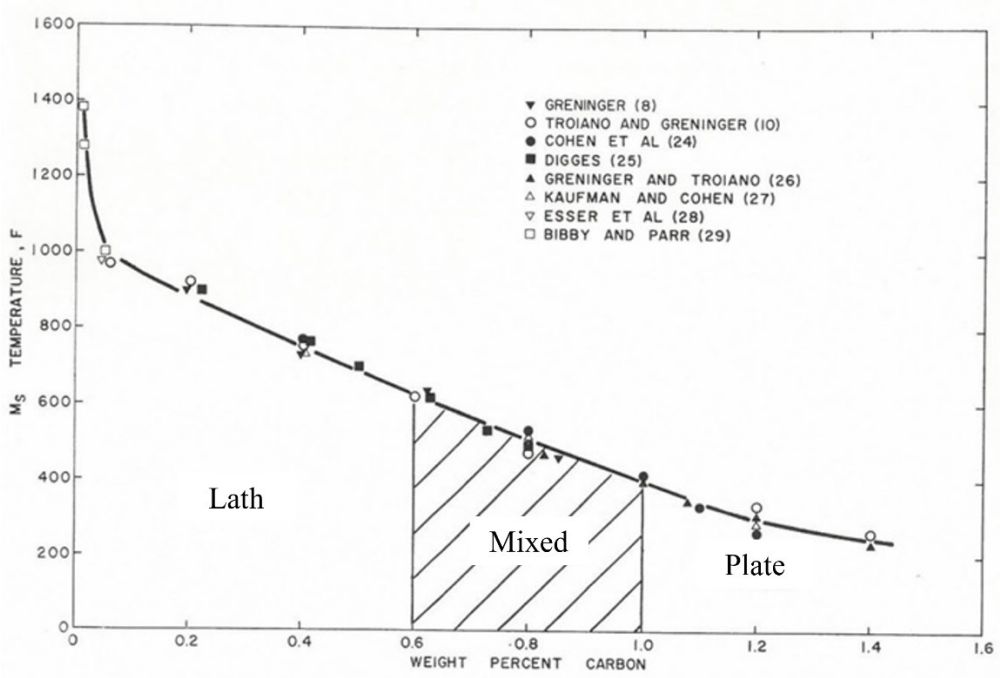

Figure 2.13: The M_s temperature (°F) as a function of carbon content (wt%), with the type of martensite formed depending on the carbon content [56], with the investigations identified by their numbers in [56]. Permission given by [56].

The BCT structure is a result of having a greater solid solubility difference of carbon than in FCC structure in austenite and the BCC ferrite [45]. The carbon will occupy the octahedral interstitial sites in the BCT structure [43], [48]. The interstitial spaces for the carbon in the FCC structure are larger than the BCC structure which leads to distortion of BCC structures' *c* axis to compensate for the change [45]. This change comes from shearing which acts on a fixed crystallographic plane producing large numbers of dislocations or twins in martensite [48].

2.21.1.1 Lath-Type Martensite

Lath-type martensite consists of lath shaped crystals separated by low-angle or high-angle grain boundaries. An example is shown in Figure 2.14 where the lathes have a

narrow strip appearance [57]. The internal structure has large amounts of tangled dislocations which retain small amounts of austenite between the laths [45], [48]. A lower carbon content will result in the laths being parallel, whereas a higher carbon content will cause the laths to become nonparallel [48]. The lath structure forms as it propagates through the austenite matrix [45]. Lath-type is thought to form due to accommodating dislocations that are fixed in place [45]. These dislocations form to reduce the high strain energy from the martensitic transformation and occur throughout single domains, resulting in the high density of tangled dislocations [45].

Figure 2.14: Micrograph of lath martensite in D2 at cooling rate of 50 K/s [57].

2.21.2 α-Iron (Ferrite)

α-iron is an equilibrium phase that has a BCC structure [45]–[47]. The α-iron phase has a maximum solid solubility of 0.02 wt% carbon [45], [48]. It can contain carbon or one or more alloying additions such as Cr, Si, Mn, and Ni [49]. The elements with a smaller atomic size such as carbon will occupy the octahedral interstitial sites. Whereas, substitutional atoms such as Ni and Mn will have a harder time diffusing [49]. The solubility of carbon in ferrite is a function of temperature. As the temperature decreases, the solubility drops to 0.008 wt% because the iron's BCC structure only allows the carbon atoms to be located at the octahedral interstitial sites since the space is smaller than that of a FCC structure of austenite [45], [48]. Ferrite can be stabilized by adding Si, Cr, and Mo which reduces the size of the austenite region [49].

2.21.3 Cementite

This phase consists of iron and carbon which forms the carbide, Fe_3C, of a fixed composition. This is a metastable phase that has an orthorhombic structure that will appear as laths [33], [43], [45], [46]. This intermetallic phase provides hardness, but it is brittle [45]. The formation of cementite occurs when carbon can no longer be accommodated in the octahedral interstitial sites, thus forming cementite [48]. Cementite commonly forms between 250 – 700°C; however, it has a tendency to coarsen and spherodize at elevated temperatures [33]. Cementite will precipitate from the interlath retained austenite at tempering temperatures below the aging temperature [43].

2.21.4 Retained Austenite

Austenite is an equilibrium phase that has an FCC crystal structure [43], [45]. The amount of austenite retained after quenching steel is a function of carbon and alloying

content, with composition influencing the M_s temperature [43]. Higher alloyed austenite will lower the M_s temperature resulting is greater concentrations of austenite because of incomplete formation of martensite. The concentration of austenite is increased as the austeniziting temperature and time are increased to allow for greater enrichment from the alloying additions [43]. Retained is unstable under the A1 temperature (725°C) and will decompose into tempered martensite during the tempering process [43], [48].

2.22 Alloying Element Influences

Compared to conventional mild carbon steels, alloying steel is an effective way of improving the mechanical properties so that they can perform in extreme environments and are able to be heat-treated. Additions of alloying elements to the steel will impact different aspects such as phase stabilization, hardenability, strength, wear resistance, and toughness. This section will cover major alloying elements of H13 tool steel and their impact on material properties. These elements are added in specific quantities to obtain very particular phase during heat treating. Increasing the amount of alloying elements will inherently raise the difficulty of manufacturing, thermodynamic interaction, and the cost of the steel.

2.22.1 Carbon (C)

Carbon is the principle element in steels and contributes to hardenability and is a solid solution strengthener as it occupies interstitial sites [48], [49]. Increasing the carbon content will improve the hardenability of the steel as it will shift other transformation reactions to the right [45]. However, a high carbon content is not desired because toughness and ductility will be lost, so other alloying additions will need to be added [48]. Carbon is an austenite stabilizer, meaning it will lower the M_s temperature, thus

increasing the ability to retain austenite upon cooling [48]. This element is important for forming martensite and the alloy carbides that provide high hardness [49]. In addition, the weldability will decrease with increasing carbon because it exhibits poor wetting which is important in the AM process [49], [58].

2.22.2 Manganese (Mn)

Adding manganese to steels will help improve the strength and hardness, depending on the amount of carbon content [49]. This alloying addition is a substitutional atom with most of the Mn dissolving in the ferrite and will contribute to hardenability [45], [49]. Increasing the Mn content will decrease the ductility and weldability [48]. Additions of Mn will counteract the impacts of sulfur by combining with it to form manganese sulfide [49]. Mn can form a carbide, but any remaining Mn will combine with cementite to form $(Fe,Mn)_3C$ [45], [59]. The carbide that forms helps with hardness retention at higher temperatures [46]. This element is an austenite stabilizer because it lowers the transformation temperature, aiding in retaining austenite at room temperature. [45]. During tempering, Mn-carbides impede cementite coalescence and control ferrite grain growth [48].

2.22.3 Silicon (Si)

Silicon is a substitutional alloying addition that provides solid solution strengthening [46], [49], [59]. Increasing the Si content will improve the strength of ferrite without significant reduction in ductility [49]. Si has also been found to improve hardness until a temperature of 315°C [46]. The presence of Si will influence temper embrittlement and can affect the formation of M_6C carbides [53]. Oxygen and silicon will combine to form non-metallic inclusions, but Si mainly dissolves in ferrite [45]. Si is considered a ferrite

stabilizer, thus it increases the transformation temperature [45]. If the Si concentration is too high, it can concentrate at the inter-dendritic boundaries and form low melting eutectic phases with elements at the grain boundaries or inter-dendritic region, resulting in cracking [17].

2.22.4 Chromium (Cr)

Chromium is a carbide former, and it is normally added for corrosion resistance which will form an oxide for protection. This element is substitutional in the α-lattice and will slowly go into solution in austenite [49]. Cr is a ferrite stabilizing element, helps with hardenability, toughness, high temperature strength and abrasion resistance [45], [49], [59]. Cr will contribute to secondary hardening at lower temperatures than molybdenum and will effectively improve the hardness above 205°C, forming either an $M_{23}C_6$ or M_7C_3 carbide [46], [60], [61].During tempering, Cr will retard the coalescence of cementite by combing with the carbon [48].

2.22.5 Molybdenum (Mo)

Molybdenum is a substitutional atom that helps with improving strength and substantially improves hardenability of the steel by suppressing the formation of pearlite [43], [45], [48], [49]. The addition of Mo helps with creep resistance and tensile strength at elevated temperatures, as well as improving toughness [45], [48]. Mo is a strong carbide former which helps with wear resistance forming MC, M_2C or M_6C [61], [62]. During tempering, Mo will retard the softening of martensite and reduce the susceptibility to temper embrittlement [48].

2.22.6 Vanadium (V)

Vanadium is an alloying addition that is a strong carbide former and can dissolve into ferrite to increase strength and toughness but only to a limited extent [49]. V is in solid solution with the austenite prior to quenching [48], [49]. The effects of V are seen during secondary hardening while tempering which will form an MC carbide, or frequently as V_4C_3 [48], [59], [61], [62]. During tempering, V will replace the cementite to form more stable high temperature carbides [48].

2.22.7 Copper (Cu)

Copper is a substitutional atom that is detrimental in higher concentrations [48], [49]. Looking at the phase diagram of Fe and Cu in Figure 2.15, solubility limits of Cu in α and γ are limited to 2.2 wt% and 13 wt% respectively [44]. The separation into Fe-rich and Cu-rich liquids is promoted by the addition of carbon [63], forming a metastable miscibility gap under the liquidus [44], [64]. It has a very low solubility in α-Fe and it is rejected from the austenite during cooling [65]. The addition of copper during printing causes overheating of Cu-rich regions to melt around the austenite grains, resulting in hot tearing [9].

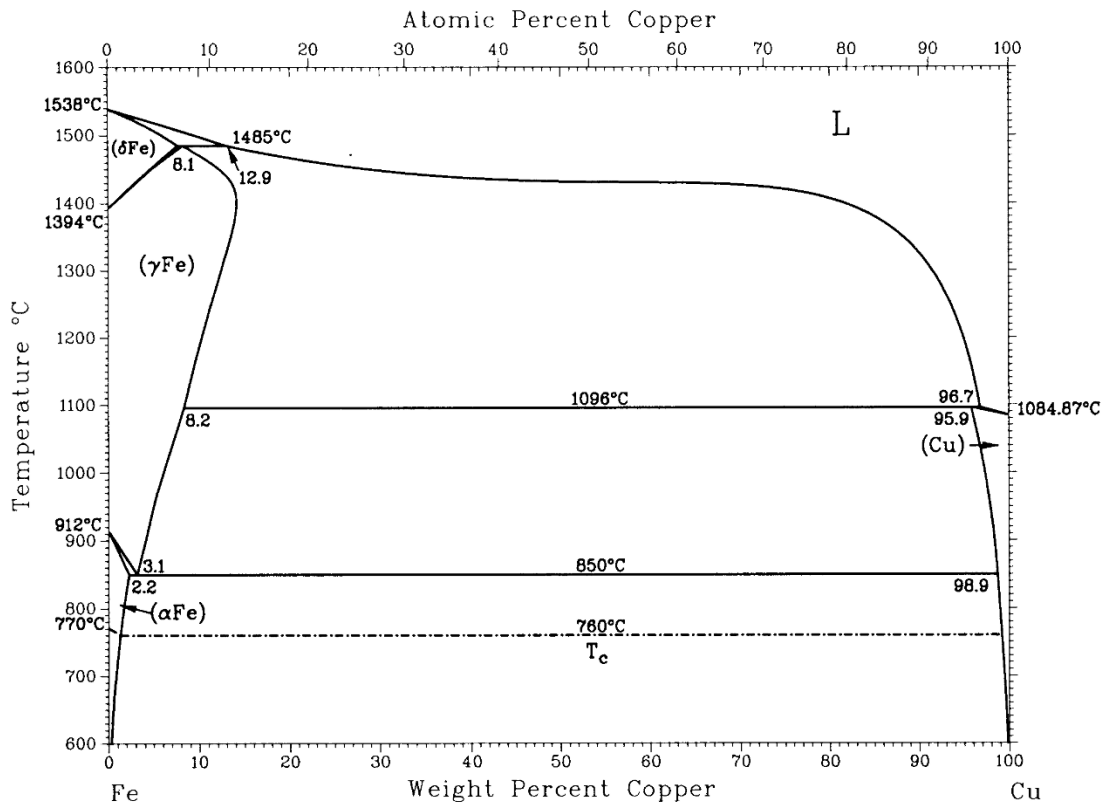

Figure 2.15: Fe-Cu phase diagram, with permission from [44].

2.22.8 Nickel (Ni)

Nickel is a substitutional alloying element and will lower the transformation temperature, thus stabilizing austenite [45], [49]. Nickel has the ability to form carbides; however, it often dissolves in ferrite [45], [48]. It provides strength and toughness to the ferrite through solid solution strengthening, but only to a small extent [46], [48]. Lastly, it improves hardenability and impact strength [48].

2.23 Functionally Graded Materials (FGMs)

The general notion of functionally graded materials (FGMs) was introduced in 1972 by *M. Shen* and *M. B. Bever* studying graded polymeric materials for a wide range of applications [66]. The application of engineered FGMs was considered in 1984 by scientists in the Sendai area of Japan, preparing metal matrix composite (MMC) thermal barrier materials able to withstand temperature gradients of 1600K for the space shuttle [67]. Grading materials is a popular area of research as it aims to maximize the engineering properties of materials. Gradients can take several forms, such as controlled porosity, orientation, microstructural, or compositionally. As well, how an FGM is produced has multiple forms. FGMs are an iteration of composites which aims to eliminate the sharp transition interface [68]. There are two major classifications of FGMs: thin and bulk [69]. Manufacturing thin FGMs involves depositing a thin layer onto a substrate using techniques such as CVD [70], PVD [71], or thermal spray [72]. Thin FGMs range in thickness from 5 – 500 nm, with some extending up to 1 – 120 μm [73]. Bulk FGMs have been produced using powder metallurgy [74], centrifugal casting [75], and free-form technologies such as additive manufacturing. The application of these materials spans numerous industries such as aerospace, automotive, defence, medical, energy, and tool and die [73], [76]. The challenge facing FMGs is the processing techniques, selection of suitable material combinations, characterization, and compiling a data base of material properties so they can be approved for industrial applications.

2.24 AM of Pure Copper and H13-Copper FGM Using AM Technologies

Combining the properties of high strength, corrosion resistant and wear resistant materials with highly thermally conductive materials is an area of interest for FGMs. This includes ferrous-based systems for molds or heat exchangers. One such material system of interest to the tool and die industry would be an FGM of H13 tool steel and copper. Copper poses a significant challenge when processed with a laser energy source due to reflectivity issues [5], [7], [77], [78]. Infrared (IR) lasers, fiber lasers, and CO_2 are commonly employed however, to overcome the reflectivity issue there have been studies using smaller wavelengths [79], [80]. Another difficulty of processing copper is that it has low solubility in iron and exhibits a miscibility gap (Figure 2.15) [44]. This material system has a large solidification range of several hundred degrees °C, which is known to be susceptibility to hot tearing and solidification cracking [58], [81]. Due to these issues, even under equilibrium and non-equilibrium conditions it is expected that this system will be inherently crack sensitive [81]. Along with this issue, the cyclic heating nature of DED combined with the effects of changing composition will result in a microstructure that is inhomogeneous and varies significantly in the compositional gradient.

H13 has several applications in the tool and die industry as previously stated, however, the thermal conductivity is approximately 13 times less than copper [48], [82]. For this reason, there is interest in combining the thermal properties of copper and the mechanical properties of H13 tool into an FGM, with a study examining the benefits of copper cores in molds [83]. There are several methods of fabricating an FGM, but additive manufacturing is a well-suited technology for producing FGMs because it can deposit material in specific places, offers a wide range of printable materials, and offers design

flexible [11], [84]. The purpose of the gradient structure is to reduce potential mismatch of material properties when joining directly dissimilar or incompatible materials together. The two most common styles of additive manufacturing technologies; L-PBF and DED have been used to manufacture an FGM of H13-Cu. DED technologies employ multiple different types of focused heat sources, which can be either laser or an alternate energy source (*i.e.,* electron beam or electric arc) for generating a melt pool on the substrate where the feedstock material is delivered [10], [11], [85], [86]. There are several studies involving DED to produce an FGM [87]–[90], with this list not being exhaustive.

Stainless steels are a common area of research due to their wide application and availability. Stainless steels are often used for heat exchanger applications in corrosive environments. *Sato et al*. studied DED of pure Cu on a 304 stainless steel substrate using blue diode lasers and still encountered porosity [91]. *Lodes et al.* produced high density pure Cu samples using LPB-F and noted that printing pure Cu is sensitive to the overall build temperature [92]. *Beal et al.* investigated an FGM of H13-Cu manufactured using L-PBF with the printed samples resulting in cracking and porosity [93]. *Imran* investigated printing H13 directly onto a copper alloy, Moldmax (0.5wt% Ni + Co and 1.9wt% Be), substrate using a CO_2 laser with a DED style system with metallurgical bonding occurring [94]. *Imran* also experimented with adding a stainless steel (316L) buffer layer to help improve metallurgical bonding [95]. Another study by *Zhang et al.* graded a structure from H13 to Cu using a nickel alloy (Deloro 22) as a buffer layer on a DED style system [96]. *Artiček* examined processing an FGM of H13/Cu onto a steel, assumed to be wrought H13 tool steel substrate, with cracking and porosity being major issues [97]. Unfortunately, the author of this study did not disclose important DED

system parameters because the work was conducted with an industrial partner. *Osipovich et al.* used an electron beam wire-feeding additive manufacturing system to produce a defect free FGM of stainless steel (304) and copper (C11000) [98]. *Beal* studied the H13-Cu system using L-PBF but experienced significant porosity [99]. *Popovich et al.* was able to achieve high density samples printing a copper alloy (Cu-Cr-Zr-Ti) using L-PBF [100]. *Constantin et al.* [101], achieved high density Cu/diamond samples by coating the powder to improve wettability. Since publishing these earlier FGM attempts, there has been advancements in laser beam reflectivity mitigation technology. However, the main issue encountered in these studies was the cracking due to the incompatibility of the Fe-Cu system.

3 WROUGHT H13 TOOL STEEL MATERIAL CHARACTERIZATION

3.1 Introduction

The purpose of this study was to gain a baseline understanding of wrought H13 tool steel and have a reference point to compare it to the DED-processed H13 tool steel. These preliminary experiments on the wrought material are necessary because it is anticipated that the DED-processed steel will have different material properties and microstructure due to the cyclic heating nature of the AM layer-by-layer building technique.

H13 tool steel was developed for dies for hot-forging, casting, and other hot-forming processes with temperatures ranging from 215 – 600°C for aluminum and zinc alloys. Heat treating tool steel with alloying additions of Cr, Mo, and V to form carbides during the double tempering process to help maintain hardness at elevated temperatures. The goal of the heat treatment is to have a balance between toughness and hardness from carbides since a martensitic microstructure is brittle even though it has high hardness.

This chapter will evaluate the effects of varying the tempering conditions upon the microstructure and scratch resistance of wrought H13. Wrought feedstock was studied in three different conditions: annealed, quenched, and double tempered. It is expected that double tempering will improve the scratch resistance due to the formation of alloy carbides compared to a fully martensitic matrix.

3.2 Experimental Procedure H13

3.3 Raw Materials and Preparation

Wrought AISI H13 hot work tool steel was purchased from Hudson Tool Steel Corporation (USA). The as-received wrought material was supplied as bar stock in diameter of 19.05 mm diameter and a length of 254 mm. 7 samples were cut from the tool steel in thickness of 5 mm for various heat treatments. To reduce oxidation, each sample was placed in a stainless-steel bag along with sponge Ti powder to preferentially oxidize over the tool steel. Tool steel was received in the annealed condition (AR). Five samples were austenitized at 1032°C for 30 mins. Double-tempered samples, identified with 'DT', were held at 300°C, 400°C, 500°C, 600°C, and 700°C for 2 hours followed by cooling to room temperature in air. The quenched sample was made by austenitizing at 1032°C 30 min (Q30) then quenched in air. The composition of the wrought H13 was determined with inductively coupled plasma optical emission spectrometry (ICP-OES) and carbon content with both tests conducted three times to get an average given in Table 3.1.

Table 3.1: Chemical composition of wrought H13 tool steel (standard specification vs. measured).

Designation	**Composition (wt%)**						
	C	**Si**	**Mn**	**Cr**	**Mo**	**V**	**Fe**
AISI H13	0.32 - 0.45	0.8 -1.2	0.2 - 0.5	4.75 - 5.5	1.1 -1.75	0.8 -1.2	Bal.
Wrought H13	0.4	0.69	0.34	4.64	1.17	0.76	Bal.

The samples were mounted in PolyFast, polished to a 1 μm finish and then etched with 5% nital by immersing the top of sample in the solution. Etching times varied for each sample. The etching was performed before hardness and scratch testing, so the etchant

would not react with the strained areas and disrupt the results with Figure 3.1 showing a cut, mounted and etched sample that has been heat-treated. The microstructure was characterized using field emission scanning electron microscope (FE-SEM; Hitachi S-4700, Hitachi High Technologies, Tokyo, Japan) operating with a V_{acc} of 3 kV and an I_e of 15 μA.

Figure 3.1: An example of a cut, polished, and etched wrought H13 sample mounted in Polyfast.

3.4 Sample Characterization

Crystallographic phase evaluation was conducted using X-ray diffraction (XRD; Bruker D-8 Advance Bruker Corp., Billerica, MA, USA) operating at 35 kV and 27 mA with CoKα radiation and a Fe filter. A step size of 0.02° and a time per step of 0.5 per second over a range of 20 – 130° for 2θ was used. The sample was cleaned with acetone before being placed in the sample holder.

Scratch testing was performed on the Universal Micro Tribometer (UMT-1; CETR, Campbell, CA, USA) using a Rockwell diamond indenter (tip radius of 200 μm). The scratch test consisted of a single pass of 5 mm in length, over 30 s, and repeated three times. Tests were conducted at room temperature (22 ± 2 °C). Applied loads of 5 N and

10 N were used to generate the scratch tracks. The coefficient of friction (COF) was determined using the *Viewer* software which received the data from the tribometer system. An average COF value was obtained from the three scratch tests. The laser confocal microscope (Keyence VK-X1000 series; Japan) was used to determine the average width of the scratch track by taking four measurements at intervals of 1 mm to determine scratch hardness (HSp) at a magnification of 20x with a resolution of 535.7 nm, using the relationship [102]:

$$HS_p = \frac{8P}{\pi W^2}$$

Equation 6: Scratch hardness formula.

Here, P, is the normal load (N) and W is the width of the track (mm). Surface roughness was analyzed using the confocal laser scanning microscope (CLSM; model VK-X1100, Keyence Corp., Osaka, Japan) by taking three locations inside the track to obtain an average. The cross-section of the tracks was analyzed using the CLSM and averaged using 100 lines with 20 μm spacing. Data from the CLSM was analyzed using the Keyence Multifile Analyzer software.

3.5 Results and Discussion

The microstructure of the annealed sample consists of spheroidized grains with large carbides at the grain boundaries with a ferrite matrix. This spheroidized microstructure will result in the lowest scratch hardness. The quenched sample has a lath martensite microstructure due the carbon content in H13 which leads to high hardness, along with possible retained austenite (Figure 3.2). At an austenitizing time of 30 min, this allows for more carbon and alloying additions to enrich the austenite which in turn lowers the martensite start temperature leading to less martensite forming [43].

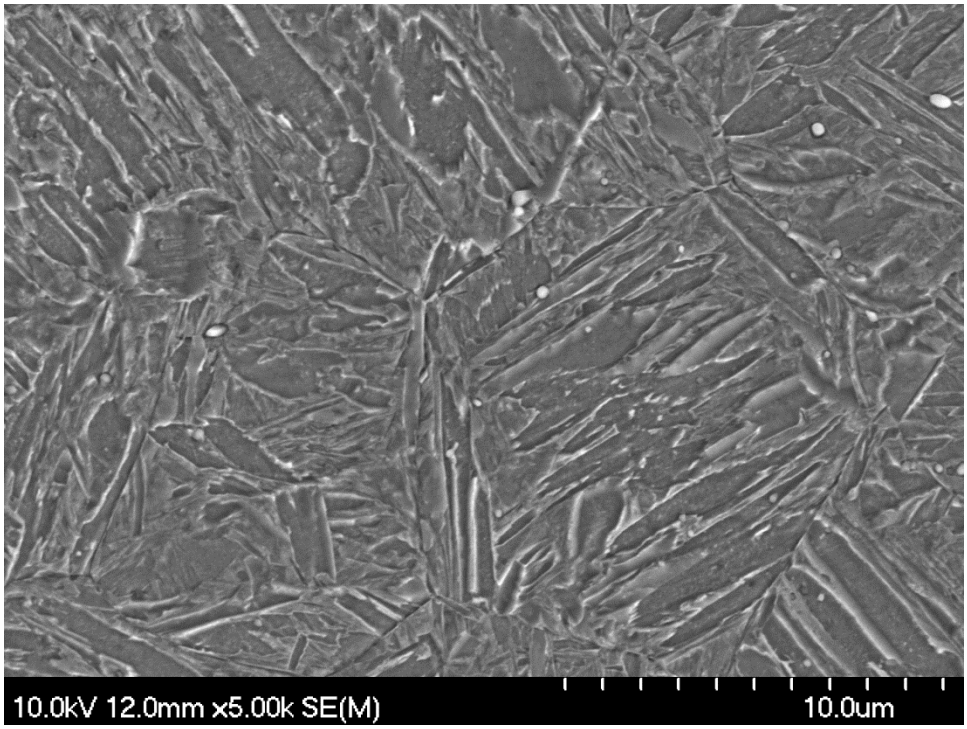

Figure 3.2: FE-SEM micrograph of wrought H13 quenched after austenitizing for 30 mins at 1032°C with alloy carbides (white circular structures).

The addition of the high carbon and high alloying content will significantly increase the isothermal transformation times leading to high hardenability [43]. Since the samples were small, air quenching the samples is sufficient to fully harden to martensite due to the carbon content and alloying additions [43]. Martensite formation is a diffusionless reaction, resulting in a volume change from austenite that has an FCC structure to a BCT structure of super saturated carbon. This distorts the equilibrium BCC lattice in the c-axis and is detected in the XRD plot shown in Figure 3.3 [43], [45].

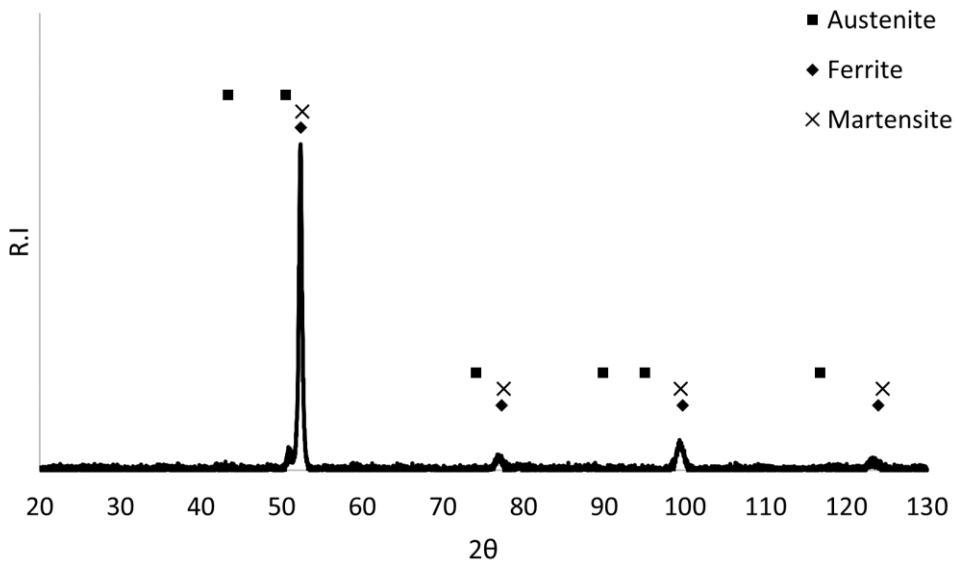

Figure 3.3: XRD trace of wrought H13 double-tempered at 400°C.

The transformation takes place by shearing and cooperative movement of the atoms in the parent phase into the martensite [43]. Tempering at 300°C, the laths of the martensite can still be seen but have coarsened due to the heat treatment process shown in Figure 3.4. Also visible are circular alloy carbides (white). The martensitic structure persists up to a tempering temperature of 400°C but is coarsening.

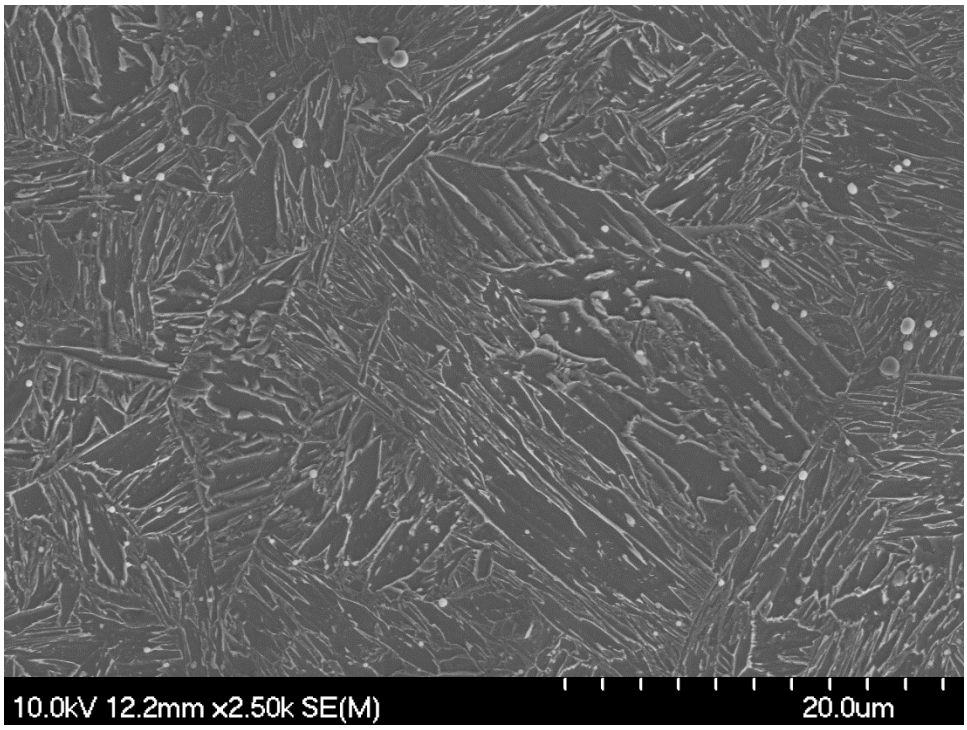

Figure 3.4: FE-SEM micrograph of wrought H13 tool steel double-tempered at 300°C.

As the tempering temperature increases the laths coarsen until the heat treatment temperature reaches 500°C (Figure 3.5), the matrix consists of tempered martensite with small and large alloy carbides. Alloy carbides are mainly along the grain boundaries with some precipitated in the grain. A further increase to 600°C, the martensitic structure is heavily tempered with alloy carbides dispersed throughout the matrix. Finally, tempering at 700°C, the XRD plot in Figure 3.6 shows prominent ferrite peaks. The microstructure shown in Figure 3.7 starts to resemble that of the annealed structure. The scratch response (Figure 3.8) presented later also showing tempering at 700°C has similarities to the annealed condition.

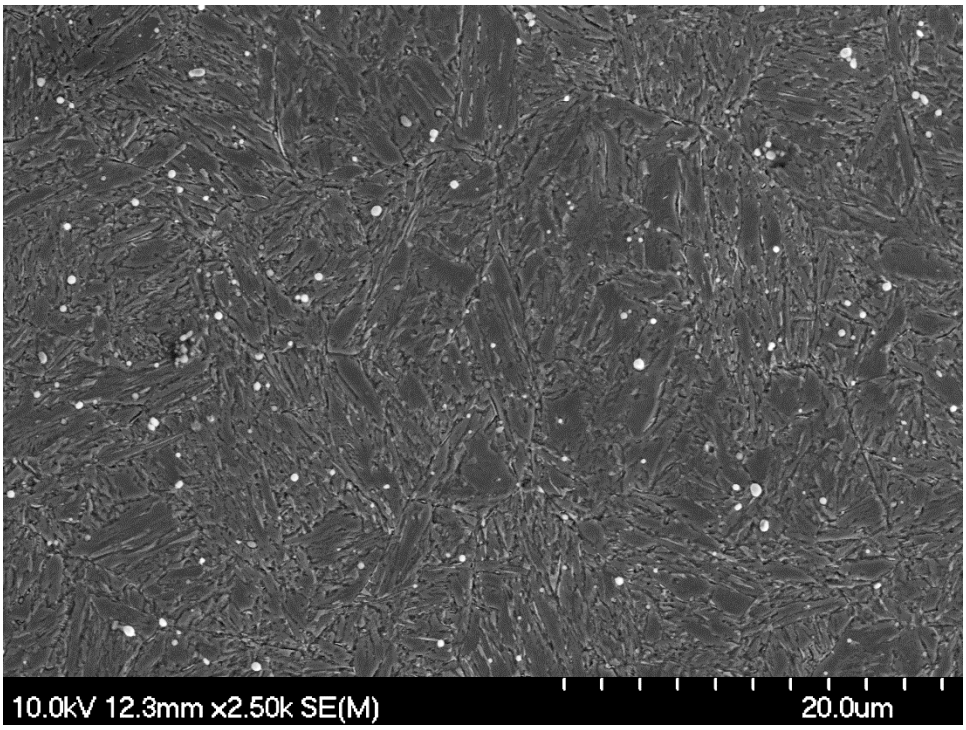

Figure 3.5: FE-SEM micrograph of wrought H13 tool steel double-tempered at 500°C.

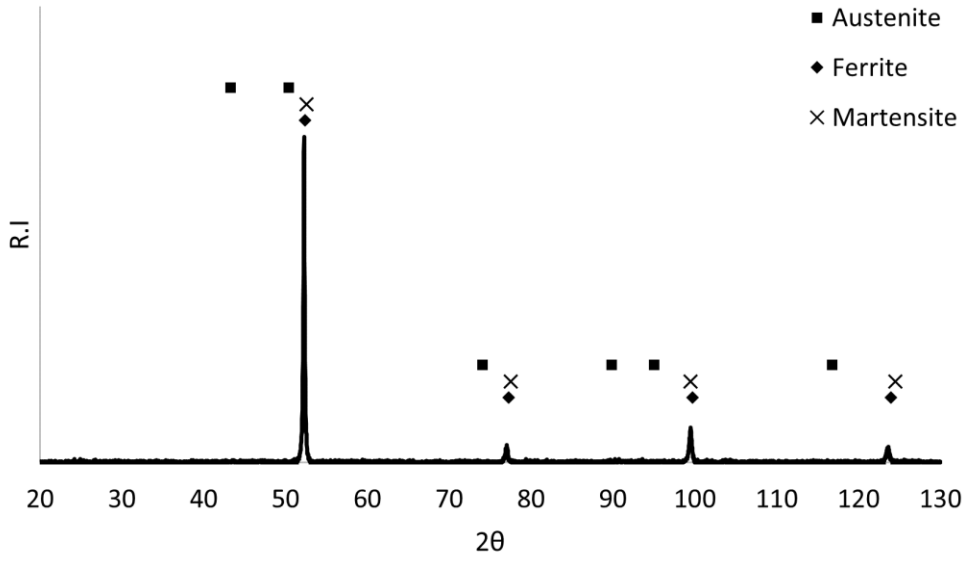

Figure 3.6: XRD trace of wrought H13 double-tempered at 700°C.

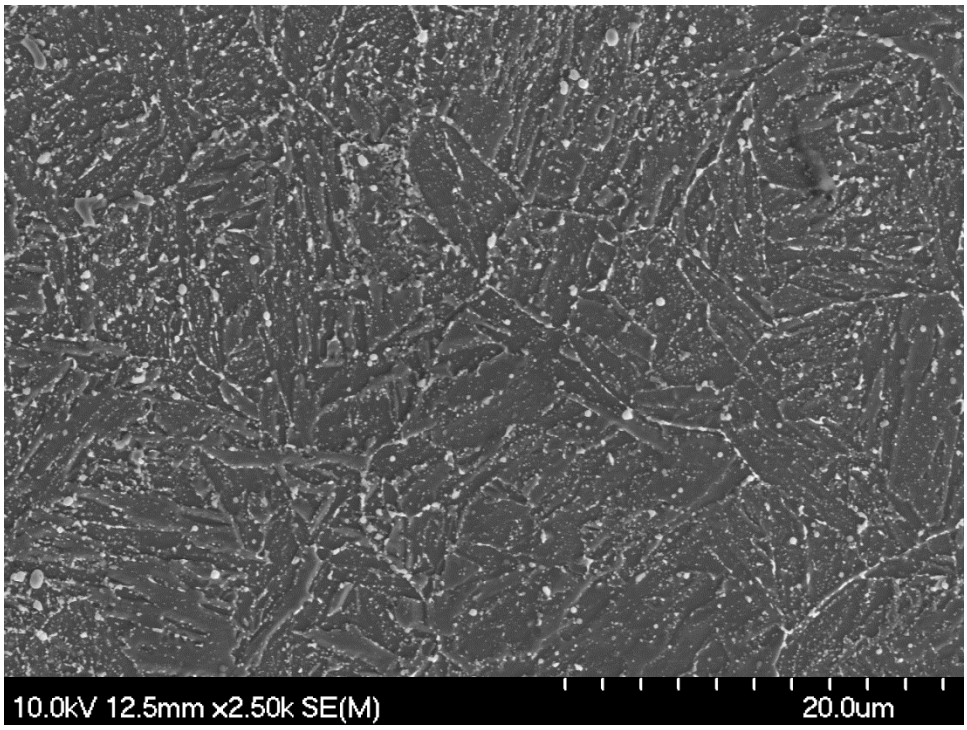

Figure 3.7: FE-SEM micrograph of wrought H13 tool steel double-tempered at 700°C.

From the XRD results of the samples tempered at 300°C and 400°C, it was difficult to differentiate the martensite (α') and ferrite (α) tempered samples up to 400°C because as the tempering temperature increased the martensite tetragonality will reduce leading a more cubic structure due to the release of carbon from the martensite matrix [43], [54]. When comparing the XRD data to the micrographs, the plots line up to what would be expected. It becomes more apparent in the double-tempered samples as they have been exposed at temperature longer, leading to more microstructural changes. In the double-tempered sample at 500°C martensite is detected but appears more ferritic. Retained austenite (γ') and martensite is observed in both the 300°C and 400°C tempered samples. Increasing the temperature further, the austenite peak is no longer noticeable. For both

tempering conditions, the 700°C sample plots match closely to the annealed state which consists of ferrite.

Applying different tempering temperatures resulted in a noticeable change in the scratch resistance of the wrought material which is plotted in Figure 3.8. For low alloyed and mild steels, quenching the sample will result in the formation of martensite which will exhibit the highest hardness. A maximum scratch hardness is measured in the quenched state with a value of 9.60 ± 0.62 GPa under a 5N load. However, if martensite is tempered it will begin to lose hardness and increase in toughness. Double-tempering at 300°C and 400°C dropped the scratch resistance of the wrought material under the tested loading conditions. At 300°C the double-tempered sample drops in scratch hardness since the martensite is being tempered but does not contain sufficiently sized alloy carbides due to the low tempering temperature. Carbide formation can be rapid even at higher cooling rates; carbides will still be seen from the quench which are likely the MC carbides that have not dissolved during austenitizing [43]. When tempering tool steels, martensite formation will undergo tempering, but the addition of alloy carbide formers will increase the hardness to a greater extent after quenching and tempering compared to mild steels. The alloy carbides will precipitate during tempering at the lower temperatures but the kinetics will be slow because of short diffusion distances associated with lower tempering temperatures [43]. Looking at the scratch hardness results; the double-tempered samples exhibit lower hardness than the quenched sample but would have higher toughness. At a 5 N load the quenched sample reaches a maximum scratch hardness of 9.60 ± 0.62 GPa. Under a 10 N load the maximum recorded scratch hardness occurred after double-tempering at 500°C which was recorded to be 7.81 ± 0.38 GPa. This increase in hardness

from secondary hardening is due to the formation of alloy carbides forming from V, Cr, and Mo [43], [46]. The decreased scratch hardness under a 10N load of the quenched sample is likely due to martensite having low work hardenability leading to a larger scratch width [103].

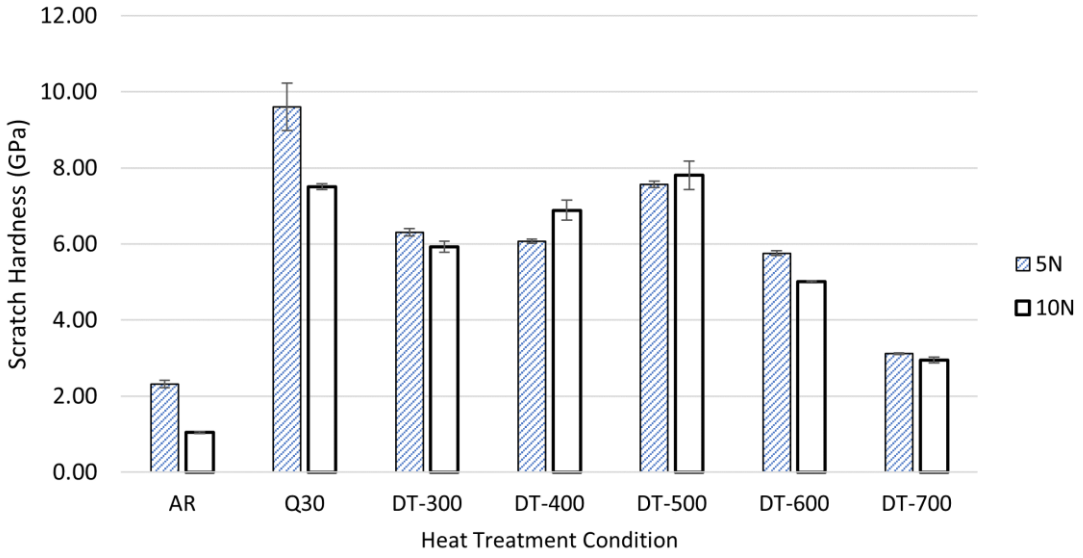

Figure 3.8: Scratch hardness of wrought annealed (AR), quenched from 1032°C with 30 min hold, and double-tempered H13 tool steel at varying tempering temperatures with error bars indicating the standard deviation.

Even though the as-quenched sample had a higher scratch hardness due to the lath martensitic structure, if higher loads were used or a reciprocating test was performed it is likely that the martensite will transform into tempered martensite due to localized heating lowering the wear resistance [104]. Finally, as the tempering temperature increases, more thermal energy is present allowing for longer diffusion distances and coarsening of carbides, thus lowering the hardness. Further increase in the heat treatment temperature

results in a drop in scratch hardness with the sample tempered at 700°C approaching that of the annealed temperature of 860°C [48].

3.6 Summary of Wrought H13 Tool Steel Characterization

There are significant differences in the material properties and microstructures when different tempering temperatures are applied to wrought H13 tool steel. Lath martensite dominates the samples double-tempered up to 400°C. The XRD data indicates as the tool steel is tempered at increasingly higher temperatures, the martensite will begin to lose its tetragonality making it appear as ferrite in the results up to 500°C. A small portion of retained austenite is observed up to 400 °C but is not detected once the tempering temperature increases further. Once the temperature reaches 700°C the plots resemble the annealed state. Scratch testing showed that a maximum hardness was achieved in the quenched state but application of the tool steel in this condition is unrealistic. Therefore, double-tempering at 500°C produced the highest hardness in this condition. The hardness from tempering is provided by the alloy carbides that have precipitated due to secondary hardening and are found at the grain boundaries and within the grains. The alloy carbides formed from the addition of V, Cr, and Mo. The scratch hardness is generally higher under the 5 N load with exceptions from the samples double-tempered at 400°C and 500°C. The scratch hardness of these double-tempered samples had an increase in hardness while the quenched sample significantly dropped under the 10 N load. The lower scratch hardness of the quenched sample at 10 N is due to the low work hardenability of martensite. This work will be followed by H13 processed using DED to compare the mechanical and microstructural differences and eventually an FGM of H13-Cu.

4 MATERIAL CHARACTERIZATION OF DED H13 TOOL STEEL

4.1 Introduction

The previous chapter provided a baseline understanding of how H13 tool steel reacts to various tempering temperatures in the wrought condition, so it can be used as a comparison to the additively manufactured H13 tool steel using DED. The tooling industry has started to adopt additive manufacturing manufacture tools because of the readily available known materials and its ability to offer design flexibility. The cost of fabricating a new tool can deter users due to high initial investments, but DED technology aims to reduce this cost by reducing the time to design and manufacture a new tool, with the added benefit of being able to repair an existing worn tool also being feasible. DED technology allows for deposition of the same tool chemistry to repair a worn tool or to produce an entirely new tool with added benefit of design flexibility afforded from AM.

This chapter will investigate the influence of varying DED system parameters, namely changing the powder feed rates and scanning speeds, on the as-printed surface roughness, microstructure, and scratch response. The DED printed H13 tool steel is tested in a heat-treated condition which involved austenitizing and double tempering the sample. It is expected that the DED-processed H13 will have improved mechanical properties compared to the wrought equivalent due to a refined microstructure formed during rapid solidification.

4.2 Raw Materials

For the studies involving the powder feedstock characterization (section 4.9.1), geometry measurements (Section 4.9.2), surface characterization (Section 4.9.3), microstructure characterization (Section 4.11.2), and initial wear response (Section 4.13), a pre-alloyed H13 gas-atomized powder was purchased from TLS Technik (Bitterfeld-Wolfen, Germany); the powder was specified at the time of order to have a nominal size within the range of 50 – 100 μm. The particle size distribution (PSD) of the 'as-received' powders was then determined using particle size analysis (model Mastersizer 3000, Malvern Instruments, Malvern, UK); three measurements were undertaken on different samples from the supplied batch to assess 'intra-batch' variability. The H13 powder surface morphology and size distribution were then examined using field emission scanning electron microscopy (FE-SEM; model S4700, Hitachi High Technologies, Tokyo, Japan). For imaging purposes, the FE-SEM was usually operated with an accelerating voltage, V_{acc}, of 5 kV and a beam current, I_e, of 20 μA. Samples of the 'as-received' powder were also cold mounted in epoxy resin, which was then polished to a 1μm surface finish, to assess their cross-sectional structure via optical microscopy (OM; model BX-51, Olympus Corp., Tokyo, Japan) and FE-SEM. In particular, this process was conducted to detect any evidence of internal porosity and, if present, to see if it has any impact on the surface finish or final component density. For the subsequent laser DED processing, the powder was sieved from -45/+135 mesh to remove any 'fines' and ensure consistent flow characteristics in the powder feeder.

The substrate material used for all deposition studies was wrought, annealed H13 plates, purchased from Hudson Tool Steel Corporation (Rockford, IL, USA), with dimensions

165.1 mm x 152.4 mm x 15.875 mm. Before any DED printing was conducted the substrate was sandblasted (-20/+60 grit). The composition of the 'as-received' H13 powder and substrate was determined with inductively coupled plasma optical emission spectrometry (ICP-OES; model Vista-PRO, Varian Inc., CA, USA), with an internal calibration standard (scandium). The carbon content was determined using a carbon-sulfur combustion analyzer (model CS2000, Eltra GmbH, Haan, Germany) following the ASTM Standard E1941-10: *Standard Test Method for Determination of Carbon in Refractory and Reactive Metals and Their Alloys by Combustion Analysis*. The ICP-OES and carbon analyses were conducted three times on both the powder and substrate to obtain an average value in each case, which is provided in Table 4.1, along with the associated AISI specifications for this steel grade. The apparent density of the as-received powder was determined following ASTM standard B703-17: *Standard Test Method for Apparent Density of Metal Powders and Related Compounds Using the Arnold Meter*. Similarly, the flow characteristics were determined using a Hall Flowmeter, following ASTM standard B213-20: *Standard Test Methods for Flow Rate of Metal Powders Using the Hall Flowmeter Funnel*.

Table 4.1: Chemical compositions of the 'as-received' H13 powder (prior to DED use), wrought H13 substrate and the post-DED 'recovered' powder. AISI standard specifications are provided vs. measured values (note that Fe comprises the balance in each case).

Designation	**Composition (wt.%)**					
	C	**Si**	**Mn**	**Cr**	**Mo**	**V**
AISI H13	0.32-0.45	0.8-1.2	0.2-0.5	4.75-5.5	1.1-1.75	0.8-1.2
As-received powder	0.372	1.02	0.42	5.74	1.46	1.05
Substrate	0.39	0.63	0.30	4.73	1.37	0.80
Recovered powder	0.36	0.74	0.42	5.57	1.44	1.12

4.3 Laser DED System Parameters

The laser DED equipment used in the present investigation was a 3-axis LENS^{TM} 450XL system (Optomec, Albuquerque, NM, USA), using a 400 W continuous Nd:YAG laser, and with high purity Ar used as both the powder carrier gas (5 L/min flow rate) and the protective shield gas (25 – 30 L/min flow rate), to minimize oxidation during deposition. The system is initially under nominally atmospheric conditions in the build chamber, at ambient temperature, with a 15-minute purge of Ar then conducted. The Ar content within the chamber then increases continuously during laser deposition. The system operating parameters employed for the single-track clad, multi-track clad, and rectangular samples are listed in Table 4.2; sample geometries are discussed in greater detail in Section 4.4.

Table 4.2: The DED system operating parameters used for the present study.

Parameter	**Value**	**Units**
Laser Power	400	W
Scan Speed	400 – 700	mm/minute
Feed Rate	5.5 – 7.5	g/minute
Hatch Spacing	0.381	mm
Layer Thickness	0.251	mm
Spot Size	600	μm
Nozzle Stand-Off	9.525	mm
Hatch Orientation	0°, 45°, 90°, 135°	degrees

4.4 Sample Test Geometries

The single-track clad, multi-track clad, and rectangular samples were deposited using a variety of laser DED printing parameters, resulting in 20 samples for each complete parameter set; Figure 4.1 presents a schematic representation of these various printed geometries. Both the single-track and multi-track clad samples have an overall length of 25 mm and are all one deposition layer thick. The multi-track cladding samples each consisted of six aligned and slightly overlapping tracks; in this instance the applied hatch spacing was 0.381 mm. The nominal dimensions of the rectangular samples were 5 mm x 25 mm x 10 mm. The identification schemes used for the single-track clad, multi-track clad, and rectangular sample are provided in Table 4.3.

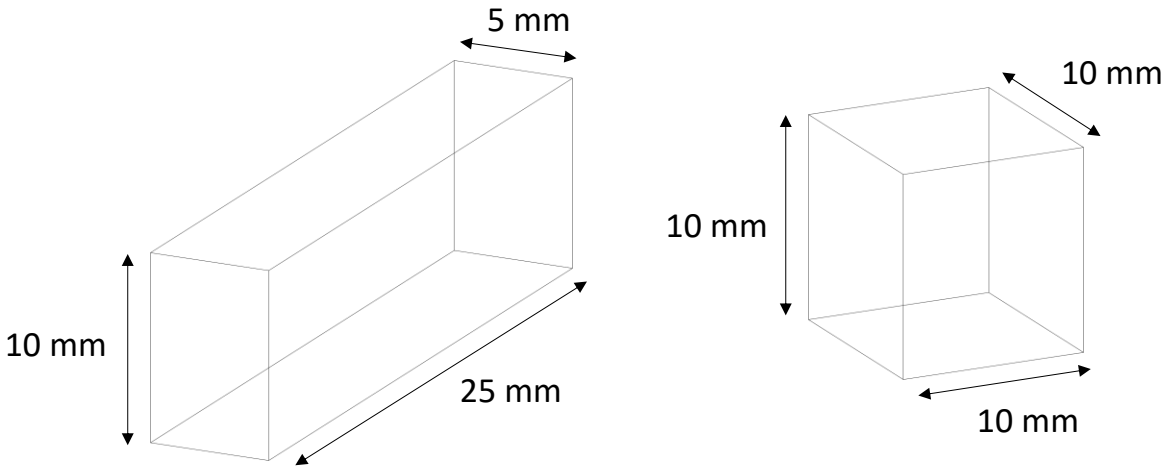

(a)

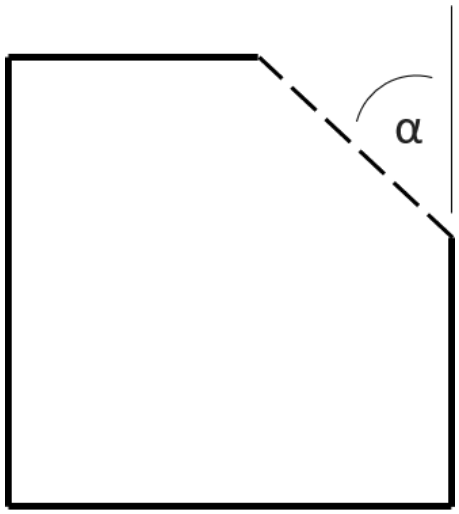

(b)

Figure 4.1: (a) Schematic representations of the rectangle and 'ideal layer thickness' sample geometries that were examined. (b) Schematic representation of the draft angle (α) sample geometry with the dashed line indicating the draft face.

Table 4.3: Sample Identification for single-track clad, multi-track clad and rectangular samples.

Sample ID		**Feed Rate (g/min)**				
		7.5	**7**	**6.5**	**6**	**5.5**
Scan Speed (mm/min)	**700**	A1	B1	C1	D1	E1
	600	A2	B2	C2	D2	E2
	500	A3	B3	C3	D3	E3
	400	A4	B4	C4	D4	E4

Two further sample geometries were also assessed, in order to investigate their impact upon the final surface finish and deposition height error. These were nominally cube-based samples, with various draft angles (α) ranging from 10 – 85°, with the dashed line indicating the 'draft face' from which the surface roughness measurements were taken (Figure 4.1(b)), and simple cubic 'ideal layer thickness' samples, with nominal deposition

layer thicknesses ranging from 0.2032 - 0.3302 mm, and with a final targeted build height of 10 mm. Regression statistical analysis (Minitab®, State College, PA, USA) was used, with a confidence interval of 0.05, to see if changes to the selected deposition parameters were significant; this means a *P*-value less than or equal to 0.05 is viewed as being significant. The ANOVA software feature was used to generate a significance 'main effects plot' and related contour plot. The main effects plots show if parameters have similar impacts on the measured values. For each feed and speed value, the software creates a mean value (the points shown on each plot). If the points are connected by horizontal lines, then each parameter has effectively the same impact. However, if the line is not horizontal, then there is different impact for each parameter. A steeper slope then indicates a greater main effect. The dotted line presented on each 'main effects' graph is the overall mean. An '*R*-squared' (*R*-sq) linear regression approach was used to predict if there is a trend in the data. The *R*-sq value (or coefficient of determination) represents the percentage of variance in the dependent variable which can explained by the independent variable [105].

4.5 Sample Characterization

The initial dimensional accuracy was measured for each of the widths, lengths and heights of the rectangular samples, together with the ideal layer thickness samples, with four measurements undertaken in each case to obtain an average dimensional value. Further dimensional analyses, including measurement of the cladding surface roughness values, were conducted using a CLSM. Data was analyzed on the CLSM using the Keyence *Multifile Analyzer* software. All samples are measured in the 'as-printed' condition, without further treatments (*e.g.*, annealing, tempering, *etc.*). For the single-

track and multi-track cladding samples, four width measurements were taken with the CLSM, using a 20x magnification objective lens (with a theoretical resolution of 535.7 nm), to obtain an average for each single-track/multi-track width, which was then assessed as a function of the DED process parameters. The cross-sectional profiles of the single clad tracks were also evaluated using the CLSM, again using the 20x magnification objective lens, with four measurements also made for each sample to determine an average value.

In terms of the as-printed surface finish, a variety of roughness parameters were evaluated using the CLSM. Surface roughness (S_a) was recorded using the *Multifile Analyzer* software. Measurements were taken using a 20x magnification objective lens, as before. Surface analysis for the rectangles and ideal layer thickness samples were taken in the build height direction (+z-direction). The side plane was normalized for all measurements. The top surface roughness was measured in the X-Y plane with no normalization. In each case, five stitched images for the side and top surfaces were recorded for each of the mean values determined from the surface analysis. The draft samples were fixed in a mount allowing them to be rotated, to make the 'draft face' normal to the CLSM beam axis, and then the angle of the plane was finally finely adjusted (normalized) using the *Multifile Analyzer* software, with five stitched images used for further analysis, as before. For the single-track clad surface analysis, a single image was captured. The multi-track clad samples used between 4 – 5 stitched images, which were stitched 'transversely' along the scanning direction. None of the single- or multi-track clad samples required normalization due to the parallel faces of the substrate plates relative to the CLSM laser beam. Analysis areas were selected that had the least

amount of attached, ‘satellite’ particles on the surface. For all samples, three data points were taken to get a mean value and associated standard deviation. No filtering was applied to the analyzed surfaces. Finally, to identify any surface porosity on the clads, FE-SEM was used, again operating with a V_{acc} of 5 kV and an I_e of 20 μA.

4.6 Microstructural Experimental Procedure

4.6.1 Heat Treatment Procedures for Wrought and DED Materials

Both the wrought and DED H13 tool steel samples were subjected to a quench and double temper heat treatment. Each sample was placed into a separate stainless steel bag, along with ≈ 5g of sponge Ti powder as an oxygen ‘getter’, to minimize oxidation of the tool steel. All samples were first austenitized at 1,032°C for 30 mins and then quenched in air. The wrought baseline and DED samples were then double-tempered by holding at 600°C for 2 hours, followed by cooling to room temperature in air, and then a second treatment at 600°C for 2 hours, followed by cooling. A tempering temperature of 600°C was selected to obtain a balance between toughness and hardness with the tempered martensite and alloy carbides. The double-tempered wrought and DED samples are identified with the addition “-DT” (e.g., A1-DT). An as-quenched wrought sample (W-Q) was also produced, austenitizing at 1,032°C for 30 minutes then quenched in air, but without the double-tempering treatment being applied.

4.6.2 Microstructural Characterization

Density measurement was performed using the Archimedes principle following ASTM Standard B962-17: *Standard Test Methods for Density of Compacted or Sintered Powder Metallurgy (PM) Products Using Archimedes’ Principle*, in water (at 19.1 – 19.4°C) and was recorded to four decimal places.

For microstructure evaluation, the samples were mounted in PolyFast, and then ground and polished to a final 1 μm finish. The polished samples were then etched with 2% nital by immersing the top of sample briefly into the solution; etching times varied for each sample. Virgin powder was mounted in epoxy and polished to a 1 μm finish to observe internal starting porosity as seen in Figure 4.2. The microstructure of the etched cross-sections was characterized using both dark field OM (Olympus BX-51, Olympus Corporation, Tokyo, Japan) and with a field emission scanning electron microscope (FE-SEM; Hitachi S-4700, Hitachi High Technologies, Tokyo, Japan). The wetting angle of the single clad samples was measured using the profile tool on a CLSM with measurements conducted three times to obtain an average. Vickers hardness profiles were measured on the polished cross-sections along the build direction (+z) using a Nanovea PB1000 (Nanovea, Inc., California, USA) with five measurements taken for an average at 0.5mm increments at 20°C. The public domain software ImageJ was used to the measure the secondary dendrite arm spacing (SDAS) and dilution of the single clad samples, with Figure 4.3 highlighting how the contact angle and dilution ratio were measured. The dilution ratio (*D*) was then determined following a simplified ratio in Equation 7, using the depth and height of the deposit [35]:

$$D = \frac{1}{1 + \frac{h}{d}} * 100\%$$

Equation 7: Dilution ratio (D) of clad deposits.

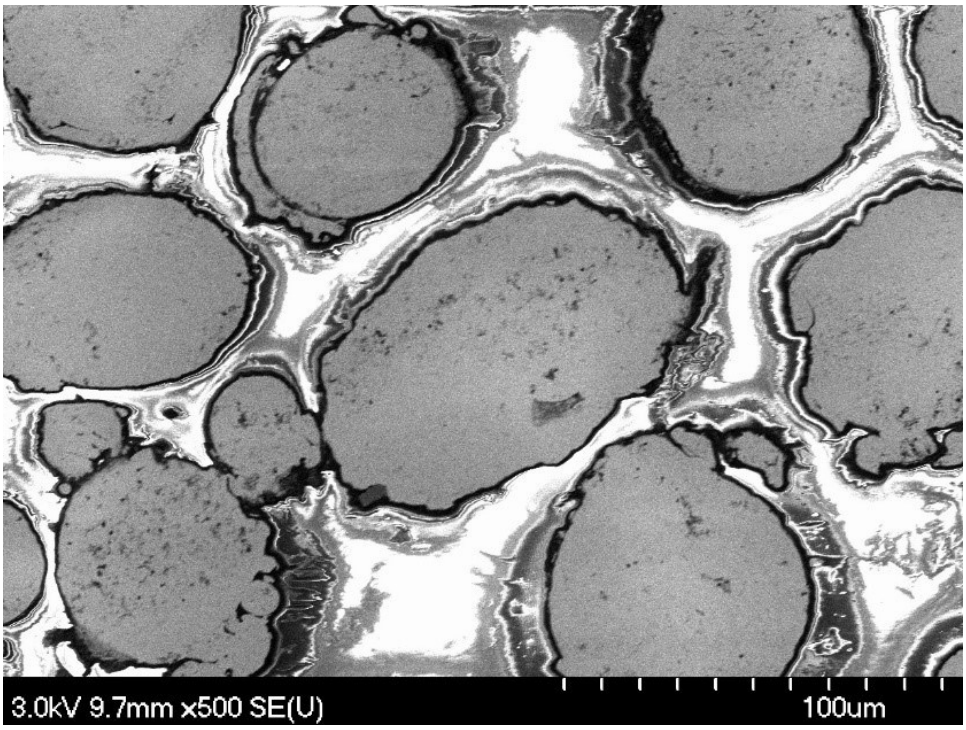

Figure 4.2: Polished cross-section of virgin H13 tool steel powder highlighting the internal porosity.

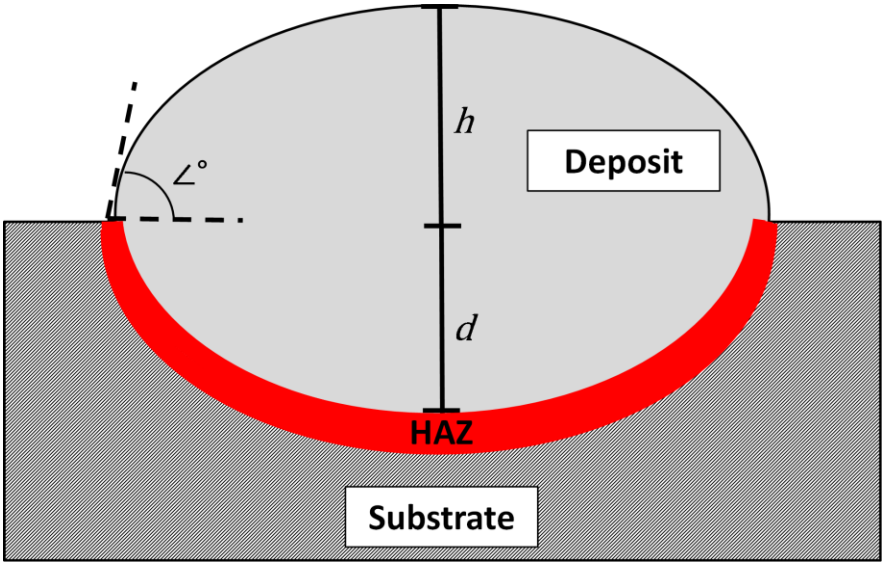

Figure 4.3: Schematic showing contact angle (∠°), the measurements (*h*) and (*d*) required for the calculation of the dilution ratio (D), and the heat affected zone (HAZ) in red below the deposit.

Crystallographic phase evaluation was conducted using XRD (Bruker D-8 Advance Bruker Corp., Billerica, MA, USA) operating at 35 kV and 27 mA with CoKα radiation and a Fe filter. A step size of 0.02° and a time per step of 0.5 per second over a range of 20 – 130° for 2θ was used. The sample was cleaned with acetone before being placed in the sample holder. Retained austenite can be measured using XRD, but alloying additions can distort the peak intensities. Furthermore, CrKα radiation is the preferred radiation, as it separates the carbide peak intensities from the austenite and ferrite/martensite peak intensities. CoKα radiation can be used but has a lower resolution [106]. Preparation of the sample using a linear precision saw (Isomet 4000., Buehler, IL, USA) may have damaged the surface of the surface by causing localized heating, decomposing the retained austenite.

4.7 Experimental Procedure for Initial Wear Response

4.7.1 Raw Materials

Wrought AISI H13 hot work tool steel was purchased from Hudson Tool Steel Corporation (Rockford, IL, USA). Tool steel was received in the annealed condition (AR). To reduce oxidation, each sample was placed in a stainless-steel bag along with sponge Ti powder to preferentially oxidize over the tool steel. All samples were austenitized at 1032°C for 30 min. Five wrought samples were double-tempered and held at 300°C, 400°C, 500°C, 600°C and 700°C for two hours followed by cooling to room temperature in air. A quenched sample was made by austenitizing at 1032°C for 30 min then quenched in air. The purpose of the wide range of tempering conditions for the wrought material was to examine how the wear response changed with temperature and

to select a suitable tempering temperature for the printed samples. The as-printed DED samples are indicated with “AP”.

4.7.2 Heat Treatment of DED Samples

Each DED-processed sample was placed in a stainless bag along with sponge Ti powder for the same reason as mentioned previously. The samples were austenitized for 30 min at 1032°C followed by an air quench. They were double-tempered at 600°C for two hours followed by cooling to room temperature in air. The heat treat DED samples are indicated with “HT”.

4.7.3 Laser DED Machine Parameters

The laser DED system used in the present investigation was a 3-axis LENS^{TM} 450XL system (Optomec, Albuquerque, NM, USA), using a 400 W continuous Nd:YAG laser and Ar as the powder carrier gas (5 L/min flow rate) and Ar as the protective shield gas (25 – 30 L/min flow rate), to inhibit oxidation. The initial chamber is under atmospheric conditions in the build chamber at ambient temperature, with a 15-minute purge of Ar but the Ar content increases continuously during deposition. The system operating parameters employed for the cylinder samples were printed using settings A3, B2, B3, and C4 which are listed in Table 4.3.

4.7.4 Sample Test Geometries

The DED samples had a diameter of 20 mm, with a height varying from 5, 15, and 25 layers (indicated by printing setting and layer height, e.g., A3-5) high resulting in three samples for each printing condition. The as-received wrought material was supplied as bar stock in diameter of 19.05 mm diameter and a length of 254 mm. 14 samples were cut from the tool steel in thickness of 5 mm for various heat treatments.

4.7.5 Scratch Hardness Set up and Scratch Track Characterization Methods

The scratch testing was performed following the procedure previously introduced in Section 3.1 using the Universal Micro Tribometer (UMT-1; CETR, Campbell, CA, USA) using a Rockwell diamond indenter (tip radius of 200 μm) sliding with a liner motion on sliding with a linear motion on the polished surface. The coefficient of friction (COF) was determined using the *Viewer* software which received the data from the tribometer system. An average COF value was obtained from the three scratch tests. A stitched image of the entire scratch track was taken using the CLSM at a magnification of 20x. Surface roughness measurements of the scratch track surface was repeated three times to obtain an average using an area of 25 μm x 500 μm, as shown in Figure 4.4, as supporting data for the COF. The cross-sectional area of the track was measured using an average profile measurement of 100 lines with 20 μm spacing, as shown in Figure 4.4. The purpose of the cross-sectional area measurement is to investigate how it changes with load (5 N and 10 N) and is supporting data for scratch hardness since the material condition (*i.e.,* as-printed and heat-treated) is expected to differ.

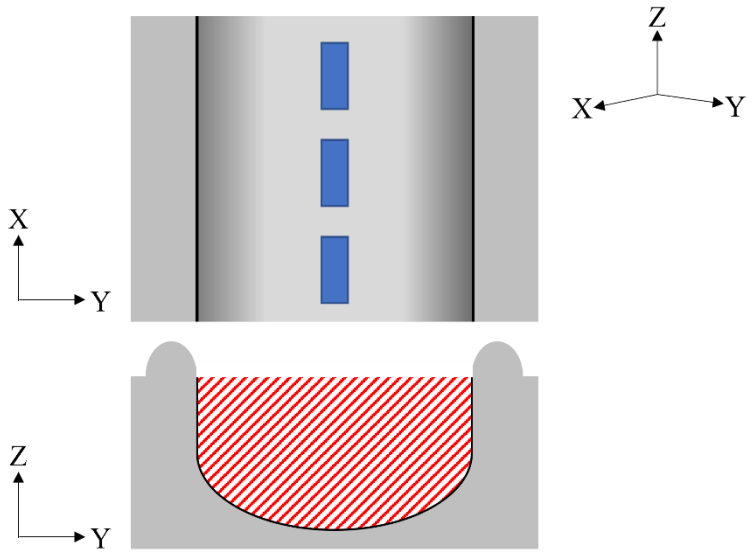

Figure 4.4: Schematic highlighting how the surface roughness area of 25 µm x 500 µm (solid blue rectangles) and the cross-sectional area (striped, red) of the scratch track, was measured using the CLSM at 20x respectively.

4.8 Sample Amount and Parameter Selection Justification

The limited number of samples measured in the various studies began with a delayed delivery of the DED system to Dalhousie University, and in the interim, characterization of the wrought H13 was studied. To accommodate NSERC HI-AM goal requirements and to progress the project, DED printing was conducted at CMQ. Once, the DED system was installed in the lab, access was limited, reducing the samples available to print. It was expected that the in-house DED would be equipped with the relevant laser requirements to process Cu due to the reflectivity issue, however this was not the case. This required contacting the DED manufacturer, Optomec, who provided contact details to the staff at NTU who offered to print the FGM samples. Lastly, access to the lab due to unforeseen restrictions in 2020 (due to the Covid-19 pandemic), hindered data collection.

Selection of varying the scanning speed and powder feed rate for printing H13 over the other available system parameters was because it was theorized it would have a significant impact on the as-printed surface roughness which was a major emphasis in this study. The other major variable system parameters, namely, laser power, hatch spacing, nozzle stand-off and layer thickness were not changed was because these settings were known to produced highly dense samples with good metallurgical bonding to substrate. The spot size was fixed with the laser system and hatch orientation was constrained by the available software.

4.9 Results and Discussion

4.9.1 H13 Powder Feedstock Characterization

Figure 4.5 demonstrates a representative PSD for the as-received powder. From the overall PSD information, the mean starting particle size has values of: D_{10} = 58.3 µm, D_{50} = 78.7 µm, and D_{90} = 107.0 µm. Figure 4.6(a) shows a representative FE-SEM image of the as-received powder, highlighting the overall particle morphology. It is apparent that the 'as-supplied', gas-atomized H13 powder has a generally spherical morphology, with some isolated satellite particles. In addition, cross-sectional examination (not shown) of the powder revealed it has minimal internal porosity. The as-received H13 powder had an apparent density of 4.260 g/cm^3, following the ASTM standard B703-17. Using a Hall Flowmeter (ASTM standard B213-20), the flow rate of the virgin powder was 15.13 seconds/50 g. After laser deposition, the used (recovered) powder had a slightly reduced flow rate of 16.73 seconds/50 g, resulting in an increase of 10.45%.

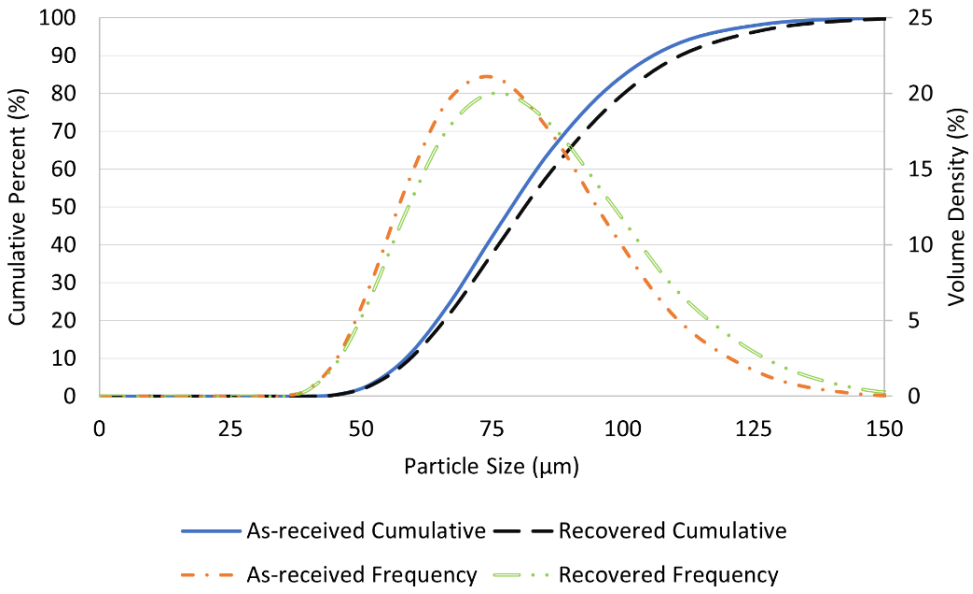

Figure 4.5: Representative examples of the particle size distributions for both the as-received and recovered H13 powder.

Figure 4.6(b) shows that the used powder, after running through the laser DED system, contains more satellites but some particles still remain without any satellites. The extra surface satellites can lead to greater particle 'interlocking', decreasing the flowability of the powder. Interlocking may lead to entrapped gas from the local atmosphere during DED. A further issue with interlocking, is that it may clog the powder feeder/nozzle head, through the possibility of powder particles jamming within the nozzle head and/or powder feeding tube, however this is difficult to fully assess [107]. *Kong et al.* noted that with a smaller PSD, the deposition process 'pulsed' [108], due to the powder particles compacting within the nozzle. When the carrier gas pressure build-up was sufficient, it would unclog the nozzle and the process would repeat itself. The observations relating to morphology changes are promising for reuse of the powder. However, a powder flow test

should still be conducted, in order to adjust the system parameters (if needed), thus ensuring the system powder feed rates remain consistent.

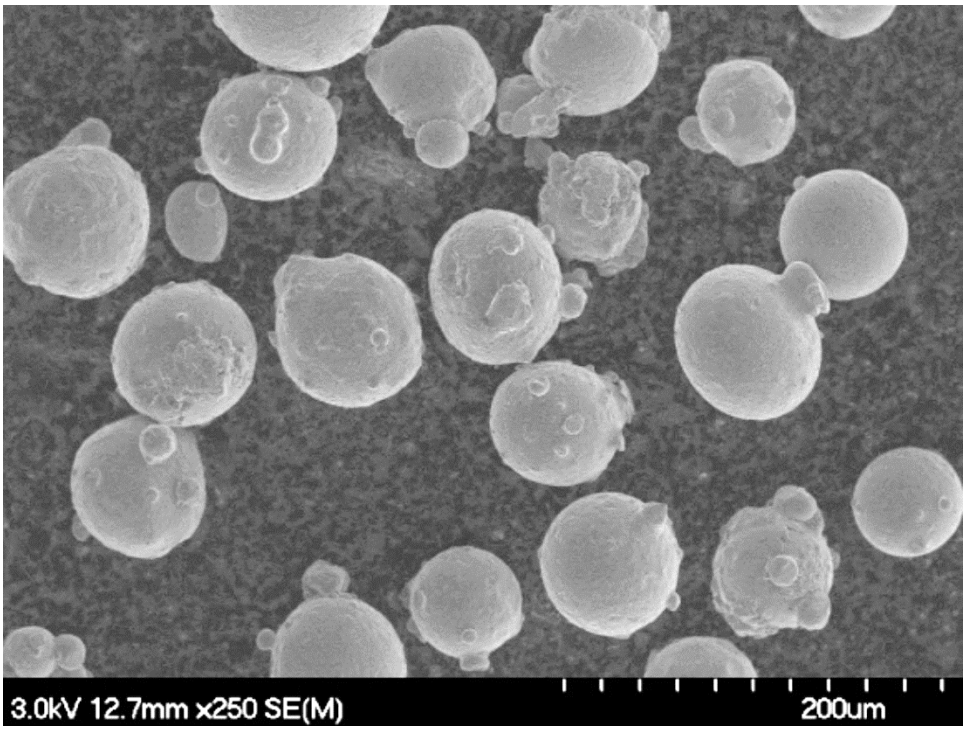

(a)

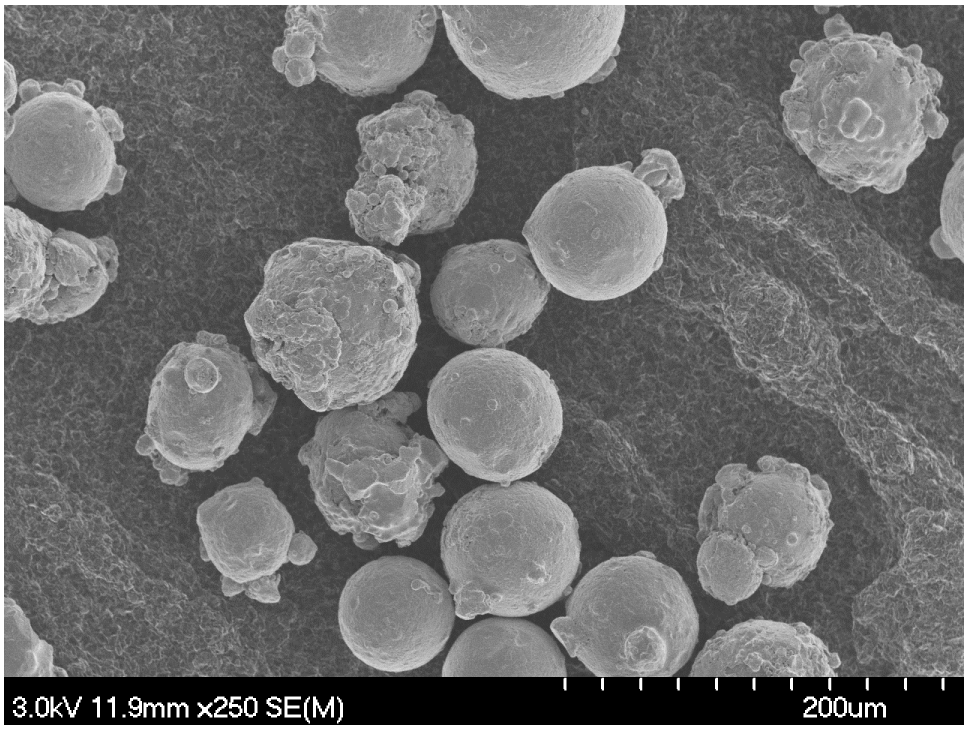

(b)

Figure 4.6: (a) Typical example of the as-received H13 powder morphology viewed using FE-SEM. (b) Used and recovered H13 powder morphology examined using FE-SEM.

4.9.2 Geometry Measurements of DED H13

4.9.2.1 Single-track Cladding Geometry Effects

A clear trend can be seen in terms of the effects of scanning speed, with faster speeds resulting in decreased single-track clad widths, as shown in Figure 4.7(a). In this instance the widths, measured via CLSM, range from 585.05 μm ± 9.43 to 674.93 μm ± 15.54. The slower scanning speeds result in a wider track because there is higher energy input per unit volume of material, which creates a larger melt pool [109]. The *R*-sq for the single-track clad widths is 82.14%. A reduction in the *R*-sq value in this instance could be attributed to noisy and high variance in the data set [105]. The *P*-values obtained for the

scanning speed and feed rate are 0.0 and 0.63, respectively (Table 4.4). Higher scanning speeds cause a reduction in the melt pool size, which consequently results in less consolidated material in each deposited track [110]. In addition, the increased feed rate means more particles are interacting with the laser beam, which in turn creates a smaller melt pool [111]. The likely reason that the scanning speed is a significant parameter is because it will determine how long powder particles can interact with both the laser beam and melt pool. Intuitively, a slower speed will result in a greater energy input, allowing for longer particle interaction with the laser and melt pool, consolidating more powder and leading to wider tracks and larger cross-sections [112]. In terms of the overall influence of the examined process parameters (Figure 4.7(b)), the powder feed rates do not have a significant impact on the track width. Conversely, the impact of the scanning speed is significant in terms of the measured track widths. Looking at the cross-sectional profiles of the single-track clads, again determined using the CLSM, the slower scan speeds resulted in the overall deposition of larger clads. The cross-sectional areas ranged from 19.5×10^3 ($\pm 3.7 \times 10^3$) μm^2 to 63.6×10^3 ($\pm 2.9 \times 10^3$) μm^2, with the highest feed rate resulting in the largest cross-sectional area (Figure 4.7(c,d)). Conversely, the fastest scanning speed and lower feed rates resulted in the smallest cross-sectional areas.

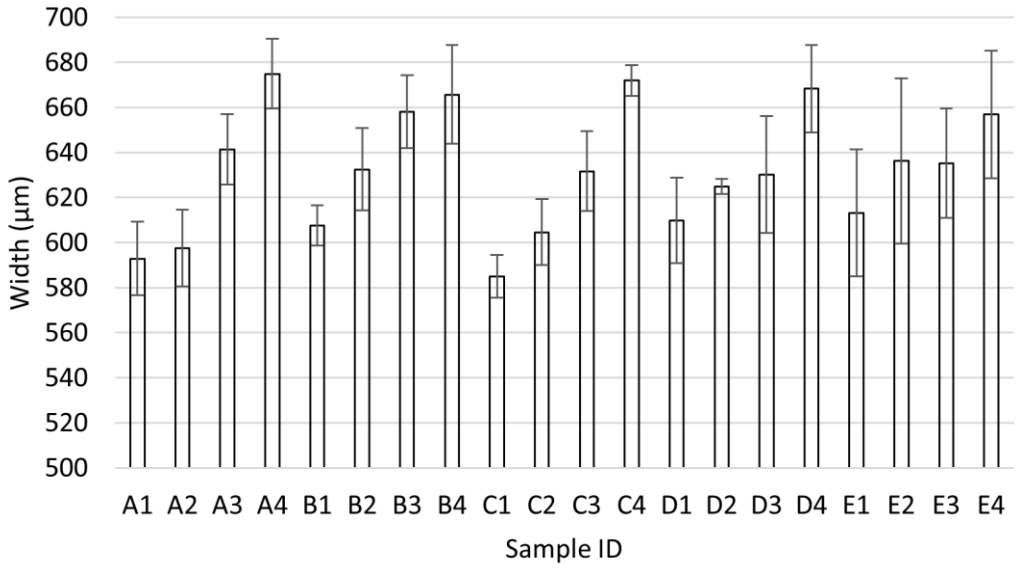
700
680
660
640
620
600
580
560
540
520
500
Width (µm)
A1 A2 A3 A4 B1 B2 B3 B4 C1 C2 C3 C4 D1 D2 D3 D4 E1 E2 E3 E4
Sample ID

(a)

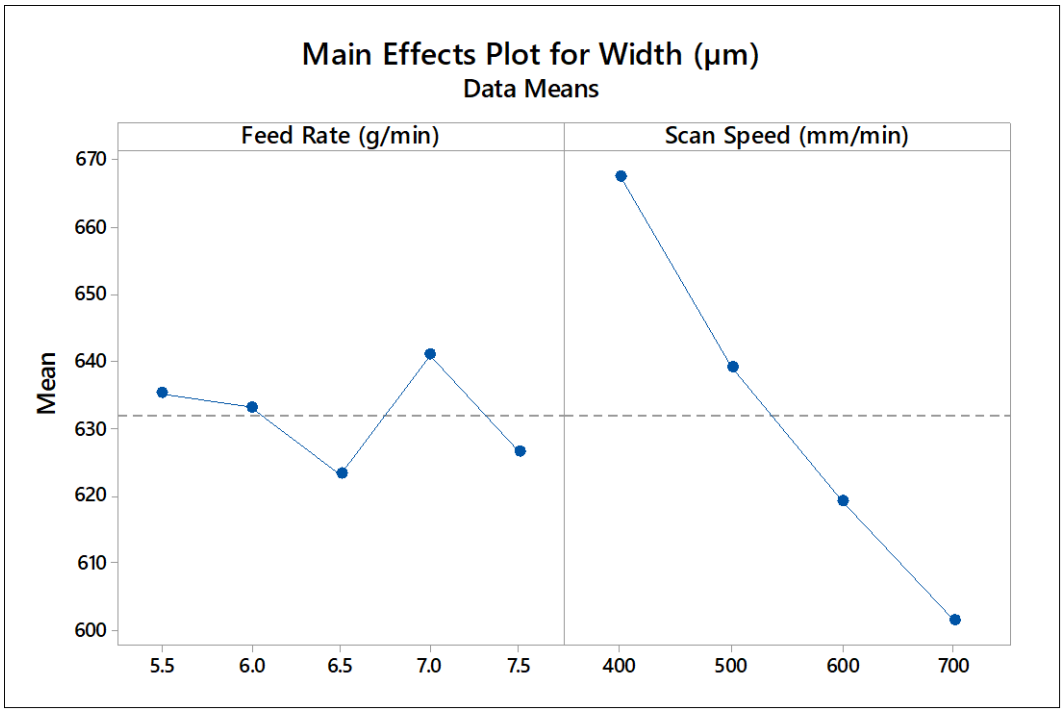
Main Effects Plot for Width (µm)
Data Means
Feed Rate (g/min)
Scan Speed (mm/min)
Mean
670
660
650
640
630
620
610
600
5.5
6.0
6.5
7.0
7.5
400
500
600
700

(b)

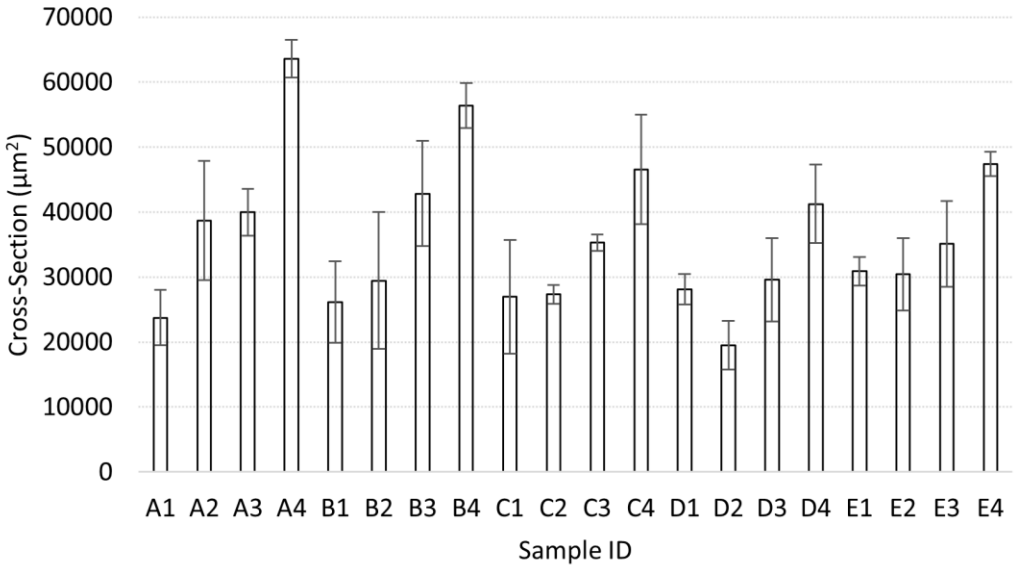
70000
60000
50000
40000
30000
20000
10000
0
Cross-Section (µm²)
A1 A2 A3 A4 B1 B2 B3 B4 C1 C2 C3 C4 D1 D2 D3 D4 E1 E2 E3 E4
Sample ID

(c)

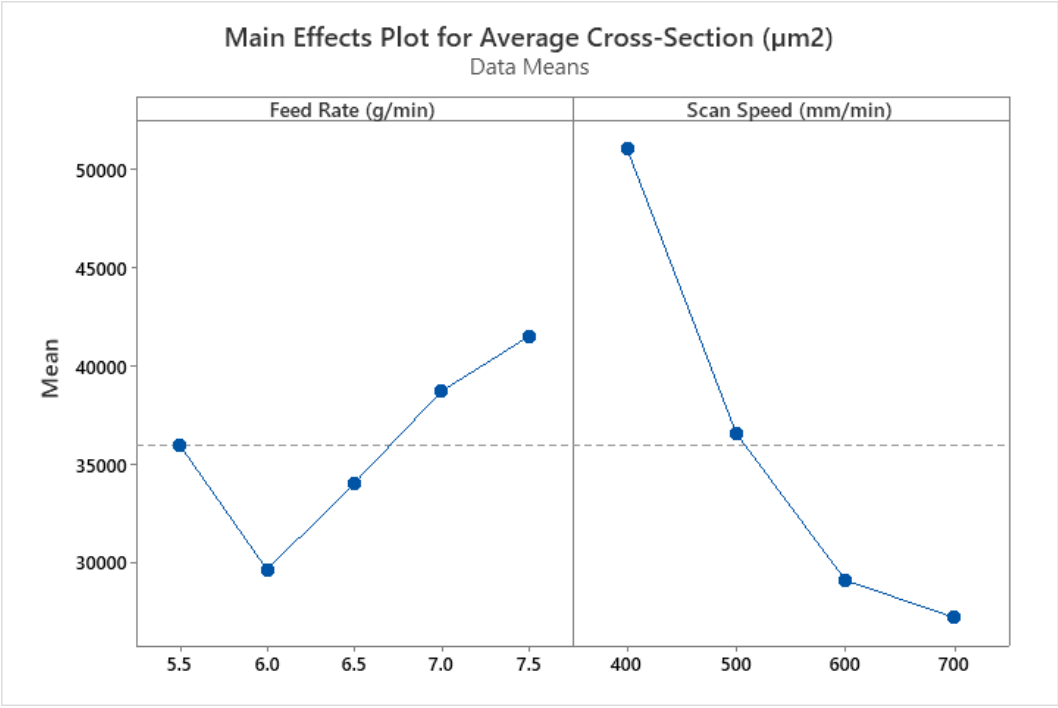
Main Effects Plot for Average Cross-Section (µm2)
Data Means
Feed Rate (g/min)
Scan Speed (mm/min)
Mean
50000
45000
40000
35000
30000
5.5
6.0
6.5
7.0
7.5
400
500
600
700

(d)

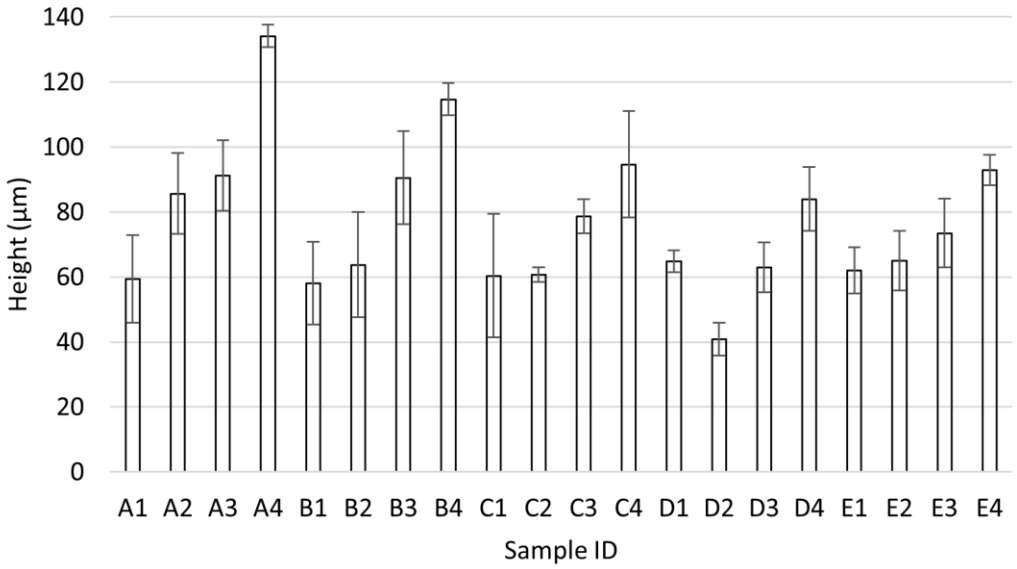

(e)

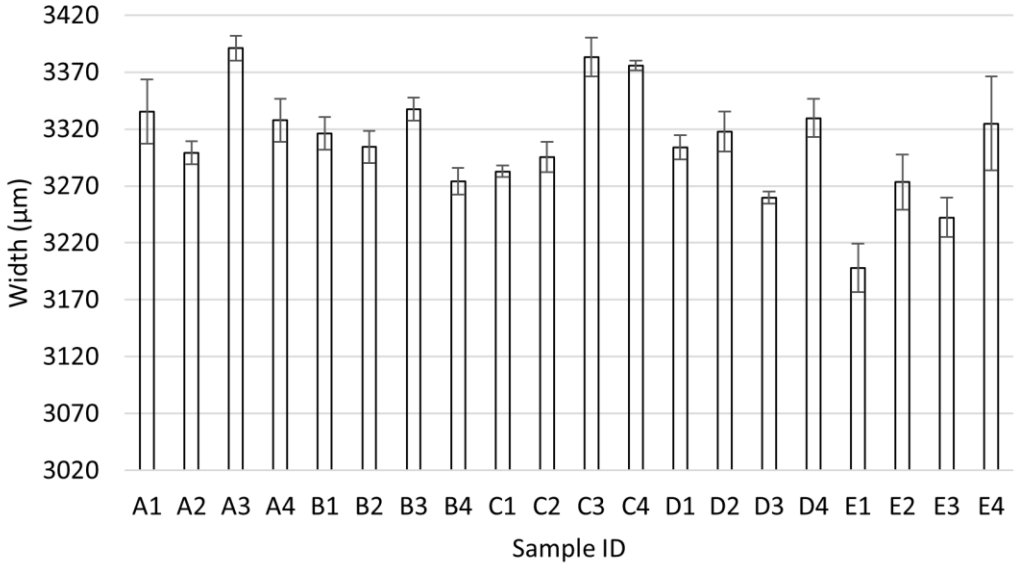

(f)

Figure 4.7: (a) The effects of varying system parameters on the single-track clad widths. (b) The resultant 'main effects plot' for single-track clad widths. (c) The effects of varying system parameters on the single-track cross-sectional areas. (d) The resultant 'main effects plot' for single-track clad cross-sectional areas. (e) The effects of varying system parameters on the single-track clad height. (f) Multi-track clad widths as a function of process conditions (provided previously in Table 4.3.)

Table 4.4: The system parameter significance (determined using ANOVA in Minitab®) on the widths of the single-track and multi-track clads, the rectangular samples, and the single-track clad cross-sectional areas (CSA).

Sample	***R*-sq (%)**	**Scanning Speed *P*-Value**	**Feed Rate *P*-Value**
Single-track Clad	82.14	0.0	0.63
Multi-track Clad	37.23	0.088	0.018
Rectangle	90.68	0.0	0.062
CSA	19.82	0.169	0.162

It is apparent that the lowest and highest examined scanning speeds, namely 400 mm/min and 700 mm/min, have the greatest influence on the amount of material consolidated (*i.e.*, cross-sectional area). The cross-sectional area *R*-sq = 19.82%, with associated *P*-values of 0.169 and 0.162 for the scanning speed and powder feed rate, respectively. It is clear there is no trend in the regression, but looking at the main effects plot, the magnitude of change in the feed rates is lower, when compared to the change in the scanning speeds from 400 mm/min to 700 mm/min.

Increasing the scanning speed results in a decrease of the clad height for the single-track clads, as shown in Figure 4.7(e), which is in general agreement with previous studies on laser cladding [113]–[117]. In contrast to the clear influence of the scan speed, the powder feed rates (ranging from 5.5 g/min. to 6.5 g/min.) do not show a significant trend with the cross-section, due to the large variance in the data. This may be due to unfavorable combinations of scanning speed and powder feed rate, although this requires further study. The single-track clad settings can give some indication as to whether a multi-layered part will be under- or over-built. In contrast to the case for single-track clads, the trend of decreasing width with increasing scan speed is not as clear for the

multi-track clad samples, with an *R*-sq of 37.23%, and *P*-values of 0.088 for the scanning speed and 0.018 for the feed rate (Table 4.4). The widths remain similar across the range of evaluated parameters, which is confirmed in Figure 4.7(f); the primary exception to this statement would be the E1 setting.

4.9.2.2 Rectangular/Ideal Layer Builds and Geometry Effects

Studies on both the single-track and multi-track clads show that, through modifying the deposition parameters, the originally intended layer thickness is not always obtained and, consequently, must be closely monitored during builds. Higher powder feed rates combined with slower scan speeds can result in over-building. This is apparent from dimensional studies of the rectangular sample heights, which ranged from 8.05 mm (± 1.32) to 13.80 mm (± 0.37), as presented in Figure 4.8(a). Similar observations to these have been made in prior studies [50], [118]. In terms of the rectangular builds, under all of the examined deposition conditions, the lengths and widths are similar across all of the examined settings; there is little variation in these dimensions, with a maximum error of about 1 mm.

Consequently, as might be anticipated, the most critical DED dimensional error arises in terms of the build height control. The height control can be corrected by dividing the desired dimension by the measured value, and then multiplying by the parameter:

$$Adjusted\ Parameter = \frac{Programmed\ Dimension}{Measured\ Dimension} * Current\ Parameter\ Used$$

This will indicate if the settings that are being used need to be changed; if the system parameter value remains the same, then the parameter does not require any adjustments. The adjusted parameter can increase or decrease, depending on the dimensional measurements. However, this will only help improve the dimensional target accuracy, but may not necessarily impact the surface finish and/or microstructure. It has been reported that the over-building observed with slower scan speeds is due to the higher power density, which consolidates extra powder particles [119], [120]. From the plot summarizing the primary parameter effects (Figure 4.8(b)), all of the examined powder feed rates have a very similar influence, indicating the increased flexibility in selecting feed rates without impacting the build response significantly. The major height error arises from the scanning speed, with the fastest speed under-building and the slowest speed over-building. Applying a regression to the height using the feed rate and scan speed, the determined *R*-sq value is 90.68% (Table 4.4). In association with this, the *P*-value for the scanning speed is 0.0, highlighting the significance of the scanning rate. In contrast, the powder feed rate has a *P*-value of 0.062, meaning it is not as significant as the scan speed.

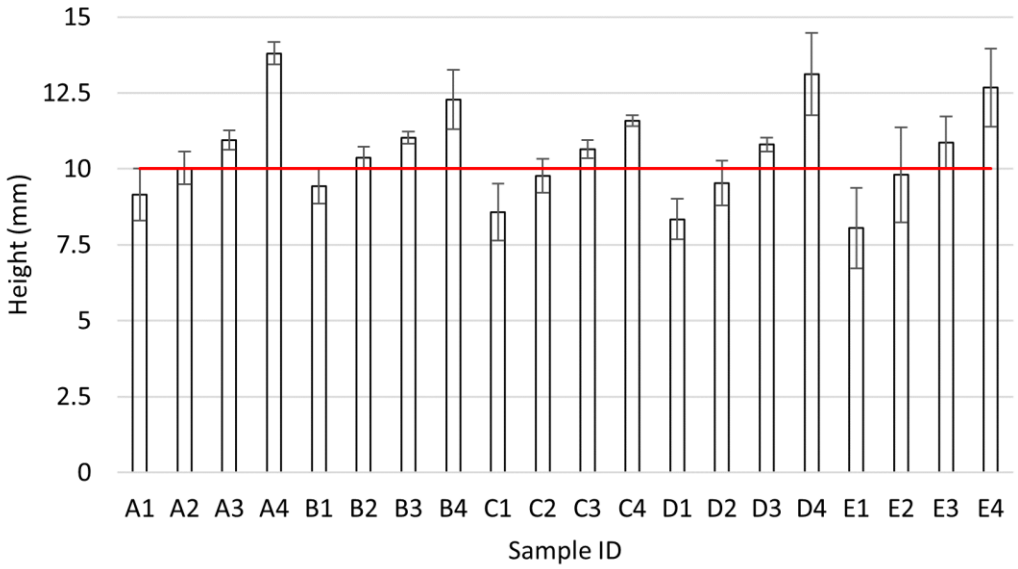

(a)

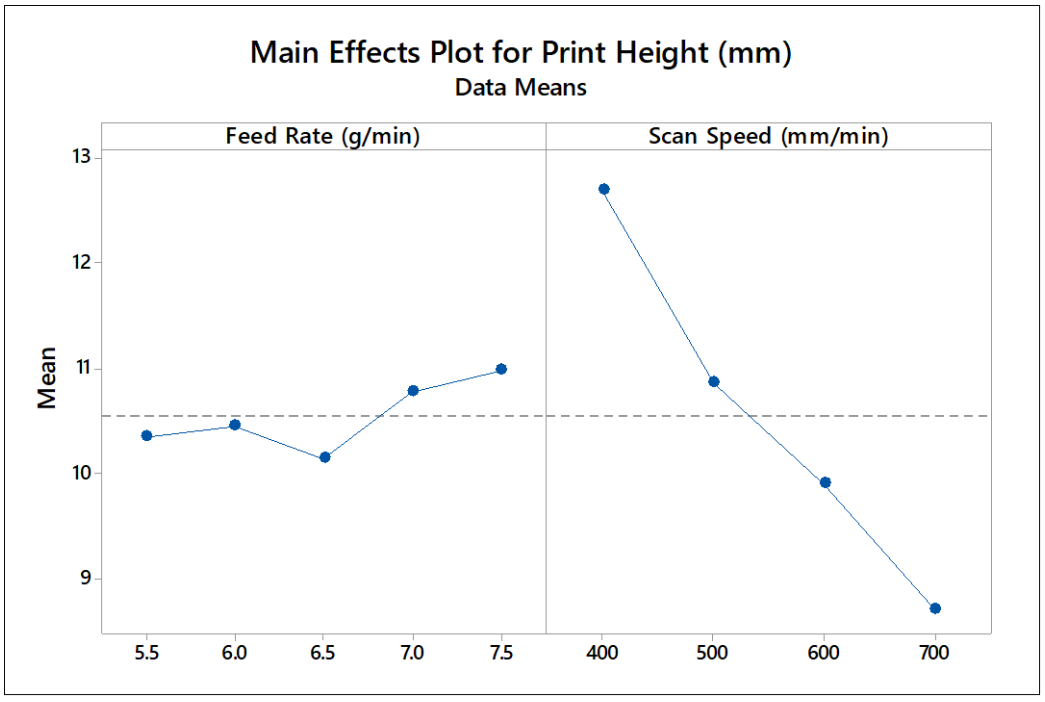

(b)

Figure 4.8: (a) Geometrical measurements for the heights of the rectangular samples as a function of process parameters. The red horizontal line indicates the pre-programmed rectangle target height. (b) The composite 'mean effects plot' for the rectangle heights.

As noted with the rectangular builds, the component width and length are comparable across the range of examined DED parameters, with the height being of more concern. To examine the effect layer thickness has on a pre-designed fixed height build in greater detail, six 'ideal layer' samples were also fabricated, as shown in Figure 4.9. When the thickness of the deposited layer is greater than desired, it results in over-building. When the layer thickness is reduced, more material is consolidated, and the build rate increases, which will decrease the actual build-to-nozzle stand-off distance; since the DED system cannot account for variations in the deposit height, finer layers will have a greater height error because over-building is more likely, and the material build "catches up" with the nozzle head. The opposite is true with a coarser layer thickness, as less material is consolidated, causing under-building. This is evident experimentally when the layer thickness has been changed (Figure 4.9), for example from 0.2032 to 0.3302 mm. This can be related to powder defocusing, in that if the powder defocusing is below the melt pool level, the height of the deposition increases because of the increased powder concentration [121]. Powder defocusing was not a system parameter controlled in this study, but it is suggested as a possible reason for the observed results and may warrant further study. For the present case it was apparent that it is difficult to obtain the desired layer thickness without adaptive controls to monitor the process [115], [122]. Under the A3 settings the layer thickness should have been changed to 0.3302 mm, as it was the closest to the desired height; this test would have to be conducted on each setting to find an optimal layer thickness.

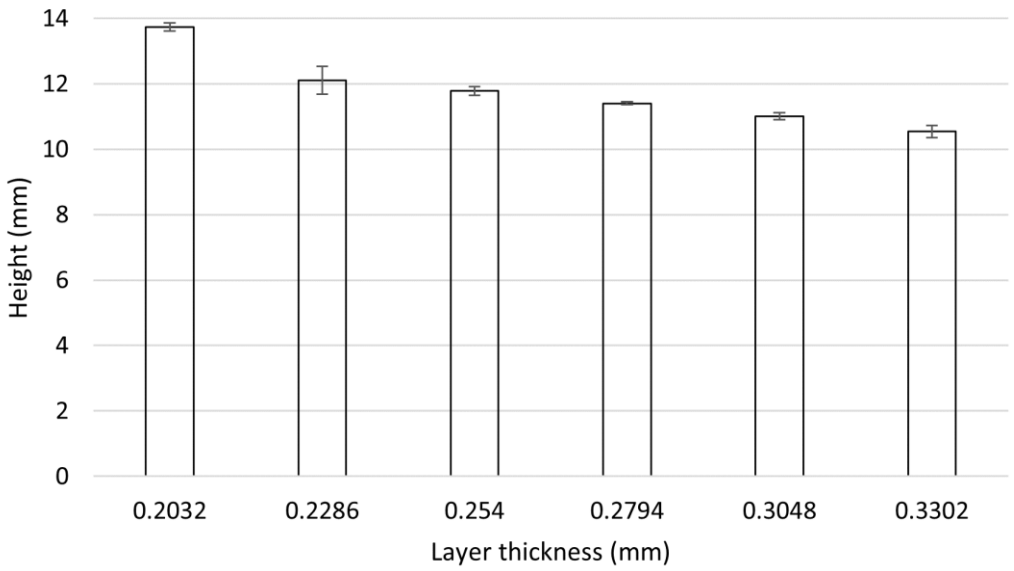

Figure 4.9: Dimensional measurements for the ideal layer height samples with error bars indicating the standard deviation.

In terms of build considerations with the present DED system and its operation, the rectangular samples that were initially printed have some evidence of limited surface oxidation, with subsequent prints having less. This is due to the build chamber nominally starting at atmosphere (*i.e.*, air) then, as printing continued, more Ar was used (as both the shield gas and powder carrier gas), thus reducing the extent of oxidation. Periodically there will be samples that will be more oxidized on the surface, with subsequently printed samples having a lower level of oxidation; this arises due to the need for periodic nozzle cleaning that requires opening the build chamber door, resulting in the chamber reverting to atmospheric conditions. There is no noticeable visual change in the single clad tracks other than the amount of oxidation. Clearly this is somewhat undesirable, with the potential to affect the interlayer structure and bonding for multi-layer builds. However, this is actually a realistic scenario for the low-cost repair of large tool steel components,

as they are likely to be processed using shield gas environments rather than enclosed chambers with a controlled inert atmosphere.

All samples also contain attached powder particles, which will ultimately lead to higher ‘as-printed’ surface roughness in components, and consequently dictate the need for some limited final machining. Adhered particles were also observed on the sides of vertical surfaces. Even though particles are seen on the side and top of each of the samples, all of the examined DED conditions produced a suitable structure, except for rectangle E1; under these specific system settings, the contour continued to build but the core filling was unsuccessful. It is unknown why this occurred, but a reasonable hypothesis may be due to the fast scanning speed used in combination with a low powder feed rate, resulting in under consolidation. The rectangle and ideal layer thickness samples have over-building on the corners, which appear to a greater or lesser extent on most of the printed samples. This was more evident in builds using the lower scanning speeds and lower feed rates, which is due to the toolpath software; as the contour is made, it will stop at the corner, pause and proceed on towards the next corner to finish the contour. The extra pause at the corner results in more material being deposited, causing the top surface to be uneven, which is clearly demonstrated in the extreme case presented in Figure 4.10. The lower speeds and lower feed rates can be expected to increase this effect because the imparted energy is greater, allowing for more powder particles to be fully melted into the built structure.

Figure 4.10: Sample D4, highlighting the more extreme ‘built-up’ corner effect, due to the scanning strategy employed (the cut substrate is shown at the bottom of the image).

A noticeable oxide layer can be seen on the sample surfaces using SEM (Figure 4.11), which has a fibrous appearance. It can be envisaged that there may be entrapped oxide on powder particle regions in builds, especially if the power density is increased [123]. Since the oxide can be anticipated to be brittle, it is arguably undesirable, but any external surface oxidation would be likely removed through finish machining. In addition, this oxide ‘curtain’ makes it difficult to identify porosity on the printed surface in comparison to the porous oxide structure itself.

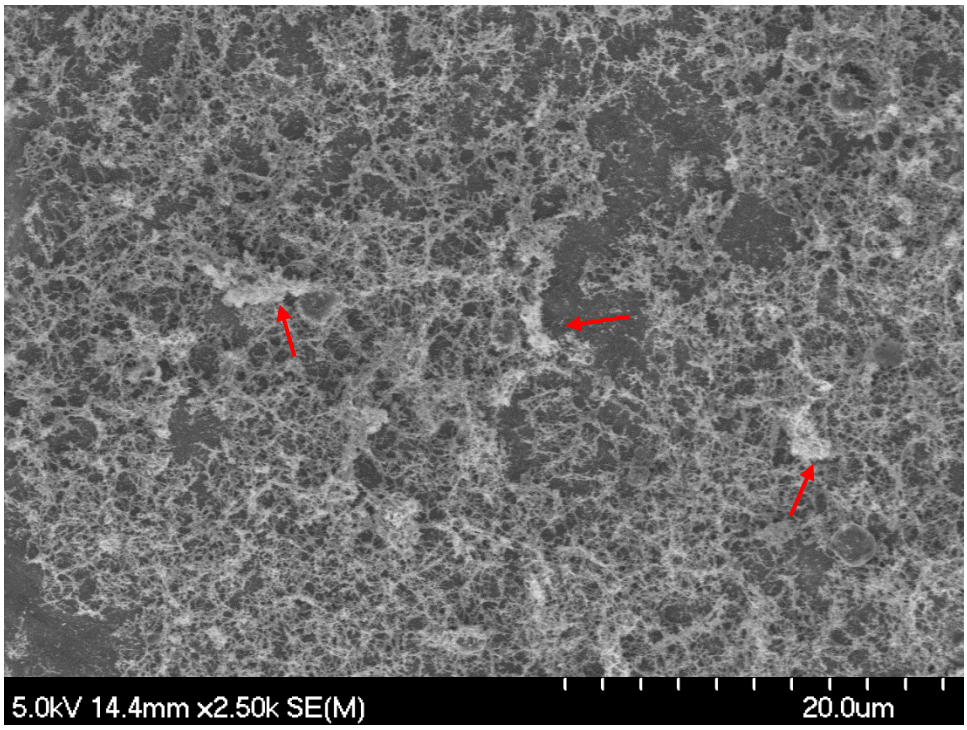

Figure 4.11: Representative FE-SEM image demonstrating the formation of some limited surface oxide. Note that the oxide lightly covers the surface with a fine, fibrous morphology; some areas of higher oxide concentration are highlighted with red arrows.

All the 3D samples have a distinct ‘wavy’ surface appearance, indicative of the laser DED build process. It has been previously noted that the use of inert gas-atomized powders creates well defined, individual layers when compared to water atomized powders [124]. In addition, it was shown that using gas-atomized powders also resulted in more partially melted particles on the surface, leading to a higher surface roughness [124]. This is because the melt pool temperature for gas-atomized powders is lower than water atomized powders, due to the increased surface coupling, arising from the powder surfaces being rougher and having more oxidation during synthesis [36]. There were no major visible signs of lack of layer fusion in the present work. In the boundary region between layers, the surface appears smooth while the side of the layer has striations that

show the melt direction. In the ideal layer samples, the larger layer thickness can be distinguished from the finest layer thickness. However, there is no significant visual change that can be seen between the differing finer layer thicknesses.

4.9.3 Surface Roughness Characterization of As-Printed DED H13

4.9.3.1 Surface Roughness of Single- and Multi-track Clads

Figure 4.12 summarizes the mean top surface roughness measurements for the single-track and multi-track clad samples. For the case of single-tracks, the surface roughness generally appeared to increase with decreasing scanning speed, with this trend clearest for parameter sets A, B and E, and less apparent for parameter sets C and D; however, there is still a generally comparable response overall. In a similar manner, the surface roughness for the multi-track cladding samples increases with decreasing scan speed. This was a clear trend for each of the DED parameter sets examined. Examining the primary process variables, it is seen that the surface roughness generally increases with increasing powder feed rate for both the single- and multi-track cladding depositions (Figure 4.13). However, in comparison to the influence of scan speed, for the multi-track clads the effects are more subtle, although the roughness values are much higher. As noted in the previous paragraph, the lowest surface roughness values generally occur at the highest examined scan speeds, for both the single-track and multi-track clads, which are highlighted in the 'mean effects plots' (Figure 4.13). The multi-track clad samples follow the same trend as the single-track clads, with slower scanning speeds and higher feed rates generally producing a higher surface roughness. However, it is clear that the multi-track clad samples are significantly more rough than the single-track clads, due to the waviness of the adjacent layers compared to the single-track.

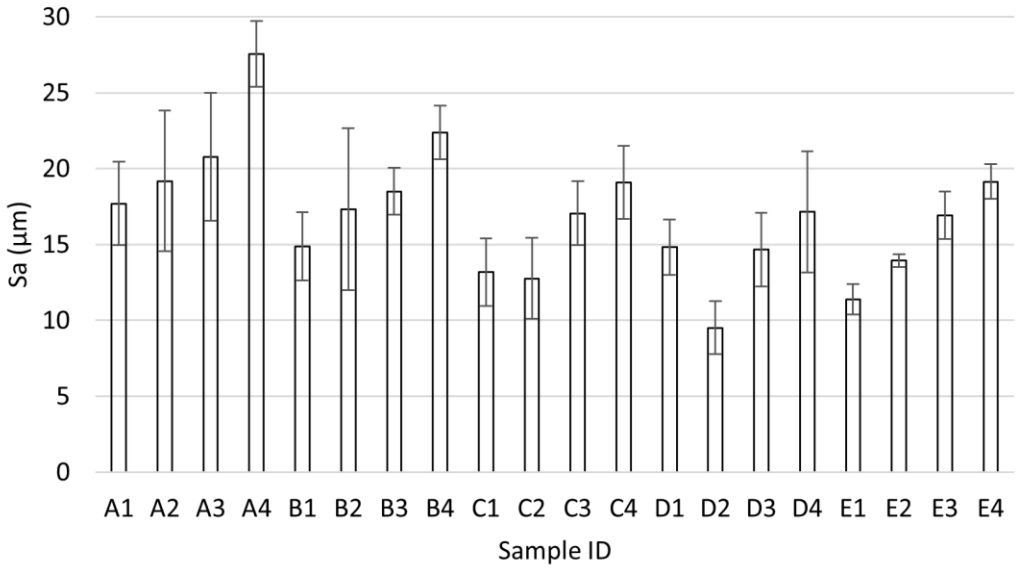

(a)

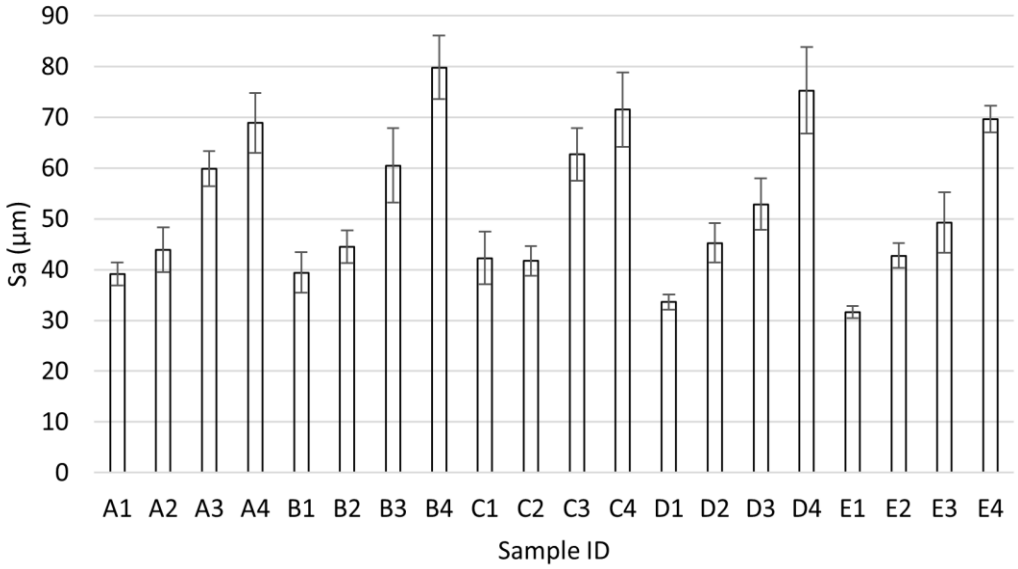

(b)

Figure 4.12:Cladding surface roughness, Sa, as a function of DED process parameters (Table 4.3): (a) single-track, and (b) multi-track clads.

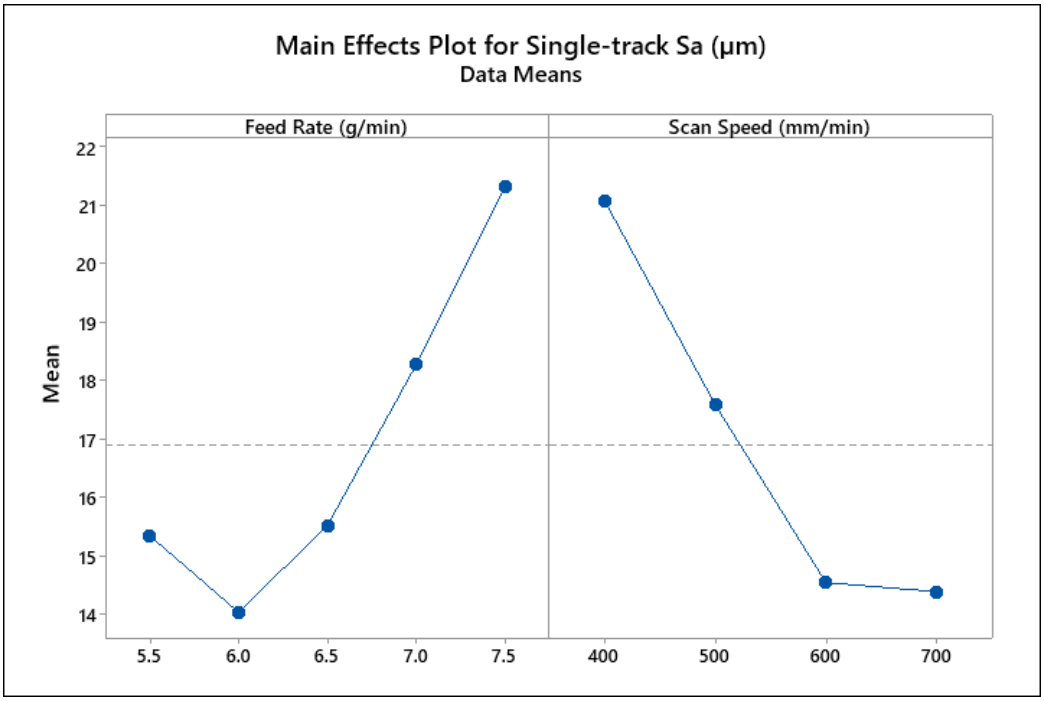

(a)

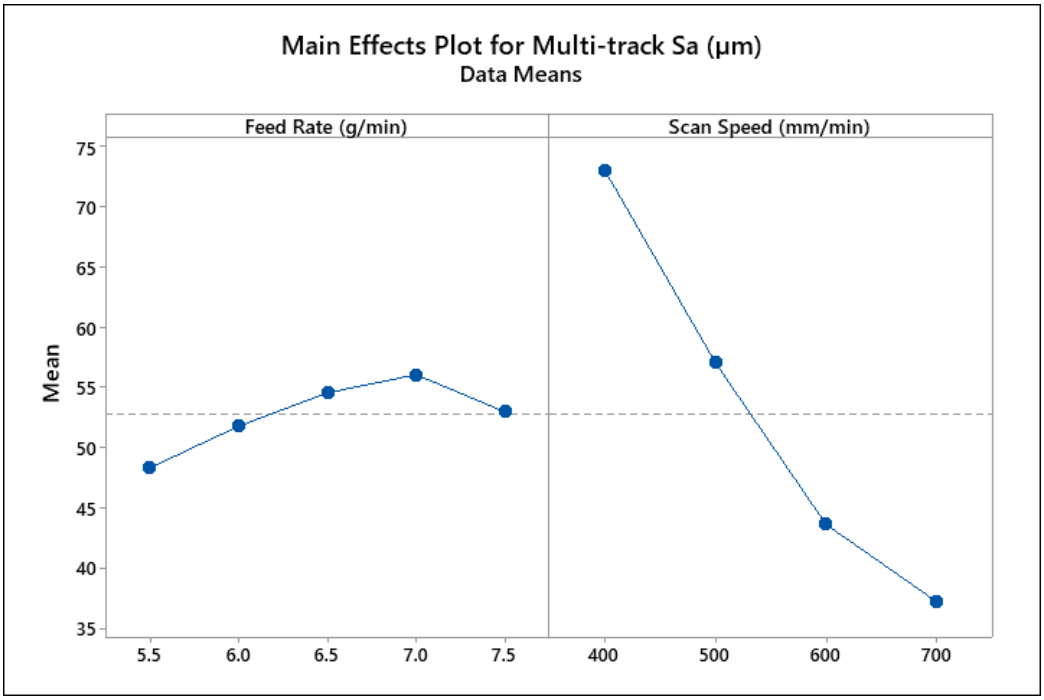

(b)

Figure 4.13: Mean effects plots of surface roughness, Sa, as a function of DED parameters for: (a) the single-track clads, and (b) the multi-track clads.

A combination of the slowest scanning speed, together with the highest feed rate, resulted in the highest surface roughness. The lower quality surface finishes (*i.e.*, higher roughness), produced by the higher feed rates, are likely due to more particles interacting with the laser beam, resulting in a smaller melt pool, as noted earlier. When the scanning speed is reduced, the surface roughness may be anticipated to decrease because there is a longer laser particle interaction period to melt the particle [109], and *vice-versa* with a faster scanning speed. The higher surface roughness for the higher feed rates is consequently believed to arise from a greater number of partially melted particles attached to the surface. In terms of statistical analysis, the single-track clad samples have *P*-values of 0.0 for both the feed rate and the scanning speed, and an *R*-sq of 75.21% (Table 4.5). In comparison, the multi-track clad samples have *P*-values of 0.073 and 0.0 for the feed rate and scanning speed, respectively, and an *R*-sq of 91.56% (Table 4.5). Contour 'maps', relating the effects of the combined scanning speed and powder feed rate parameters on surface roughness, are shown for both single- and multi-track clads in Figure 4.14.

Table 4.5: System parameter significance (determined using ANOVA in Minitab®) on surface roughness (Sa) values determined for the single-track and multi-track clads, and the rectangular samples.

Sample	***R*-sq (%)**	**Scanning Speed *P*-Value**	**Feed Rate *P*-Value**
Single-track Clad	75.21	0.0	0.0
Multi-track Clad	91.56	0.0	0.073
Rectangle (Side)	9.75	0.235	0.577
Rectangle (Top)	5.721	0.35	0.928

To assess a nominal deposition 'wetting angle' for the single-track clads (defined as a 'clad angle', α), cross-sections (cut perpendicular to the laser scanning direction of track)

were evaluated to determine the angle the clad track makes with the substrate (Figure 4.15); the defined ‘wetting angle’ measurement used in the present case is shown schematically in Figure 4.15(a). It is apparent that faster laser scanning speeds generate a lower angle in the single-track clads when compared to slower speeds (Figure 4.15(b)). This is likely due to the melt pool flattening out due to the shorter dwell time of the laser for the faster scanning speeds. With a slower scanning speed, the temperature gradient and surface tension in the melt pool is reduced due to the higher energy input, the fluid flow decreases and this results in the bead forming a ‘hump’ shape [125], [126].

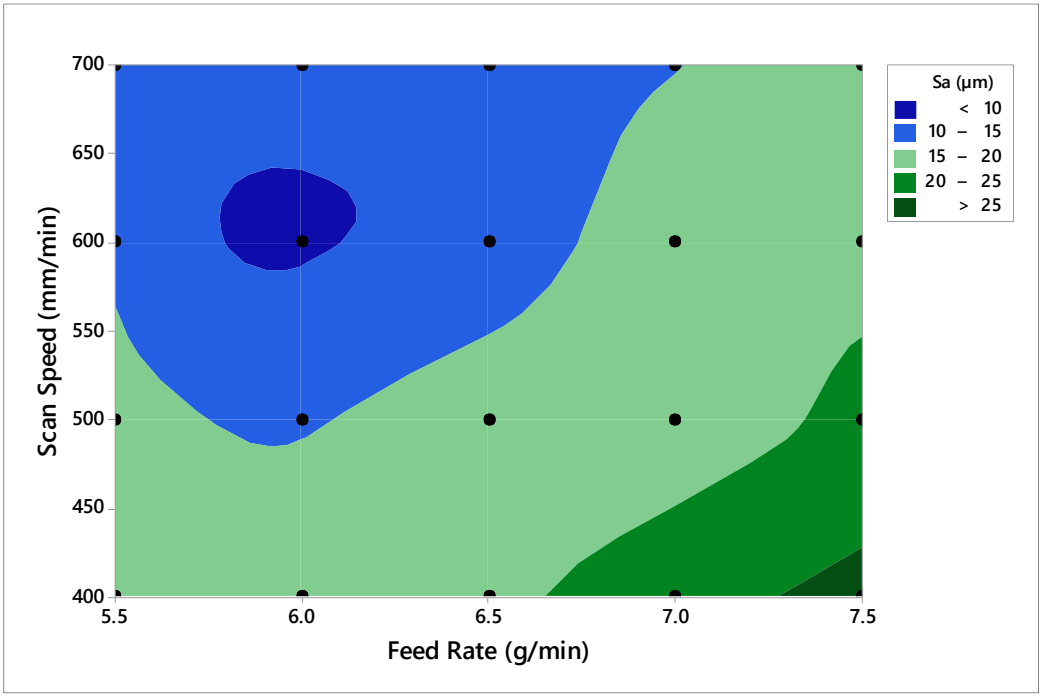

(a)

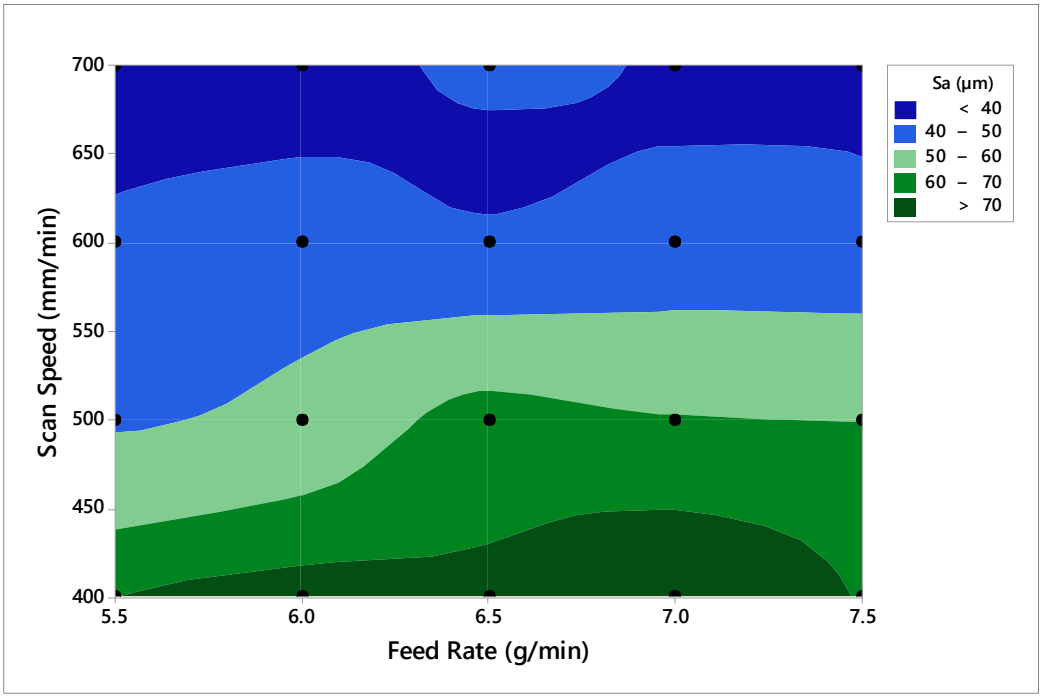

(b)

Figure 4.14: Surface roughness, Sa, contour maps for: (a) the single-track clads, and (b) the multi-track clads over the varying system parameters.

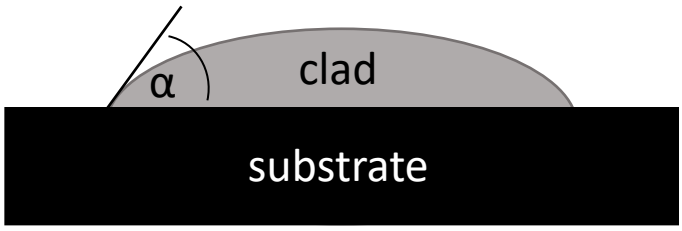

(a)

(b)

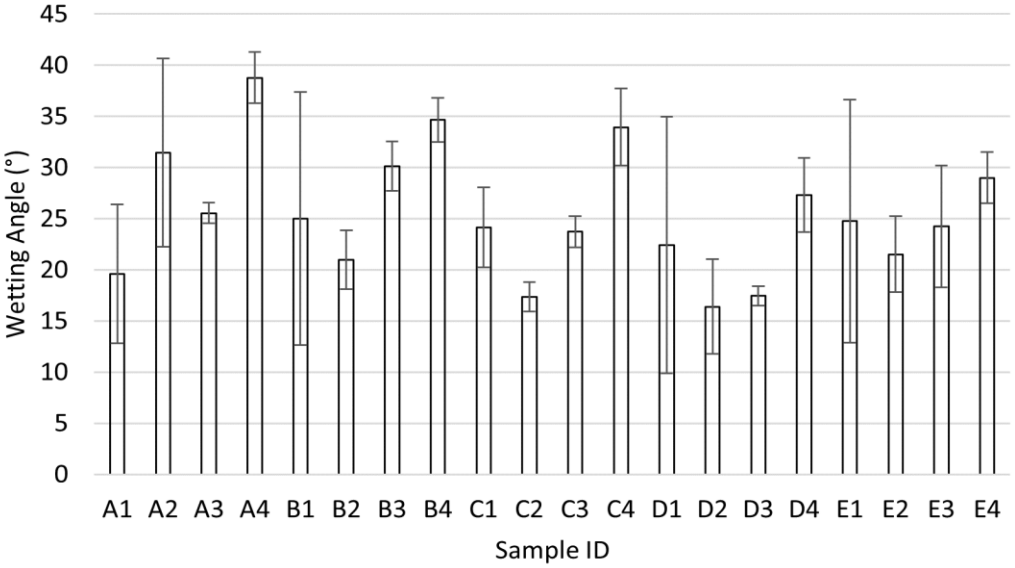

(c)

Figure 4.15: (a) The 'wetting angle' (α) definition used in the present work. (b) Example CLSM optical (white light) image of the cross-section of a single-track clad (processing condition B4). (c) The mean single-track clad 'wetting angle', as a function of laser DED process parameters.

4.9.4 Surface Roughness of Rectangular Geometry Samples

In order to see if there is a correlation between the wetting angle of the single clad samples and the side surface roughness of rectangular samples, the side surface roughness was determined for the rectangle builds (Figure 4.16). In the 'A' set of samples it appears that with increasing clad angle, α (data from Figure 4.15), the side surface roughness also increases, the exception being setting A2, having a lower side surface roughness. The 'B' and 'D' parameters have a general correlation between the clad angle and side roughness, with settings B4 and D3 not following this trend. The 'C' and 'E' settings do not follow the trends. Overall, based on this comparison, there does not seem to be a significant correlation between the deposit clad angle and side surface roughness. In addition, the profile of the single-track clad can vary widely across the track. Faster scanning speeds had the most variance in the clad angle, with slower scanning speeds resulting in more consistent clad profiles. This interaction of using the clad angle to predict the side surface roughness could be useful, but since there are material and heat interactions with the previous layer in multi-layered builds, it becomes increasingly more difficult to predict the potential impact.

Although there is a clear spread of measured surface roughness values, as a function of the examined DED process parameters, there does not appear to be a clear trend of parameter dependence in terms of the surface roughness for either the sides (Figure 4.16) or tops (Figure 4.17) of the rectangular samples. This is in contrast to the prior observations for the single- and multi-track clads, where the slower scan speeds had a higher surface roughness; this observation highlights the need for caution in extrapolating 3D build expectations of surface finish for multi-layer samples from single- or multi-

track clad analysis. Comparing these two figures, it is clear that the side finish roughness values are consistently slightly lower than those of the top surfaces. This may be due to the larger surface area for particles to remain ‘trapped’ on top of the sample with the slower scanning speeds, combined with a larger amount of material being used, as the top surface will remain at an elevated temperature creating the possibility of bonding with these extra particles. Broadly speaking, from the contour map for the rectangle side roughness, the values determined decrease with increasing scan speed (Figure 4.16(c)). The lower powder flow rates also produce a slightly higher side surface roughness, although this trend is relatively subtle, but especially notable in combination with the lower scan speeds. In comparison, the top surface roughness values show no clear trend with either the laser scanning or powder flow rates.

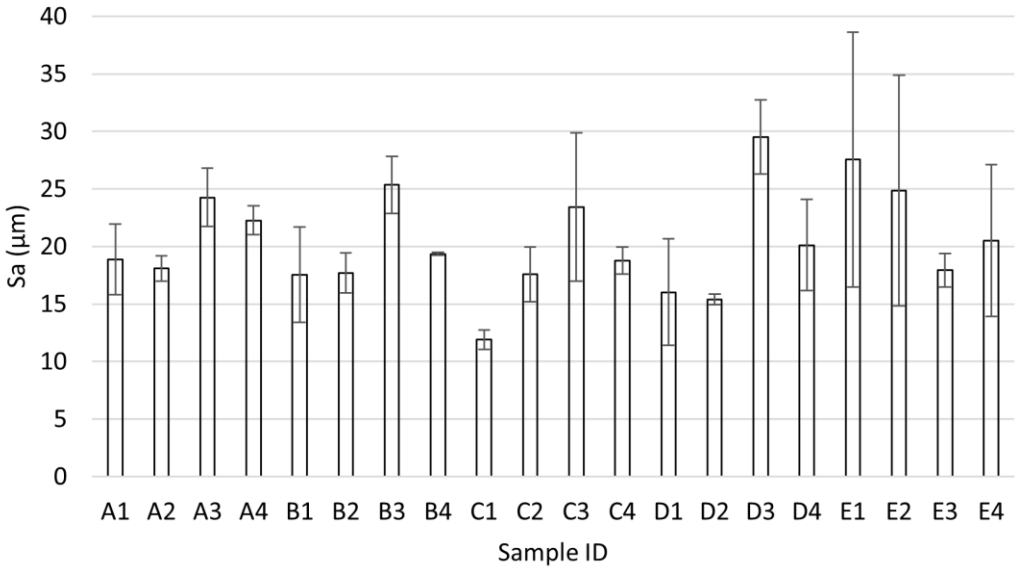
Sa (µm)
40
35
30
25
20
15
10
5
0
A1 A2 A3 A4 B1 B2 B3 B4 C1 C2 C3 C4 D1 D2 D3 D4 E1 E2 E3 E4
Sample ID

(a)

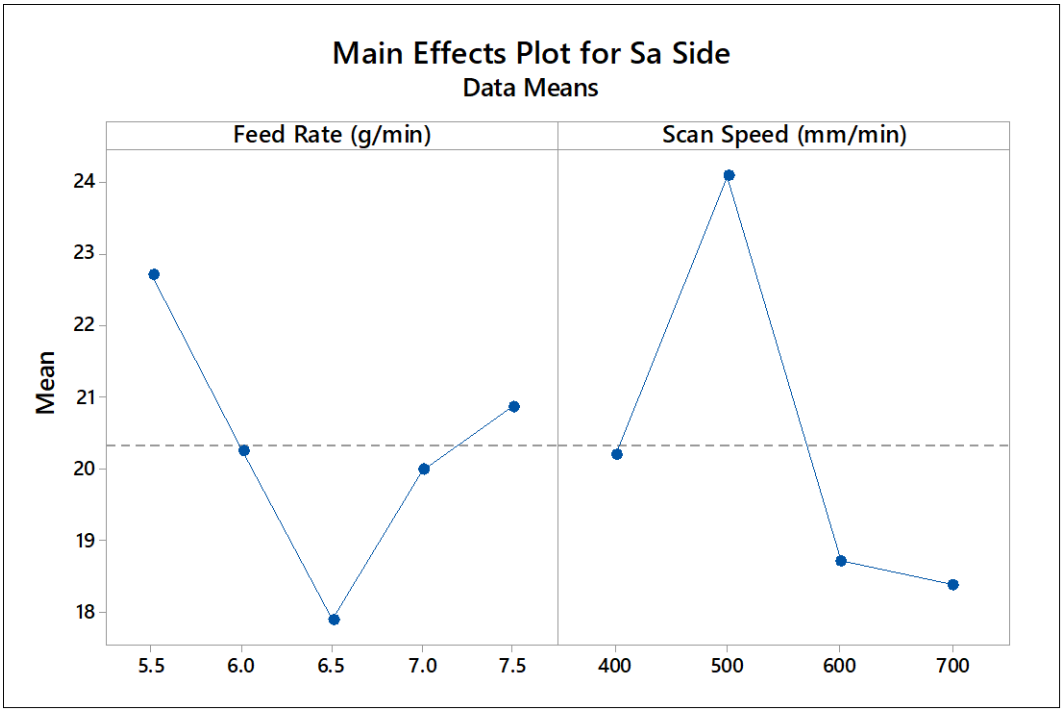
Main Effects Plot for Sa Side
Data Means
Feed Rate (g/min)
Scan Speed (mm/min)
Mean
24
23
22
21
20
19
18
5.5
6.0
6.5
7.0
7.5
400
500
600
700

(b)

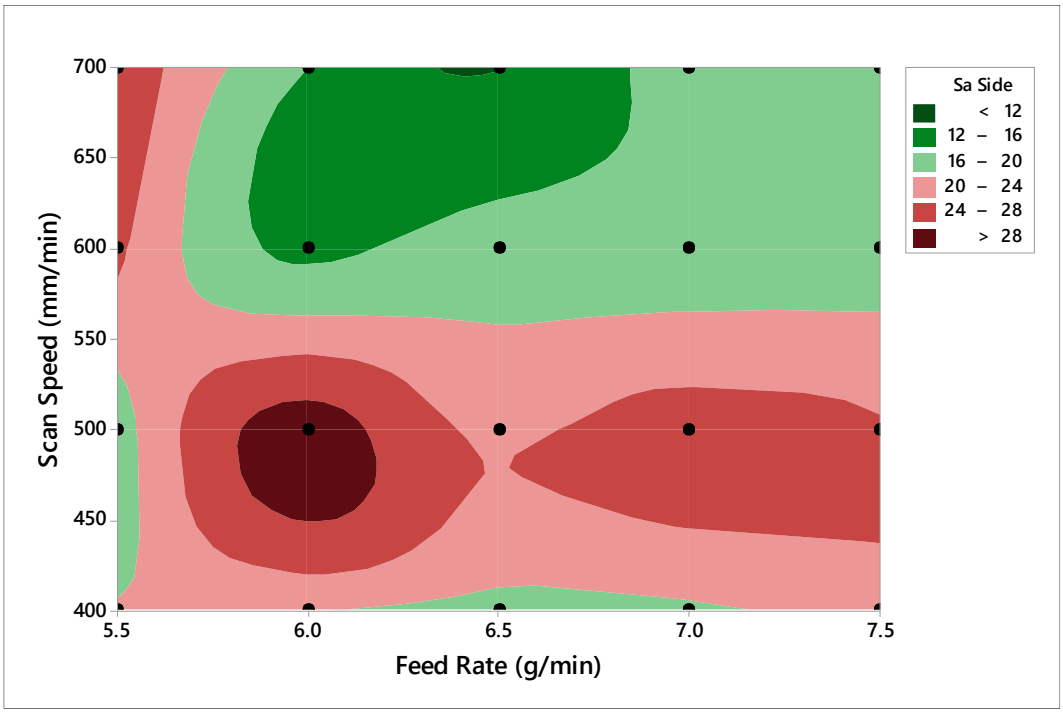

(c)

Figure 4.16: (a) The mean rectangle side surface roughness, Sa, values for each of the assessed DED parameter sets. (b) The 'main effects plot' for the surface roughness of the rectangle sides. (c) The surface roughness contour map for the rectangle sides.

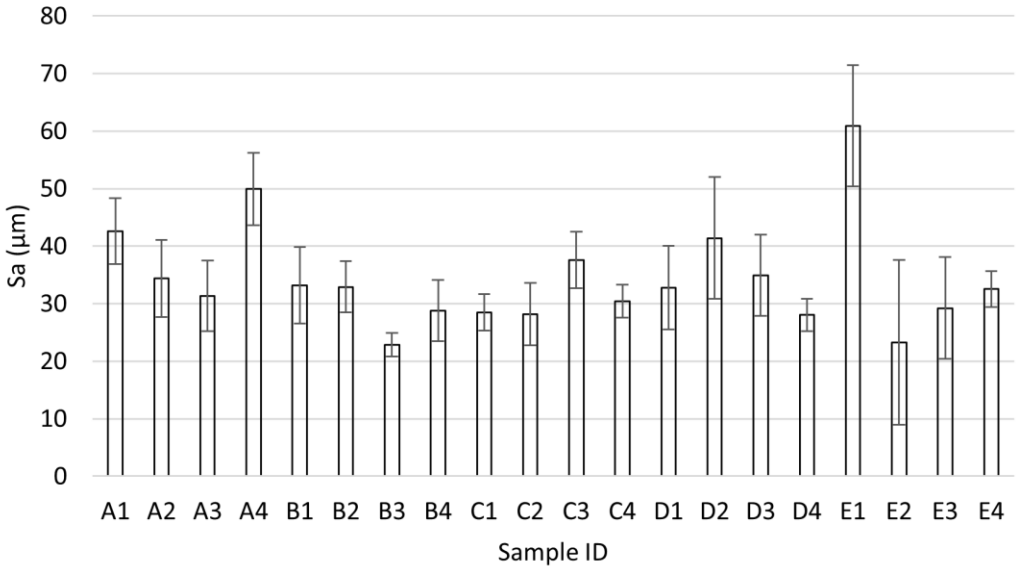
80
70
60
50
40
30
20
10
0
Sa (µm)
A1 A2 A3 A4 B1 B2 B3 B4 C1 C2 C3 C4 D1 D2 D3 D4 E1 E2 E3 E4
Sample ID

(a)

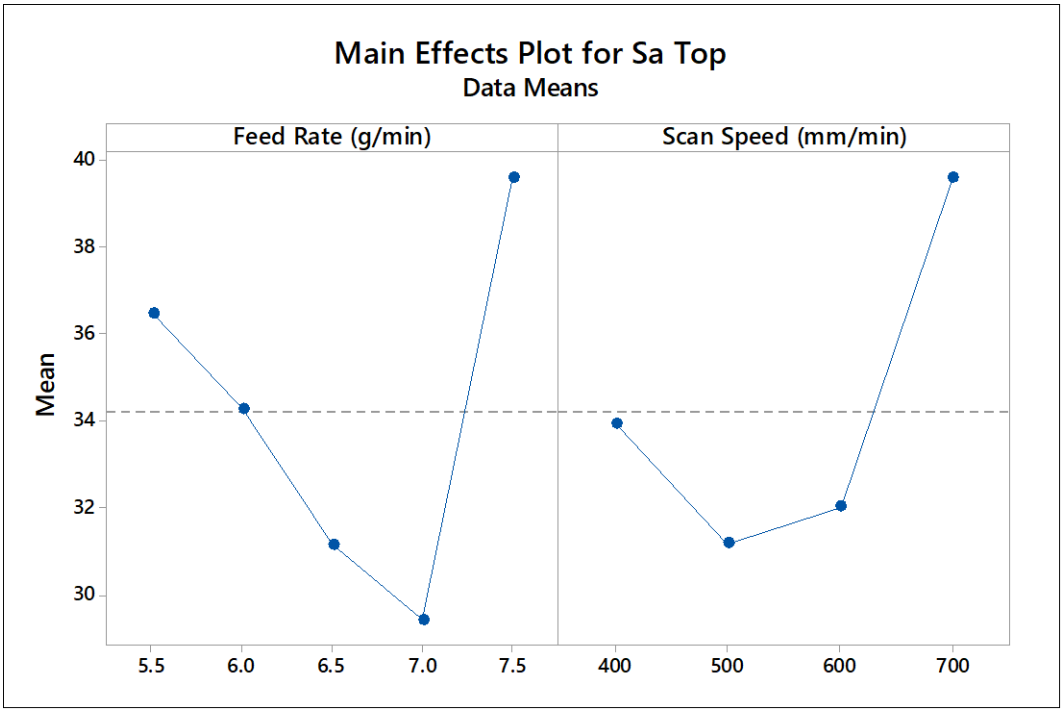
Main Effects Plot for Sa Top
Data Means
Feed Rate (g/min)
Scan Speed (mm/min)
Mean
40
38
36
34
32
30
5.5
6.0
6.5
7.0
7.5
400
500
600
700

(b)

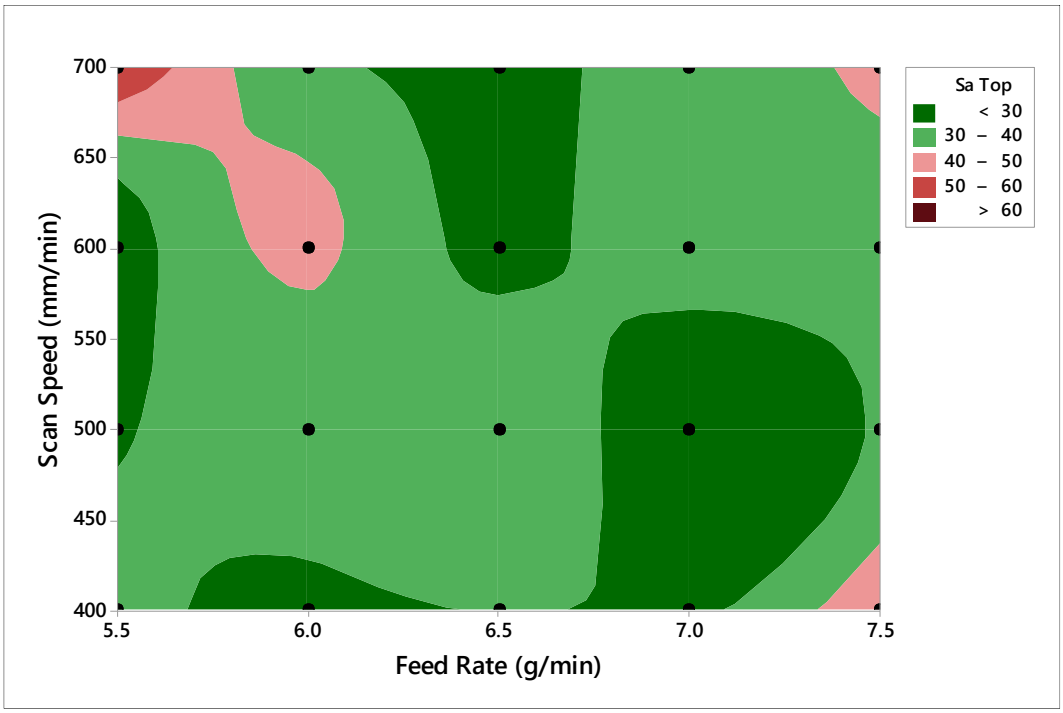

(c)

Figure 4.17: (a) The mean rectangle top surface roughness, Sa, values for each of the assessed DED parameter sets. (b) The main effects plot for the surface roughness of the rectangle tops. (c) The surface roughness contour map for the rectangle tops.

In the literature there is conflicting evidence for the effects of the scan speed on as-printed surface roughness. *Gharbi et al.* noted that the use of higher scanning speeds and higher laser powers promoted shorter melt pool durations, which produced the best surface finishes [127]. This is attributed to faster scanning speeds consolidating less material compared to slower speeds, thereby reducing the height of the layer, which results in a reduction of the surface 'waviness'. The higher power contributes to improved melting of the powder particles, causing them to disperse on the surface rather than being partially melted and agglomerating on the surface. Conversely, *Mahamood et al*. mentions that decreasing the energy density (*i.e.*, fast scanning speed) results in a

higher surface roughness [109]. The rheology and production of powders can have an impact with gas-atomized powders, which invariably have a higher surface roughness [128]. Under these different system parameters, the variation in surface roughness on a single DED sample can be significant, due to the attached unmelted particles on the surface. At lower powder feed rates there is less interaction with the laser beam, resulting in the laser making a more effective melt pool. The melt pool will be larger with a lower powder feed rate resulting in more melting.

Even though the varying system parameters produce different results, a clear trend in the data cannot be found. When a linear regression is performed on the surface roughness, the side *R*-sq is 9.75% and the top *R*-sq is 5.21%, indicating that there is little correlation associated with the examined the DED parameters. The *P*-values for the side surface roughness are 0.577 and 0.235, for the powder feed rate and laser scanning speed, respectively. Similarly, the *P*-values for the top surface roughness are 0.928 and 0.35 for the feed rate and scanning speed, respectively. It can be stated that, overall, these settings will produce very similar surface finishes. That is not to say that the settings are insufficient for building, but that clear 'ideal' parameter settings have not been identified. A targeted surface finish is not a sufficient measurement on its own, when selecting system parameters for 3D builds, the user must also consider the dimensions, density and microstructure, and the resultant mechanical behavior. If a higher laser power was available, the surface roughness would likely decrease because there is more energy to fully melt the powders [122], [129]. The 'main effects plot' for the side surface (Figure 4.16(b)), showed that changing the feed rate will impact the surface finish more than the scanning speed.

In addition, another significant parameter that helps to improve the surface finish on all sides of the rectangle samples is using a properly aligned nozzle head. If the nozzle head is slightly shifted to one side of the sample, it will deposit unintended material; when the nozzle is off-center, the powder feed nozzles spray particles on the side instead of on the subsequent layer. This will create a 'balling' effect on the surface, where extra material has been consolidated that continues up the sample. Evidence of this can be seen in all the samples (*e.g.*, Figure 4.10), which likely increases the side surface roughness values. Due to this specific process-/equipment-related artifact, the surface roughness was not measured on the side impacted by the nozzle alignment. None of the printed surfaces would be satisfactory for most applications, and machining would still be required to achieve the required surface tolerances. In addition, for a forming mold application, designers have to account for over-building, so that all the original part lies inside the machining volume. By obtaining a near-net shape that has a low surface roughness, the cost to manufacture new mold tooling will decrease as less material is needed to be removed [11].

4.9.5 Roughness as a Function of Draft Angle

From the data presented in Figure 4.18, it is apparent that as the draft angle is increased (as previously defined in Figure 4.1(b)), the 'draft face' surface roughness simultaneously increases. Consequently, the lower draft angles, from 10 - 45°, produce the best 'as-deposited' surface finish. The reduction in roughness for the shallow draft angles is likely due to the next layer being slightly offset from the previous one, which allows greater flattening out compared to when the layers are stacked normal to each other, resulting in a more pronounced individual layer at the higher draft angles. When the draft angle

reaches 50°, the roughness values reach those of the top surfaces of the rectangle samples. When building a vertical structure, a small draft angle may be selected to improve the side surface roughness for a 3-axis system. This would be limited to the geometry of the desired part, but it could be incorporated in the design of vertical sides. In line with this, it has been noted in prior work that as the sloped angle increases (*i.e.*, increasing draft angle), so does the roughness of the deposited material [130], [131]. For the present case, the *P*-value of the regression is 0.0, with an *R*-sq of 62.23%, indicating that the draft angle does have a significant impact on the surface roughness.

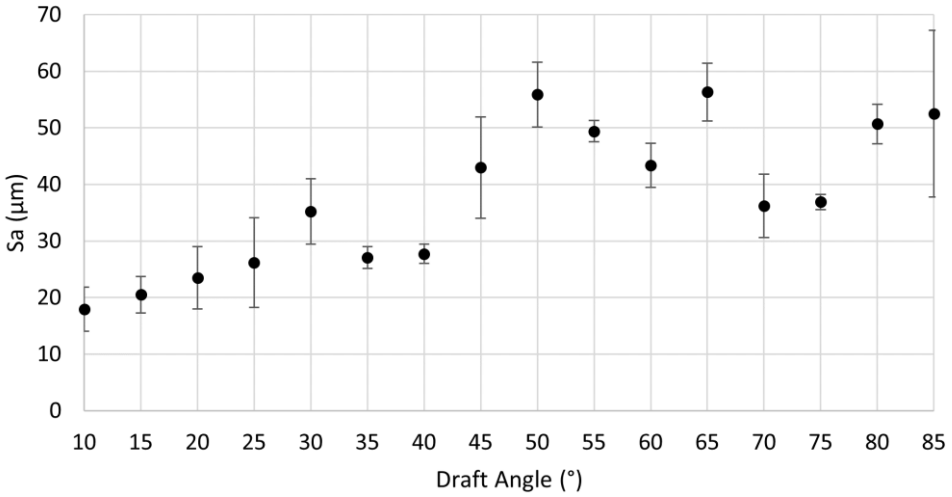

Figure 4.18: Draft angle surface roughness, Sa, of the DED-processed samples. The draft angle samples were all prepared using the A3 DED process settings (*i.e.,* powder feed rate of 7.5 g/minute and laser scanning speed of 500 mm/minute).

4.9.6 Fabrication of Ideal Layer Thickness Test Samples

Depending on the system parameters, the deposited layer can potentially be smaller or larger than the desired layer thickness. With a smaller layer thickness there should, in principle, be a be a finer gap between consecutive layers when compared to a larger layer

thickness, but this does not appear to be the case. The ‘as-deposited’ side surface finish, in terms of roughness, has been shown to be broadly consistent for the different defined layer thicknesses, assuming the scan speed and powder feed rate are the same (Figure 4.19(a)). Layer thicknesses of 0.2032 mm, 0.2794 mm or 0.3302 mm were seen to produce the lowest surface roughness ($S_a \sim 20$ μm) on the side, although this surface does not present any clear trend within the analyzed data. The observed ‘waviness’ of a finer layer thickness is greater than with a coarser layer thickness (Figure 4.19(b,c)). The surface roughness actually has a minimum with a layer thickness of 0.2794 mm, for both the top and side of the sample; in this instance the top surface roughness increases with either an increasing or decreasing layer thickness from this value. Under the A3 settings a 0.2794 mm layer thickness produces the best surface finish. The *P*-values for layer thickness effects on the side and top surface roughness values are 0.626 and 0.939, respectively. Similarly, the *R*-sq value for the side surface roughness is 6.49%, while it is 0.17% for the top surface roughness.

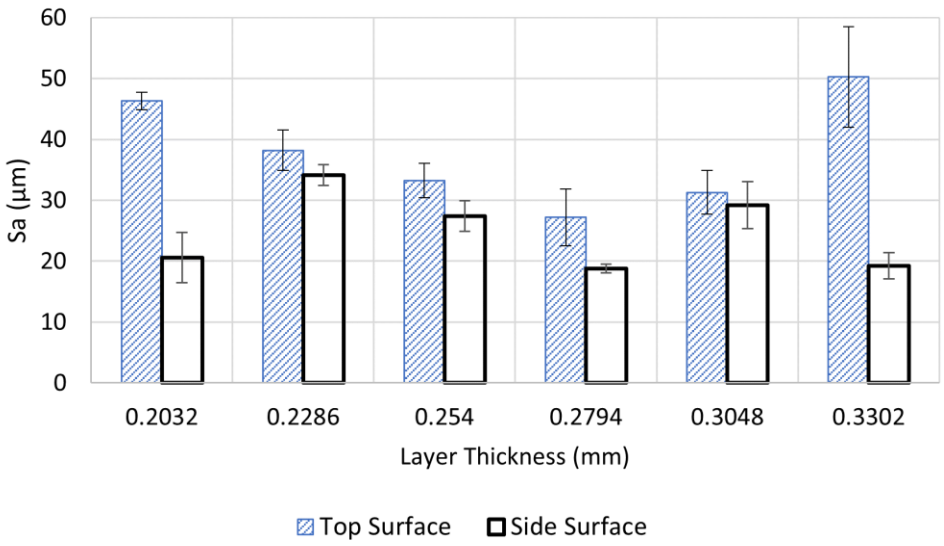
60
50
40
30
20
10
0
Sa (µm)
0.2032
0.2286
0.254
0.2794
0.3048
0.3302
Layer Thickness (mm)
Top Surface
Side Surface

(a)

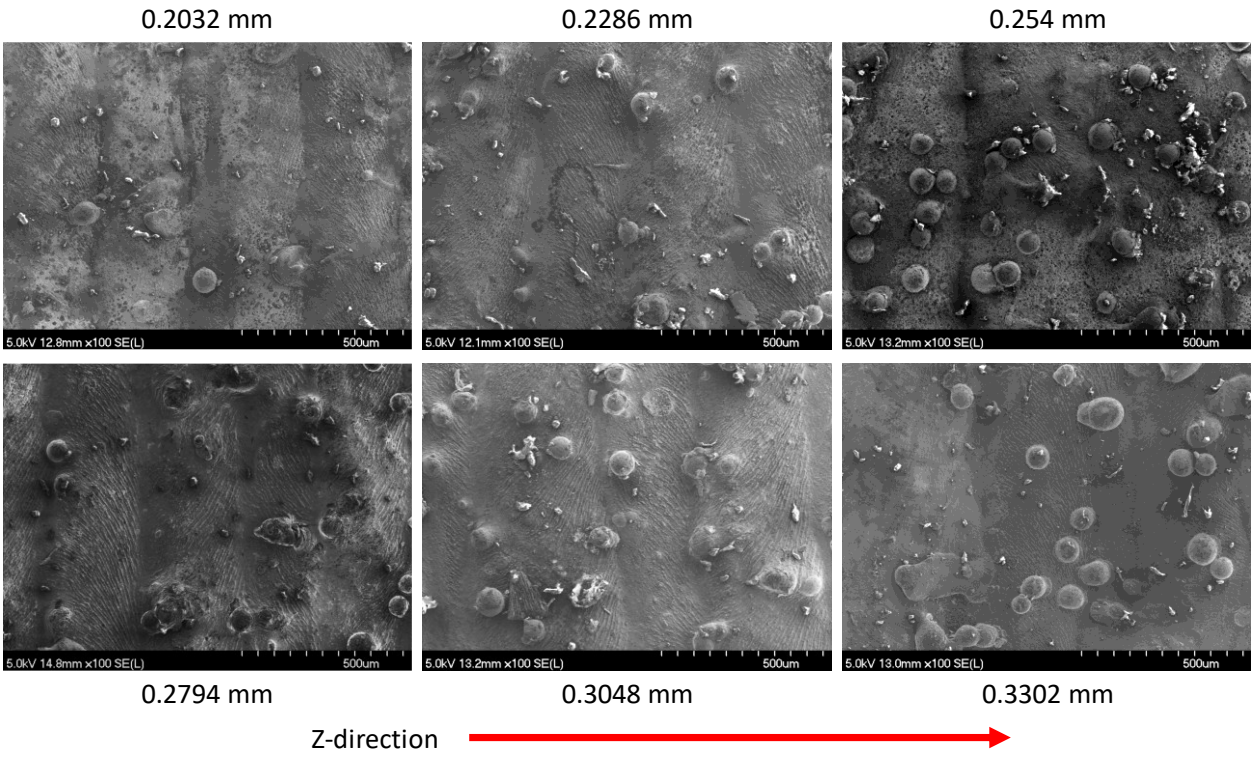
0.2032 mm
0.2286 mm
0.254 mm
5.0kV 12.8mm x100 SE(L)
500um
5.0kV 12.1mm x100 SE(L)
500um
5.0kV 13.2mm x100 SE(L)
500um
5.0kV 14.8mm x100 SE(L)
500um
5.0kV 13.2mm x100 SE(L)
500um
5.0kV 13.0mm x100 SE(L)
500um
0.2794 mm
0.3048 mm
0.3302 mm
Z-direction

(b)

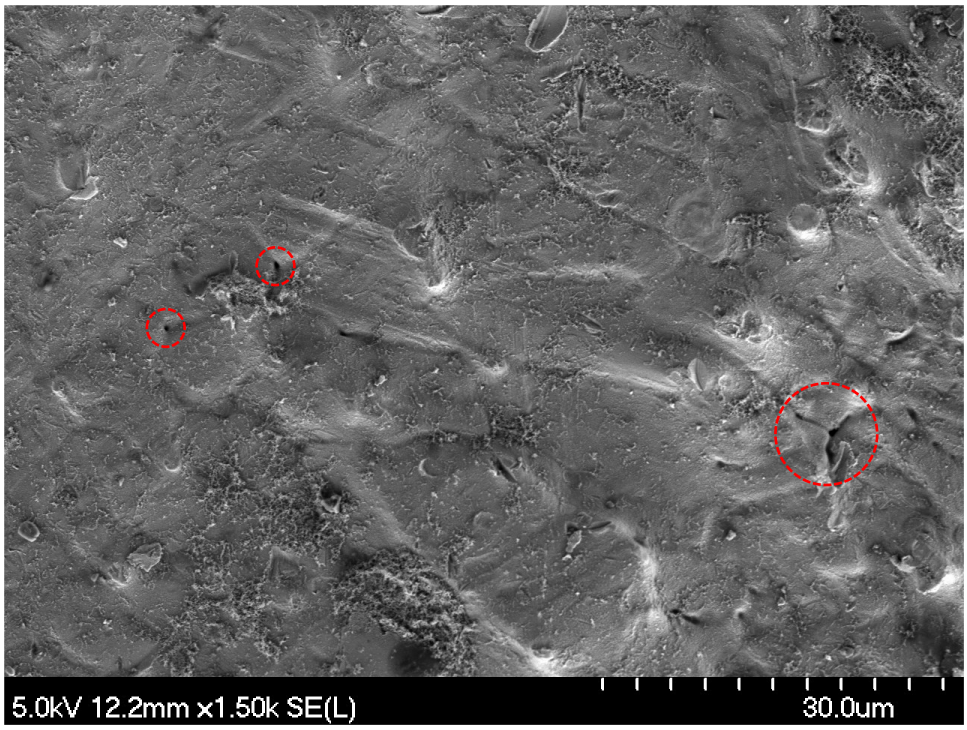

(c)

Figure 4.19: (a) The mean top and side surface roughness, Sa, of the 'ideal layer' samples as a function of layer thickness. Samples were prepared using settings A3 from Table 4.3 (i.e., a feed rate of 7.5 g/minute and a laser scanning rate of 500 mm/minute). (b) Representative FE-SEM images of the side surfaces of the ideal layer samples shown in (a). (c) Higher magnification FE-SEM image of the side of an ideal layer sample located between layers prepared with a layer thickness of 0.2286 mm with surface porosity highlighted by the red circles.

4.10 Summary of As-Printed DED H13 Geometry and Surface Roughness

Based on the presented work, with the DED system employed, an optimal combination of the laser scanning and powder feed rates can be found to minimize the surface roughness. However, these settings do not show significant outliers within the range of parameters that were examined, highlighting a degree of process flexibility. Even though the tests were not always statistically significant, the results show a qualitative understanding of

what is occurring. Slower scanning speeds (400 mm/min) resulted in over-building in the z-direction, with the opposite being true for increasing scanning speeds (700 mm/min). Ideally, the selected system settings should provide components with good dimensional accuracy and low surface roughness. Within the currently examined parameters, a recommended combination of settings for a 3D part is in the middle of the ranges examined, which would be parameter set B2, with a scanning speed of 600 mm/min and powder feed rate of 7 g/min; these conditions resulted in a top surface roughness of 32.91 μm and a side surface roughness of 17.69 μm. Slight over-building would be acceptable because it is likely consolidated parts will require final machining prior to use. With those considerations in mind, the B2 settings only over-built by 3.6% and still present an acceptable as-printed surface. Another way of improving the side surface roughness would be adding a shallow draft angle (10 - 25°) to a vertical wall.

The as-printed surfaces invariably have attached powder particles, which proved unavoidable within the examined range of conditions, and which clearly lead to higher surface roughness values. In the single-track and multi-track clad samples there is a clear trend of increasing surface roughness with decreasing scanning speed, with the scanning speed being more significant (P-value = 0.0) in both sets than the feed rate. Printing in an air atmosphere, even with the use of a shield gas, resulted in the initial printed samples exhibiting traces of oxidation, which decreased through the build cycle. Finally, changing the layer thickness using A3 settings did not have a clear impact on the top surface roughness (P-value = 0.939) and side surface roughness (P-value = 0.626).

4.11 Microstructure Characterization of DED H13

4.11.1 DED Process Parameter and Geometrical Effects on Density

No major cracking or pore evolution evidence was observed at the interface of the annealed H13 substrate and deposited H13 material. Under the selected DED parameters, the rectangular samples resulted in as-deposited densities ranging from 98.6% to 99.8% of theoretical density. In terms of the analyzed process parameters, the A3 settings produced the highest density (~99.8% of theoretical), while the A4 settings produced the lowest density (~98.6% of theoretical). There are two main types of porosity that can typically be identified in DED processes, namely, a lack of fusion (interlayer) or gas porosity (intralayer) [132]. The morphology of the defect assists significantly in determining the type of porosity seen. *Kobryn et al.* noted that lack of fusion is invariably present as an elongated and often irregularly shaped pore, whereas gas porosity is spherical in nature [120]. Gas porosity was observed within the clad deposit (intralayer porosity). Lack of fusion was mainly located in the lower layers, with the top of the samples showing good bonding. Interlayer defects were noted occasionally at the layer boundaries, and appeared to be randomly distributed throughout the sample; this is likely related insufficient laser fluence, which was noted by *Hua* and *Choi* [133]. Lack of fusion is more likely to be seen at the substrate. For the present study, this type of defect was only seen for the rectangular A4-AP sample. Intuitively, a thinner substrate will heat up more rapidly than a thicker substrate, which will require more heat energy to retain heat and have improved fusion at the substrate.

As printing continues with successive layer additions, the heat input is increased, and the substrate and previous layers will remain at a higher temperature, altering both the heat

flow behavior and cooling rates. The pores observed in the printed samples in the present study are larger than those present in the starting powder (shown previously in Figure 4.2), indicating that this is process parameter related, and arises from entrapment of the shielding gas during laser deposition. Porosity in the starting powder seems to have little correlation to porosity in the deposit, as also noted in prior work [132]. *Kobryn et al.* [120] also noted that samples processed using faster scanning speeds have higher densities, as that less powder is being consolidated, resulting in fewer partially melted particles adhering to the surface and between layers. However, this issue was not encountered during this study and is a suggested reason for the higher densities observed for the H13 samples. For the present study, the nozzle stand-off distance was sufficient to be successfully generating a melt pool, but the likely reason the parameters for sample A4-AP produced a lower density is because the gas pressure on the bead surface is decreasing [125].

Single clad tracks were used to see if a relationship existed between the powder feed rate, laser scanning speed, and wetting angle, and whether it had any impact in terms of the density of the rectangular samples. No visual trend was observed in the data. This is likely attributed to the fact that the clad tracks were not symmetrical down the entire track length, and that this data is taken from single clad tracks. Once subsequent layers are printed on top, this will distort the shape of the lower deposited clad track.

Increasing the scan speed from 400 mm/min resulted in the greatest improvement in density. Conversely, reducing the scan speed from 700 mm/min tended to lower the density, even though the energy input increases. Based on the evaluated parameters in the present study, an ideal setting for maximizing the deposition density is a powder feed rate

of 6.5 g/min and a scan rate of 600 mm/min for the H13 powder that was used. Higher contact angles from the slower speeds would distort the beam geometry, and increase the chance of entrapped gases between successively deposited layers, consequently lowering the density [134]. This trend can be seen in Figure 4.20, with the samples with the slowest speed having a lower experimental density. The A4 settings resulted in the largest contact angle of 38.8° ± 2.5 and D2 had lowest contact angle of 16.4° ± 4.6. The A3 settings which produced the highest theoretical density had a contact angle of 25.5° ± 1.0. Decreasing the scanning speed and increasing powder feed rate increased the wetting angle [118].

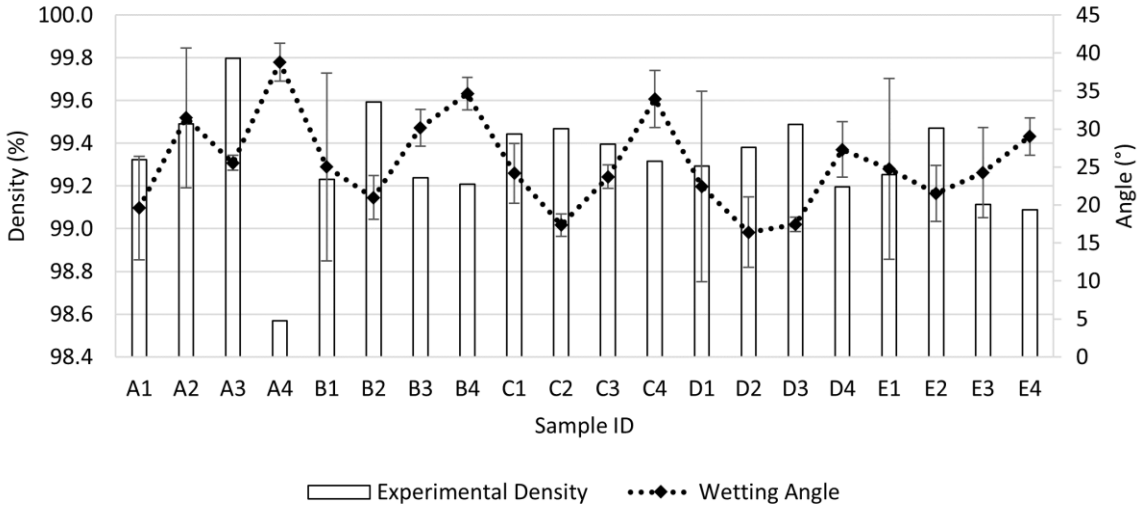

Figure 4.20: Experimental rectangle sample densities compared to the single clad wetting angle with error bars indicating the standard deviation in the wetting angle.

While there was a minimal amount of porosity observed within the samples, when gas porosity was observed, it occurred above the centerline of the sample, where the cooling

rate was reduced because the part had already been saturated with heat, as noted in prior work [135]. The only sample that had clear porosity issues was the rectangular sample processed using the A4 parameters, with spherical gas porosity prevalent as the height increased shown in Figure 4.21. The parameters (laser power, powder feed rate, scanning speed, and hatch spacing) will each potentially influence the final deposited density. The faster scanning rate did show a decrease in porosity, but this is likely due to less powder particles reaching the melt pool and being partially melted [120]. Jang *et al.* reported that insufficient bonding can occur with higher scanning speeds due to shortened laser material interaction time [116]. In the present case, this is likely due to the slower scanning speed combined with the high powder feed rate, which creates a layer greater than the desired layer height. Sample A4-AP had the highest wetting contact angle from the slower scanning speed, increasing the chances of entrapped gases from the distorted bead size, which has also been observed in a previous study [134]. In addition, due to the high number of powder particles interacting with the laser beam, it would make it difficult to make a successful melt pool. Figure 4.22 shows typical examples of both gas porosity and lack of fusion defects.

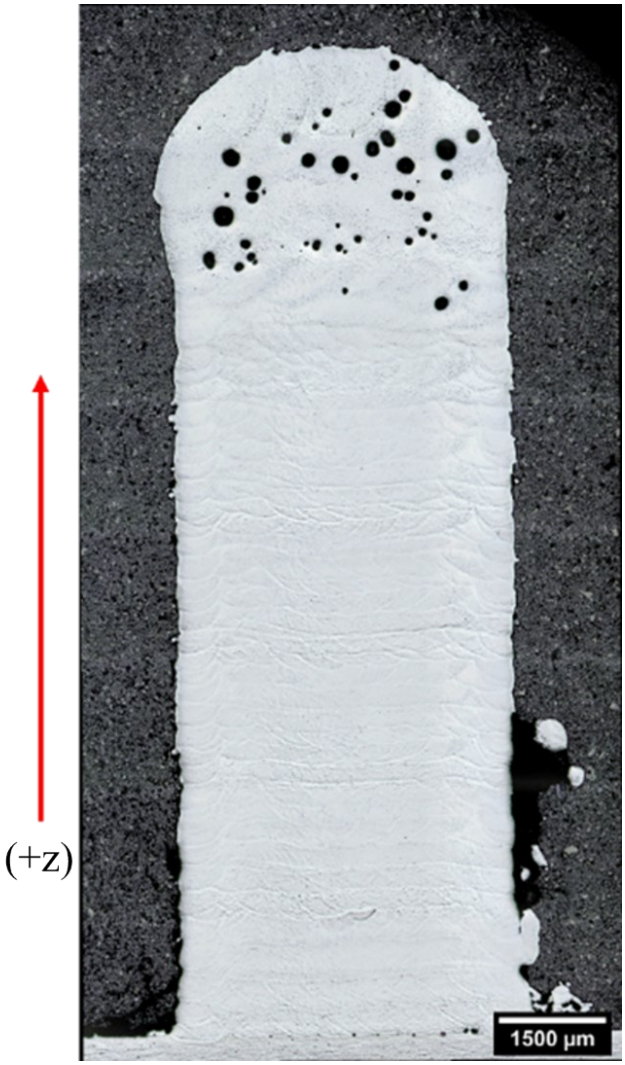

Figure 4.21: CLSM optical image to highlight the gas porosity in the top half of the rectangular sample processed under A4 DED conditions. The red arrow indicates the build direction (+z).

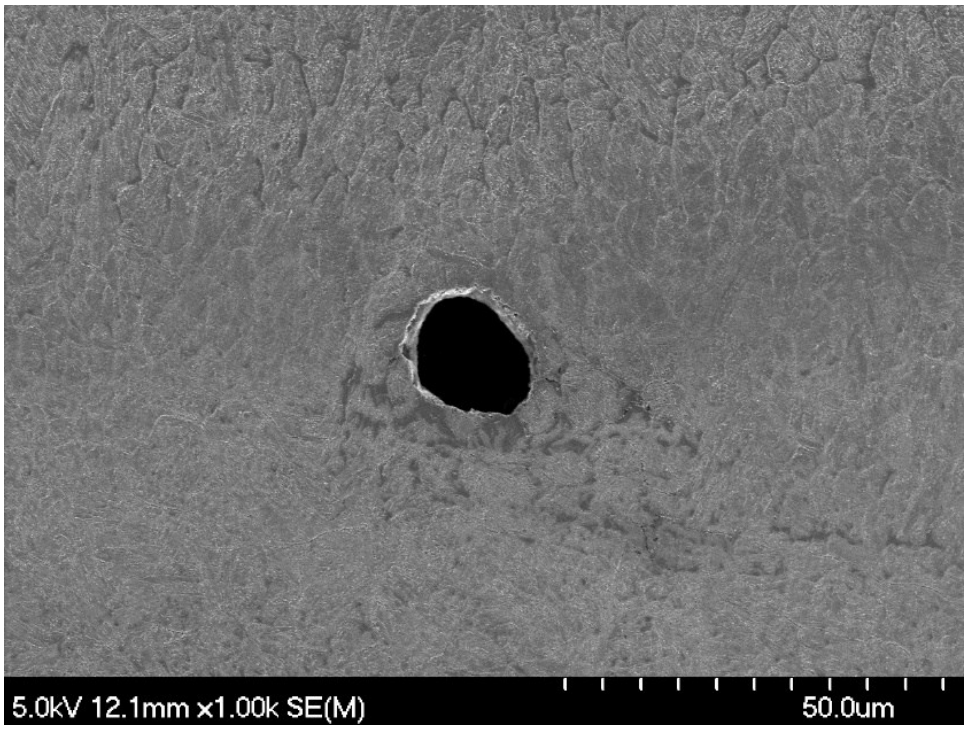

(a)

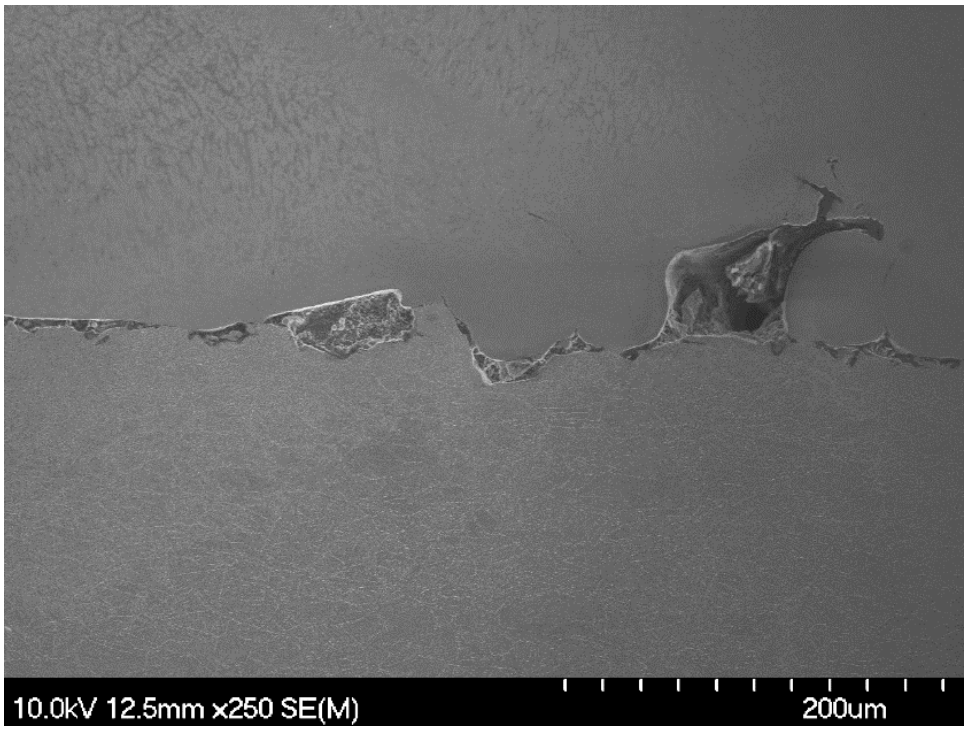

(b)

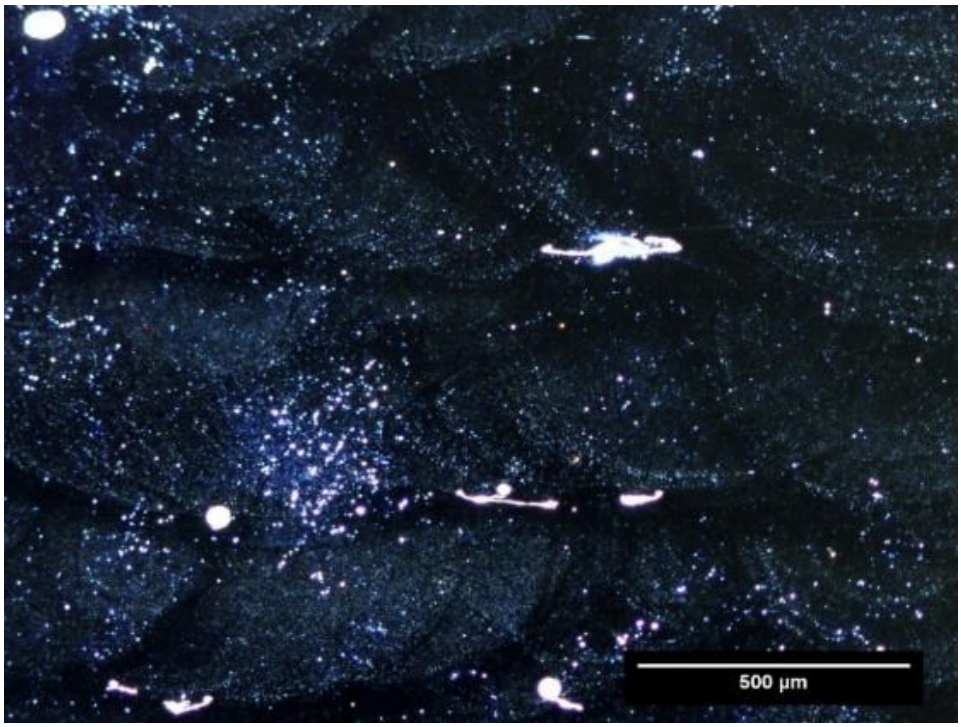

(c)

Figure 4.22: (a) Gas porosity in rectangle A1 in a clad deposit, (b) shows lack of fusion to the substrate in rectangle A4, and (c) are both types of defects which appear white in the image in rectangle D4 using dark field imaging on an unetched sample.

The densities of the varying ideal layer thickness cubic samples ranged from 98.9% to 99.7% of theoretical. Figure 4.23 shows there is little variation to the experimental densities when changing the layer thickness, with the only exception being when using a layer thickness of 0.2032 mm. Pre-heating of the substrate or using a controlled atmosphere was not required to achieve a fully dense and crack free sample in the present case. By pre-heating the substrate the crack susceptibility can be reduced, which arises from maintaining a more uniform temperature gradient, and the associated reduction in residual stresses, [38], [41]. However, this may not always be the case, as the printed part geometry will influence the heat transfer.

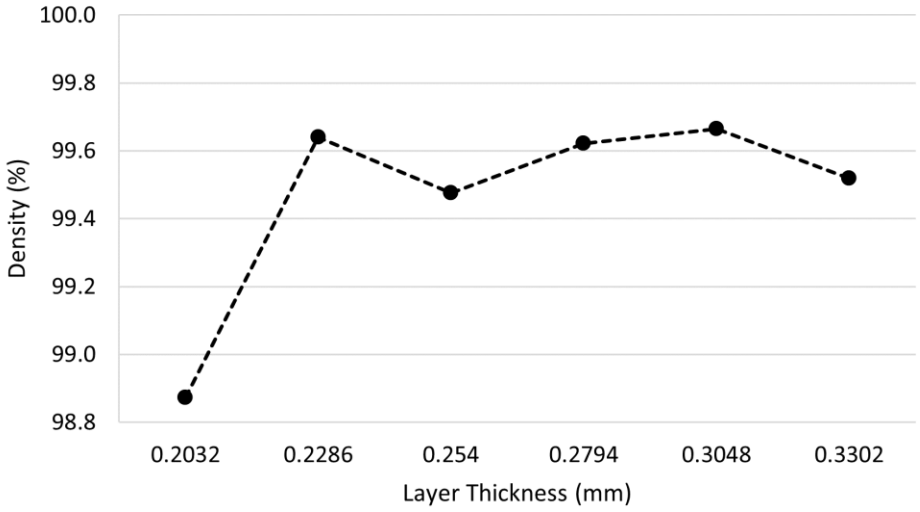

Figure 4.23: Experimental densities of changing the layer thickness using setting A3.

4.11.2 Microstructure and Phases of As-Processed DED Samples

4.11.2.1 Clad Tracks

The single clad samples exhibited three solidification zones, which can be described as follows: (i) the planar zone, which is at the substrate/deposit interface, (ii) a cellular dendritic zone, which follows the direction of heat flow, and (iii) an equiaxed dendritic zone, in the middle of the deposit. Since the clads were sectioned transversely, it is difficult to see how the cooling rate changes moving from the substrate to the top of the clad. Close to the substrate the cellular dendrites are perpendicular to the substrate, and they gradually become parallel to the substrate at the top of the deposit. Due to the high cooling rate, the deposit will solidify through the austenite (γ) region, and it is rapidly quenched, forming lath martensite (α'), which has a high dislocation density [43], [45], [136], [137]. It is also likely that austenite is retained due to the high cooling rates, but

peaks were not easily distinguished as the dominating phase would be martensite. Comparing the A1 processing parameters (fastest scanning speed and highest feed rate) to those for the A4-AP sample (slowest scanning and highest feed), the equiaxed zone at the top of the clad is more disconnected with the slower scanning speed, whereas with the fastest speed the cellular structure is intact with lath martensite present. The cross-section of the single clad A1-AP and E4-AP samples are presented in Figure 4.24.

(a)

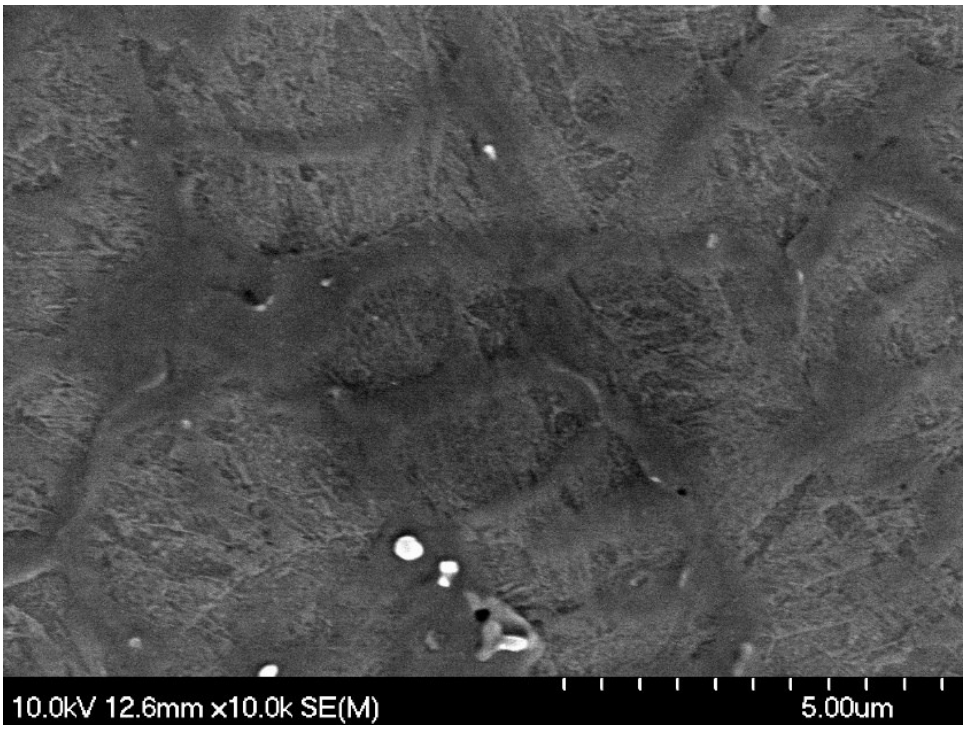

(b)

Figure 4.24: Representative FE-SEM images of the cross-section of the single clads: (a) A1, and (b) E4, used to measure the SDAS. The clad deposits have been sectioned transversely, with the laser travel direction into the page.

The cooling rates, *T*, for the A- and E- set of sample process conditions were estimated using measured secondary dendrite arm spacing (λ_2^3) in meters, and Equation 8 as developed by *Kurz* and *Fisher* for a 0.35 wt% C steel [138], [139], as follows:

$$T = \frac{1}{\lambda_2^3}\left(3.87x10^{-13}\frac{Km^3}{s}\right)$$

Equation 8: Estimated cooling rate for a 0.35 wt% C steel by measuring the secondary dendrite arm spacing (SDAS) [138], [139].

where K is temperature is in Kelvin, m is the secondary dendrite arm spacing in meters, and s is time in seconds. Based on this information, the predicted cooling rate was highest for the A1 process conditions, at 2.01 x 10^5 K/s, while the slowest cooling rate would be expected using the E4 process conditions, at 0.24 x 10^5 K/s. A trend of decreasing cooling rate is seen with decreasing speed, as seen in Figure 4.25, showing the predicted cooling rates. This arises due to the higher energy input because the melt pool will be locally retained for a longer duration. The slower speeds resulted in a larger clad deposit, which will reduce the cooling rate due to the greater amount of material that is deposited. Even though the A4 and E4 conditions nominally have similar cooling rates, realistically, setting E4 likely has a slower cooling rate because less powder particles are interacting with the laser beam. The cooling rates of the A-series samples are projected to be higher than the E-series samples. This is likely due to the higher powder feed rate for these samples, making it more difficult to generate a larger melt pool because the laser is interacting with more powder particles [111].

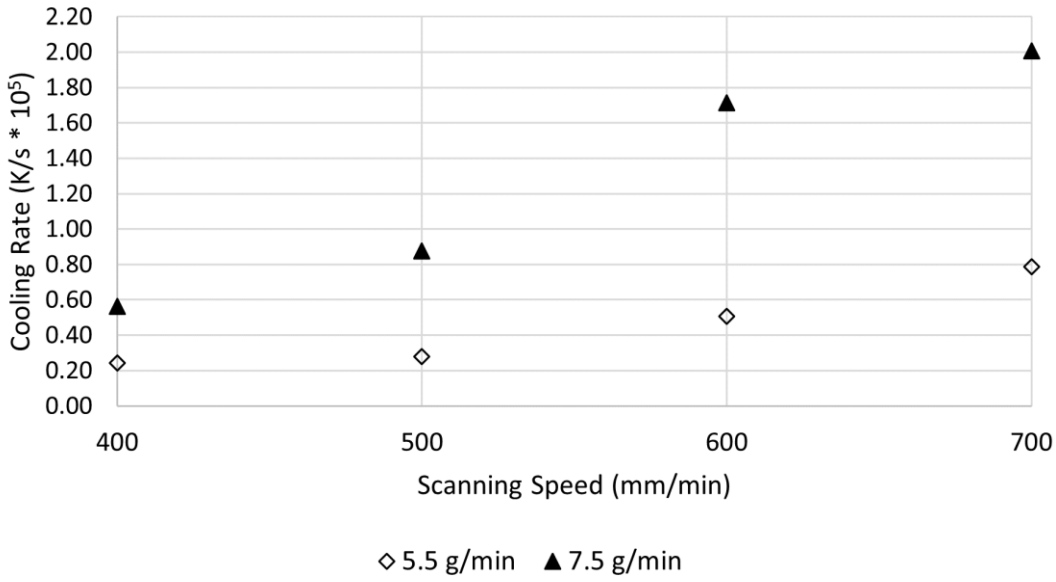

Figure 4.25: Predicted cooling rates for the single clad samples using the A- and E- set of DED system process parameters.

A lower powder feed rate should have resulted in higher dilution, because of the longer substrate and laser interaction, but this was not the case with no clear trend to the dilution and applied system parameters. In the present case the dilution depth (*d*) ranges from 103.87 µm to 140.00 µm and the heights (*h*) ranged from 40.85 µm to 134.15 µm.

From the literature [117], [140]–[143], the dilution ratio varies depending on the material system, and it appears in the present case that the ratios measured resulted in excellent bonding, with no debonding of the multi-layered parts. Under these parameters the dilution ratio ranged from 45.98% to 77.41%.

4.11.2.2 Rectangle and Ideal (Cubic) Layer

The transverse section (Figure 4.26) of the consolidated 3-dimensional samples showed the distinct, layer-wise, morphology that is associated with AM-processed parts. In each deposited layer, it consists of directionally solidified dendrites and fine equiaxed cells.

The SEM images confirm that there is directional solidification, with the cells changing orientation in the direction of the highest temperature gradient. It is clear from the DED H13 deposits that the material has undergone a rapid solidification stage, due to the fine scale microstructure that is observed. As expected, the microstructure of the single clad sample does not undergo a tempering effect, as no subsequent layers are being deposited on top. This results in a more homogenous microstructure within the clad. Comparing this to the multi-layer DED samples, the lower layers will experience a tempering effect, which arises from the sequential deposition of the upper layers, and the associated cyclic heating. This results in an inhomogeneous microstructure within the build. The planar/re-melted zone can still be distinguished at the deposit interface of the multi-layer builds, which transitions to a cellular dendritic structure. Three distinct zones can be observed at the interface of the deposited material and substrate, which are shown in Figure 4.27, namely: (i) the deposit zone, (ii) the planar/re-melted zone, and (iii) the HAZ. The occurrence of these zones has also been reported in several prior studies [38], [144], [145]. Looking at the lower and middle layers of the as-printed, 3-dimensional samples, the previous layers have gone through a mild temper due to the cyclic heating of the additive process. The microstructure then consists of tempered martensite with a cellular structure and fine alloy carbides. Lower layers in the build had a greater volume of fine carbides present at the grain boundaries, which are likely MC-type carbides and a small amount of M_7C_3 [146]. The stable vanadium-rich MC pin the growth of the austenite grains, refining the grain size [43], [59]. Comparing the lower layers of rectangle A1-AP with those of E4-AP, the slower scanning speed seems to allow for a greater precipitation

of alloy carbides (Figure 4.28). In these cases, the darker spots are vanadium-rich carbides, and the white spots are molybdenum-rich carbides [147].

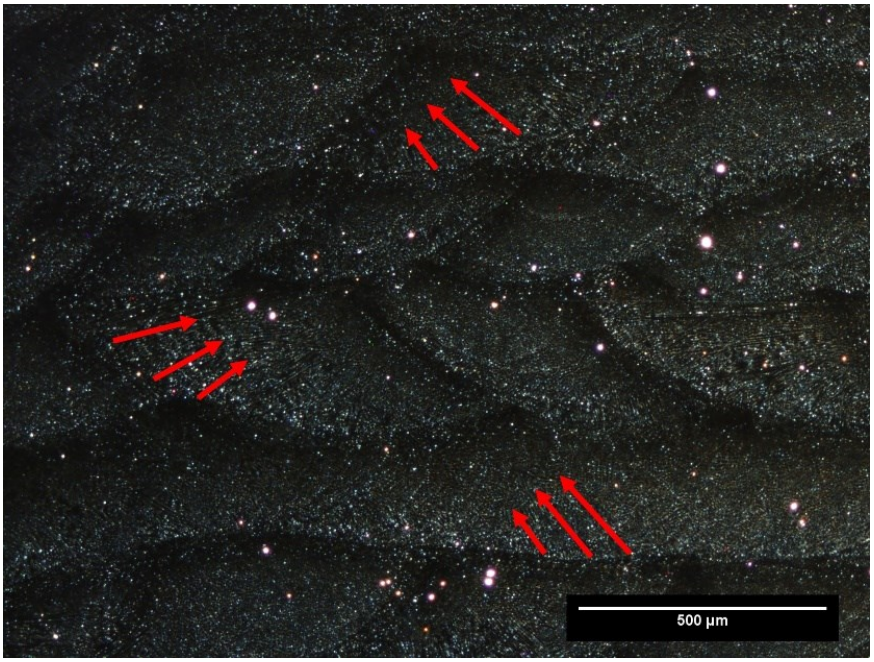

Figure 4.26: Dark field optical microscopy image of an unetched rectangle (process conditions A3), showing the layer-wise structure of an AM-processed part. The red arrows indicate the directions of grain growth in different layers.

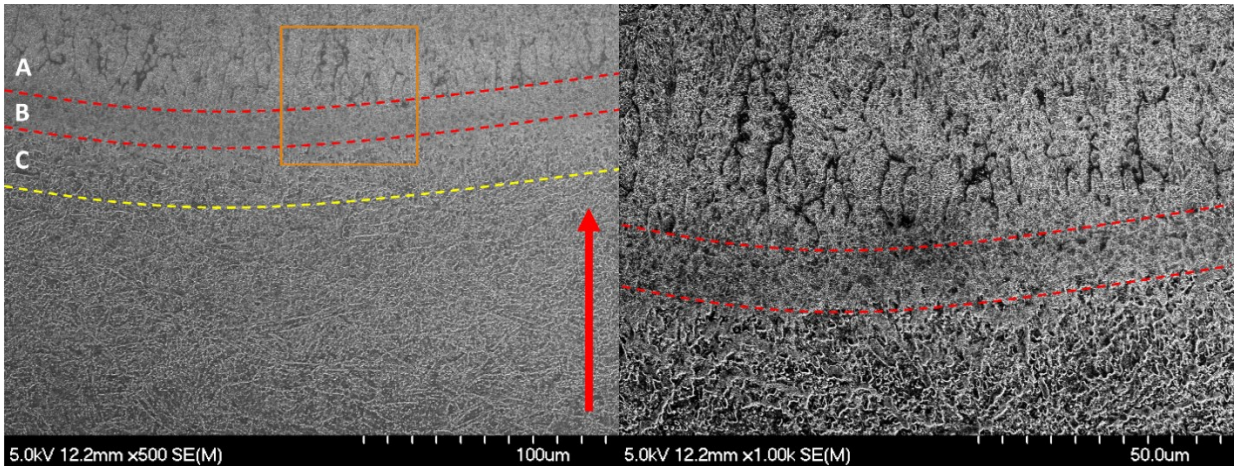

Figure 4.27: FE-SEM images of the first layer of rectangular sample A1-AP showing: the (A) deposit zone, (B) the plana/re-melted zone, and (C) the HAZ. The right image is an enlarged section of the orange box. The arrow indicates the +z-build direction.

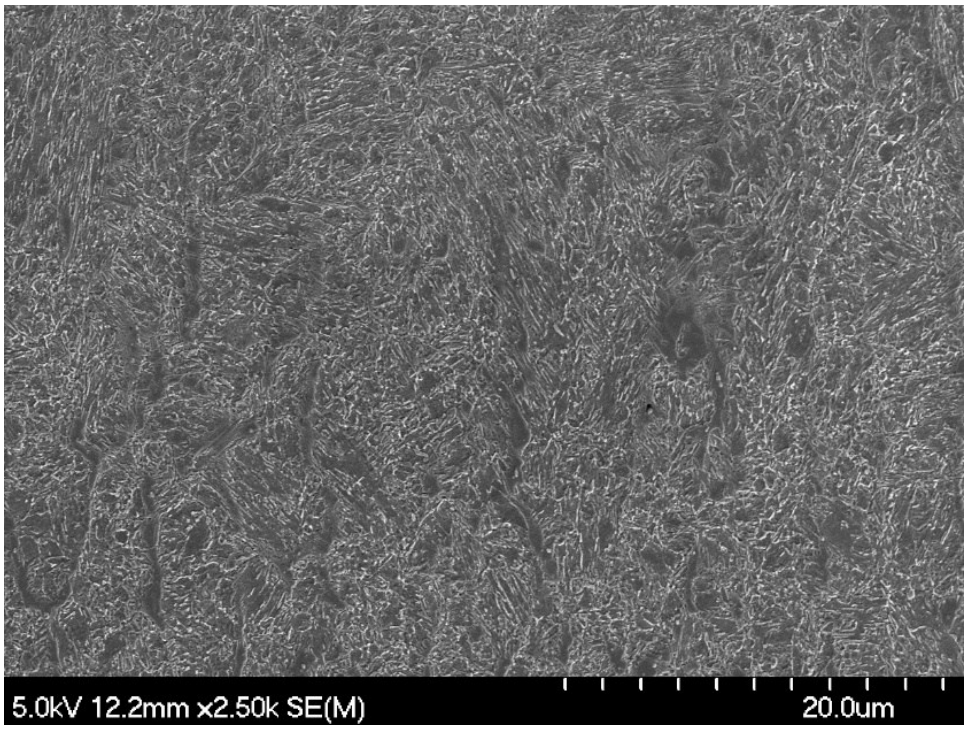

(a)

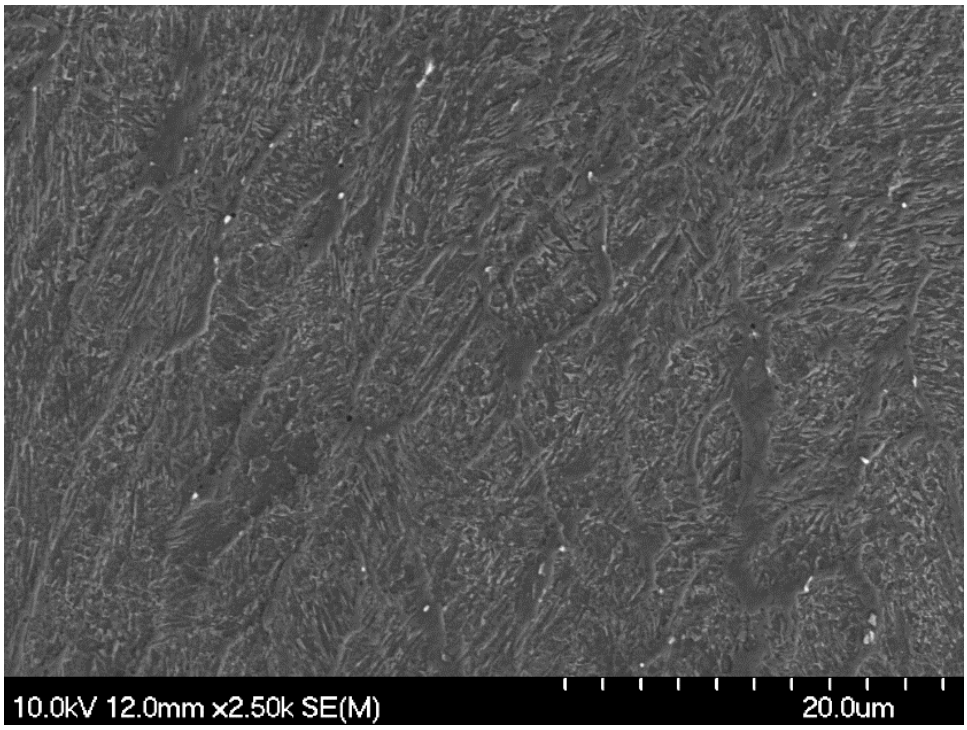

(b)

Figure 4.28: Comparison FE-SEM images of the lower layer regions in the as-processed DED rectangular samples: (a) A1-AP, and (b) E4-AP.

Figure 4.29 illustrates that the AM-processed samples show a fine tempered martensitic structure and alloy fine carbides near the middle of the sample. Comparing this to a wrought H13 that has undergone a conventional heat treatment which consists of highly tempered martensitic matrix and coarser alloy carbides in greater volume. Prior work has demonstrated that the inter-dendritic/cellular regions should be richer in V and Cr [146], [148]. In the current study, this was confirmed through EDS analysis, which indicated that there is an enrichment of the inter-dendritic region with V and Cr, whereas the darker contrast regions (within the dendrite) were depleted, as shown in Figure 4.30 for the rectangular sample processed under A1 DED conditions.

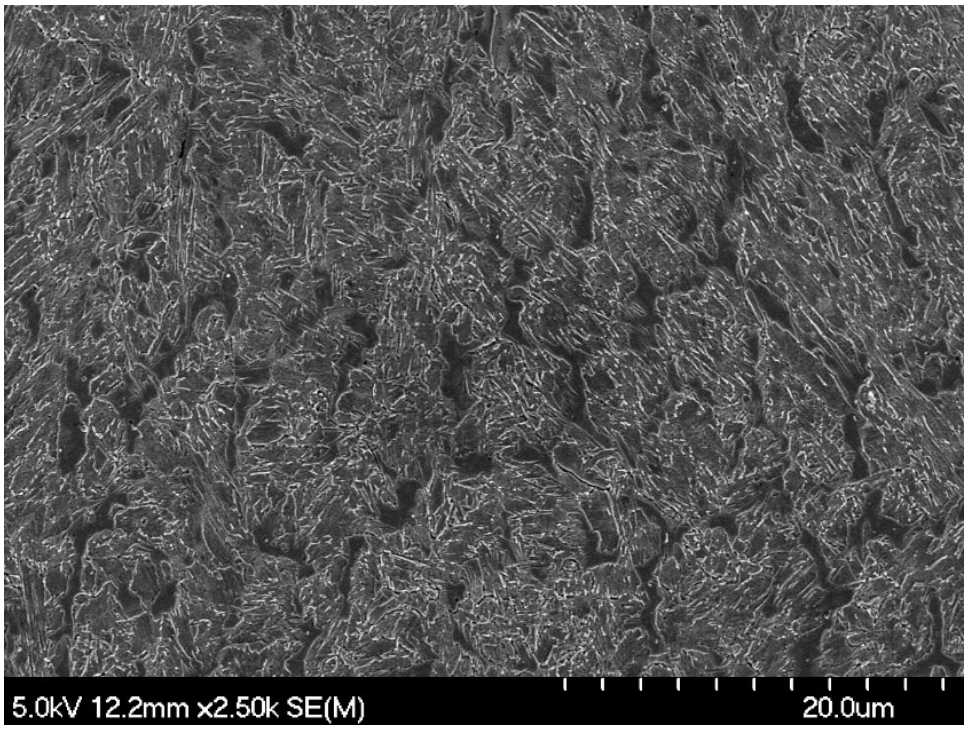

(a)

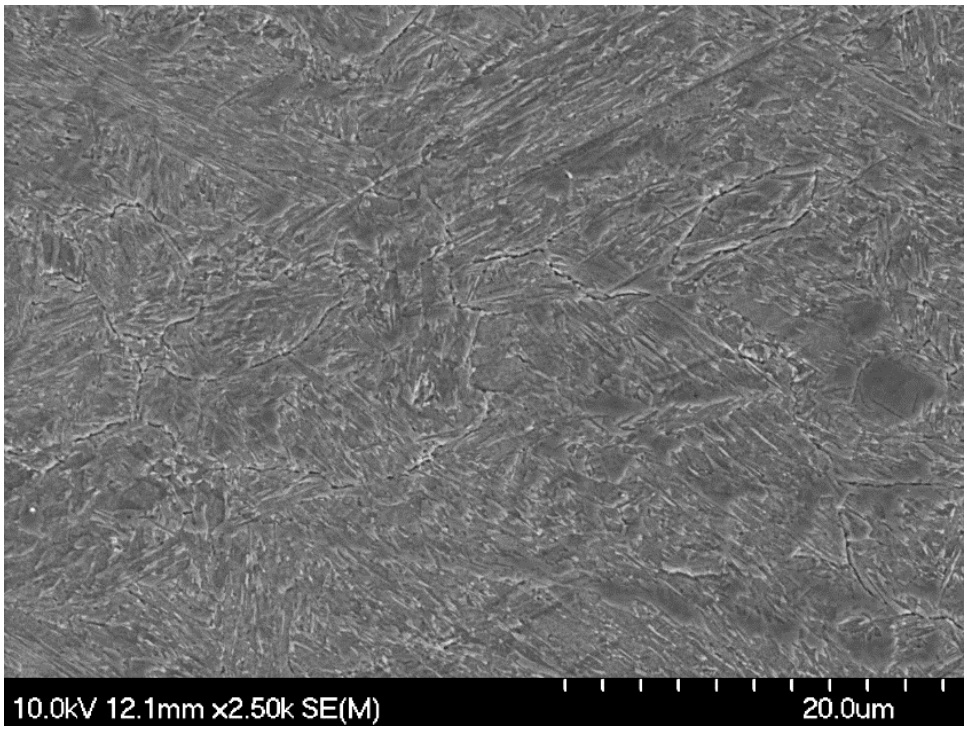

(b)

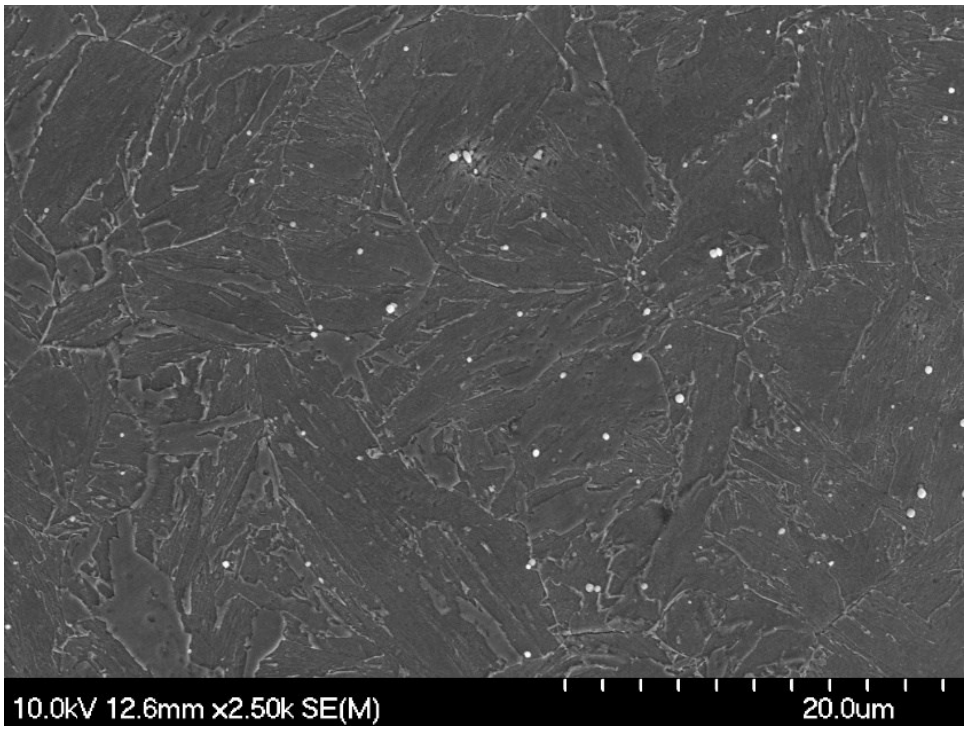

(c)

Figure 4.29: Comparison FE-SEM images of the as-printed additive manufactured H13 taken at the middle sections of: (a) the A1-AP, and (b) the E4-AP rectangles. (c) An example of a wrought H13 baseline sample that has undergone a double-tempering heat treatment. A tempered martensite matrix, with alloy carbides, can be seen in the microstructure of both materials.

The cellular structure indicates micro-segregation during solidification, which will enrich the inter-dendritic regions with alloying elements, in particular carbon will help stabilize austenite [149]. During the process, the molten deposit will cool through the δ-iron region (BCC), then through austenite (γ-iron, FCC), where it continues to be rapidly cooled to form a martensite microstructure [136]. The austenite nuclei will nucleate first at the solid/liquid interface due to the high undercooling resulting in a fine cellular structure. The cellular structure will directionally follow the maximum temperature

gradient, as noted previously [146]. In the current materials, the top layers appear to consist of very fine lath martensite and retained austenite, similar to that observed by *Pinkerton* and *Li* [37]. This was also seen by *Choi* and *Chang*, which they attributed to the expectation that the cooling rate is faster during deposition of the last set of layers, due to less thermal cycling and the convection from shielding gas [50]. *McHugh et al.* noted that the deposited material was forced cooled by convection of the nitrogen gas [150].

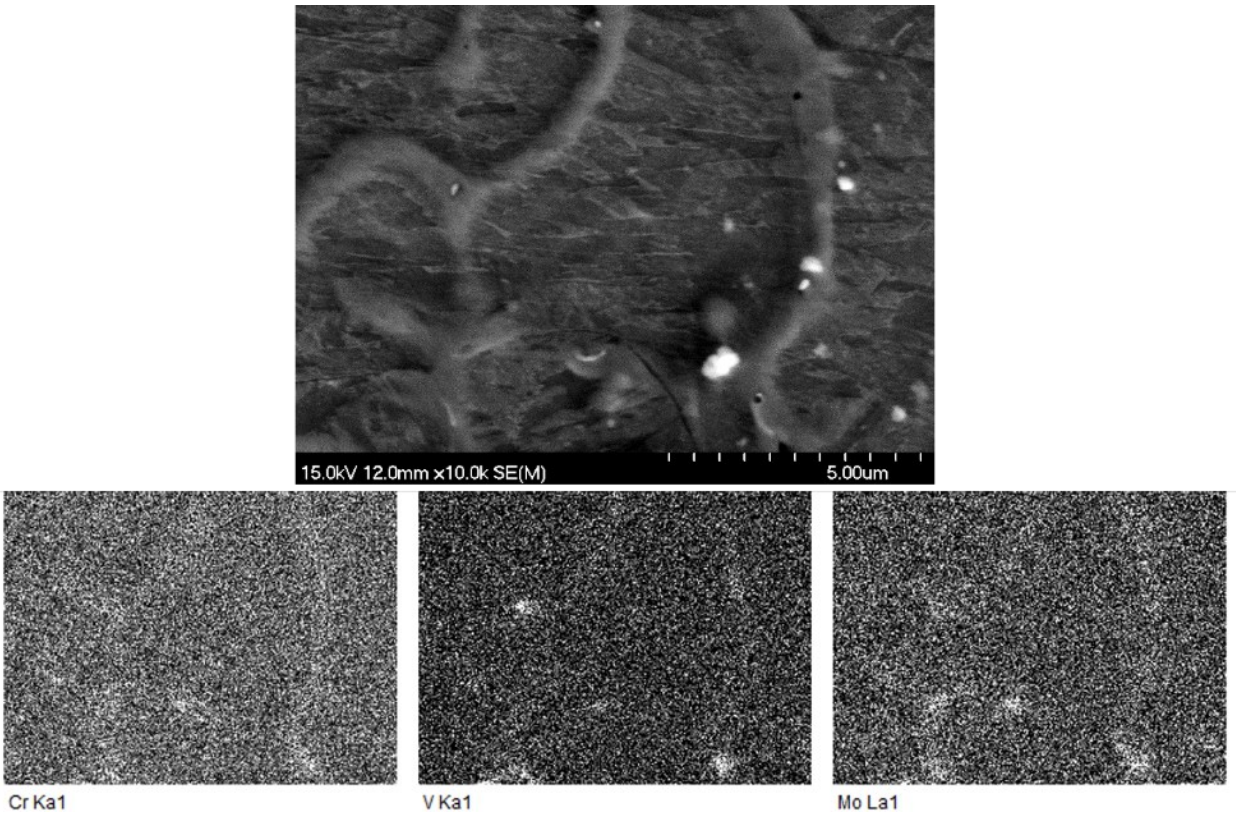

Figure 4.30: A representative FE-SEM image, and associated Cr, V, and Mo EDS maps, of the inter-dendritic region of a rectangular sample A1-AP.

The previous layers, that would have resulted in martensite and retained austenite, would have been re-heated to within the austenite region transforming back into new martensite

upon cooling. This is seen in the re-quenched zones between layers, which presents a martensitic structure, as shown in Figure 4.31. The lower layer, consisting of martensite, can transform back to austenite when the layer above is being deposited due to re-heating. The newly formed austenite can transform back to martensite, but because the lower layers have been saturated with heat it might not reach the martensite finish temperature. This means there will be retained austenite which is stabilized from the super-saturated martensite, which is similar to the quench and partitioning heat treatment process [151]–[153].

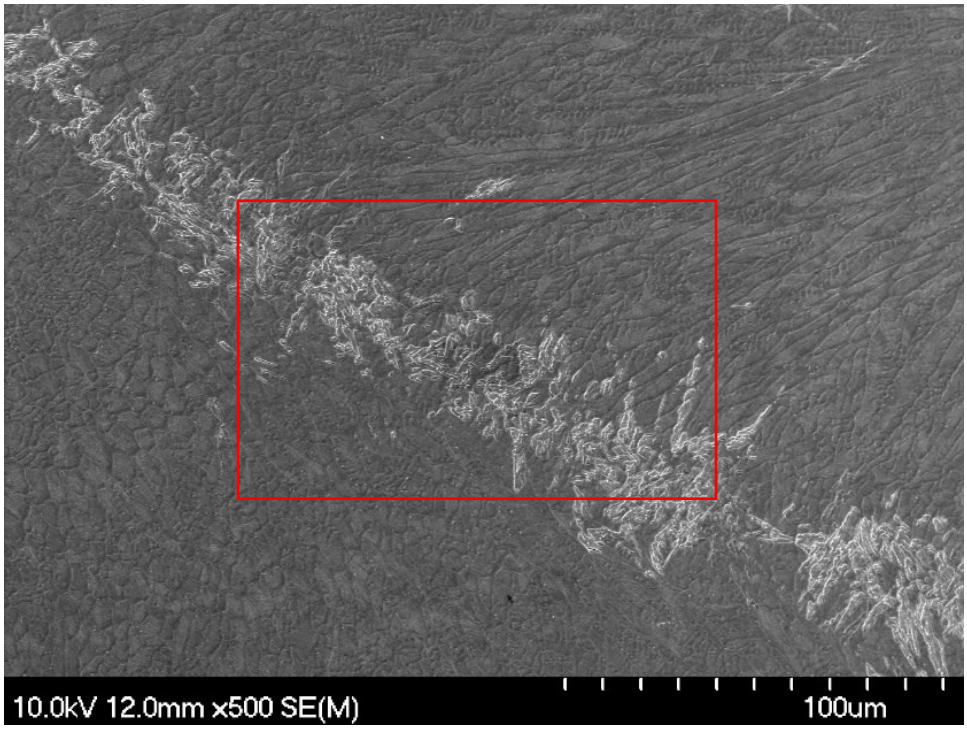

(a)

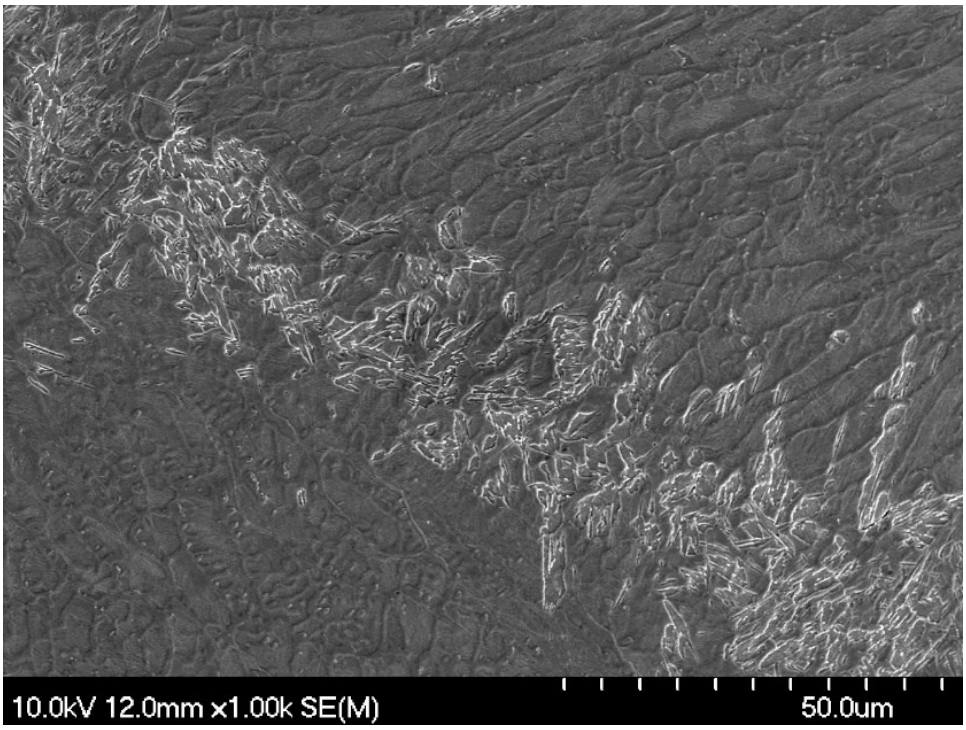

(b)

Figure 4.31: (a) FE-SEM image of the re-quenched zone in a cube sample, prepared using settings A3 and a 0.2032 mm layer thickness, which consists of fine lath martensite (light contrast area). (b) Higher magnification SEM image of the highlighted region in (a).

In terms of quench and partitioning, it is a heat treatment where carbon can diffuse from the martensite to the untransformed austenite and stabilize it at room temperature. The steel is first austenitized (fully or partially), followed by an interrupted quench between the martensite start and finish temperatures. The addition of silicon can be used to suppress the cementite precipitation, by keeping the carbon in solution to stabilize the austenite [154].

4.11.3 Microstructural Development and Hardness of Heat-Treated DED Samples

After applying a quench and double-tempering heat treatment, directly from the as-processed state, the microstructure of the DED (and wrought) samples consisted of a tempered martensite and alloy carbides at the grain boundaries, in accordance with prior studies [149], [155], [156]. The application of heat treatment has removed the cellular dendritic matrix originating from the DED process, and this is replaced with an equiaxed grain structure, as illustrated in Figure 4.32. The Vickers hardness of the cross-section of samples A1 are plotted (Figure 4.33(a)) and E4 (Figure 4.33(b)) in the as-processed and heat-treated conditions as a function of build height. The hardness in as-processed condition for both samples have a large variation at each increment as well as long the build direction (+z). This variation is attributed to the complex in-situ tempering that occurs from the layer-by-layer building [40], [138], [157], [158]. Hardness measured at -0.5 mm from the interface (0 mm) is at a minimum. At the -0.5 mm location the hardness is slightly higher in A1-AP than E4-AP due to the faster scanning speed (*i.e.,* lower thermal energy input) resulting in less tempering.

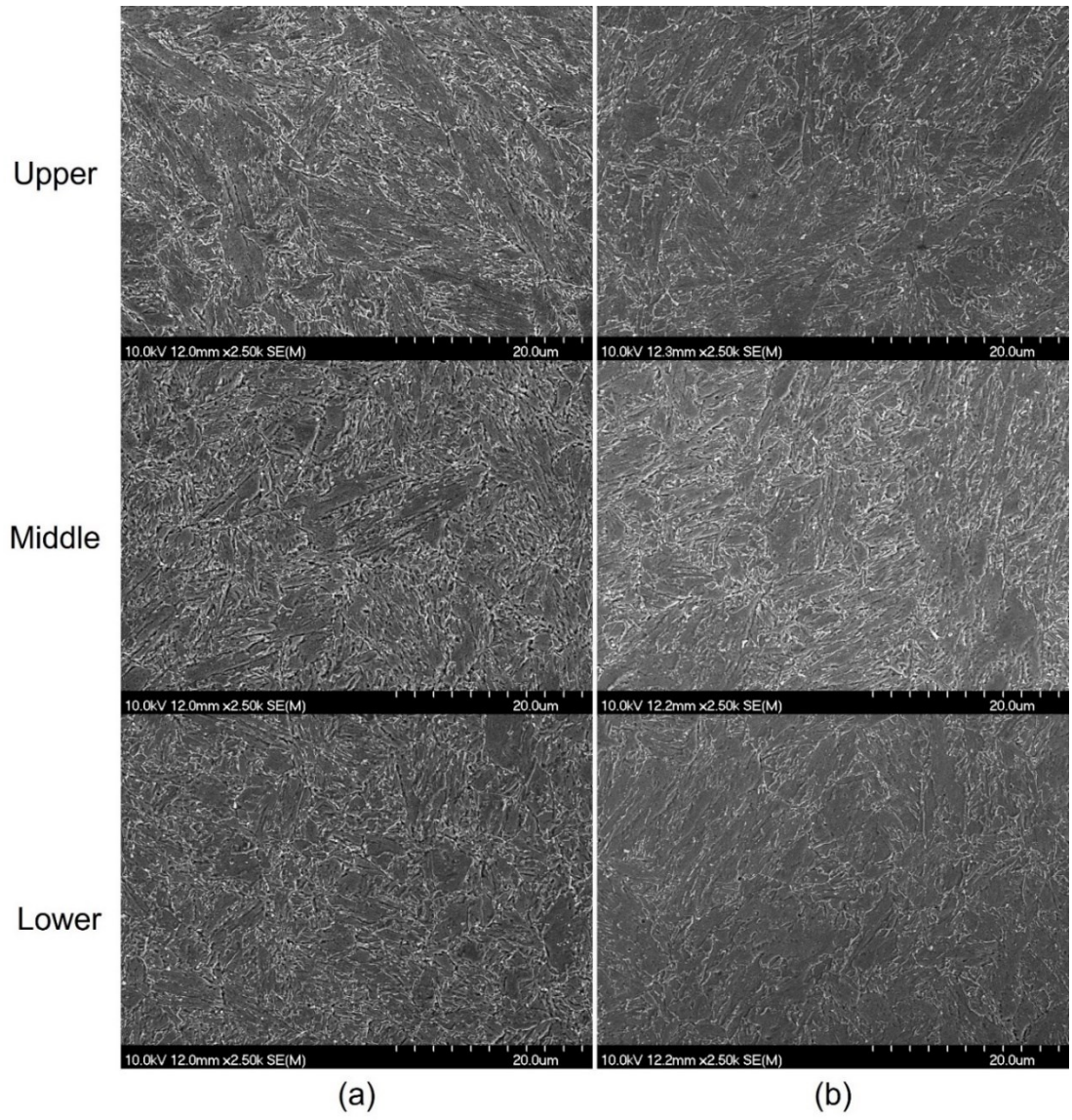

Figure 4.32: Representative FE-SEM micrographs of the lower, middle, and upper layers of the DED-processed and double-tempered rectangular samples: (a) A1-DT, and (b) E4-DT.

The hardness was observed to be higher in the bottom and middle sections of the samples. The top of the as-processed samples significantly drops compared to the lower sections of the sample likely due to retained austenite where the cooling rate was high. Comparing the as-processed condition to the wrought quenched sample with a $HV_{0.3}$ =

719.43 ± 58.89 and the wrought double-tempered sample with a $HV_{0.3}$ = 307.34 ± 26.76. After applying a heat treatment to the DED-processed samples there is a meaningful drop in the hardness, also observed by *Telasang et al.* [32]. However, the heat-treated DED samples have comparable hardness to the conventionally heat-treat wrought material. A noticeable increase in hardness from +8 mm to +10.5 mm in E4-HT was observed. The hardness in A1-HT was maintained through the build direction likely due to less over-tempering due to the faster scanning speed compared to that in the lower layers observed in E4-HT. The hardness variation at each increment has a smaller deviation than the as-processed hardness at the same measured location.

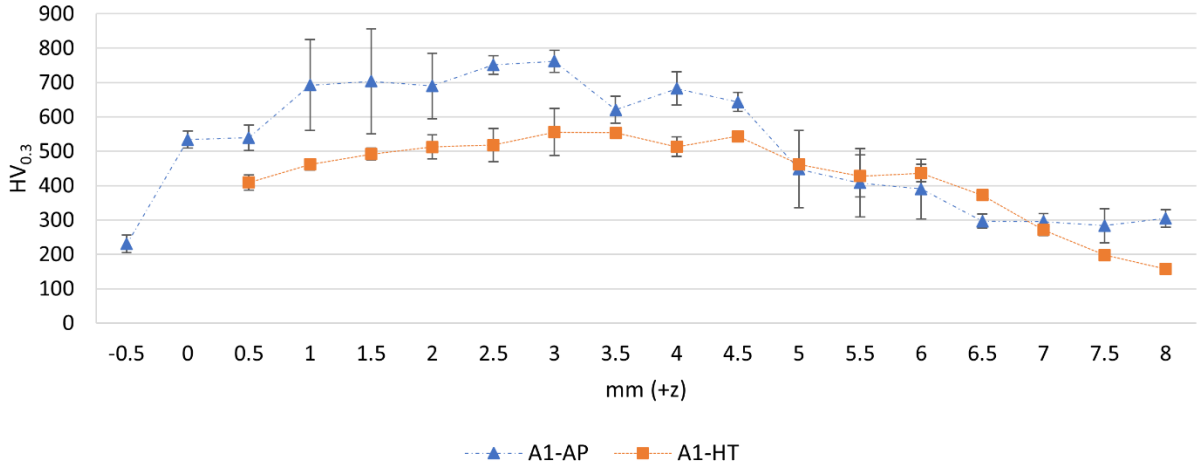

(a)

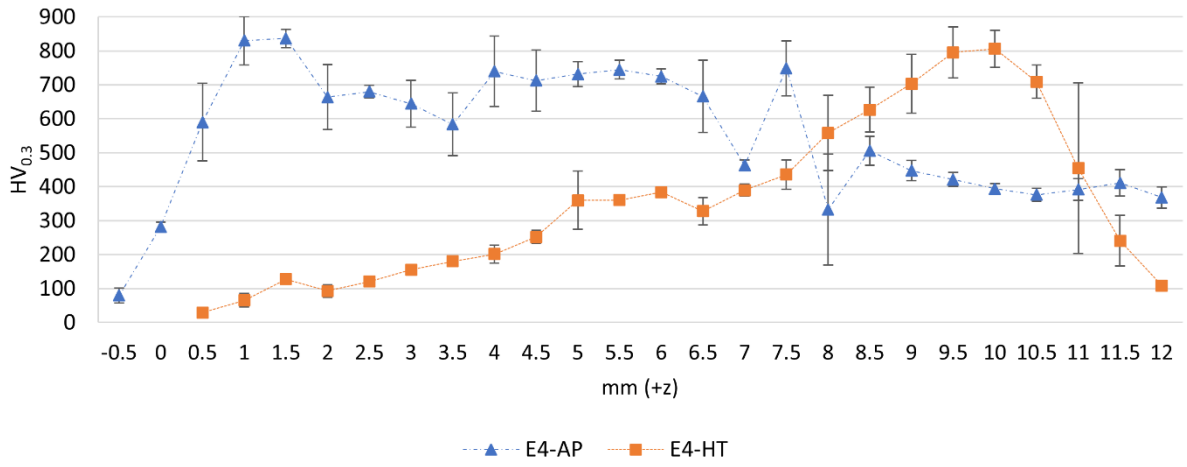

(b)

Figure 4.33: Vickers hardness profile of the cross-sections along the build direction of samples A1- and E4- in the as-processed (AP) and heat-treated (HT) conditions.

It appears the as-processed DED samples may not require a double temper as the cyclic heating is providing an in-situ heat treatment. This microstructural transition arises due to diffusion, such that micro-segregation is decreased [149]. Figure 4.34 presents the XRD traces for both as-printed DED samples, and for the sample process conditions after double-tempering. Retained austenite peaks from the as-processed DED samples were not detected after double-tempering, indicating a decomposition of the phase during the tempering process, which was also noted by *Deirmina et al.* [149] The matrix grain sizes and carbide formed after the double-tempering treatment in the DED-processed samples are notably finer, when compared to the wrought baseline material after double-tempering (Figure 4.35). In addition, the martensite lath size is finer in the DED-processed materials compared to the wrought equivalent. As observed in the quenched wrought sample, the prior austenite grains are visible with the same result detected in the

last layers (*i.e.,* top layers) of the heat-treated DED-processed samples. However, the prior austenite grain size is reduced since the cooling rate experienced by the DED samples is higher than the wrought equivalent. The top of the double-tempered DED samples consists of prior austenite grains, still retained, but with a tempered martensite structure and alloyed carbides (Figure 4.35(a,b)), compared to the fully martensitic structure and few undissolved carbides present in the quenched wrought sample (Figure 4.35(c)).

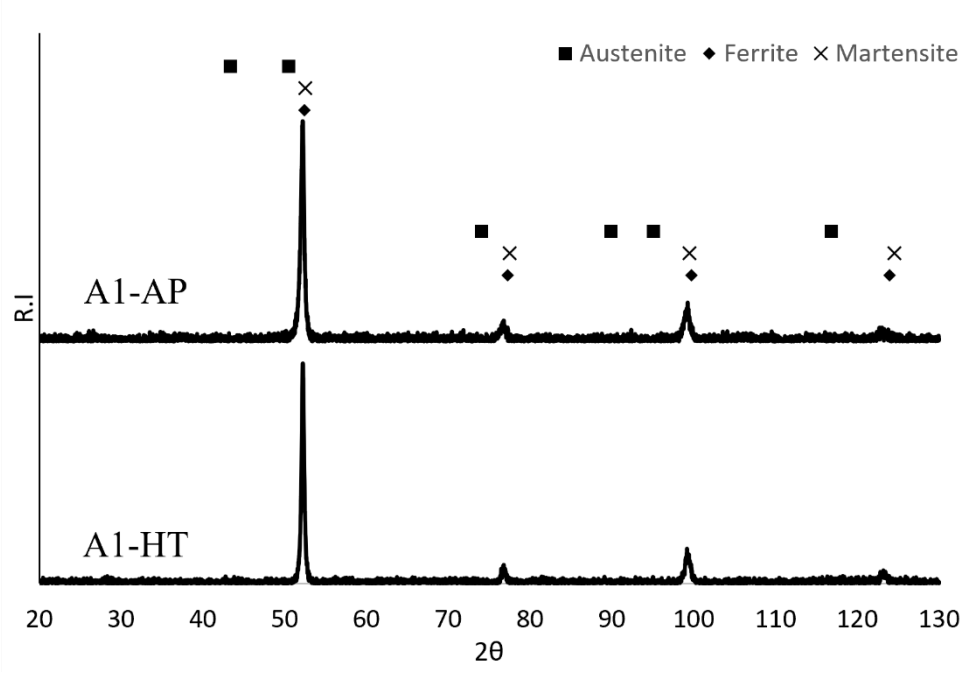

(a)

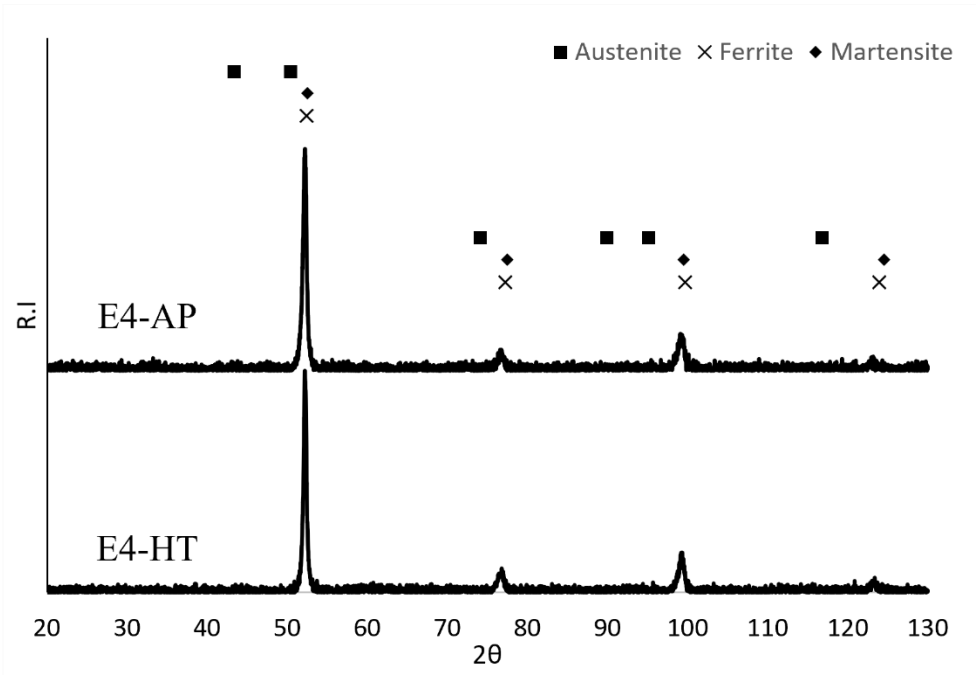

(b)

Figure 4.34: XRD traces for the DED-processed rectangle samples: (a) as-processed and double-tempered (sample initially fabricated using A1 DED conditions), and (b) as-processed and double-tempered (sample initially fabricated using E4 DED conditions).

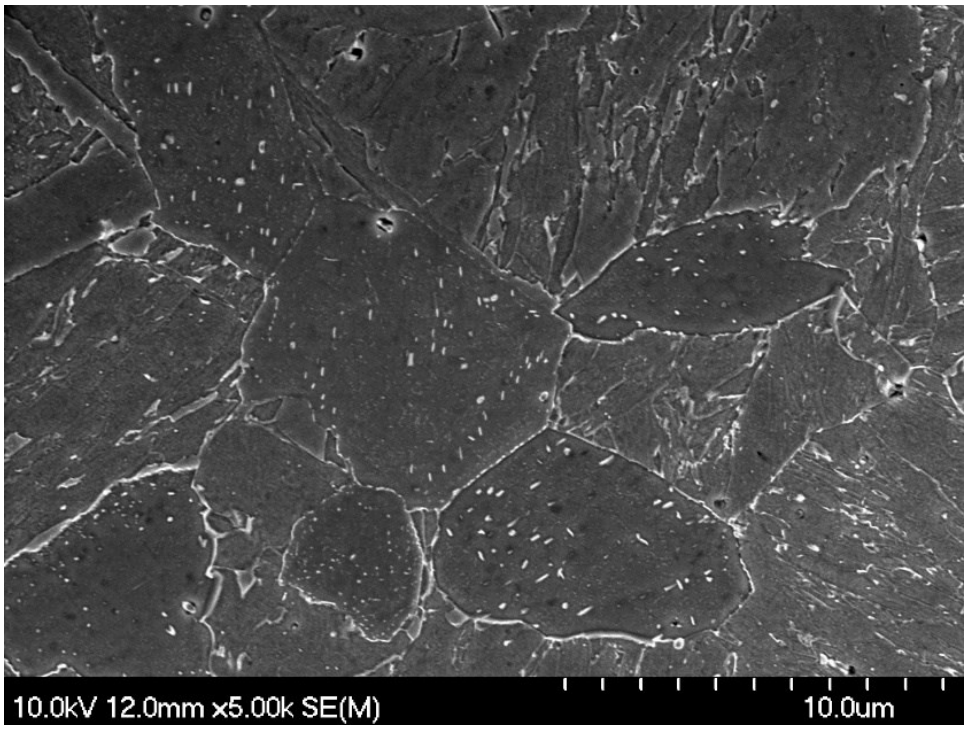

(a)

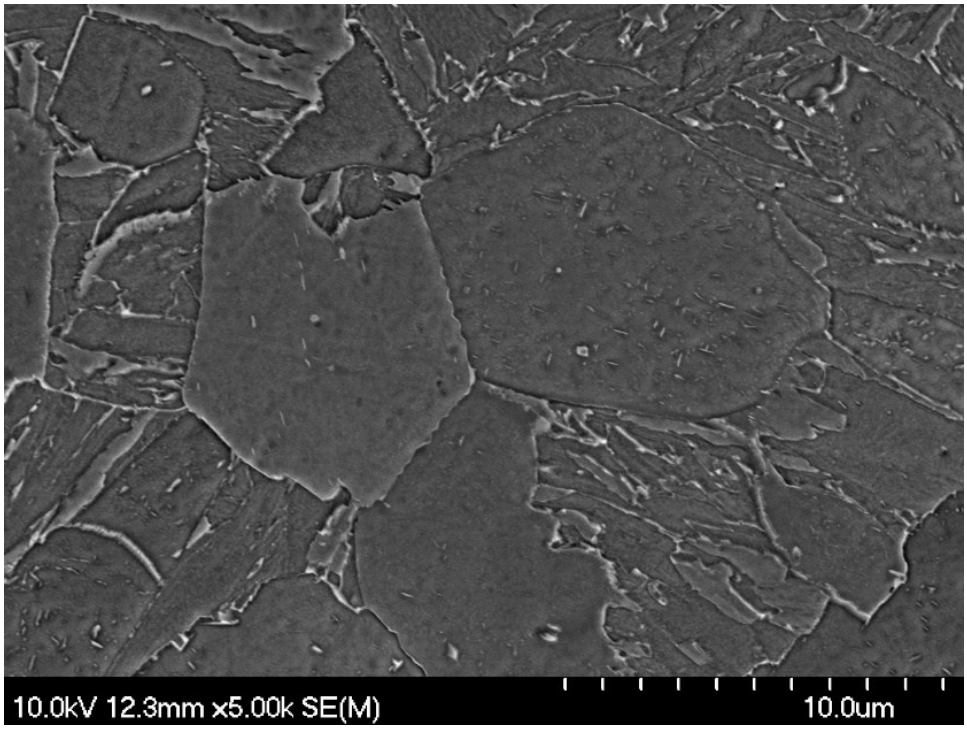

(b)

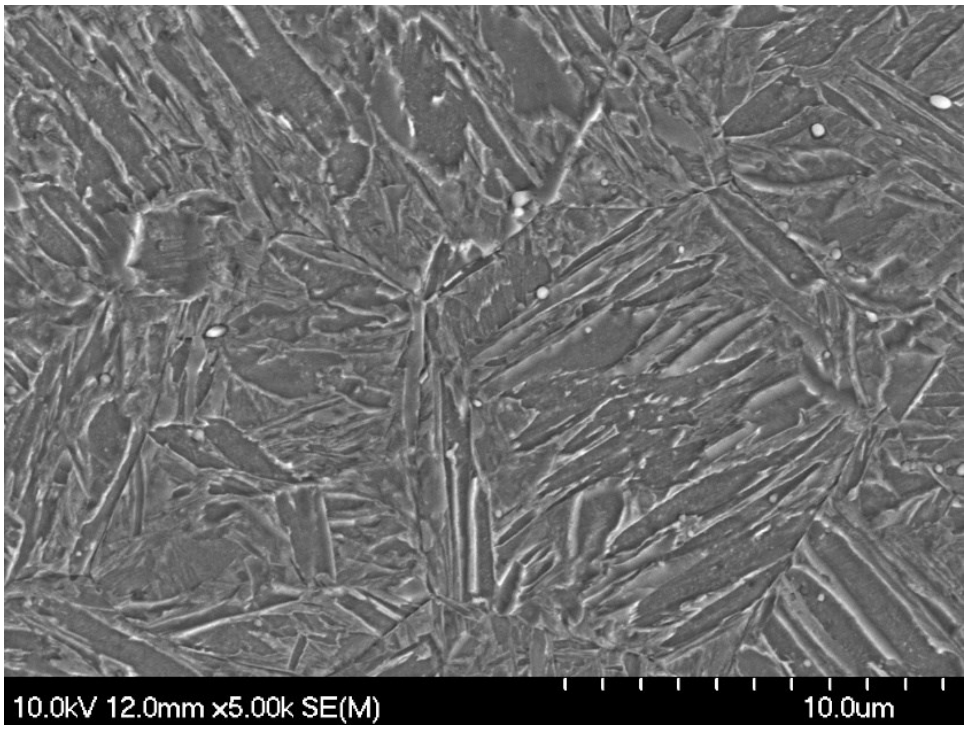

(c)

Figure 4.35: Typical FE-SEM images of the prior austenite grains in the top layers of rectangular samples: (a) A1-DT, and (b) E4-DT. A representative SEM image of the wrought baseline material after quenching (not double-tempered).

4.12 Summary of DED-Processed H13 Tool Steel Microstructure

H13 tool steel clads were successfully deposited onto annealed wrought H13 substrates using a variety of laser DED parameters, in terms of laser scanning speeds and powder feed rates. When comparing with a wrought H13 component, an austenitizing and tempering heat treatment cycle would invariably be applied, to produce the required hardness at elevated temperatures that can only be achieved through fine carbide precipitation. As a consequence, the present study has applied such double-tempering heat treatments to DED-processed samples to assess their impact. A higher wetting angle

during DED processing, which arises with selected parameters, results in a decrease in the density of the deposit. This is because the deposit shape becomes distorted, leading to the potential for gas entrapment. This issue arises with high powder feed rates, combined with a slow scanning speed, which causes the bead to become distorted. Deposited samples undergo rapid solidification, with very high projected cooling rates, resulting in refined microstructures that are indicative of AM-processed parts. The dilution ratios achieved under the examined DED parameters produces sound bonding to the substrate with only one extreme set of conditions, settings A4,4 showing a significant lack of fusion at the substrate. The rapid cooling rates from DED result in a cellular dendritic structure, with lath martensite, retained austenite, and fine metal carbides (MC and M_7C_3) making up the microstructure. In multi-layer clads, since the previous layer re-melts, due to the subsequent deposit on top of it, re-quenching of the layer boundary occurs, resulting in martensite formation. The cyclic heating nature of the DED process will temper previously deposited layers, resulting in tempered martensite and the precipitation of fine alloy carbides. This tempering effect is similar to secondary hardening in a quench and temper heat treatment process for wrought tool steels. In this instance, the top layer results in a very fine lath martensite and retained austenite structure. The cyclic heating creates an in-situ tempering effect that will cause the hardness to vary in the as-processed condition. The hardness of the as-processed samples was seen in be the highest in the middle of the sample and lowered at the top. After applying a heat treatment to the DED-processed samples, the hardness dropped but the variation in hardness at each location was reduced indicating that the heat treatment makes the microstructure more homogenous. Applying a quench and double temper heat treatment to the as-printed

DED-processed materials results the transformation of the cellular dendritic structure to an equiaxed grain structure consisting of a tempered martensite matrix with alloy carbides at the grain boundaries.

4.13 Initial Wear Response of DED H13 Compared to Wrought H13

4.13.1 Initial Microstructure

The annealed wrought microstructure consists of spheroidized grains, large carbides at the grain boundaries with a ferritic (α) matrix. Due to the carbon content and alloying additions, the quenched wrought sample has a lath martensite matrix (α') with some possible retained austenite (γ') and residual alloy carbides that did not dissolve during austenitizing. Compared to the tool steel produced by DED, it consists of fine cellular lath martensite, retained austenite, and fine alloy carbides, due to the rapid solidification rates [50], [89], [146], [159]. Since H13 tool steel contains more alloying additions than in mild steels it allows for retained austenite to remain stable at higher temperatures, but in small amounts. The retained austenite should decompose at ~350°C, but small amounts can still be detected in the 400°C double-tempered wrought sample, likely due to the alloying [59], [145]. As the tempering temperature is increased, the martensite tetragonality reduces, leading to a cubic structure and the release of carbon to form alloy carbides [43], [54]. Double-tempering at the lower temperatures will cause the martensite to shift to a tempered martensite/ferritic lath structure [59]. When the tempering temperatures are increased, the laths begin to coarsen and the retained austenite will transform to martensite [159]–[161]. The wrought microstructure does not have any significant changes from 300°C to 500°C. Once the temperature reaches 600°C, there are still pockets of lath martensite but alloy carbides are forming at the grain boundaries and

within the grains. This should be expected, as secondary hardening from alloy carbides formation starts between 500 – 600°C which can remain stable for extended periods of time [43], [59]. To accurately analyze the carbides with XRD, the carbides must be extracted by chemical or electrochemical dissolution. This is due to the diameter of the beam being larger than the particles in the microstructure [43].

The as-quenched wrought sample consists of a lath martensite due to the rapid cooling, even undissolved carbides can be seen in the martensitic matrix that have a spherical shape [43], [62], [162]. Austenitizing at 1032°C should result in more Cr and Mo entering the matrix, with V-rich carbides remaining [147]. By austenitizing at 1032°C for a relatively short time, less alloying elements are dissolved into the matrix leading to more undissolved carbides retarding austenite grain growth leading to less austenite upon quenching [163]. These carbides tend not to form an interconnected network to help resist wear [164]. The small MC carbides, likely a vanadium rich carbide, have a higher hardness than the surrounding matrix and can be torn out when the matrix has been worn away [165]. The EDS data presented in Figure 4.36(a) suggests that the carbides are V-rich. Clover-shaped MC carbides were also observed (Figure 4.36(b)), notably in the wrought samples tempered at 600°C, which are known to help anchor the matrix under wear conditions [166]. EDS mapping suggested that the clover-shaped precipitates were Mo-rich and fine V-rich carbides dispersed in the matrix.

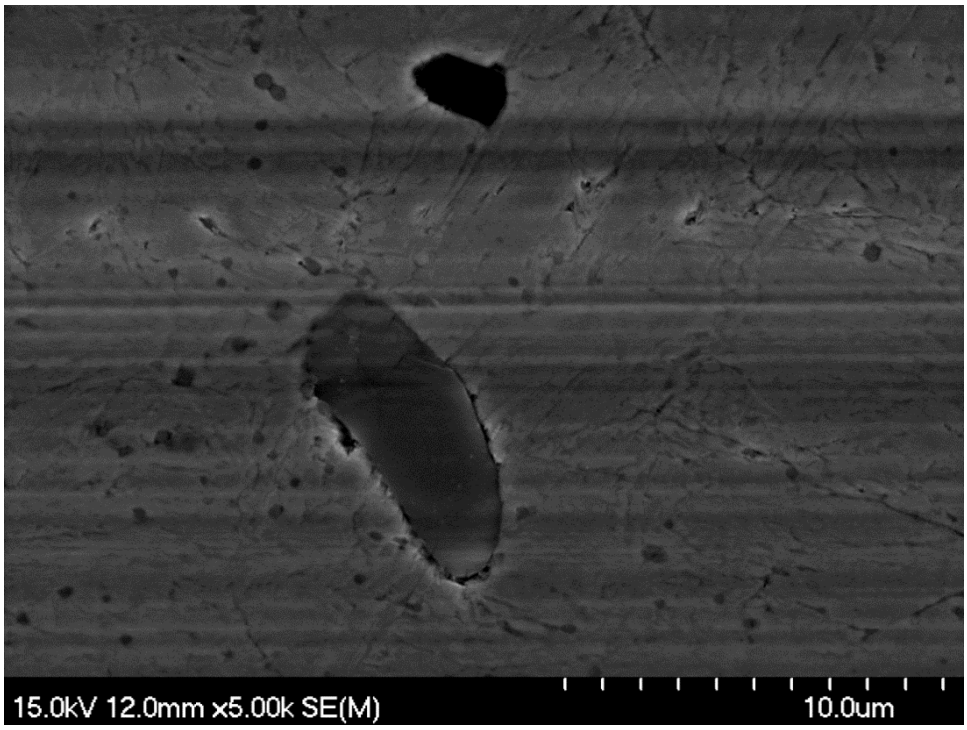

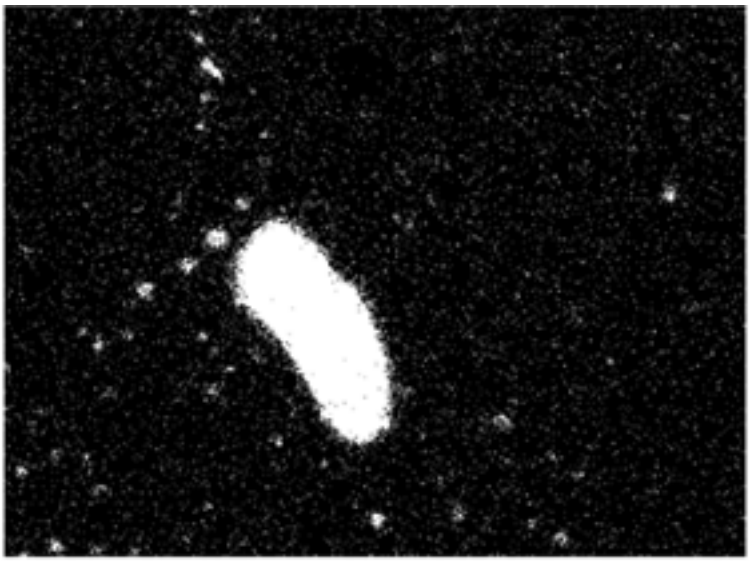

(a)

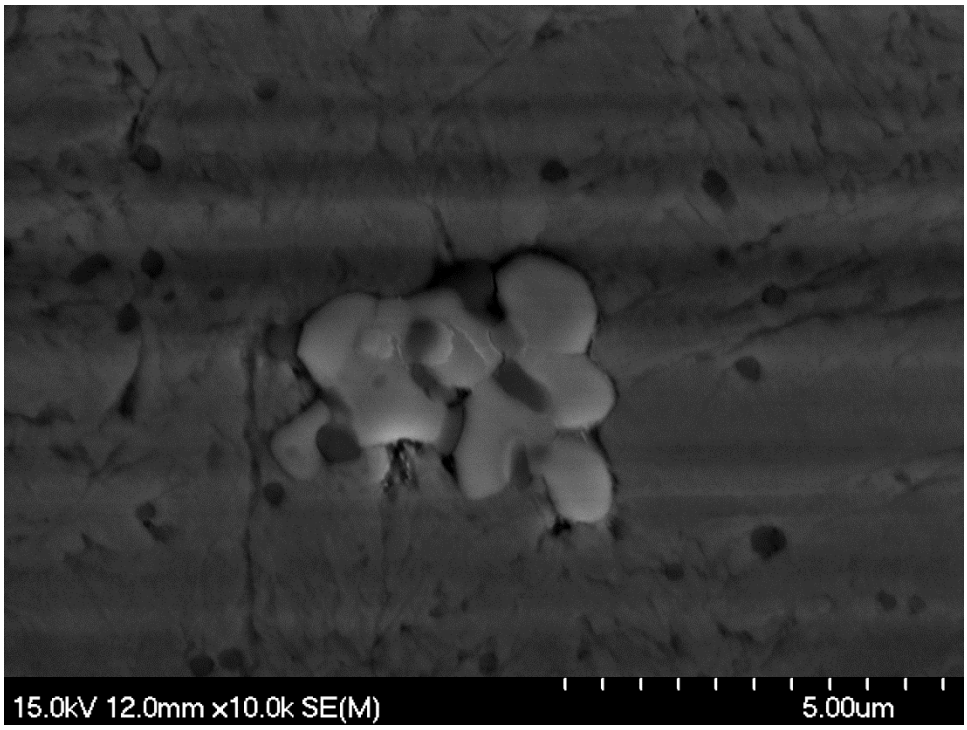

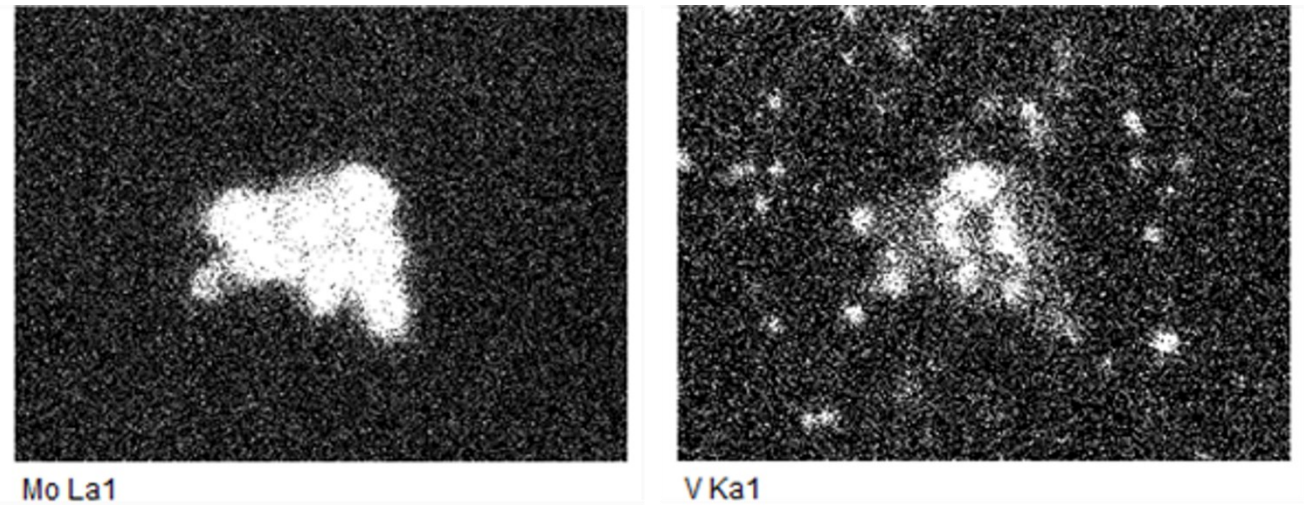

(b)

Figure 4.36: EDS mapping of WDT 600 suggesting a V-rich carbide (a) and a Mo-rich carbide with smaller V-rich carbides inside and surrounding it (b).

The printed samples showed excellent bonding between layers, however, there were internal defects revealed by the scratch testing in the form of gas porosity, as shown in

Figure 4.37. The as-printed samples top layer consist of very fine cellular lath martensite, fine alloy carbides, and retained austenite [37], which is to be expected due to the rapid cooling indicative of the DED process where cooling rates can reach 10^3 – 10^5 °C/s [11].

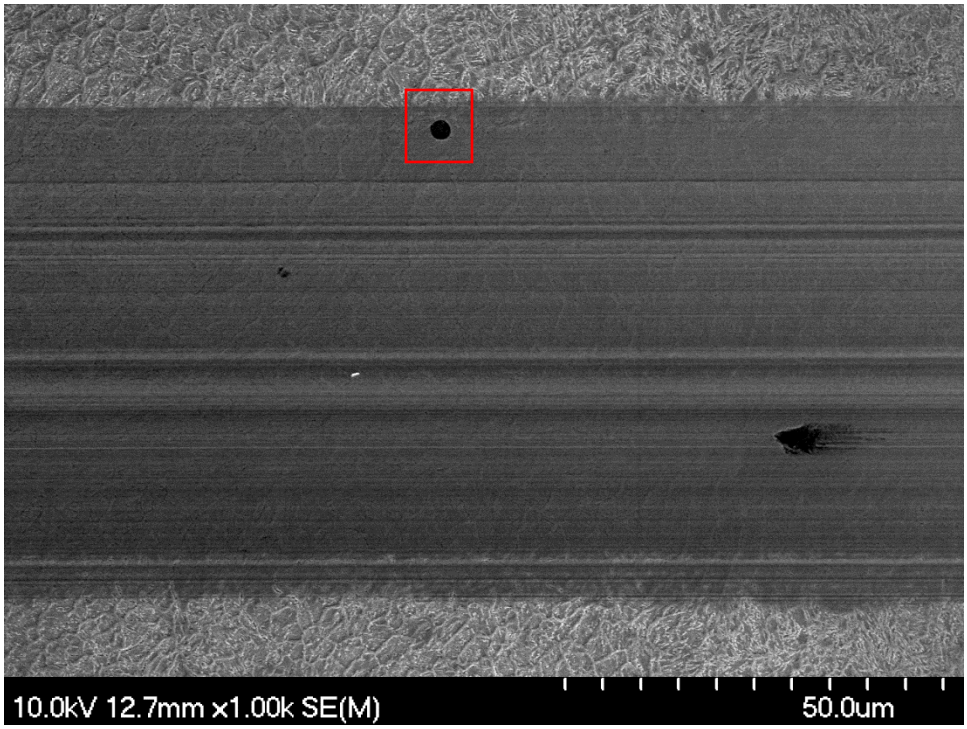

Figure 4.37: FE-SEM image of as-printed DED sample B2-5 under a 10N load. The red box is highlighting internal gas porosity revealed by the scratch test.

Due to the DED process having a moving melt pool, there is directional solidification in the highest temperature gradient. The cooling rate is expected to be faster during deposition of the last set of layers, due to less thermal cycling and the convection from the shielding gas [50]. In the as-printed samples the layer overlaps were easier to identify and at these locations remelting occurs resulting in martensite forming. The scratch track appears to widen at the track overlap, where the martensite is brittle, unable to accommodate the load as seen in Figure 4.38. Widening of the scratch track at layer

overlaps is not observed in the 600°C heat-treated DED samples as the retained austenite would have transformed into a fully tempered martensitic matrix with alloy carbides resulting in a homogenous hardness and matrix. It would be expected that looking at the cross-section of the as-printed samples the microstructure will be inhomogeneous due to the cyclic heating. The lower layers will experience a tempering effect while the top layer will cool the fastest.

Applying a heat treatment to the DED-processed samples resulted in a tempered martensitic matrix with fine alloy carbides located in the grains and grain boundaries (Figure 4.39). Compared to that of the wrought tempered samples, the alloy carbides that have precipitated in the DED samples are finer.

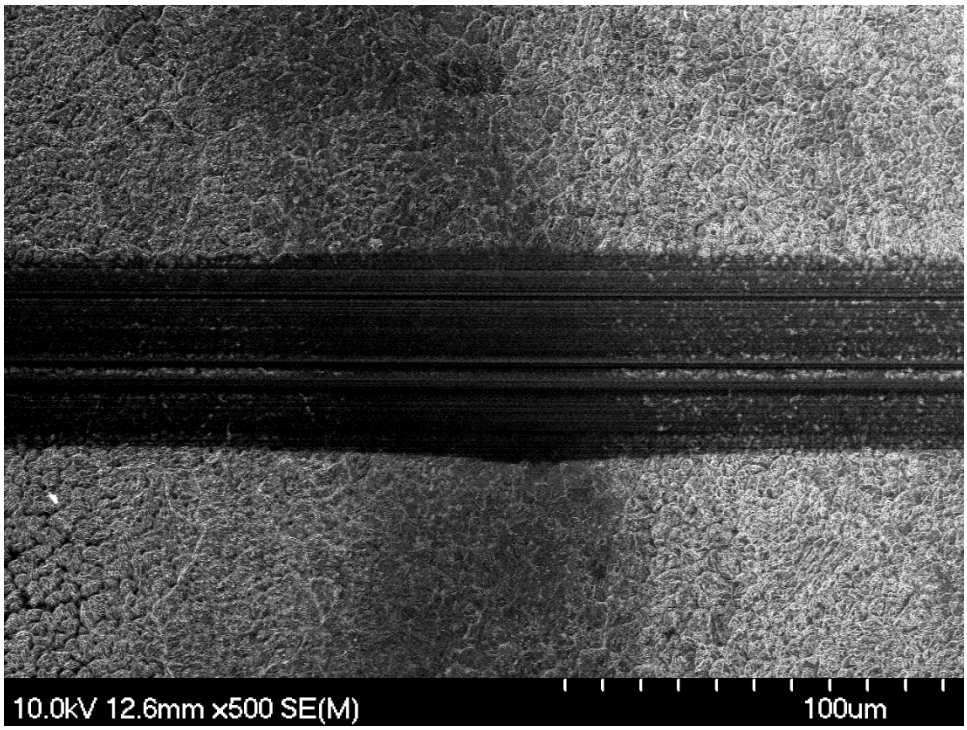

Figure 4.38: FE-SEM image of as-printed sample A3-25 under a 5N load highlighting the track broadening at the track overlap.

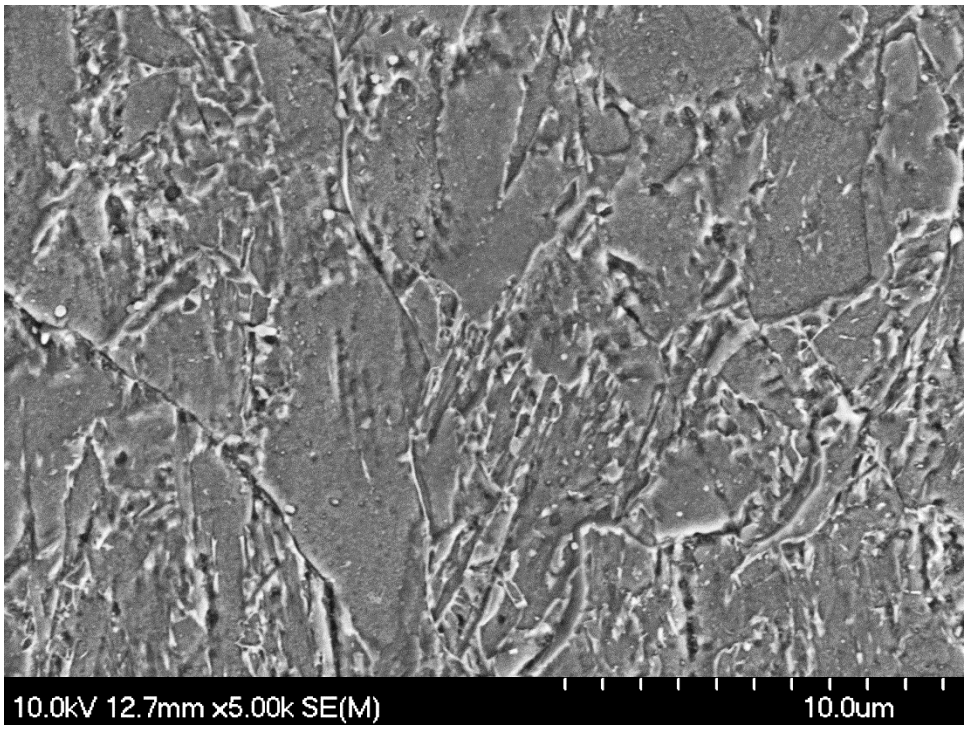

Figure 4.39: FE-SEM micrograph of sample A-15 double-tempered at 600°C with alloy carbides (white spheres) located at grain boundaries and within grains.

4.14 Scratch Hardness and Surface Analysis

A noticeable change in the scratch hardness was observed when applying different tempering temperatures to the wrought material. A maximum scratch hardness is measured in the quenched state with a value of 9.60 ± 0.62 GPa under a 5N load. Double-tempering at 300°C and 400°C dropped the scratch resistance of the wrought material under the tested loading conditions. However, under a 10 N load the maximum recorded scratch hardness occurred after double-tempering at 500°C which was measured to be 7.81 ± 0.38 GPa. This increase in hardness is attributed to the secondary hardening from the precipitation of the alloy carbides. Even though the as-quenched sample had a higher scratch hardness due to the lath martensitic structure under a 5N and comparable scratch

resistance under a 10N; if higher loads were used or a reciprocating test was performed it is likely that the martensite will transform into tempered martensite due to localized heating lowering the wear resistance [104]. Double-tempering at 700°C resulted in the wrought sample approaching the annealed scratch hardness as this temperature is nearing the annealing temperature of H13 of 845 – 900°C [48].

The as-printed condition showed no clear trend when the powder feed rate, scanning speed, or the number of printed layers was varied. A maximum scratch hardness of 7.54 ± 0.20 GPa under a 5 N load is achieved with settings C4-5 (*i.e.,* 6.5 g/min and 400 mm/min). Under a 10 N load in the as-printed condition, settings C4-25 produced the highest scratch hardness of 8.35 ± 0.46 GPa. Even though a martensitic structure and finer grains are obtained in the as-printed samples, the scratch resistance is lower than the wrought quenched sample (Figure 3.8) under a 5 N load but is comparable in scratch hardness under a 10 N load. This comparable scratch hardness is due to martensite having a low work hardenability in the wrought quenched sample, whereas the as-printed martensitic matrix would be slightly tougher from the small tempering effect from the cyclic heating. Applying a heat treatment to the printed samples lowered the wear resistance of many of them, as to be expected, due the tougher tempered martensite and alloy carbide matrix. The as-printed and heat-treated DED samples scratch hardness are plotted in Figure 4.40. *Wang et al.* have noted a similar reduction in wear resistance after heat treating additive manufactured tool steels [165]. A maximum scratch hardness for the heat-treated DED sample occurred using settings B3-15 with a scratch hardness of 5.96.79 ± 0.19 GPa under a 5 N load. The maximum scratch hardness after heating treating under a load of 10 N was sample A3-15 measured at 6.17 ± 0.26 GPa. However,

the deviation in the scratch hardness is reduced under the tested loading conditions, leading to predicable wear rates. No clear trend was observed with changing the amount of deposited material under both loading conditions. The only exception to this was the heat-treated B2 and C4 settings resulting in the wear resistance significantly dropping. Both printed sample sets had a higher scratch hardness than the equivalent wrought tempering condition at 600°C. The comparable scratch resistance of the printed samples can be attributed to the refined structure from the DED process and V-rich MC carbides [157]. The MC carbides under both loading conditions did not appear to be torn out when perpendicular to the force but carbide tear out seems to be more prevalent on the sides of the tracks where it is more of a shearing force. The MC carbides are excellent at supporting the load and provide anchorage [157]. The V-rich carbides (MC) will contribute to the high hardness and to some extent the Cr and Mo alloy carbides as they are able to maintain a fine dispersion in the matrix even with temperatures approaching 700°C [43], [59]. Carbide formation can be rapid even at higher cooling rates, with carbides seen in the quenched sample which are likely the MC carbides that have not dissolved during austenitizing [43]. Vanadium carbides nucleate at the dislocations within the ferrite, with the Cr_3C_7 nucleating along the Fe_3C and ferrite interfaces, along with other fine alloy carbides of Cr or Mo [46], [59].

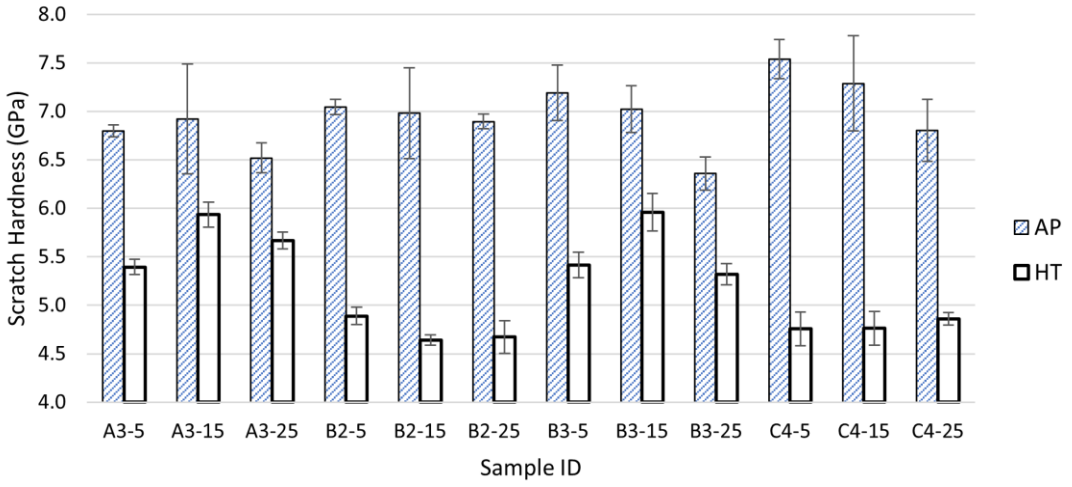

(a)

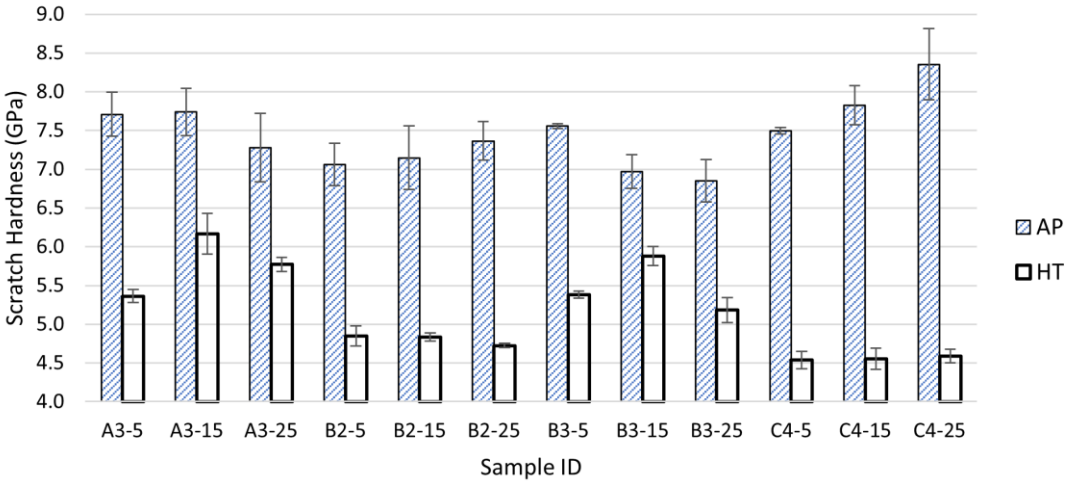

(b)

Figure 4.40: Scratch hardness of DED-processed H13 tool steel under a 5N load (a) and a 10N load (b) under varying system parameters. The error bars are indicating standard deviation.

Using the CLSM profile analysis of the scratch tracks plotted in Figure 4.41(a),

tempering the wrought material has no noticeable change in the cross-sectional area

under a 5 N load until the tempering temperature reaches 600°C where the variation increases. Additionally, increasing the loading to 10 N, the cross-sectional area observes a noticeable increase. The cross-sectional area of the annealed and 700°C double-tempered samples tracks have the largest area over both loading conditions, which is to be anticipated. The cross-sectional area significantly drops for the quenched and tempered samples for both loading conditions due to the significant hardening provided by martensite and alloy carbides. The smallest cross-sectional area under a 5 N load was recorded at 14.73 ± 1.62 μm^2 when double-tempered at 500°C. Increasing the load to 10 N, double-tempering at 500°C recorded the smallest cross-sectional area of 41.09 ± 1.65 μm^2.

In the DED-processed samples the cross-sectional area (Figure 4.41(c,d)) is smaller in the as-printed condition with no observable trend under 5 N or 10 N loads. However, when a heat treatment is applied the cross-sectional area increases but with no trend to the data. There is one major outlier which is the heat-treated C4-25 sample that has a cross-sectional area of 113.183 ± 18.56 μm^2 for 5 N and 400.100 μm^2 for 10 N respectively. If this sample is excluded from the analysis, the cross-sectional area did not increase significantly over the selected varying system parameters. The lowest recorded cross-sectionally area was 18.87 ± 2.25 μm^2 under a 5 N load using settings A3-25 in the as-printed condition. Interestingly, using the same system parameters, the cross-sectional area decreased to 17.47 ± μm^2, which is a reduction of 7.74%. This reduction of cross-sectional area after heat treating the DED sample was also observed using settings B3-25, with a decrease of 10.69%. The minimum recorded cross-sectional area for the heat-treated samples was 23.07 ± 0.91 μm^2 under a 5 N load using settings B3-5. Increasing

the load to 10 N the lowest cross-sectional area in the as-printed state was 55.56 ± 1.00 μm^2, using setting A3-25. In the heat-treated condition, the largest cross-sectional area (excluding setting C4-25) was 74.36 ± 2.32 μm^2, using settings C4-15. Samples A3-25 and B3-25 had a reduction of cross-sectional area after heat treating of 0.28% and 13.17% respectively under a 10 N load.

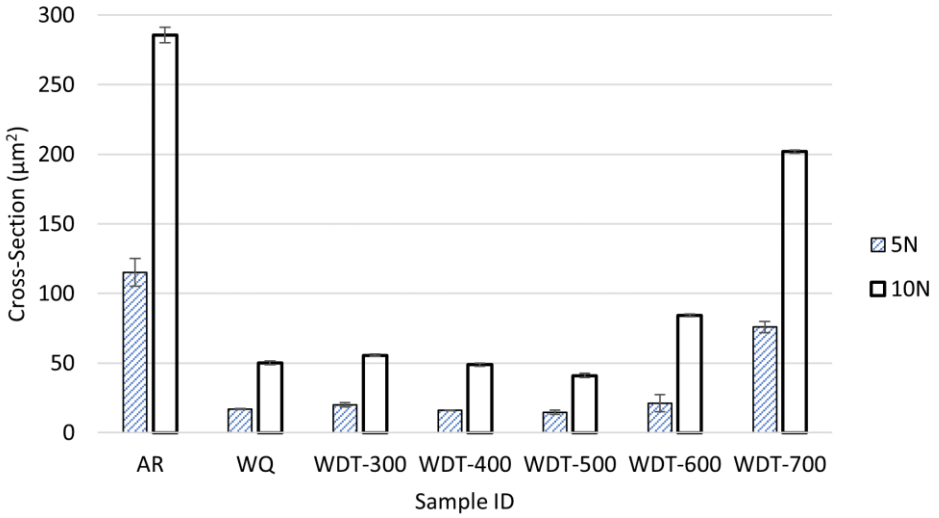

(a)

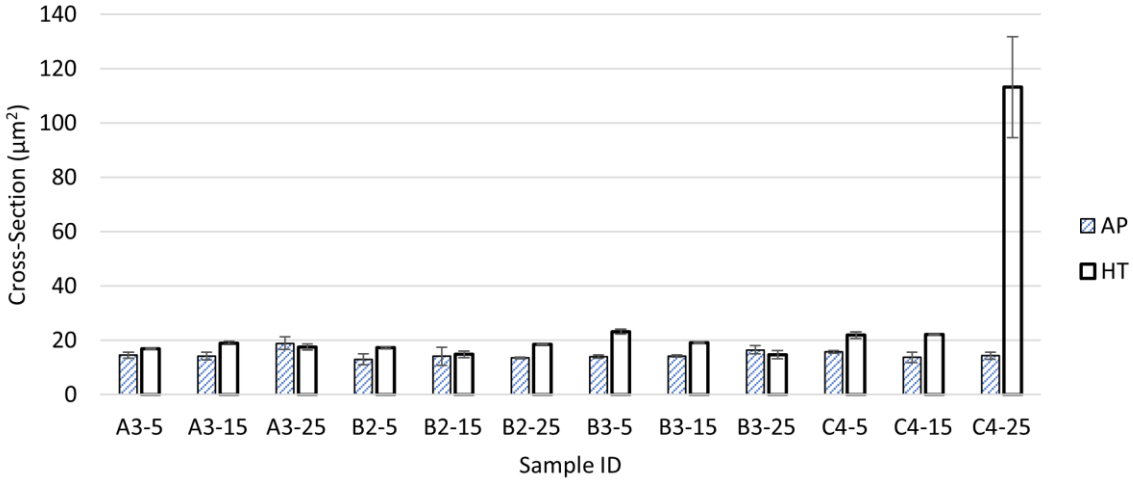

(b)

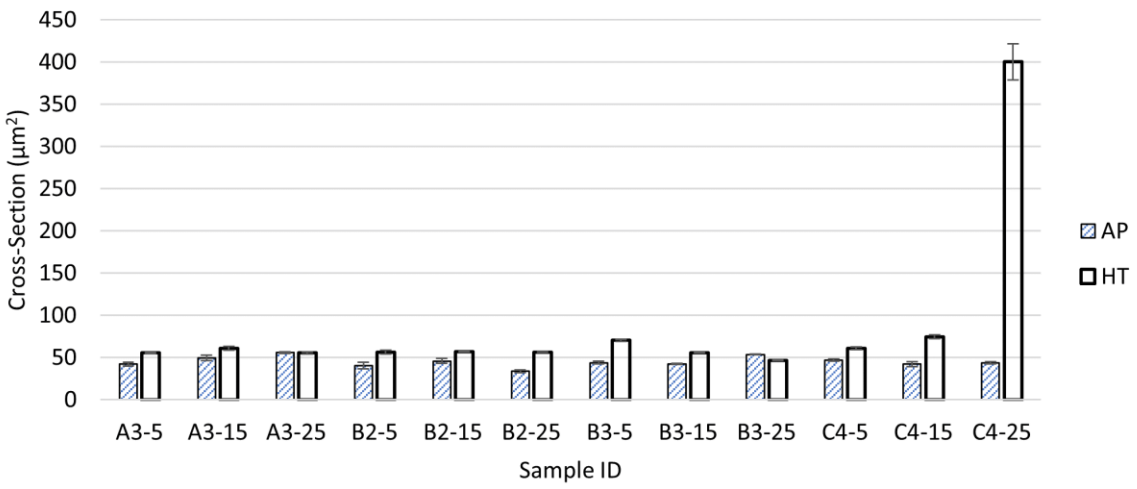

(c)

Figure 4.41: Cross-sectional area of scratch track in wrought H13 under 5N and 10N loads (a). Cross-sectional area of scratch track of DED H13 under a 5N (b) and 10N load (c). The error bars are indicating standard deviation.

Surface roughness for the wrought and DED samples under the tested loads are plotted in Figure 4.42. The surface roughness of the annealed and double-tempered 700°C wrought material had the highest surface roughness values under both scratch loading conditions. The remaining wrought tempered samples having similar roughness values with a minimum of 0.10 ± 0.01 µm under 5 N when quenched. The surface roughness of the wrought samples, increase when the load is raised to 10 N. A minimum surface roughness for the wrought material under 10 N, was recorded at 0.13 ± 0.02 µm, after double-tempering at 300°C. The slight tempering of the martensite increased the toughness of the matrix compared to the quenched sample. The harder surfaces from the quenched and tempered samples will help lower the surface roughness compared a more ductile surface (*i.e.,* the annealed and double-tempered at 700°C). Under the 10 N load

the AR and double-tempered 700°C samples had very high variations in the surface roughness likely attributed to stick and slip due to the softer surface [167]. The wrought samples had a higher surface roughness, compared to the printed samples which consist of a refined matrix. The surface roughness remained consistent across the printed and heat-treated samples at ≈ 0.11 μm under 5 N. Notable exceptions being the heat-treated B2-25 and C4-25 samples at 5 N with values of 0.23 ± 0.16 μm and 0.16 ± 0.02 μm, respectively. No explicit reason could be determined as to why this happened, as the remaining samples have comparable values. When the loading changed to 10N, the surface roughness of the wrought material was slightly higher than the as-printed and heat-treated DED samples. The surface roughness under a 10 N load for the as-printed and heat treat samples ranged from 0.13 – 0.15 μm, except for the heat-treated C4-25 sample which had a value of 0.25 ± 0.06 μm. This slight increase in surface roughness under a 10 N load could be from material flaking off contributing to the wear debris leading to three-body abrasion [157]. Applying the heat treatment to the DED-processed sample did not appear to have significant impact on the surface roughness. The wear response of the material is similar to a two-body abrasion condition. If the conditions changed to a higher load or a reciprocating set up, three-body abrasion would be expected.

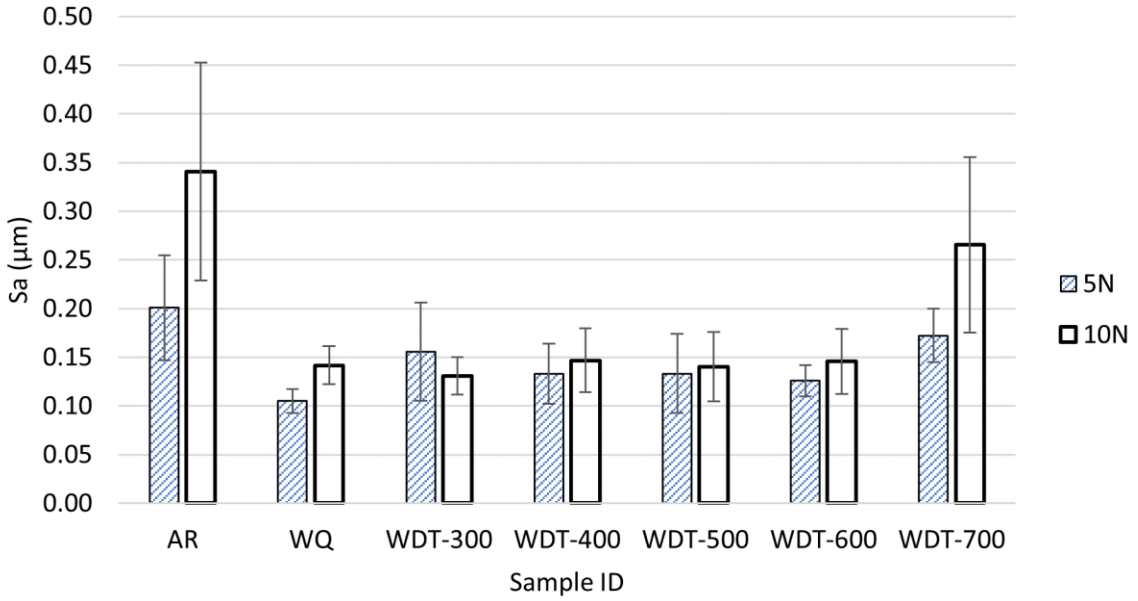
0.50
0.45
0.40
0.35
0.30
0.25
0.20
0.15
0.10
0.05
0.00
Sa (µm)
AR
WQ
WDT-300
WDT-400
WDT-500
WDT-600
WDT-700
Sample ID
5N
10N

(a)

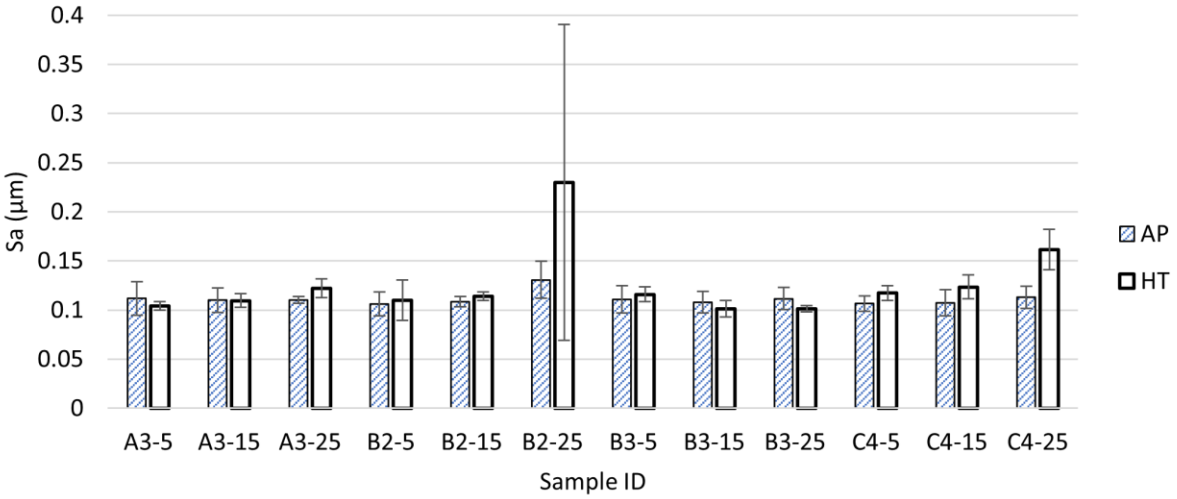
0.4
0.35
0.3
0.25
0.2
0.15
0.1
0.05
0
Sa (µm)
A3-5
A3-15
A3-25
B2-5
B2-15
B2-25
B3-5
B3-15
B3-25
C4-5
C4-15
C4-25
Sample ID
AP
HT

(b)

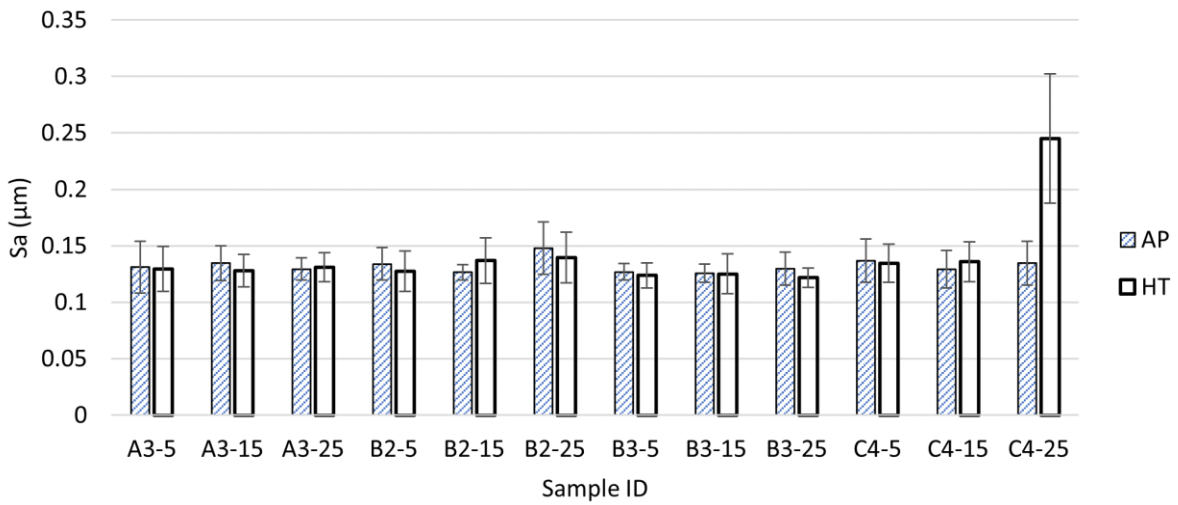

(c)

Figure 4.42: Wrought H13 surface roughness of scratch track under 5N and 10N loads (a). DED samples surface roughness under a 5N (b) and 10N load (c). The error bars indicating the standard deviation.

The COF for the wrought and DED materials are plotted in Figure 4.43. The COF values for the wrought material were comparable across the tested tempering conditions except for the annealed sample or tempering at 700°C. No trend was observed between the scratch testing set up and the varying system parameters or number of layers printed. The annealed wrought sample had the highest COF for both loading conditions recorded at 0.240 ± 0.027 and 0.324 ± 0.027 for 5 N and 10 N, respectively. A minimum wrought COF under a 5 N and 10 N load was measured at 0.076 ± 0.001 and 0.084 ± 0.001 respectively, when double-tempered at 300°C. A minimum COF in the as-printed condition at a 5 N load was measured at 0.068 ± 0.0 using settings C4-5. At the same loading, the minimum COF of the heat-treated DED samples was measured at 0.054 ± 0.0 using settings B3-255. At a 10 N load, the lowest measured COF in the as-printed

condition was 0.077 ± 0.001 using parameters C4-25. In the heat-treated state, the lowest COF was 0.086 ± 0.0 using settings B3-15. For the DED samples under a 5 N load, the COF decreases after applying a heat treatment for settings A3 and B3. However, at 10 N, the COF for the heat-treated DED samples have a significant increase to the likely due to a softer matrix after tempering. The heat-treated DED samples have slightly higher COF compared to the wrought tempered samples.

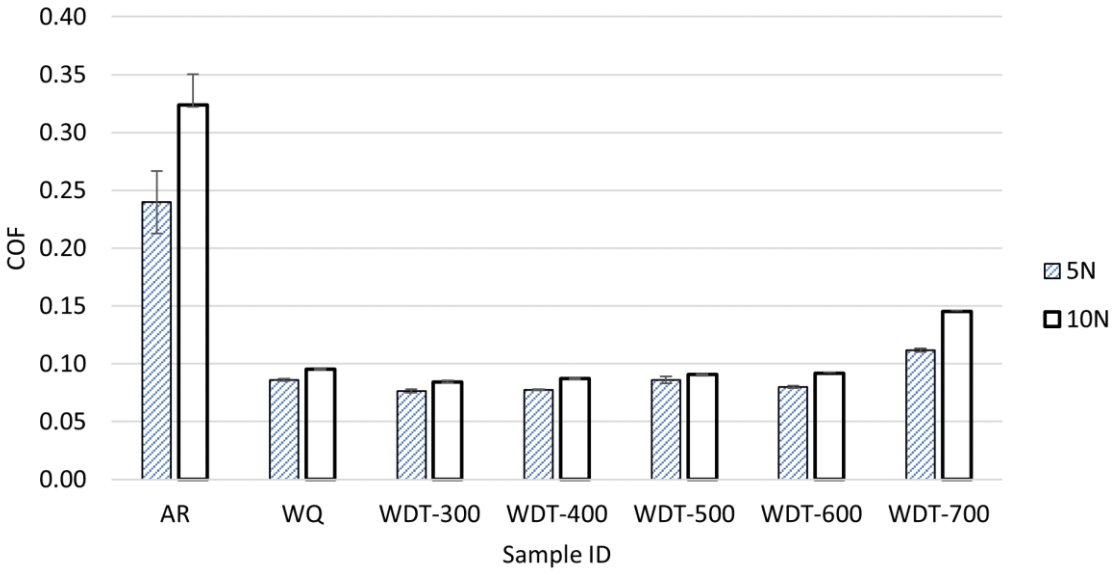

(a)

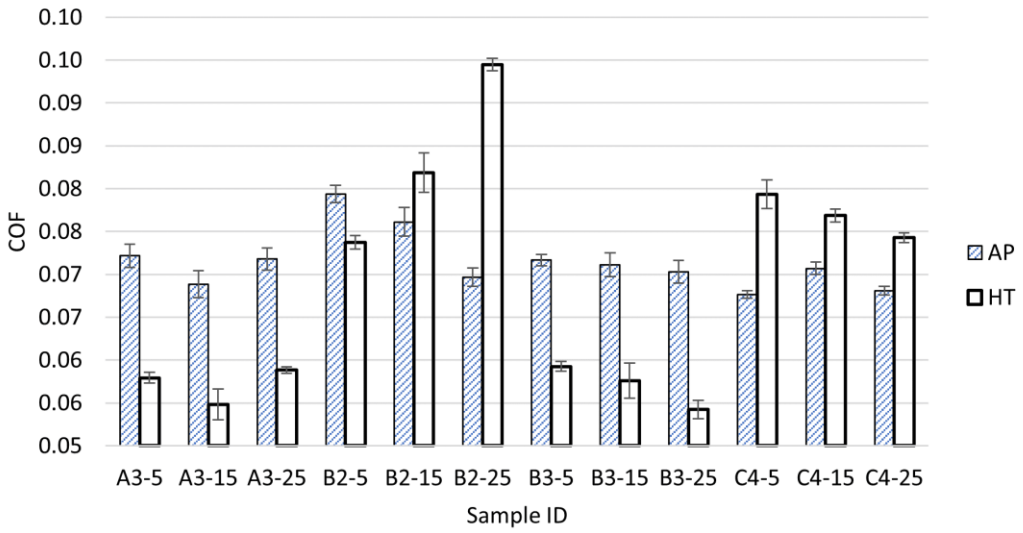

(b)

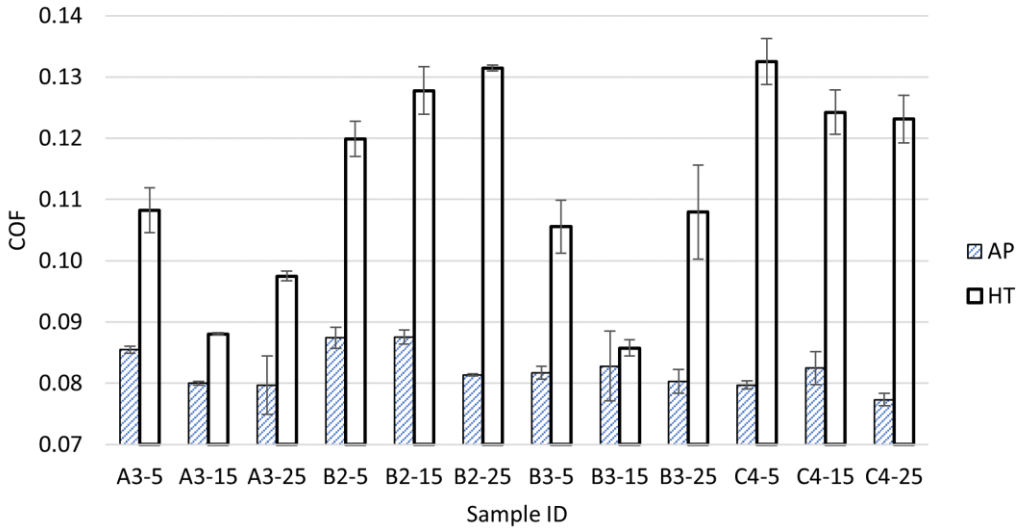

(c)

Figure 4.43: COF of wrought H13 under 5N and 10N loads (a). DED H13 under a 5N load (b) and DED H13 under a 10N load (c). The error bars indicating the standard deviation.

4.15 Summary of DED-Processed H13 Wear Response

Out of all the tested material conditions, the wrought quenched sample had the highest measured scratch hardness of 9.60 ± 0.62 GPa due to the martensitic matrix. After double-tempering the wrought material at 500°C, a maximum scratch hardness was measured at 7.81 ± 0. 38 GPa under a 10 N load. EDS analysis suggested that MC and clover-shaped MC carbides in the wrought material that precipitated during the tempering process provided high scratch resistance. The drop in scratch resistance from the quenched sample under the equivalent load is attributed to the low work hardenability of martensite.

No noticeable trend was observed in the as-printed samples with a quench and double temper heat treatment lowering the overall scratch resistance. The higher scratch hardness of the as-printed samples is credited to the refined cellular martensite structure with retained austenite. All samples showed excellent metallurgical bonding with the substrate, but scratch testing revealed internal defects in the form of gas porosity. Applying a quench and double temper heat treatment at 600°C resulted in the microstructure consisting of tempered martensite and fine alloy carbides. The highest measured scratch hardness for the DED-processed material was 7.54 ± 0.20 GPa under a 5 N load using settings C4-5, in the as-printed condition. The as-printed condition resulted in the highest recorded scratch hardness under a 10 N load of 8.35 ± 0.46 GPa using settings C4-25. The heat-treated DED samples resulted in comparable scratch hardness to the 500°C double-tempered and quenched wrought samples. However, it dropped the scratch overall scratch resistance with a highest measured hardness of 6.79 ± 0.33 GPa using settings B3-15 under a 5 N load. Increasing to a 10 N load, the highest

recorded scratch hardness of the heat-treated DED samples was 7.28 ± 0.13 GPa using settings B3-25.

The cross-sectional area had a clear trend in the wrought material. Under the examined conditions, the smallest cross-sectional area occurred when the tempering temperature was 500°C with areas of 14.73 ± 1.62 μm^2 and 41.09 ± 1.65 μm^2, under 5 N and 10 N loads respectively. No clear trend was observed with the DED-processed material when the number of layers, powder feed rate, or scanning speed changed. The notable exception was the heat-treated DED sample using settings C4-25. Excluding this sample from the results, under a 5 N load in the smallest as-printed cross-sectional area was measured to be 18.87 ± 2.25 μm^2 using settings A3-25. In the heat-treated condition under a 5 N load, the smallest recorded area was 23.07 ± 0.91 μm^2 using settings B3-5. Under a 10 N load, the smallest measured area in the as-printed state was 55.56 ± 1.00 μm^2. Under the same loading conditions, the smallest area of the heat-treated DED samples was recorded at 74.36 ± 2.32 μm^2 using settings C4-15.

CLSM surface roughness analysis showed that that wrought material had comparable values under the tested loading conditions except for the annealed and double-tempering at 700°C samples. A minimum surface roughness occurred in the quenched state and using a 300°C double temper under a 5 N and 10 N load respectively. No observable trend was seen in the DED-processed samples with the various system parameters examined. In the as-printed condition the surface roughness remained around 0.11 μm for both scratch loads. Heat treating the DED samples resulted in the surface roughness slightly increasing to a range of 0.13 – 0.15 μm. Finally, the COF for the wrought material occurred using a 300°C tempering temperature. For the as-printed DED samples,

a minimum COF occurred using settings C4-5 and C4-25 under 5 N and 10 N loads respectively. Heat treating the DED samples resulted in the COF decreasing for settings A3 and B3 under a 5N, however under a 10 N load all the COF values increased for the tested system parameters. Minimum COF values after heat treating the DED samples under a 5 N and 10 N load occurred using settings B3-25 and B3-15, respectively.

4.16 DED H13 Tool Steel Summary

From this study, successful process parameters were determined that produced highly dense samples with excellent metallurgical bonding to the wrought H13 substrate. The mechanical properties showed promising results with similar or slightly improved properties due to the highly refined cellular dendritic microstructure of martensite and fine distribution of alloy carbides formed during rapid solidification. Heat treating the DED-processed H13 also showed the deposited material is similar to wrought consisting of tempered martensite and precipitation of adequately sized alloy carbides dispersed in a tempered martensitic matrix. The DED tempered martensite matrix does not appear to be as overly tempered compared to the wrought at the equivalent tempering temperature. The system parameters and findings of the DED-processed H13 can then be transferred to the DED-processed FGM H13-Cu study as a starting point.

5 MATERIAL CHARACTERIZATION OF FUNCTIONALLY GRADED H13-CU

5.1 Introduction

Developing new advanced materials that offer a longer service life and reduce the cycling time of the tool is desired by the tooling industry. There is an evolution in the AM sector to manufacture innovative parts using multiple materials. The aim of these new materials is to utilize the positive attributes of each respective material, while trying to minimize the negative attributes. This category of material is commonly referred to as an FGM, where gradients can take the form of controlled porosity, orientation, microstructure, or composition. For the tooling industry, cooling the large tools is difficult, so there is interest to combine tool steels with copper to increase the thermal transfer from the surface of the tool while maintaining the strength and wear resistance. H13 tool steel is frequently used in elevated tooling applications but has a poor thermal conductivity, so DED technology would be utilized to print an FGM of H13-Cu. However, this material system will prove to be difficult to process because of the reflectivity issues at near infrared-wavelengths for Cu, a large coefficient of thermal expansion difference, and Fe-Cu exhibiting a miscibility gap.

This chapter will summarize the process route of printing an H13-Cu FGM using a DED system with changing laser powers, starting with various in-situ blended compositions of H13-Cu onto a wrought substrate. This was followed by deposition onto a pure Cu substrate to investigate if the various blends can be achieved with sufficient metallurgical bonding.

5.2 Experimental Procedure

Pre-alloyed gas-atomized H13 powder and oxygen-free high thermal conductivity (OFHC) Cu was purchased from TLS Technik (Bitterfeld-Wolfen, Germany); with a PSD specified between 50 – 100 µm. Figure 5.1 is a combined PSD and volume distribution of the virgin powders that were analyzed using particle size analysis (model Mastersizer 3000, Malvern Instruments, Malvern, UK); three measurements were undertaken on different samples from the supplied batch to assess 'intra-batch' variability. The apparent density (g/cm^3) was determined using ASTM standard B212-17 [168]. Likewise, the flow properties were measured using the Hall flow test, using 50g of powder, following ASTM standard B213-17 [169]. For the pre-alloyed gas-atomized H13 powder, the apparent density and Hall flow properties were 4.68 g/cm^3 and 3.89 g/s respectively. The apparent density and Hall flow properties for the OFHC copper were 5.0 g/cm^3 and 4.03 g/s respectively.

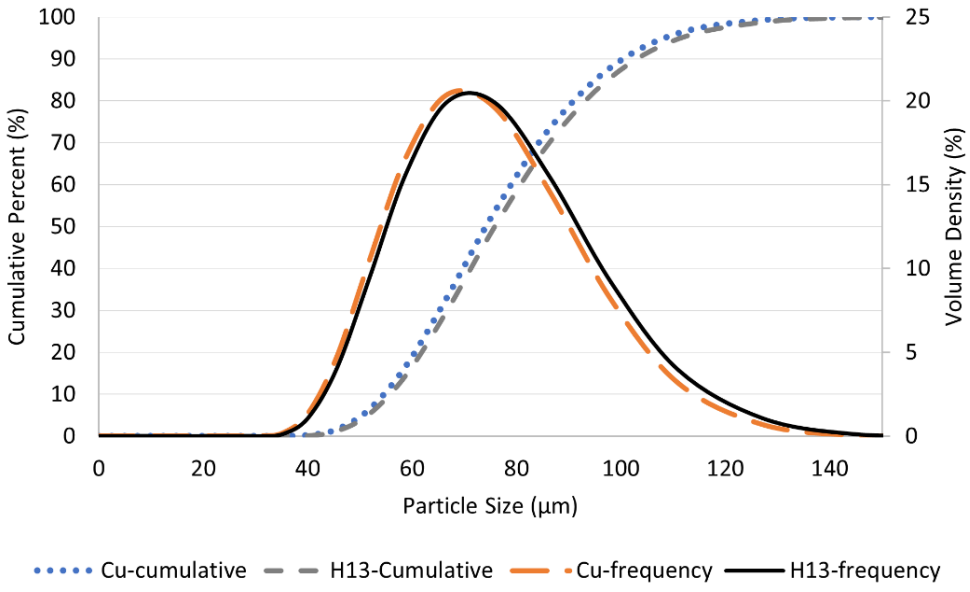

Figure 5.1: Particle size distribution (PSD) and volume distribution of the virgin gas-atomized H13 and OFHC Cu powders.

Field emission scanning electron microscopy (FE-SEM; model S4700, Hitachi High Technologies, Tokyo, Japan) was used to characterize the morphology of the virgin powder and printed samples; operating with an accelerating voltage, Vacc, of 5 kV and a beam current, Ie, of 20 μA. EDS analysis of the printed samples was conducted at an accelerating voltage of 5 kV to distinguish between Fe and Cu using the Lα X-ray.

Crystallographic phase evaluation was conducted using XRD (Bruker D-8 Advance Bruker Corp., Billerica, MA, USA) operating at 35 kV and 27 mA with CoKα radiation and a Fe filter. A step size of 0.02° and a time per step of 0.5 per second over a range of 20 – 130° for 2θ was used. The sample was cleaned with acetone before being placed in the sample holder.

The substrate material for this study was wrought annealed H13 purchased from Hudson Tool Steel Corporation (Rockford, IL, USA), with dimensions of 152.4 mm x 152.4 mm x 12.7 mm. The surface for deposition was roughened using glass beads (Blast-O-Lite) with a mesh size of 60 – 120. The composition of the substrate and powders were determined with inductively coupled plasma optical emission spectrometry (ICP-OES; model Vista-PRO, Varian Inc., CA, USA), with an internal calibration standard (scandium). The carbon content was determined using a carbon-sulfur combustion analyzer (model CS2000, Eltra GmbH, Haan, Germany) following the ASTM Standard E1941-10: *Standard Test Method for Determination of Carbon in Refractory and Reactive Metals and Their Alloys by Combustion Analysis*. The ICP-OES and carbon content analyses were conducted three times to obtain an average listed in Table 5.1 along with the associated AISI compositional standard for H13 tool steel.

Table 5.1: Chemical composition of raw materials used for printing FGMs of H13-Cu and blending for DSC trials.

Designation	Composition (wt.%)						
	C	Si	Mn	Cr	Mo	V	Cu
AISI H13	0.32 - 0.45	0.8 - 1.2	0.2 - 0.5	4.75 - 5.5	1.1 - 1.75	0.8 - 1.2	-
ASTM C110	-	-	-	-	-	-	99.99
Virgin H13 powder	0.372	1.02	0.42	5.74	1.46	1.05	-
Virgin Cu powder	-	-	-	-	-	-	99.99
H13 - Substrate	0.39	0.63	0.30	4.73	1.37	0.80	-
C110 Substrate	-	-	-	-	-	-	99.99

5.3 DED System Parameters and Sample Geometries

In this present investigation, the DED equipment was a 3-axis LENS^{TM} 500 hybrid controlled atmosphere (Optomec, NM, USA) system, using a fiber laser (nLIGHT, WA, USA) with a 1080 nm wavelength combined with a back-reflection protection system. Listed in Table 5.2 are the operating parameters for the DED equipment.

A baggy test was used on the virgin powder to determine the RPMs required for printing. This was done by weighing bags of captured powder at various RPMs for two minutes at each varying RPM settings. From this initial test, the corresponding g/min could be determined by plotting the results and applying a linear trendline. The calculated g/min along with the estimated weight percent's (wt%) are listed in Table 5.3. Both virgin powders used the same RPM's due to the close rheological properties.

Table 5.2: DED system parameters for printing H13, Cu, and varying blends of H13-Cu onto a wrought annealed H13 substrate.

Parameter	Value	Units
Laser Power	-	W
Scan Speed	400	mm/min
Feed Rate	-	g/min
Powder Delivery Gas (Ar)	2	L/min
Hatch Spacing	0.381	mm
Layer Thickness	0.254	mm
Spot Size	600	µm
Nozzle Stand-Off	9.525	mm
Hatch Orientation*	0, 90, 0, 90	°

Six different H13-Cu compositions were blended using the multi-powder feeder set up on this DED system. The laser powers for printing on the wrought H13 substrate ranged from 400 – 500 W, with 25 W increments, resulting in a total of five different power conditions. Due to the reflectivity issues of printing on a pure Cu substrate, higher powers and slower scanning speeds were required. Laser powers for printing on the pure Cu substrate ranged from 850 – 950 W, with increments of 25 W, using a constant scanning speed of 127 mm/min at each power level. This again resulted in five different power conditions. A second printing condition was investigated on a reduced pure Cu substrate size, with dimensions of 76.2 mm x 76.2 mm x 12.7 mm. The new Cu substrate was preheated using the DED laser to raster a 63.5 mm x 63.5 mm area on the substrate surface with a constant laser power of 300 W, a hatch spacing of 0.381 mm, and a scanning speed of 127 mm/min. Laser powers of 700 – 950 W with 50 W increments were investigated on the preheated Cu substrate, totaling six different power conditions.

Table 5.3: Powder feeder RPMs and corresponding approximated weight percentages (wt%) of H13 and Cu powders.

RPM (H13)	≈ wt% (H13)	≈ wt% (Cu)	RPM (Cu)
0	0	100	3.5
0.75	24	76	2.75
1.5	42	58	2
2	55	45	1.5
2.75	75	25	0.75
3.5	100	0	0

5.4 Sample Geometry

There were three different sample geometries examined in this study. This included single layer and 3-layer tracks 25 mm in length, used to analyze bonding characteristics to the wrought H13 and Cu substrates using the six different H13-Cu compositions. Lastly, a rectangular FGM was printed with programmed dimensions of 5 mm x 25 mm x 25 mm, with the six different compositions changing every 16 layers in the z-direction.

5.5 DSC Analysis of H13 and Cu Powder Blends

Varying powder blends were investigated on pure Cu and H13 powders using differential scanning calorimetry (DSC) analysis to understand the solidification behavior. Cu has a low melting point (*i.e.,* T_m = 1085°C) compared to that of H13 tool steel (*i.e.,* T_m = 1427°C) which is near the safe operating temperature of the system. Measurements were conducted using a Netzsch Jupiter® STA 449 F1 Simultaneous Thermal Analyzer

(differential scanning calorimetry and thermogravimetric analysis) with a SiC furnace using an Al_2O_3 (Advalue Technologies, Inc.) crucible. The highest heating and cooling rate of 20 °C/min was used to simulate as closely as possible AM non-equilibrium conditions. Loose, pre-blended powder samples were made to the desired compositions using the powder mentioned previously and mechanically blended for 30 mins to ensure complete mixing. Eight powder compositions were examined, listed in Table 5.4, beginning with pure Cu then H13-Cu blends of increasing Cu-content.

Table 5.4: DSC trial compositions, sample weights, and corresponding identification numbers.

Run	H13 (wt%)	Cu (wt%)	Total Weight (mg)
A	95	5	153.77
B	75	25	147.99
C	62.5	37.5	147.58
D	50	50	148.08
E	37.5	62.5	148.49
F	25	75	148.05
G	12.5	87.5	148.86
H	-	100	149.97

A pure H13 analysis was attempted but the system was unable to properly resolve the peaks as the melting point exceeded the safe operating conditions. The peaks for heating and cooling are identified from left to right (*i.e.,* Peak 1 is the left most peak and Peak 4 is the right most peak). Two sets of temperature ranges were examined for the varying compositions: a partial melt to 1200°C and melt to 1477°C followed by immediate cooling. For the EDS analysis of the DSC samples, an accelerating voltage of 20 kV and

a beam current, Ie, of 15 μA, was used to ensure sufficient excitation (Kα X-ray) of all the elements in the material system, with the only exception being Mo, which used the Lα X-ray for identification.

5.6 Results and Discussion

5.6.1 DSC H13 and Copper Powders

There was a large variety in the DSC microstructures due to the large composition range examined. All the H13-Cu blended samples showed a clear separation of the Fe-rich and Cu-rich zones. The 25 wt%, 37.5 wt% (Figure 5.2(a)), and 50 wt% Cu samples consisted of a semi-cohesive circular H13 center with cellular dendritic structures on the edge extending into the surrounding Cu-rich matrix. The H13 center had randomly distributed Cu-rich zones. A similar microstructure was observed by *Ishida* [170], and noted that the diffusion of Cu into Fe at temperatures between 1100 – 1200°C was at grain boundaries. Whereas, at temperatures between 1300 – 1400°C solid solution diffusion dominates. A noticeable change in the microstructure appears when the Cu composition is increased to 62.5 wt% and 75 wt%, which consists of H13 dendrites randomly distributed throughout the Cu-rich matrix, as shown in Figure 5.2(b). Finally, at 87.5 wt% Cu (Figure 5.2(c)), the microstructure consisted of a spherical H13 center with Cu-rich zones inside surrounded by the Cu-rich matrix. The circular structure consisted of a continuous solid band on the edge, however the inside was not cohesive as previously observed with small amounts of eutectic structures, Cu-rich pockets, and dendrites extending into the Cu-matrix. Alloys with a miscibility gap are known to form these globule structures [171].

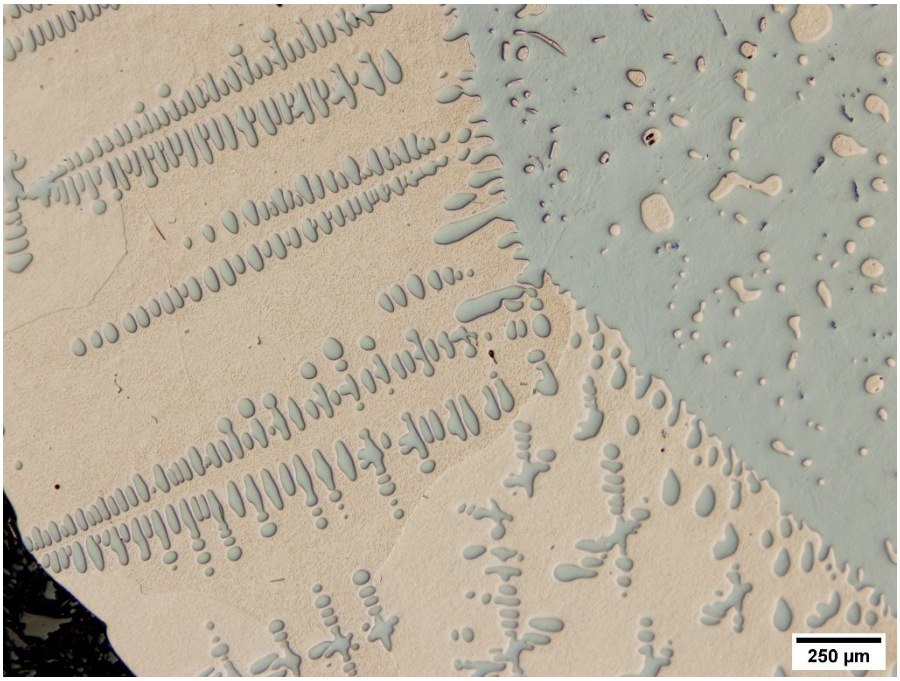

(a)

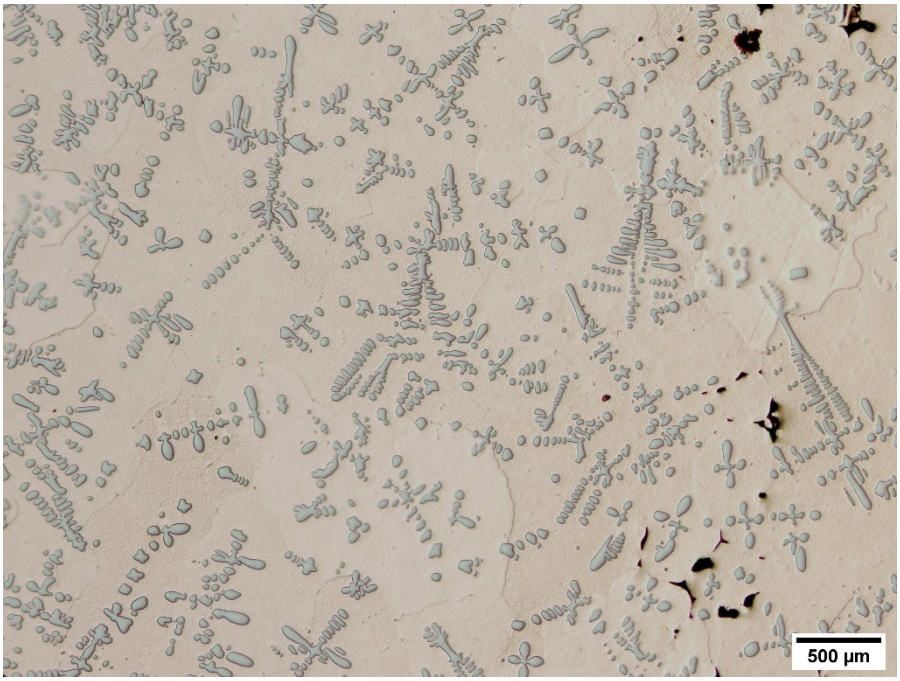

(b)

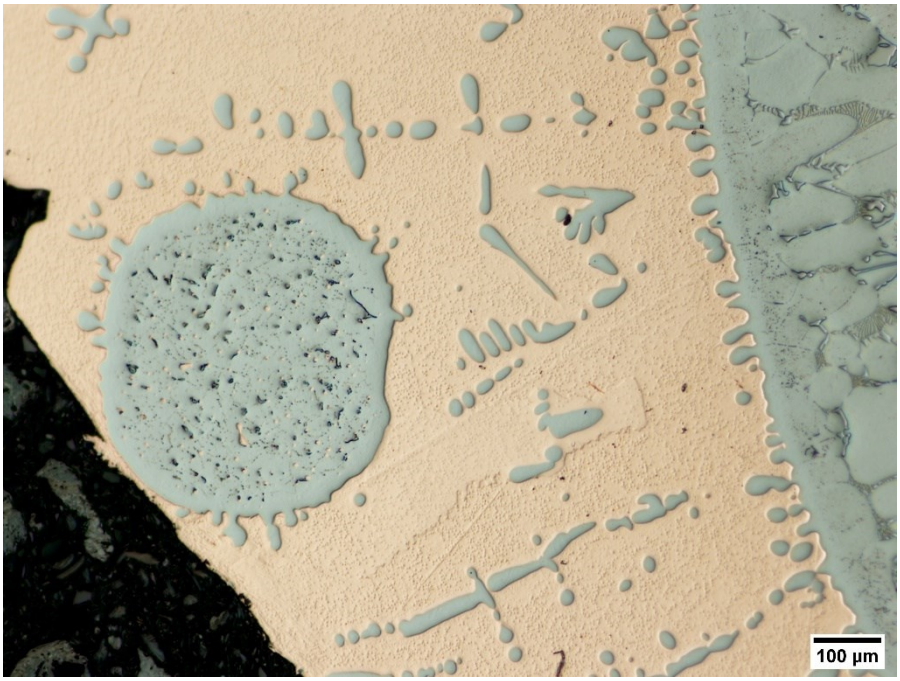

(c)

Figure 5.2: Unetched optical cross-section micrographs of 37.5 wt% Cu (a), 62.5 wt% Cu (b), and 87.5 wt% Cu (c) from a full DSC melt to 1477°C.

From EDS analysis in Figure 5.3, the Cu-content range was estimated from 3.62 – 13.89 wt%. Higher Cu wt% were estimated in the H13-rich solid for certain points during the EDS analysis, but this can be attributed to the interaction volume accounting spreading into the Cu-rich matrix. The maximum Cu concentration agrees with the Fe-Cu phase diagram as γ-Fe can accommodate 13 wt% Cu [44]. In the eutectic structure, the EDS analysis in Figure 5.4, suggested that the Cu wt% was approximately 3.62 wt%. This is slightly higher than the reported maximum solid solubility of α-Fe which reaches 2.2 wt% Cu [44].

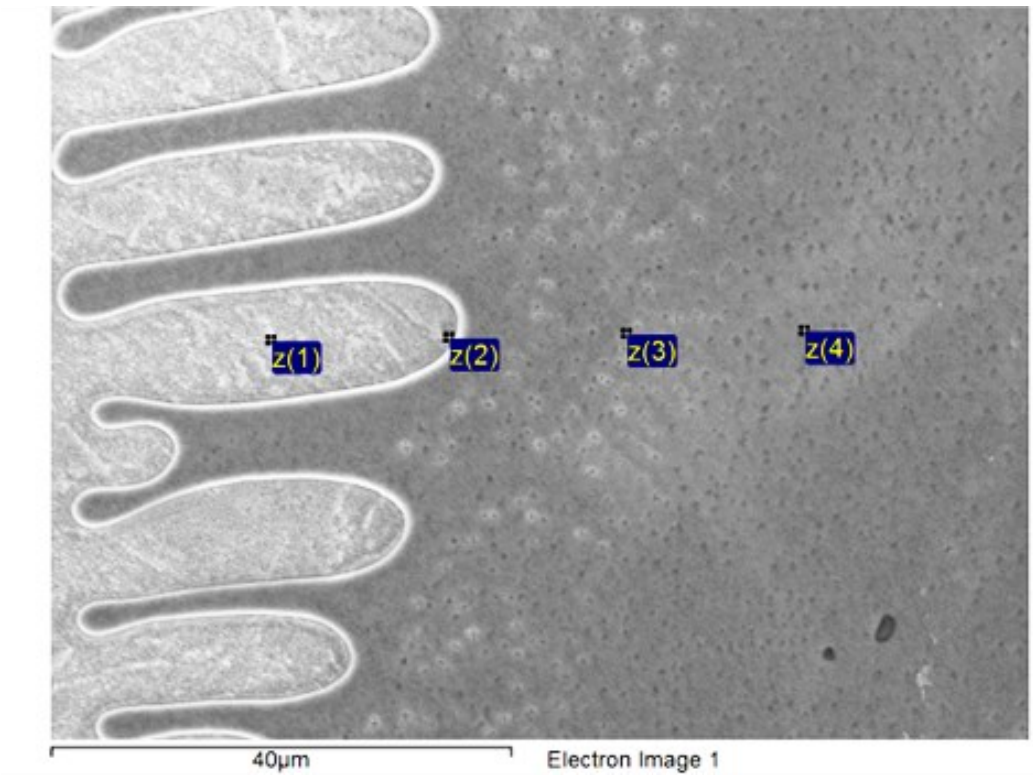

Point	Composition (wt %)							
	Fe	**C**	**Si**	**Mn**	**Cr**	**Mo**	**V**	**Cu**
1	68.33	9.24	0.47	0.10	3.20	0.22	0.32	18.12
2	73.27	8.31	0.69	0.12	3.30	0.21	0.21	13.89
3	1.25	11.26	-0.06	0.14	0.02	-0.01	-0.01	87.41
4	1.22	10.56	-0.04	0.16	0.09	0.01	0.01	87.98

Figure 5.3: EDS analysis of 62.5 wt% Cu sample from the full DSC melt to 1477°C with the corresponding table of the composition of the analyzed points recorded in wt%.

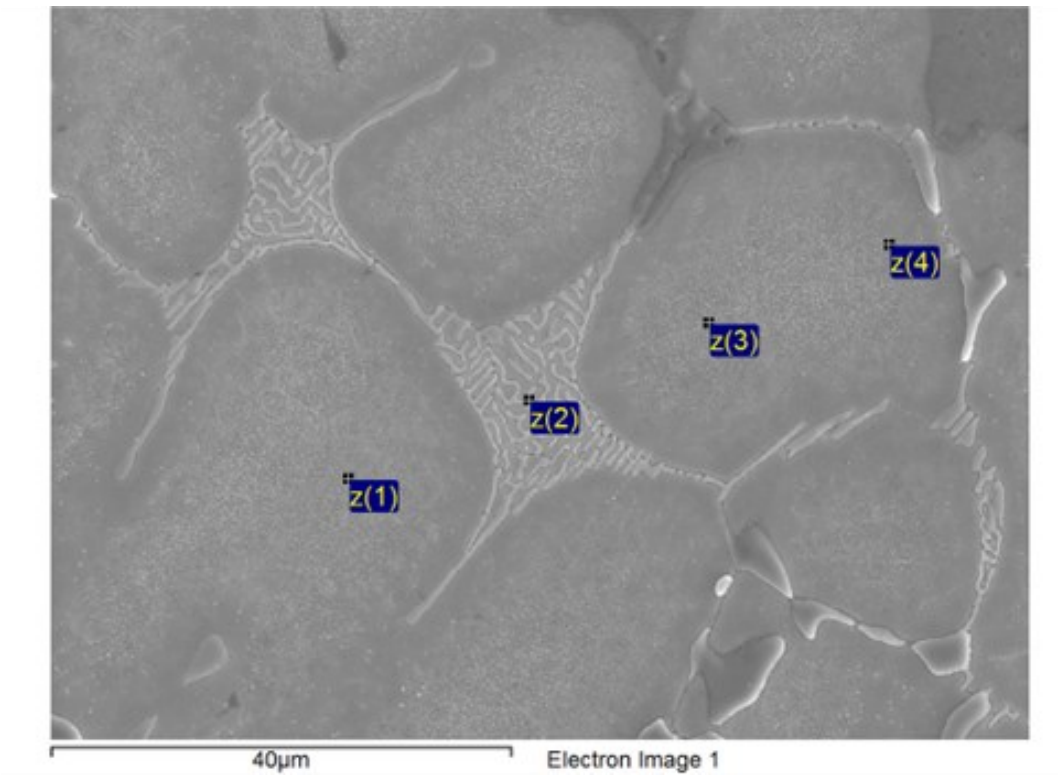

Point	Composition (wt %)							
	Fe	C	Si	Mn	Cr	Mo	V	Cu
1	74.15	8.23	0.54	0.09	4.78	3.10	1.47	7.66
2	58.26	12.19	0.50	0.09	8.50	13.99	2.85	3.62
3	73.30	8.67	0.51	0.07	4.53	2.91	1.62	8.38
4	73.65	8.40	0.52	0.07	4.80	3.18	1.48	7.90

Figure 5.4: EDS analysis of 87.5 wt% Cu sample from the full DSC melt to 1477°C with the corresponding table of the composition of the analyzed points recorded in wt%.

The microstructures in the interrupted melt DSC runs, consist of unmelted H13 particles with dissolution at the edges indicating solid-state diffusion was beginning, highlighted in Figure 5.5(a).

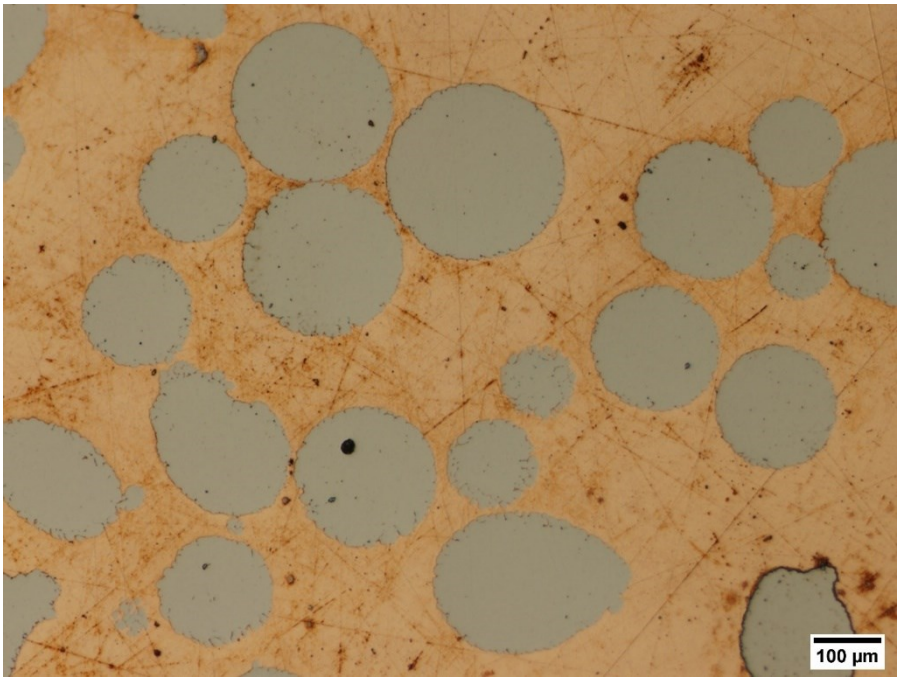

(a)

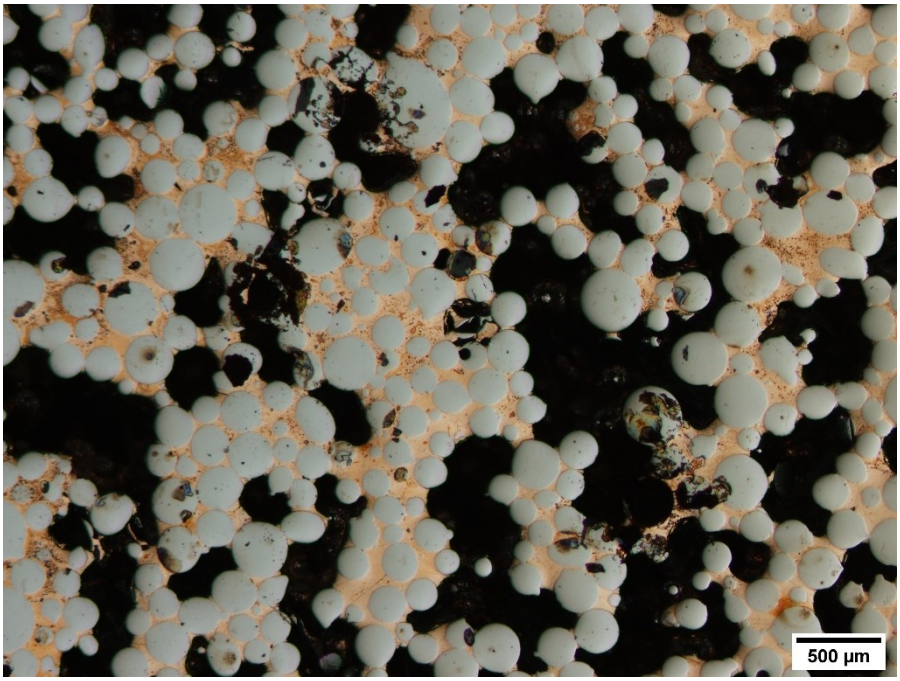

(b)

Figure 5.5: Unetched optical cross-section micrograph of 62.5 wt% Cu (a) and 25 wt% Cu (b) from an interrupted melt to 1125°C.

However, greater dissolution of smaller H13 particles was seen, with particles beginning to dissolve. At low Cu-concentrations (Figure 5.5(b)), H13 particles were held together in pockets connected by Cu bridges. As the Cu-content increased the sample was more consolidated as there was a great amount of liquid copper. From the DSC heating traces in Figure 5.6, two peaks are seen before the onset melting point of pure Cu, which appears to be at 1074°C, slightly lower than the melting point with this error being attributed to system accuracy and selection of the peak. Referring to the phase diagram generated using Thermo-Calc software by *Besler et al.*, these first two peaks are likely the dissolution of alloy carbides [136]. The initial liquid to start forming is expected to be from the Cu, starting at ≈ 1085°C (*i.e.,* melting point of pure Cu). In the dilute H13-5Cu sample (Run A), the Cu-peak is visible but is considerably diminished compared to the higher H13-Cu blends. Interestingly, the H13-rich peak is distorted compared to the other traces and is likely due to the H13 having a high melting point that the system is unable to handle resulting in inaccurate readings. As the Cu-content increases, the peak begins to increase in area indicating that the initial amount of liquid forming has increased and has a double peak which is not observed on the pure Cu sample, while the H13 peak diminishes in area. The enthalpy values for the full melt upon heating and immediate cool are listed in Table 5.5 and Table 5.6 respectively.

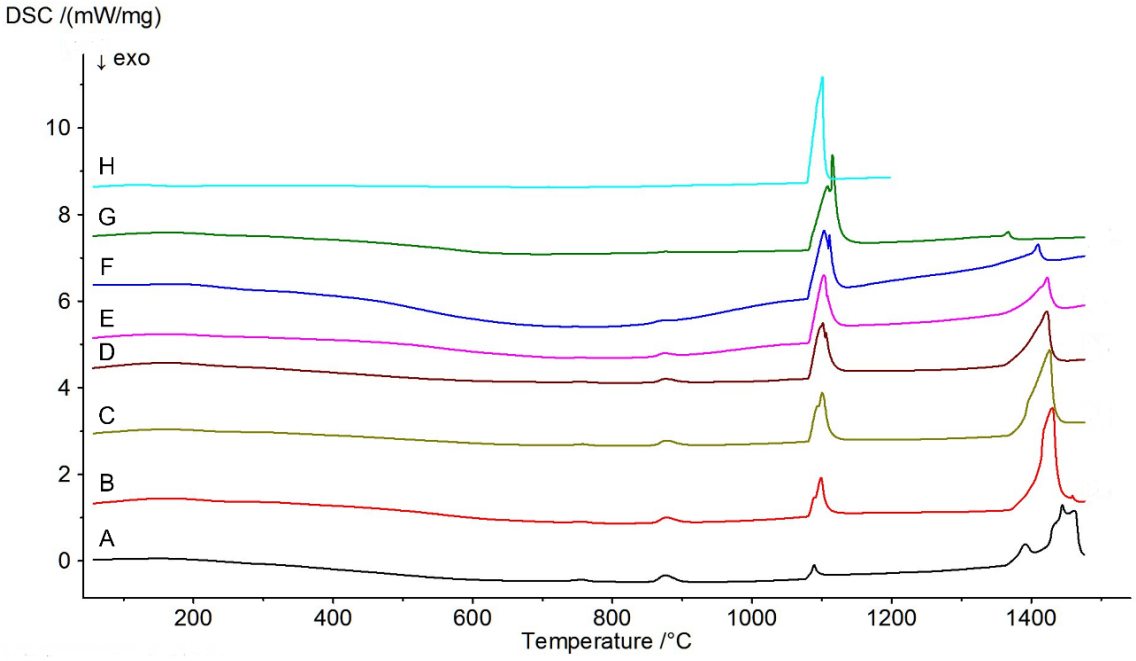

Figure 5.6: DSC traces of the various powder blends (Runs A – G) and heated to 1477°C and pure Cu (Run H) heated to 1200°C.

Table 5.5: DSC enthalpy full melt values upon heating of H13-Cu of varying compositions (absolute values). Peaks are identified from left to right.

Run	Peak 1 (J/g)	Peak 2 (J/g)	Peak 3 (J/g)	Peak 4 (J/g)
A	2.8	11.7	9.4	160.4
B	1.1	8.4	40.7	190.0
C	1.0	8.4	62.5	156.5
D	1.1	5.9	79.2	108.0
E	0.7	4.2	89.8	64.8
F	0.1	0.2	105.8	28.6
G	-	1.3	135.8	3.6
H	-	-	102	-

Due to the limitations of the system used, a rapid quench is not possible to simulate AM non-equilibrium conditions, but the analysis still provides useful information into the H13

and Cu solidification behavior. The cooling DSC traces of the full melt are plotted in Figure 5.7. On the cooling curves, there is a noticeable double peak occurring for the 5 wt% Cu (Run A) and 25 wt% Cu (Run B) which is diminished with increasing Cu-content. The starting temperature for the 5 wt% Cu trace shows the H13-rich peak (Peak 2) beginning at the highest temperature of 1442°C. As the Cu-content increases the H13 peak decrease in area and shifting closer to the Cu-peak (Peak 1) which increases in area, lowering the melting point of H13. The Cu-peak is not resolved in the 5 wt% Cu sample meaning it is likely in solid solution.

Comparing the enthalpy values of the interrupted traces upon heating listed in Table 5.7, the Cu-rich peak areas are lower than the full melt (*i.e.,* Peak 3). This is due to less time for dissolution of H13. As well, the enthalpy values measured upon immediate cooling of the interrupted melt are lower than the full melt traces (*i.e.,* Peak 1) due to the decreased dissolution of H13 during heating. Only one peak will be resolved during the interrupted trials because the maximum programmed temperature of 1125°C is considerably lower than the melting point of H13.

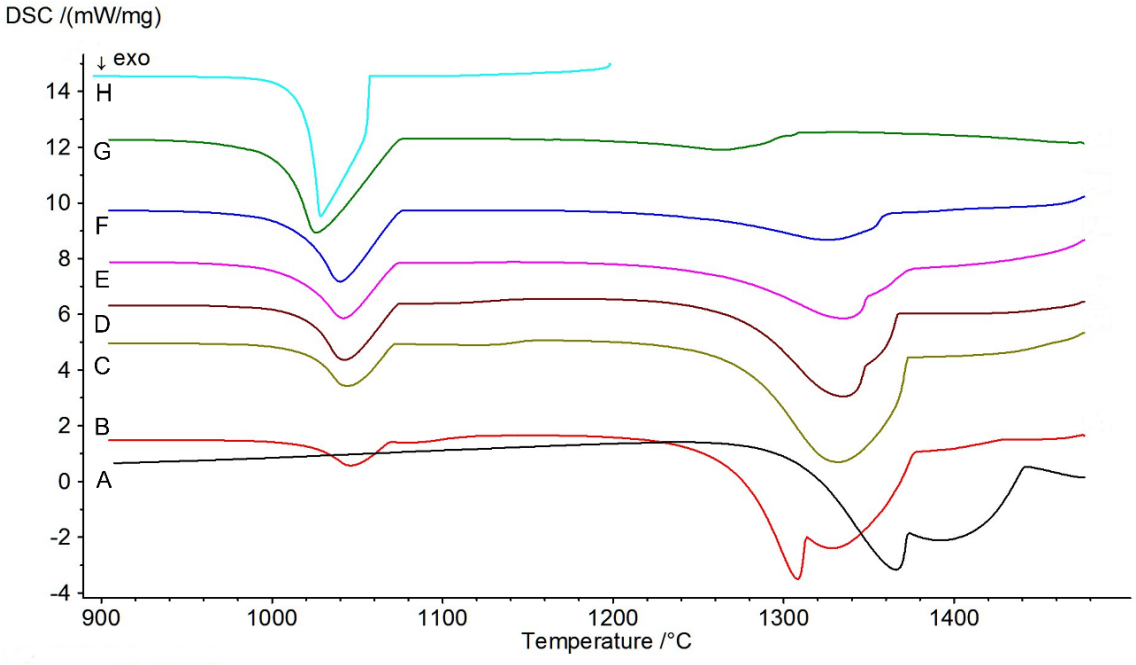

Figure 5.7: DSC traces of various powder blends (Runs A – G) immediately cooled from 1477°C and pure Cu immediately (Run H) cooled from 1200°C.

Table 5.6: DSC enthalpy full melt values upon immediate cooling of H13-Cu of varying compositions (absolute values). Peaks are identified from left to right.

Run	Peak 1 (J/g)	Peak 2 (J/g)
A	-	148.4
B	30.0	178.8
C	48.6	130.7
D	65.1	91.6
E	72.6	64.8
F	94.6	49.0
G	121.1	21.08
H	110.0	-

Table 5.7: Enthalpy values for interrupted DSC melt to 1125°C upon heating and immediate cooling of H13-Cu of varying compositions (absolute values).

Run	Heating (J/g)	Cooling (J/g)
B	35.8	23.9
C	51.3	34.3
D	64.3	66.4
E	75.6	74.0
F	86.7	85.6
G	94.2	94.0

As the Cu is mixed with H13, the melting point starts to increase due to some alloying. EDS analysis suggests that this is occurring. Referring to the Fe-Cu phase diagram, the melting point increases slightly with the addition of Fe. For simplification, the H13-Cu thermodynamic behavior appears to be following that of the binary Fe-Cu phase diagram. Plotting the change in temperature (Δ°C) of the peak's onset and end temperatures from the cooling traces shown in Figure 5.8, there is a maximum of Δ°C = 154.3°C in the H13-rich peak with 25 wt% Cu. The large solidification range will promote solidification cracking. The H13-rich peaks over the varying Cu-contents begin to decline until it reaches a sudden increase at a concentration of 75 wt% Cu. The Cu-rich, Δ°C, has a gradual increase with increasing Cu-content with a notable dip occurring at a concentration of 50 wt% Cu. Finally, at 87.5 wt% Cu, both the H13-rich and Cu-rich Δ°C reach comparable values, with Δ°C = 69.4°C and Δ°C = 63.4°C respectively.

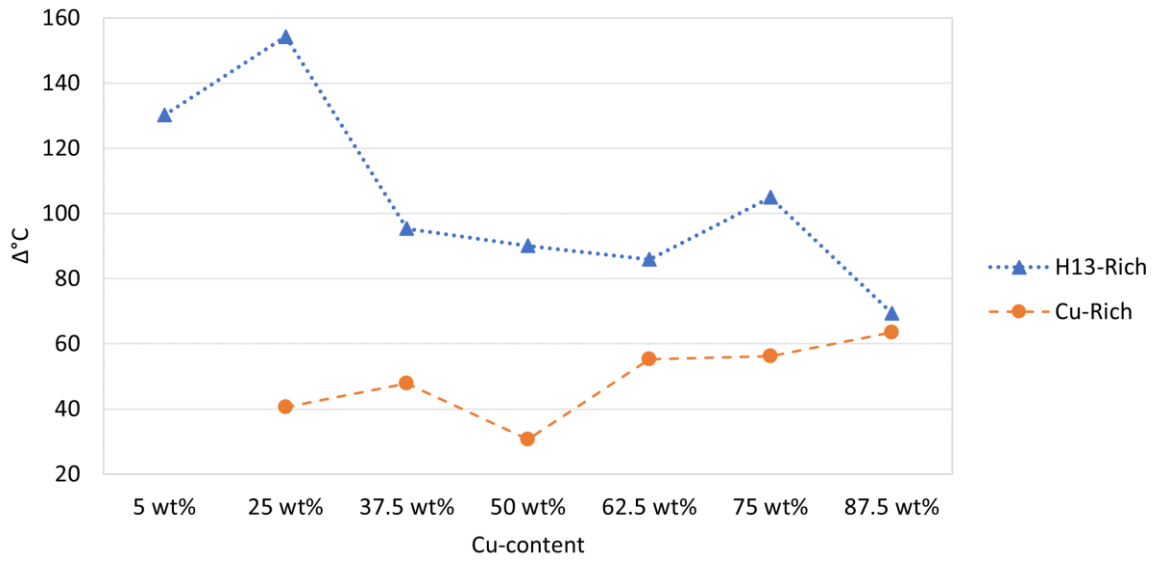

Figure 5.8: Change in temperature (Δ°C) of the start and end of H13-rich peak and Cu-rich peak upon immediate cooling during a full melt. The 5 wt% Cu-rich point is omitted because it was not resolved in the trace.

5.6.2 Single and 3-Layer Clad Sample Characterization on Wrought H13

Depositing single and 3-layer clads over the selected H13-Cu compositions showed no major bonding issues onto the H13 substrate upon visual inspection. There seems to be a wide range of available powers to deposit H13-Cu blends directly onto a steel substrate. Visual inspection of the tracks showed no cracking on the surface for the tested laser powers ranging from 400 – 500 W. In the single clad samples, visually there is no noticeable difference in the shape of the clad deposit with increasing laser power. Changes to the clad deposit are more obvious with the 3-layer samples. Looking at the profile of the 3-layer builds, the tracks show a rounded deposit at compositions of 100 wt% H13 and ≈ 25 wt% Cu. As the Cu-content is increased, the deposit flattens out slightly but is still rounded. The ≈ 100 wt% Cu clads had a noticeable change in the shape which appeared flattened out across all the examined laser powers.

All examined laser powers show significant mixing with the substrate when Cu was deposited onto the substrate. Referring to the work conducted by *Noecker* and *Dupont* [81], a range of cracking ≈ 5 – 43 wt% Cu, was determined that agrees with the results observed in the current study. Even though the higher copper contents should avoid the cracking, this issue was still encountered. The Cu compositions outside of the range did not experience cracking at the top of the clad with the issue situated below the deposit. This is due to the mixing with the substrate, causing the wt% of Cu to drop into the solidification cracking range.

Defects are in the lower region of the deposit, with it extending below the surface of the substrate. Penetration of Cu into the substrate is to be expected as the focus point of the laser is slightly below the surface to ensure sufficient melting. Additionally, Cu was observed to infiltrate along the grain boundaries under brazing conditions [172]. The major defect observed in both the single clad and 3-layer clad samples was centerline cracking at higher Cu compositions beginning at ≈ 45 wt%, highlighted in Figure 5.9 and Figure 5.10. Since the Fe-rich liquid will solidify first, as shown in the DSC analysis, combined with the low back-diffusion of Cu-Fe into the solid, this will lead to greater terminal liquid which follows the peritectic reaction according to the Fe-Cu phase diagram [81]. The vertical cracking seen in the cladded samples is indicative of solidification cracking [79], [173]–[177]. Similar failure mechanisms are seen in surface hot shortness with steels containing Cu [48]. When this microstructure is re-heated the lower melting element (Cu) will create thin liquid film between the grains reducing the mechanical integrity [178], [179]. In the cracks, Cu can be seen lining the edges, as shown in the EDS analysis, Figure 5.9(b), suggesting that this is the case. Since the Cu-

liquid is last to solidify, as confirmed by the DSC analysis, during solidification the steel is s contracting causing strain on the remaining liquid, resulting in a tear. The greater the solidification range is, the higher the susceptibility of cracking is [180], [181], as shown in Figure 5.8.

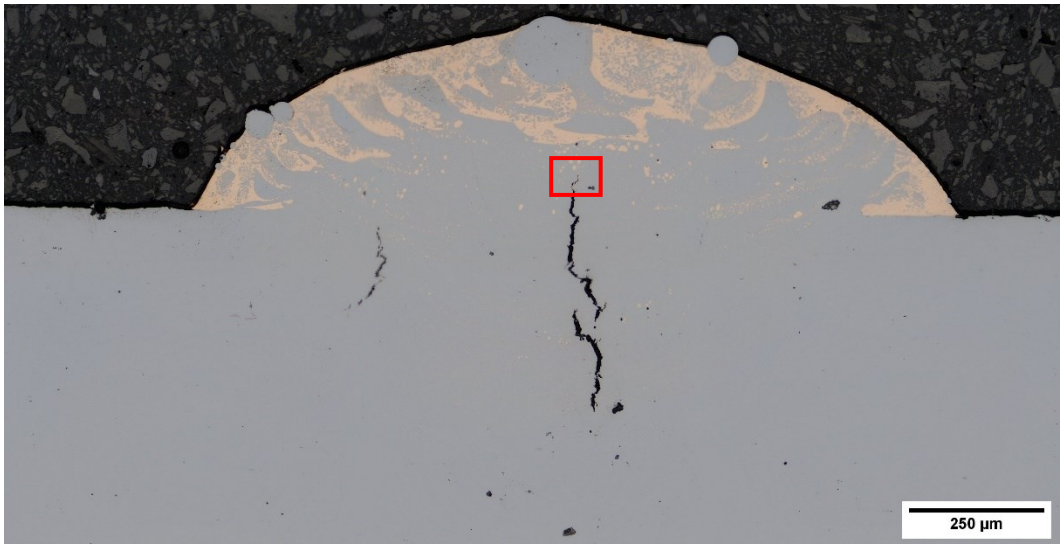

(a)

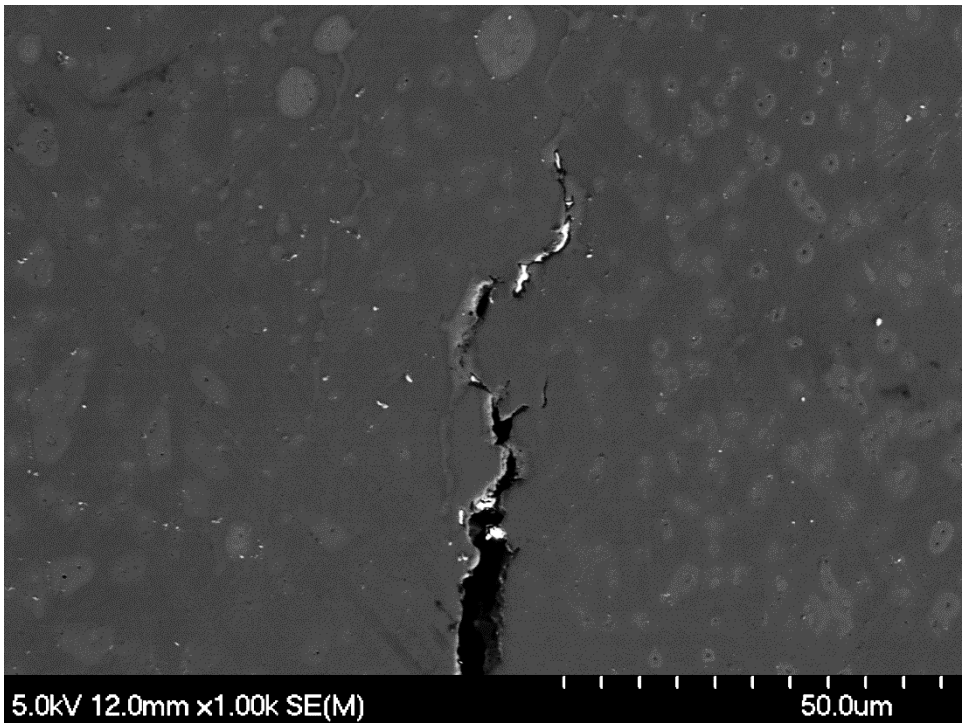

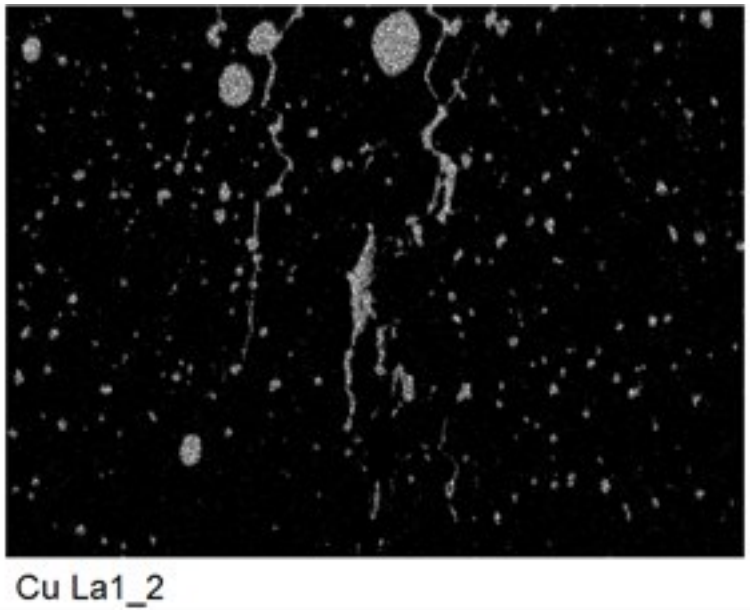

(b)

Figure 5.9: Unetched CLSM cross-section image of ≈ 45wt% Cu 3-layer clad processed at 500 W (a). EDS analysis of the crack suggesting Cu-rich phase is located along the edges (b).

The sharp transition of cladding copper directly onto ferrous-based alloys is difficult due to the lack of solubility, crystal structure mismatch, and coefficient of thermal expansion differences resulting in residual stresses and the promotion of cracking. Increasing the scanning speed may help reduce the dilution of Cu into the substrate, thereby reducing potential cracking and porosity issues [182].

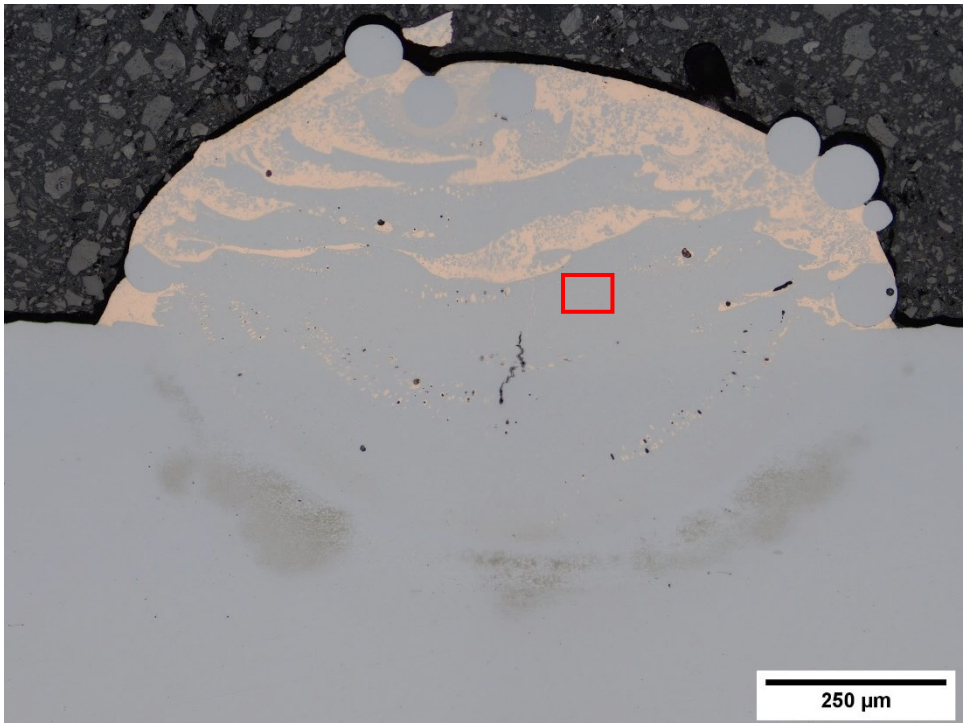

Figure 5.10: Unetched cross-section image using CSLM of ≈ 45 wt% Cu, 3-layer clad sample processed at 400 W. Large cracking due to solidification cracking can be observed at the centerline of the track. The red box indicates the area for Figure 5.11.

In all the copper containing samples, small pockets of Cu-rich zones can be observed with many of them containing pores. Looking at the SEM micrograph in Figure 5.11, there is micro-porosity at the inter-dendritic regions. In the cells, it appears that sub-

micron circular precipitates (white) have formed due to rapid solidification. These precipitates are ε-Cu and have been reported by another study [183]. The amount of Cu in γ-Fe reaches a maximum of 13 wt% under equilibrium conditions, but under rapid solidification this range has been reported to extend up to 35 wt% due to solute trapping [183].

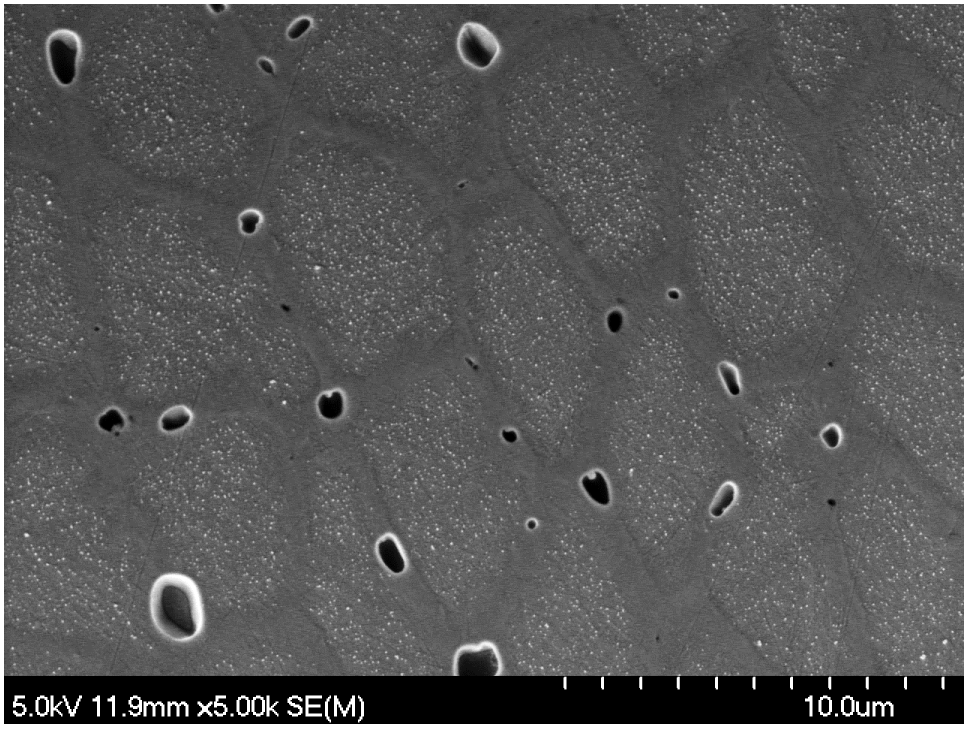

(a)

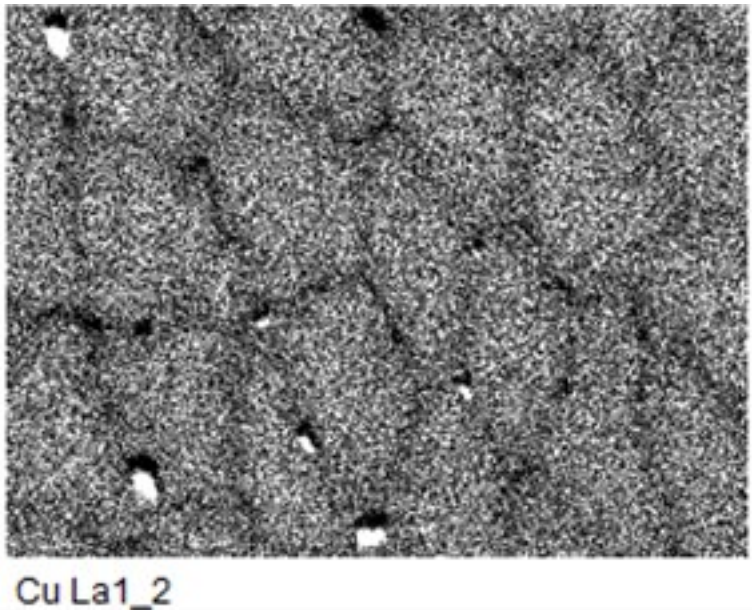

(b)

Figure 5.11: Unetched enlarged FE-SEM micrograph of the red box (Figure 5.10) of ≈ 45 wt% Cu,3-layer processed at 400 W with sub-micron ε-Cu precipitates (white) visible within the cells (a). EDS mapping suggests that the cells are Cu-rich as well as the surfaces of the pores (b).

This decreasing solid solubility with decreasing temperature will promote the formation of precipitates [184], with higher cooling rates producing finer particles. It is however more likely that liquid quenching is estimated to only extend the solubility of Cu up to ≈ 19 wt% [185]. *Yao et. al.* [186], reported that defect joints can be achieved when the amount of dissolved copper in the steel is low. EDS mapping of the cross-section of the 3-layer tracks processed at 400 W, (Figure 5.11(b)) suggests that the precipitates are Cu-rich. In the highest laser power setting (500 W), the sub-micron Cu-rich particles were not observed as seen in Figure 5.12, but consisted of isolated larger pockets of copper. The increased heat input would have slowed the cooling rate, leading to less Cu in solid solution of the Fe-rich matrix.

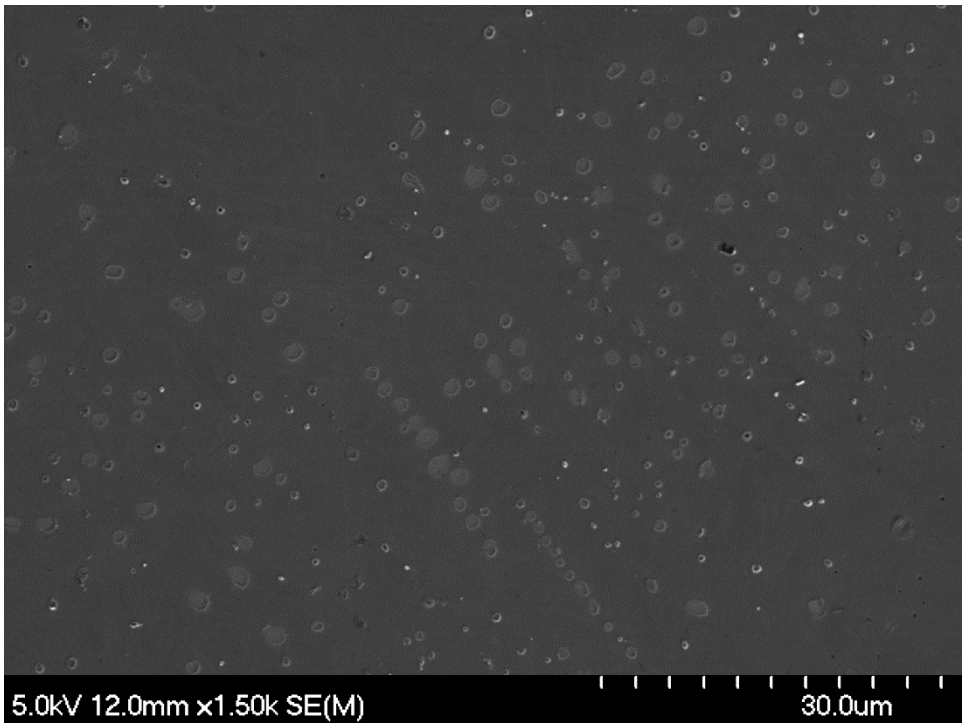

Figure 5.12: Unetched FE-SEM image of ≈ 45 wt% Cu, 3-layer clad processed at 500W sample highlighting Cu-rich pockets (light) in the H13-rich matrix.

5.6.3 H13-Cu FGM Rectangles Printed on Wrought H13

An FGM of H13-Cu was successfully deposited onto a wrought annealed substrate. Looking at the cross-section, the microstructure of the FGM rectangle samples exhibit varying microstructures as the composition changes in the build direction (+z) due to the large differences in Cu concentrations. At the substrate, where 100% was deposited with sound metallurgical bonding (Figure 5.13), the matrix consisted of a cellular dendritic structure with tempered martensite, as previously seen in the homogenously printed samples. There is some porosity in this region, likely attributed to the hatch orientation being set to 0°, 90°, 0°, 90°, the incorrect hatch spacing, different laser power distribution compared to the previous studies, or a combination of the three.

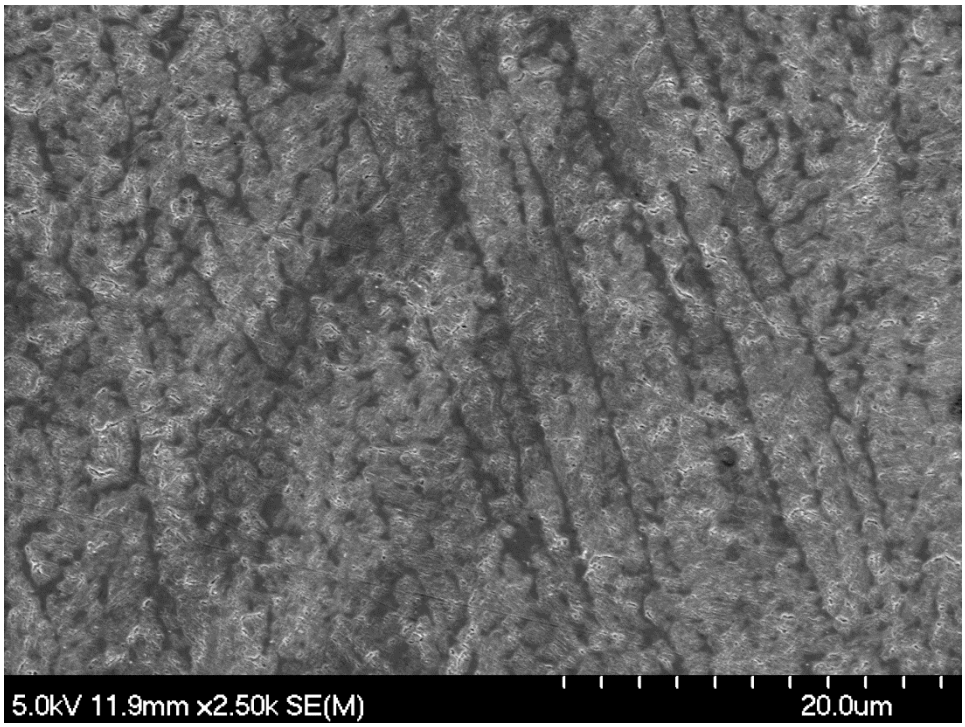

Figure 5.13: Etched FE-SEM micrograph of an H13-Cu FGM rectangle processed at 400 W in the 100 wt% H13 layer highlighting a cellular dendritic structure with tempered martensite.

Moving up to the ≈ 25 wt% Cu-layers, these layers consist of long columnar dendrites with tempered martensite, and isolated micro-porosity (Figure 5.14). This porosity issue aligns with Cu concentration for cracking to occur, as previously mentioned [81].

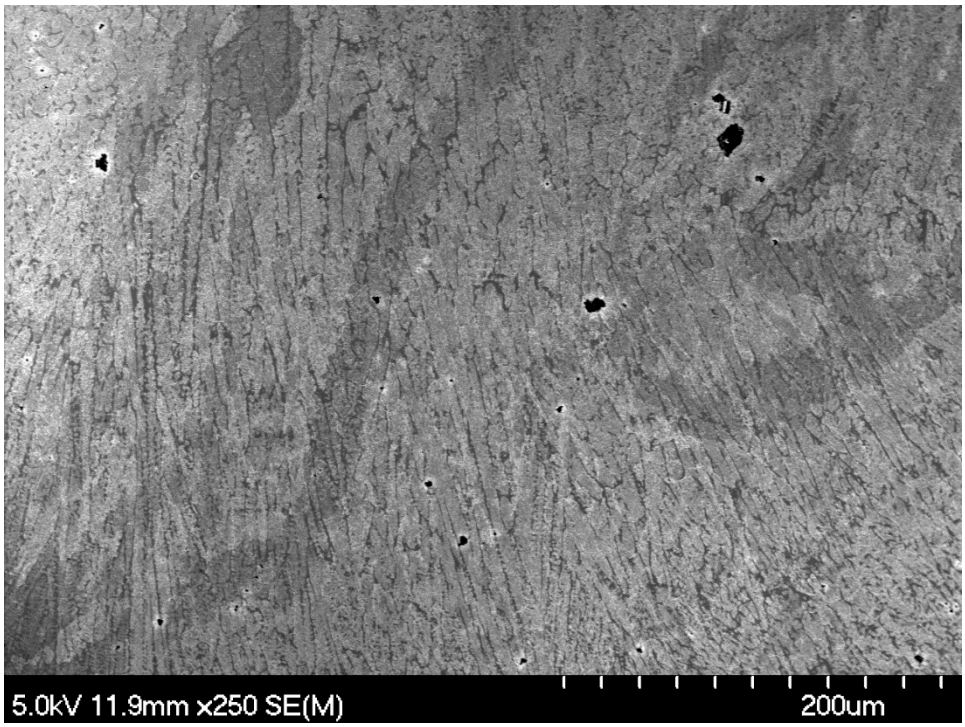

Figure 5.14: Etched FE-SEM micrograph of an H13-Cu FGM rectangle processed at 400 W in the ≈ 25 wt% Cu section highlighting long cellular dendrites and microporosity in the section containing.

In the section containing ≈ 45 wt% Cu, multiple different microstructures were observed along with large amounts of cracking and porosity. The cellular dendritic structure transitions to a highly refined martensite appearance as it approaches the Cu-rich zone due to rapid cooling aided by the high thermal conductivity of Cu as shown in Figure 5.15(a). In this region, the sub-micron Cu-precipitates are visible inside the dendrites, Figure 5.15(b), which were previously observed in the cladded sample. Increasing to the ≈ 58 wt% Cu region, a cellular dendritic structure of H13 with pockets of Cu were observed as shown in Figure 5.16. Even though this Cu-content lies outside the solidification cracking range, the complex mixing and separation due to the miscibility gap combined with the differences in the thermal coefficient of expansion of H13 and Cu will result in cracking and porosity. Some of the Cu-rich pockets are connected by thin

Cu trails in the inter-dendritic regions, as highlighted by the red arrow, which backfilled cracks during the peritectic reaction.

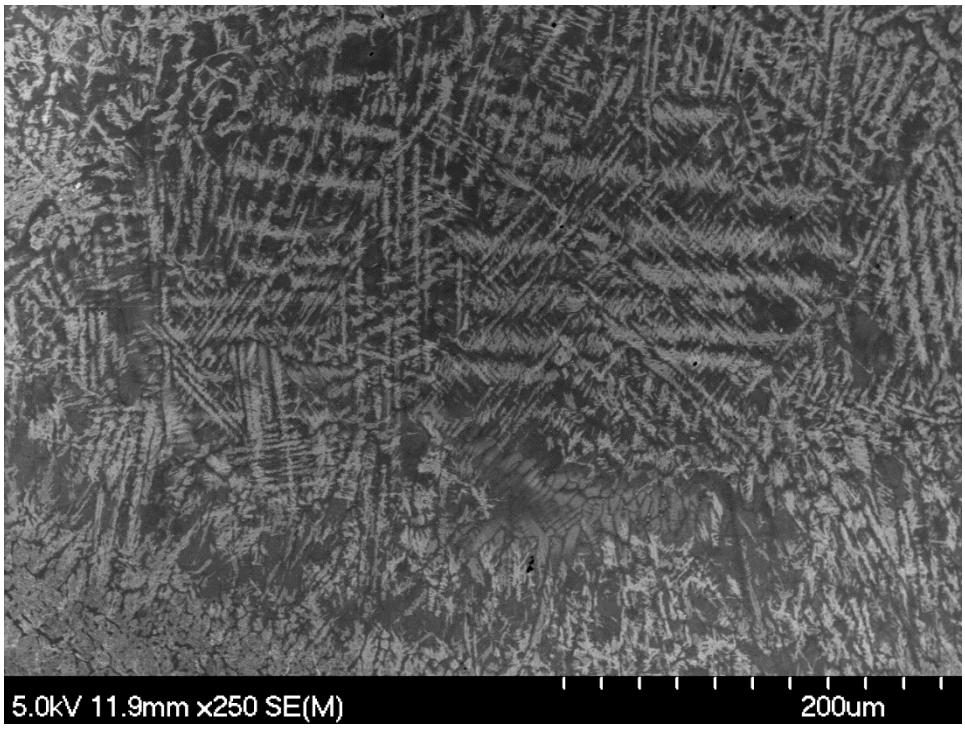

(a)

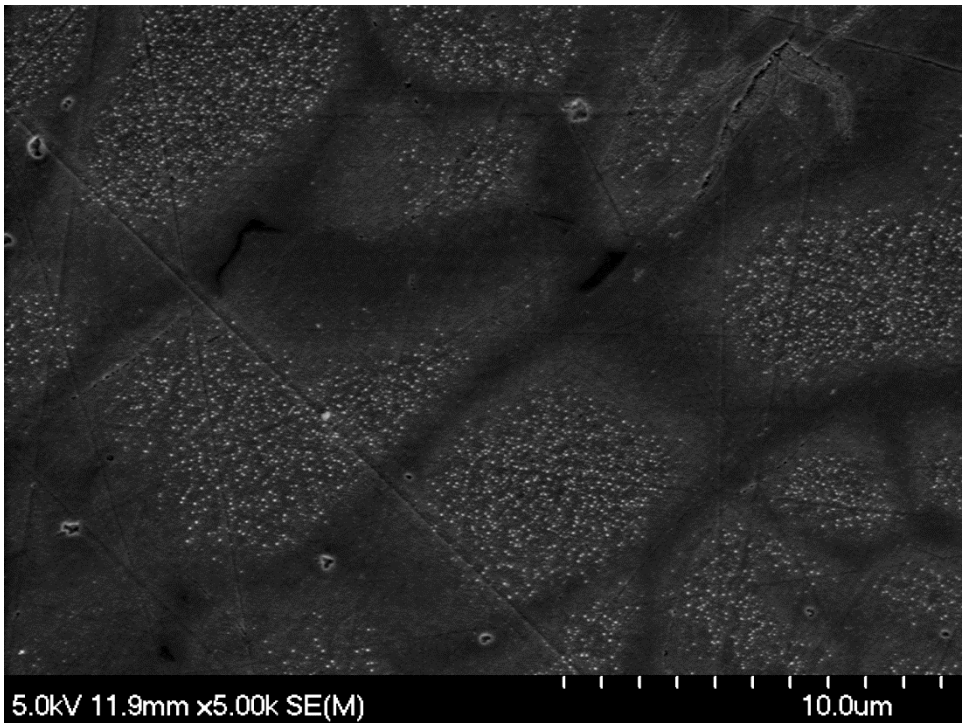

(b)

Figure 5.15: Etched FE-SEM micrographs of an H13-Cu FGM rectangle processed at 400 W in an ≈ 45 wt% Cu layer highlighting refined martensite (a) and sub-micron Cu-precipitates (b).

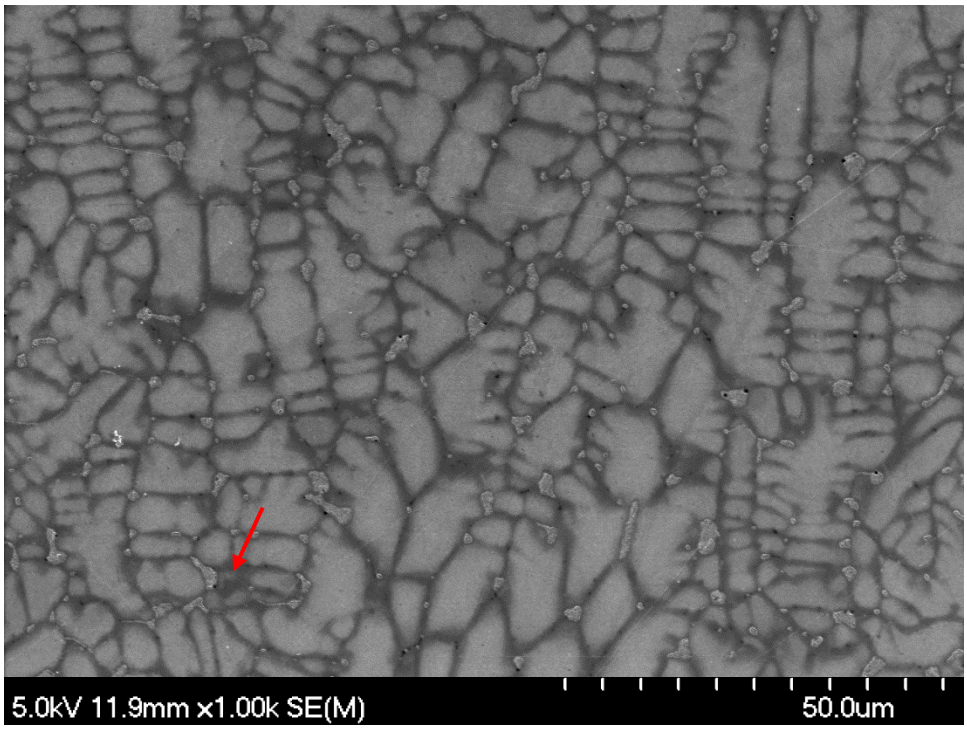

Figure 5.16: Etched FE-SEM micrograph of an H13-Cu FGM rectangle processed at 400 W in the ≈ 58 wt% Cu layer with the red arrow indicating a backfilled crack with terminal Cu-rich liquid.

In the ≈ 76 wt% Cu-layers, clear liquid separation is displayed as shown in Figure 5.17(a). This is induced by the rapid cooling into an miscibility gap, previously noted by *Chen et al.* [187]. At this composition, the high cooling rates promote the separation of the liquids mentioned previously. The shape of the H13-rich zones in the clad deposit follows the direction of the scan direction. The Fe-rich zones have a cellular dendritic structure with Cu-rich pockets inside. Also located in this region are randomly dispersed H13 particles in the Cu-matrix. Figure 5.17(b) shows some of the partial H13 particles surrounded by an H13-Cu alloyed outer shell, as suggested by EDS. The dissolution of some of the particles is similar to the interrupted DSC runs. The intended 100 wt% Cu-layers resemble the previous ≈ 76 wt% Cu-layers due to residual H13 particles still in the

powder delivery lines. H13 globules and small spherical particles are situated in a Cu-rich matrix (Figure 5.18) which was also observed by *Liu et al.* [188].

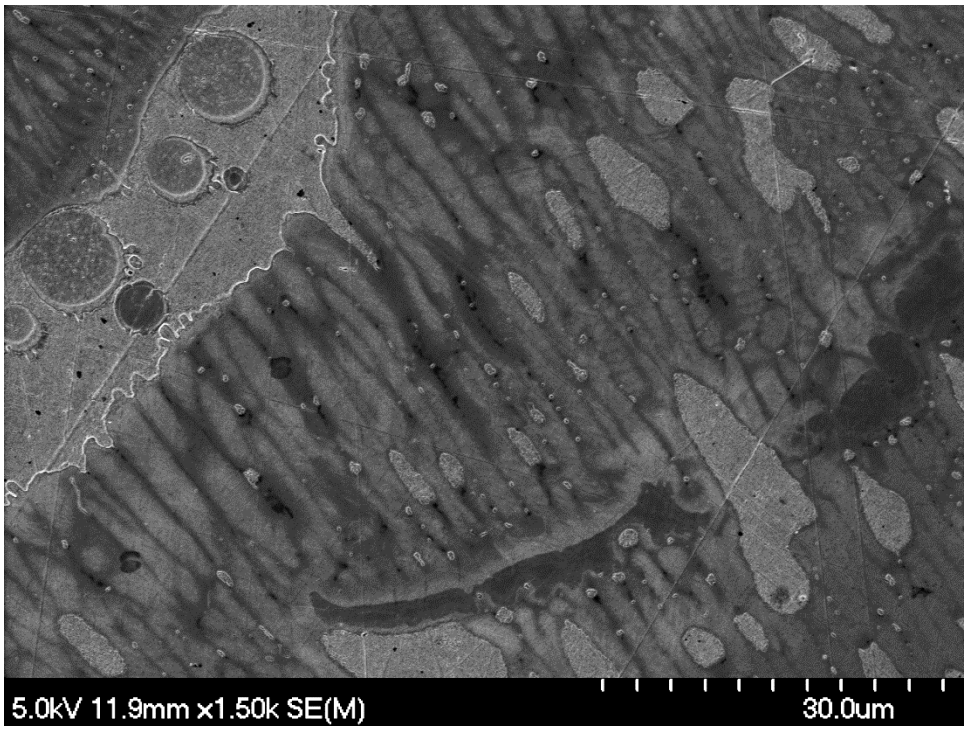

(a)

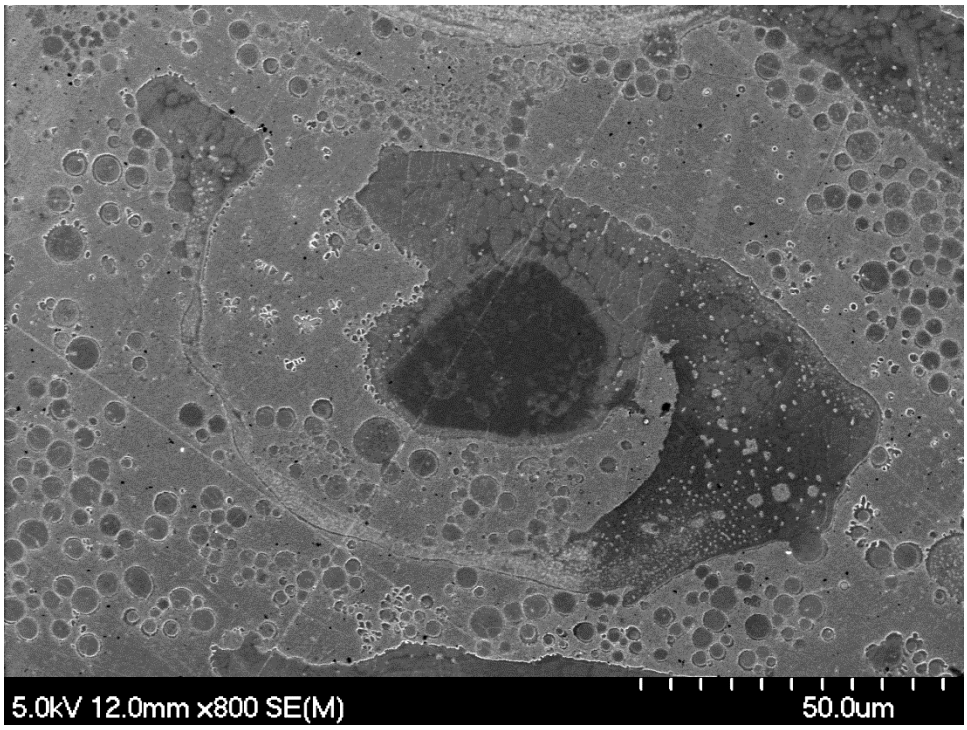

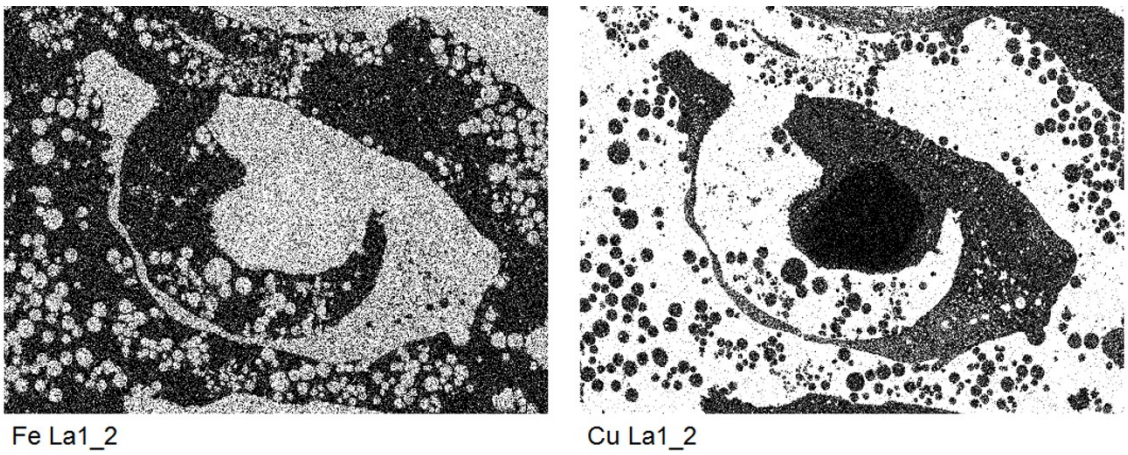

(b)

Figure 5.17: Etched FE-SEM micrograph of FGM rectangle processed at 400 W in the ≈ 76 wt% Cu layer (a) and EDS analysis indicating alloying between H13 and Cu (b).

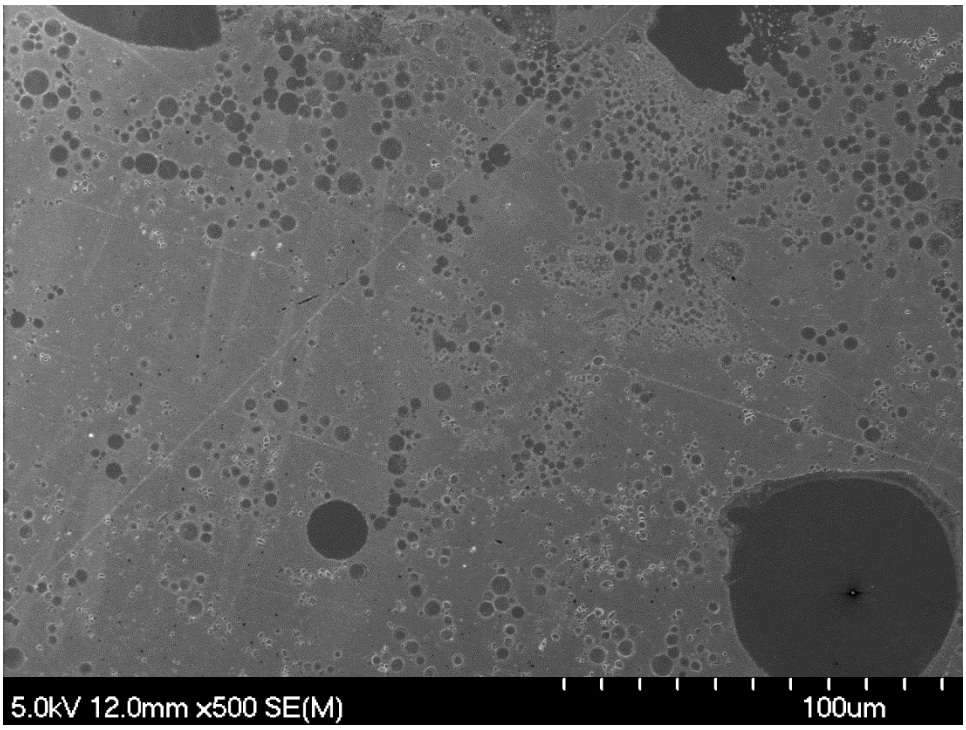

Figure 5.18: Etched FE-SEM micrograph of FGM rectangle processed at 400 W in the ≈ 100 wt% Cu layer

XRD analysis of the cross-sections of the FGM samples processed at 400W (Figure 5.19(a)) and 460W (Figure 5.19(b)), detected ferrite (α), martensite (α'), retained austenite (γ), Cu, $Cu_{0.4}Fe_{0.6}$, and $Cu_{0.99}Fe_{0.01}$. At 2θ = 50°, austenite, Cu, $Cu_{0.4}Fe_{0.6}$, and $Cu_{0.99}Fe_{0.01}$ appear to be overlapping suggesting that there was alloying. As well, Cu is a known austenite stabilizer [189] and has increased solubility in austenite. In the XRD trace for the sample processed at 460 W, the 2θ = 52° shows a higher relative intensity of ferrite, since the power density would have been higher, the cooling rate would have decreased. Martensite formed at the bottom layers near the substrate would experience a tempering effect resulting in the tetragonality of the BCT structure to be closer to a BCC, resulting in the detection of α-Fe. Since C [44], Cr [190], V [191], and Mo [192] have

very limited solid solubility in Cu, it can be expected that little mixing of these carbide forming elements occurred meaning they should still precipitate out during tempering of the tool steel.

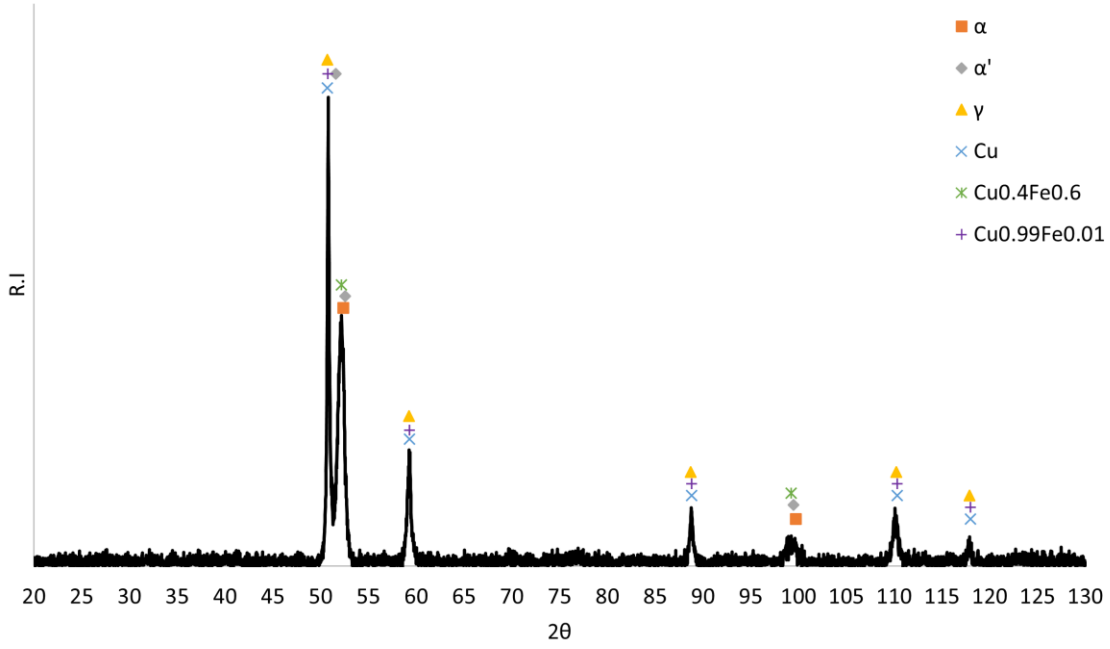

(a)

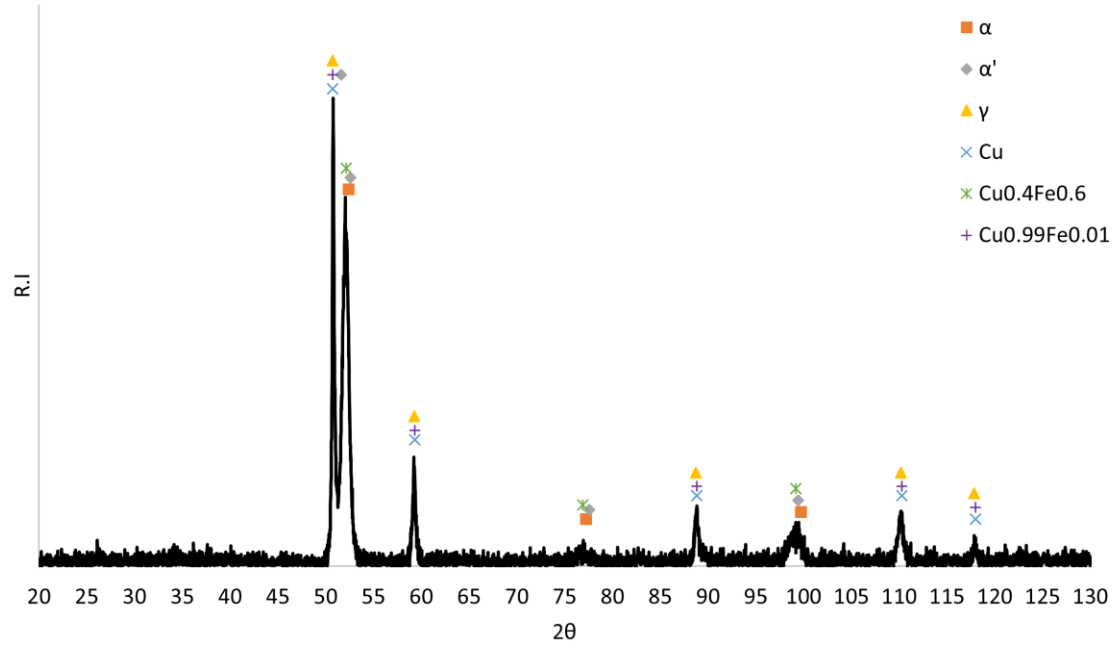

(b)

Figure 5.19: XRD traces for FGM rectangle samples processed at 400 W (a) and 460 W (b).

Major defects were encountered in the two sets of FGM rectangular samples compositionally graded from H13 to pure Cu, notably cracking highlighted in Figure 5.21(a) and Figure 5.21. Looking at the SEM image (Figure 5.21(b)) of the transverse cracking, terminal Cu-liquid, has backfilled cracks. The cracking propagated through the weaker copper matrix and around unmelted H13 powder particles. The transverse cracking is likely a combination of the coefficient of thermal expansion (CTE) differences creating residual stresses and the tendency for Cu to promote solidification cracking. The cyclic heating of the DED process also creates expanding and contracting when printing multi-layered samples [193], [194].

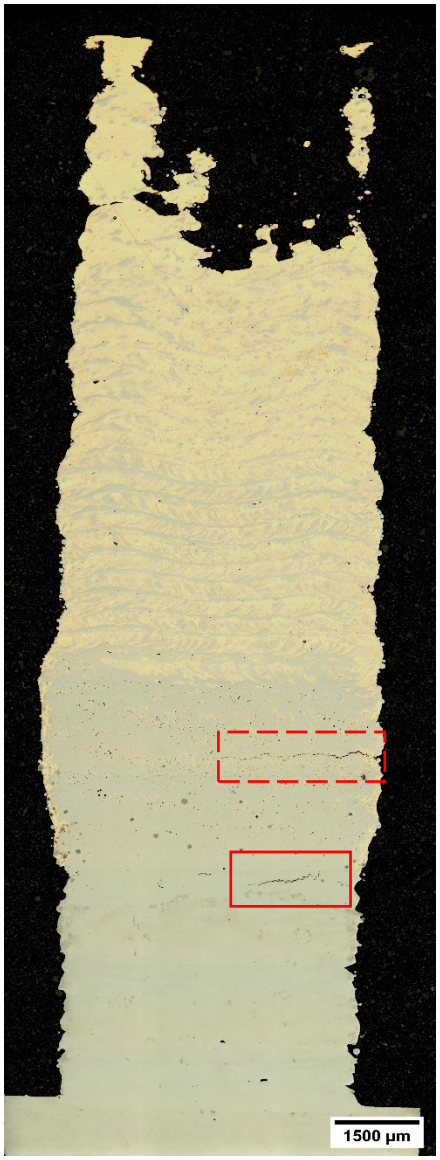

(a)

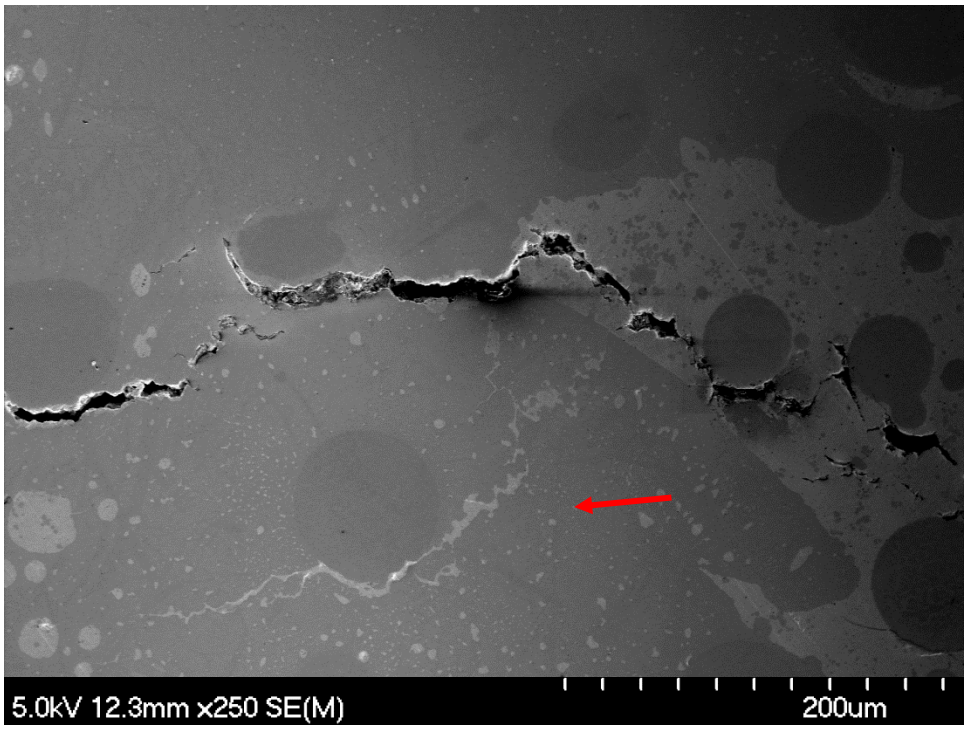

(b)

Figure 5.20: An H13-Cu FGM sample processed at 400 W, with red boxes (dashed and solid) indicating the major transverse cracking, imaged using CLSM (a). Enlarged FE-SEM micrograph of the red dashed box highlighting the cracking, as well as a back filled crack (red arrow) by terminal Cu-liquid in ≈ 45 wt% Cu section (b).

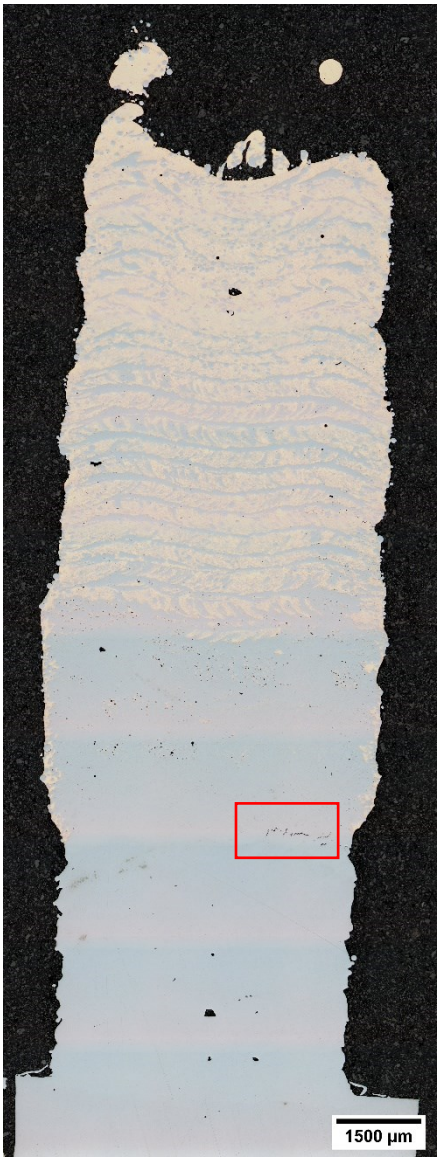

Figure 5.21: An H13-Cu FGM sample processed at 460 W with the solid red box indicating cracking, imaged using CLSM.

However, as the Cu-content increases towards the top of the sample, porosity and cracking is reduced (above ≈ 58wt% Cu) which agrees with the cracking range proposed by *Noecker* and *Dupont* [81]. Since this composition exceeds the potential solidification cracking range, these layers could be improved by system optimization. It appears that the sample processed at the higher laser power results in less large porosity in the ≈ 25 –

45 wt% Cu sections. The increase in laser power however did not resolve the micro-porosity in the same Cu-rich sections of the sample processed 460 W, indicating that optimizing the process parameters will be difficult. These difficulties were also reported by *Kim et al*. processing an Fe-10Cu alloy using L-PBF [194]. Another study using LPB-F conditions, noted the Cu-layers had significant porosity due to the reflectivity and thermal conductivity issues [188]. It is challenging to translate process parameters across different printing technologies but provides a useful starting point.

The FGM samples produced transverse cracking in nearly identical locations situated in the ≈ 25 – 45 wt% Cu sections. This indicates that system parameter optimization is going to be very challenging or unsuccessful due to the natural incompatibility of this material system. The tests from the changing power in the cladding suggests that this might be the case. For this reason, an addition of a Ni or Ni-rich alloy buffer layer could be added, as it has solubility in Fe and Cu but also helps reduce hot shortness [48]. For the intended 100 wt% Cu-layers (*i.e.,* top layers) that still contain H13 powder, likely as residual powder in the delivery lines, a delay in printing would remove this issue. However, this pause in printing may make bonding to the previous layer difficult, since absorptivity increases with temperature and there may be issues with reflectivity.

5.6.4 Printing on C110 Substrate

Under the selected system parameters, bonding and clad track stability was an issue when depositing directly onto a C110 substrate with either no deposited material adhering or discontinuous 'balled' tracks attached. Since the thermal conductivity of H13 is significantly lower than Cu, it is easier to sustain a higher printing temperature. Initial laser power testing was conducted at 400 – 500 W with 25 W increments. Under these power conditions, there was no evidence of 100 wt% Cu clad tracks bonding with the substrate. As the H13 content increased, there was some material that bonded, but too a very limited amount. It is theorized that at these power levels, there is insufficient laser power density to generate a melt pool on a pure Cu substrate which will rapidly conduct away the heat. Due these issues, laser remelting tests were performed by varying laser power and scanning speed to see if a melt pool could be generated on the substrate. Laser powers ranged from 650 – 900 W with 50 W increments using a scanning speeds of 254 mm/min. The remelt tests were repeated with the same powers, with the scanning speed reduced to 127 mm/min. From the laser remelting tests, the higher powers (*i.e.,* 800W, 850W, and 900W) combined with the reduced scanning speed of 127 mm/min, resulted in a continuous melt pool forming. From the laser remelting test, the laser power was increased to a range from 850 – 950 W with 25 W increments with a scanning speed of 127 mm/min to examine if bonding is feasible. Again, there was major lack of bonding to the substrate for the 100 wt% Cu lines, but the 100 wt% H13 showed greater promise with the higher powers, with discontinuous 'balled' tracks still occurring. The balling issue is exaggerated on the 3-layer tracks , with no continuous bead and large balled

material, which has a similar morphology to pure Cu printed on 304 stainless steel [80]. Similar balling issues noted by *Constantin et al.* [101].

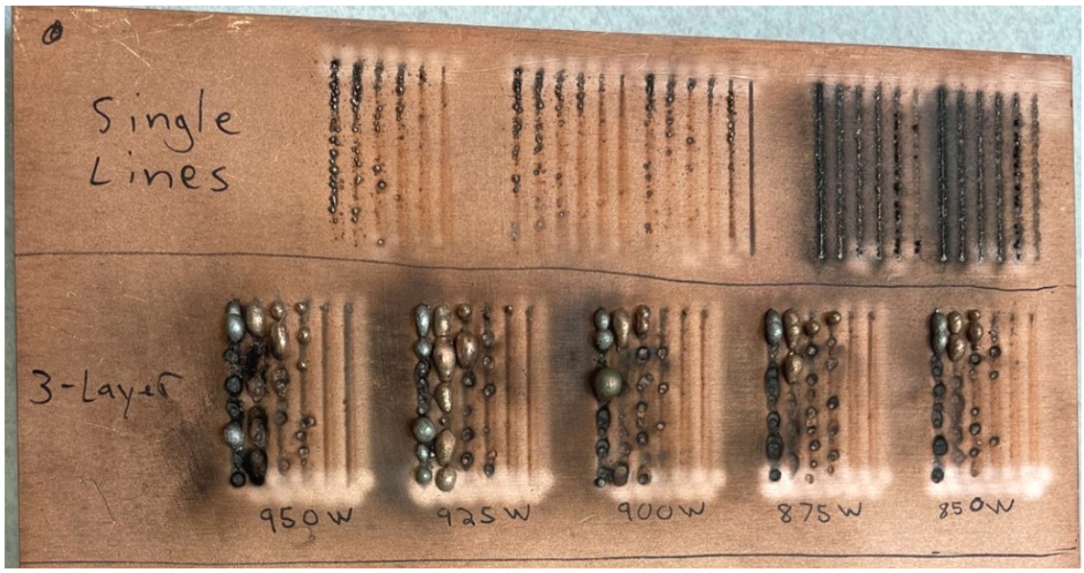

Figure 5.22: Single and 3-layer clad tracks (clustered in groups of six tracks) of varying H13-Cu blends with increasing Cu-content moving left to right, processed with a scanning speed of 127 mm/min and laser powers ranging from 850 – 950W in 25W increments.

To diminish the heatsink effect compared to the larger substrate, and help improve metallurgical bonding, the size of the substrate was reduced, combined with preheating from the laser. The current substrate was machined to dimensions of 76.2 mm x 76.2 mm x 12.7 mm. Then an area of 63.5 mm x 63.5 mm was rastered on the surface using a laser power of 300 W, hatch spacing of 0.381 mm, and a scanning speed of 127 mm/min. Laser powers of 700 - 950 W with 50 W increments, using the same powder blends and system parameters as in the previous test conducted on the room temperature Cu-substrate. This resulted in six different laser power conditions listed in Table 5.8.

Table 5.8: Run identification number and corresponding laser power for printing onto a preheated pure Cu-substrate.

Run Identification	Laser Power (W)
1	950
2	850
3	750
4	900
5	800
6	700

However, deposition proved to be difficult to obtain a sound metallurgical and consistent bond to the pure Cu substrate, even with pre-heating from the laser, as shown in Figure 5.23. Printing the pure Cu powder onto the pure pre-heated Cu substrate did not appear to make any metallurgical bond. Only as the H13 content increased, did beads appear to bond, but only at the beginning of the track. Visual inspection indicates the balling issue seems to be slightly reduced after pre-heating, compared to printing onto a room temperature pure Cu-substrate.

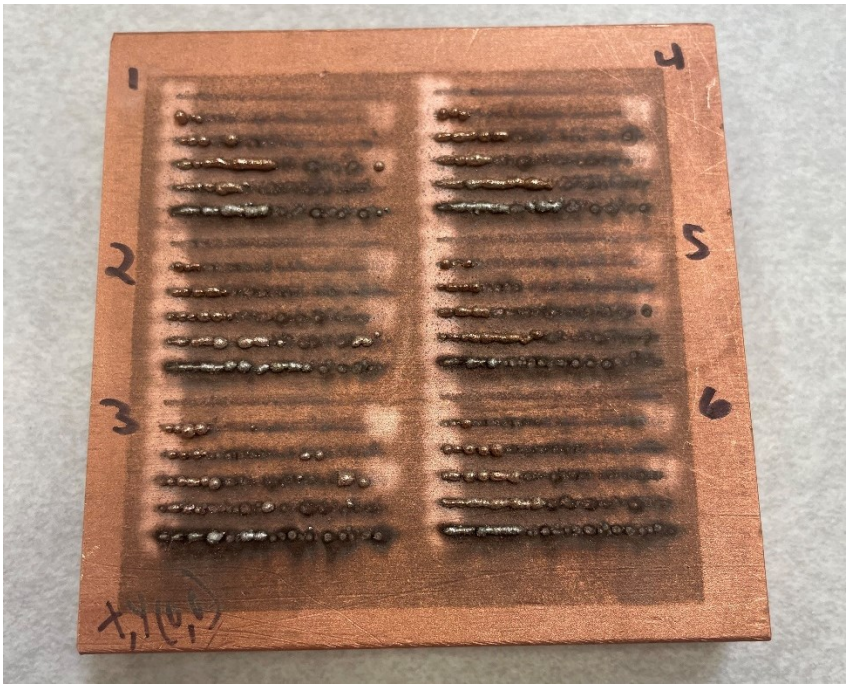

Figure 5.23: Deposition of single clad tracks (clustered in groups of six) with increasing Cu moving from bottom to top, onto a pure Cu-substrate after preheating using the laser to raster a 63.5 mm x 63.5 mm area on the surface with a laser power of 300 W, hatch spacing of 0.381 mm, and a scanning speed of 127 mm/min.

5.7 Summary of DED FGM of H13 and Copper

In conclusion, this work involved varying laser power settings to successfully deposit H13 and OFHC copper (Cu) into a single, compositionally graded sample, known as an FGM, using DED. This began with two DSC analyses, a full melt to 1477°C and an interrupted melt to 1200°C, of varying H13 and Cu loose powder blends to examine the thermodynamic behavior of the material system. From the full melt traces upon heating, as the Cu-content increased the H13-rich peaks diminished in area. During immediate cooling, the starting temperature of the H13-rich peak begins to lower. As well, the starting temperature of the H13-rich peak lowers. Examining the change in temperature during cooling, there is a maximum of Δ°C = 154.3°C in the H13-rich peak with a 25 wt% Cu concentration. Finally, at 87.5 wt% Cu, both the H13-rich and Cu-rich reach comparable values, with Δ°C = 69.4°C and Δ°C = 63.4°C respectively. The large solidification range of the Fe-Cu system, mainly a peritectic reaction over a large Cu range, results in terminal liquid of the lower melting Cu. Additionally, a miscibility gap exists in the Fe-Cu system, where Fe-rich (H13-rich) and Cu-rich liquids separate. This was clearly observed in the full melt DSC samples. EDS suggested that the solid solubility of Cu in Fe agreed with the binary phase diagram of these elements. A variety of microstructures were observed in the full melt and interrupted DSC samples. In the fully melted samples below 50 wt% Cu, a H13 center with a cellular structure extending into the surrounding Cu-rich matrix was seen. Some H13-rich dendritic structures were scattered in the Cu-matrix. The microstructure changes for the fully melted samples containing 62.5 wt% and 75 wt% Cu, showing randomly scattered H13 dendritic structures in a Cu-matrix. At the highest Cu-content of 87.5 wt%, a circular H13 structure

consisted of a continuous solid band, with small amounts of eutectic structures, all surrounded by a Cu-matrix. As expected, the microstructure of the interrupted DSC runs show that the H13 powders did not melt. However, dissolution of the H13 particle edges was observed.

In the single layer and 3-layer tracks of varying mixtures of H13-Cu printed with the selected DED system parameters large vertical cracking and porosity was observed. The cracks are due to solidification cracking of the terminal Cu-liquid. EDS suggested that Cu was situated around the crack. Clad samples containing Cu showed small pockets of Cu-rich zones, many of them containing pores and micro-porosity. Due to the increasing solid solubility of Cu into austenite with increasing temperature, once rapidly solidified, sub-micron circular ε-Cu precipitates formed.

The H13-Cu FGM's were printed starting from pure H13 tool steel at the wrought H13 substrate to pure Cu with six compositional changes in the build direction (z+). Looking at the cross-section, it showed severe transverse cracking, porosity, and micro-porosity in the layers containing larger amounts of copper. This is likely a combination of the tendency for Cu to promote solidification cracking and the thermal CTE differences creating residual stresses. Additionally, the cyclic heating inherent to the DED process causes expanding and contracting. XRD traces detected the phases ferrite (α), martensite (α'), retained austenite (γ), Cu, $Cu_{0.4}Fe_{0.6}$, and $Cu_{0.99}Fe_{0.01}$. A wide variety of microstructures were seen as the composition changed. In the 100 wt% H13 layers, the matrix consisted of a cellular dendritic structure with tempered martensite. Increasing the Cu-content ≈ 25 wt%, the layers consist of long columnar dendrites with tempered martensite, and isolated porosity. An increase to ≈ 45 wt% Cu, multiple different

microstructures were observed. The cellular dendritic structure transitions to a highly refined martensite appearance as it approaches the Cu-rich zone. This region also contained sub-micron Cu-precipitates visible inside the dendrites. The ≈ 58 wt% Cu zone, consisted of a cellular dendritic structure of H13 with pockets of Cu. In the ≈ 76 wt% Cu-layers, there is clear liquid separation as a result of the miscibility gap. The shape of the H13-rich zones in the clad follows the direction of the scan direction. The H13-rich zones have a cellular dendritic structure with Cu-rich pockets inside. Finally, at the highest intended Cu-layers residual H13 globules and small particles are dispersed in a Cu-matrix due to residual H13 powder in the delivery lines.

A sound metallurgical bond was not achieved when printing the varying H13-Cu mixtures on a C110 Cu substrate. The poor results are credited to the high thermal conductivity of copper making bonding an issue. Laser powers of 400 – 500W with 25W increments showed minimal bonding as the H13 content increased, with no pure Cu adhering to the substrate. Laser remelting showed that a continuous melt pool could be achieved with a scanning speed of 127 mm/min using laser powers of 800W, 850W, and 900W. Higher laser powers ranging from 800 – 950W with 25W increments and scanning speed of 127 mm/min, showed minimal improvement to the bonding issues experienced with the lower examined laser powers. The 100 wt% Cu clad tracks had no bonding to the substrate. The 100 wt% H13 showed greater promise with the higher powers but still experienced balling and had no continuous bead.

6 SURFACE TREATMENT OF DED H13 USING A PACK BORIDING METHOD

6.1 Introduction

Boriding or boronizing, is a thermochemical surface hardening technique that is commonly applied to ferrous materials, but also has applications with non-ferrous and cermet materials. Boronizing is achieved by having the sample in contact with a boronaceous state in either solid powder, paste, liquid, or gas form at temperatures ranging from 700 – 1200°C for diffusion to occur [195], [196]. At these elevated temperatures the boron atoms diffuse into the metal lattice forming borides with the substrate and alloying elements constructing a boride layer. The time and temperature of this process will influence the thickness of the boride layer, with higher temperatures and longer processing times promoting a faster diffusion times and thicker layers [46], [195], [197]. Typical boride layer thicknesses range from 12.5 – 50 μm [197]. The purpose of this process is to enhance the surface hardness and abrasive wear resistance of the wearing surface. The hardness can reach values of 2000 HV for steels, while maintaining a low coefficient of friction and can retain the hardness at higher temperatures compared to other surface hardening techniques [46], [195], [196]. Boriding also combats other wear mechanisms such as adhesion, tribo-oxidation, and surface fatigue [197]. The boron layer does not need to be quenched to achieve the high hardness, but for tool steels processed in the austenitizing temperature range, a quench is required to harden. It is possible to reharden the substrate material without damaging the boride layer by taking certain precautions such as avoiding oxidation passed temperatures of 650°C [195], [197]. In steels, FeB and Fe_2B are the dominate phases that develop with the growth of

the boride layer. The formation of the boride layer can be single-phase or dual-phase, that forms a saw-tooth appearance. The single-phase is comprised of Fe_2B and the dual-phase is comprised of an exterior FeB layer and interior Fe_2B layer [195]–[197]. The FeB phase is undesired because it is brittle and is under tensile stresses due to the coefficient of expansion of 8.7×10^{-8} K^{-1} compared to that of iron with a coefficient of expansion of 5.7×10^{-8} K^{-1}. Whereas, the Fe_2B is less brittle and is under compressive stresses (2.9×10^{-8} K^{-1}) [195], [196]. The FeB layer is only detrimental if the layer is continuous and can lead to cracking between the FeB/Fe_2B interface [197]. The formation of the boride layer is influenced by the composition of the substrate. Other than nickel, cobalt, and manganese, alloying additions retard the growth of the boride layer. Silicon and carbon are insoluble in both FeB and Fe_2B and are driven ahead of the layer [195], [197]. If the silicon content exceeds 0.8 wt%, it promotes the failure of the brittle boride layer due to the soft ferrite being retained which is situated under the layer leading to a lower loading capacity [195], [197]. Molybdenum, vanadium, and chromium also reduce the boride layer thickness, but chromium content has a greater influence on the boride layer morphology. As the chromium content increases, it forms chromium-boron phases and flattens the boride layer [196], [197]. A major disadvantage of boriding is the layer is easily removed or fractured from grinding and care must be taken to obtain close tolerances [197]. Another disadvantage is the inflexibility of the process, time, and labor required, which is not as cost effective as other thermochemical surface hardening techniques [197]. Pack boriding is the most common method due to the ease of handling, safety, and possibility to change the boron powder chemistry [46]. Powder is packed around the sample and placed in a heat resistant container. For this method it is

recommend that the process be performed in a controlled atmosphere because oxygen bearing compounds adversely affect the boriding process [197]. The powder contains an active source of boron (B_4C), an inert filler (SiC) which acts as a diluent, and an activator compound such as KBF_4 [195], [197].

There are several studies that have investigated boriding tool steel, with this list not being exhaustive [198]–[202]. The focus of this study was examining the influence of pack boriding DED-processed H13 tool under varying process temperature and comparing the additive manufactured samples to the wrought borided equivalent.

6.2 Experimental Procedure

6.2.1 Raw Materials and Sample Geometries

In this investigation, gas-atomized, pre-alloyed H13 powder was used, with a starting particle size of D_{10} = 58.3 μm, D_{50} = 78.7 μm, and D_{90} = 107 μm. The apparent density of the powder was 4.260 g/cm^3. Four cylindrical samples were printed onto a wrought annealed H13 tool steel substrate (101.6 mm x 101.6 mm x 6.35 mm) using the printing parameters listed in Table 6.1. The printed samples have a diameter of 20 mm and a height of 15 layers. Wrought AISI H13 hot work tool steel was also purchased from Hudson Tool Steel Corporation (Rockford, IL, USA) for baseline evaluation. Wrought material was supplied as bar stock, with a diameter of 19.05 mm, with four samples sectioned into a thickness of 5 mm; the bar was also received in the annealed condition. The composition of the materials used in the study are listed in Table 6.2 determined using inductively coupled plasma optical emission spectrometry (ICP-OES; model Vista-PRO, Varian Inc., CA, USA), with an internal calibration standard (scandium). The carbon content was determined using a carbon-sulfur combustion analyzer (model

CS2000, Eltra GmbH, Haan, Germany) following the ASTM Standard E1941-10: *Standard Test Method for Determination of Carbon in Refractory and Reactive Metals and Their Alloys by Combustion Analysis*. The ICP-OES and carbon content analyses were conducted three times to obtain an average.

Table 6.1: DED system printing parameters for boride samples.

Parameters	**Value**	**Units**
Laser Power	400	W
Scan Speed	500	mm/minute
Feed Rate	7.5	g/minute
Hatch Spacing	0.381	mm
Layer Thickness	0.251	μm
Spot Size	600	mm
Nozzle Stand-Off	9.525	mm
Hatch Orientation	0, 45, 90, 135	degrees

Table 6.2: Chemical compositions of the 'as-received' H13 powder (prior to DED use), wrought H13 substrate. AISI standard specifications are provided vs. measured values (note that Fe comprises the balance in each case)

Designation	**Composition (wt.%)**					
	C	**Si**	**Mn**	**Cr**	**Mo**	**V**
AISI H13	0.32-0.45	0.8-1.2	0.2-0.5	4.75-5.5	1.1-1.75	0.8-1.2
Wrought H13	0.4	0.69	0.34	4.64	1.17	0.76
As-received powder	0.372	1.02	0.42	5.74	1.46	1.05
H13 Substrate	0.39	0.63	0.30	4.73	1.37	0.80

6.2.2 Baseline Heat Treatments

All samples were polished before heat treating to a 1 μm finish. The heat treatments consisted of pack boriding samples in stainless steel bags with a solid boride medium (Ekabor-II powder), conducted in a vacuum furnace at a pressure of $1x10^{-6}$ kPa, at temperatures of 800°C, 850°C, 900°C, and 950°C with 4 hour hold times. This was followed by a furnace cool to room temperature. The wrought samples are identified by the prefix "W" followed by the heat treatment temperature (*i.e.,* W800). The laser DED printed samples are identified in a similar manner, identified with the prefix "DED" and the corresponding heat treatment temperature (*i.e.,* DED800).

6.2.3 Characterization Techniques

The surface roughness was analyzed using a CLSM, using a 20x magnification objective lens with three measurements taken to obtain an average. Data was analyzed on the CLSM using the Keyence *Multifile Analyzer* software.

Crystallographic phase evaluation of the borided surface was conducted using XRD (Bruker D-8 Advance Bruker Corp., Billerica, MA, USA) operating at 35 kV and 27 mA with CoKα radiation and a Fe filter. A step size of 0.02° and a time per step of 0.5 per second over a range of 20 – 130° for 2θ was used. The sample was cleaned with acetone before being placed in the sample holder.

To examine the cross-section, all samples were sectioned with care taken to ensure the boride layer remained intact. The microstructure was examined using FE-SEM (model S4700, Hitachi High Technologies, Tokyo, Japan) operating with varying accelerating voltages and beam currents to obtain a clear image. EDS analysis was conducted at an accelerating voltage of 15 kV. Wavelength dispersive spectroscopy (WDS) using an

electron probe micro-analyzer (EPMA; model JXA-8200, JEOL, Tokyo, Japan) operating at 15 kV, a beam current of 20 nA, and a spot size of 1 μm, was used to accurately measure the distribution of the alloying elements. For all elements, peak intensities were counted for 20 seconds and both lower and upper backgrounds were counted for 10 seconds. The standards used for calibration purposes were all pure-element standards. Operation of the equipment was conducted by Dan MacDonald in the Earth and Environment Sciences Department at Dalhousie University.

6.3 Results and Discussion

6.3.1 Surface Characterization

Using the CLSM, the surface roughness of the wrought material was shown to slightly increase with boriding temperature, as shown in **Error! Reference source not found.**. This increase in roughness was observed in prior research [200]–[202]. Increasing roughness is due to the formation of the boride crystals [203]. SEM imaging of the boride surface shows a porous appearance, as illustrated in Figure 6.1. Since FeB has tensile residual stresses, cracking can be seen on the as-borided surface. The cracking was prevalent on the samples borided at the higher temperature due to greater formation of the FeB layer.

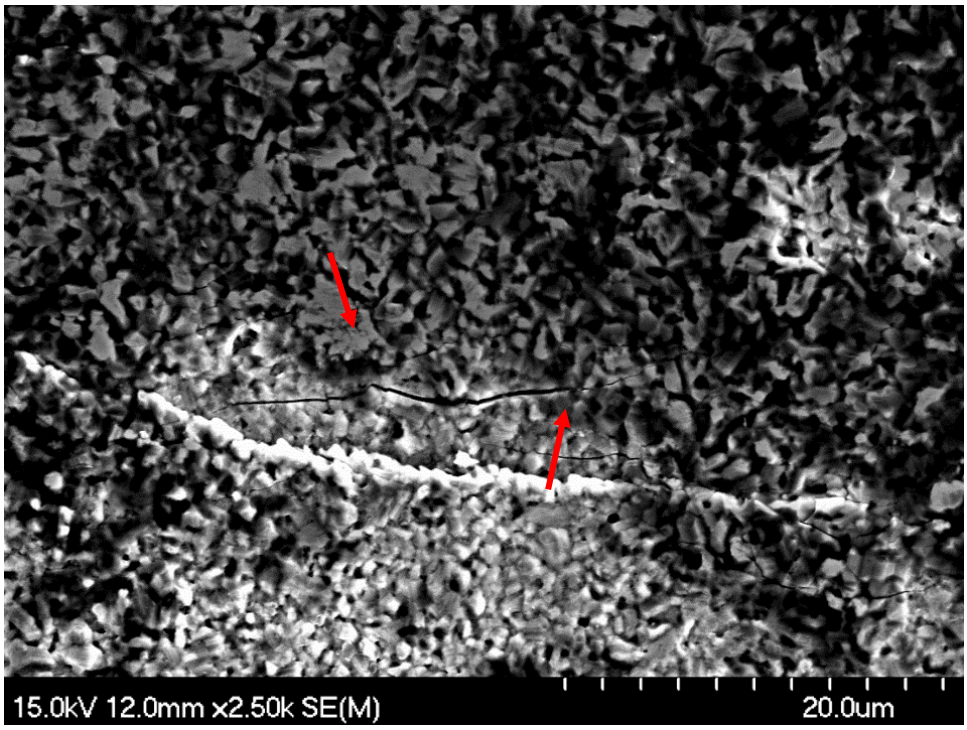

Figure 6.1: FE_SEM image of the as-borided surface of wrought H13 heat-treated at 950°C with a 4 hour hold time. The red arrow indicating surface cracking.

6.3.2 Microstructural and Phase Analysis

Typical of the boriding process for steels of lower chromium content, the boride layer consists of a FeB on the outer surface with a 'saw-tooth' morphology, appearing darker in contrast to the lighter Fe_2B inner layer, as seen in Figure 6.2, and confirmed by XRD shown in Figure 6.3. The wrought material XRD scans of the surface indicate that FeB and Fe_2B are present along with possible MoB, CrB, and Cr_2B phases. The FeB peak at $2\theta = 74.74°$ in samples W850, W900, and W950 have a pronounced FeB peaks compared to sample W800 due to a thicker top layer. Whereas the Fe_2B peak at $2\theta = 49.78°$ is at a higher intensity for samples W800 and W850 compared to the higher boriding temperatures tested. It is known that the FeB is brittle and is under tensile residual

stresses with transverse cracking observed in this layer. Portions of the FeB layer were also observed to be spalling off. The process temperature influenced the thickness of the boride layer, with processing temperatures of 950°C and 800°C producing the thickest and thinnest layers respectively.

Table 6.3: Surface roughness (Sa) of as-borided wrought and DED H13 tool steel borided at 800°C, 850°C, 900°C, and 950°C with 4 hour hold times.

Sample	**Sa (µm)**
W800	0.232 ± 0.007
DED800	0.223 ± 0.002
W850	0.202 ± 0.006
DED850	0.220 ± 0.002
W900	0.254 ± 0.027
DED900	0.257 ± 0.005
W950	0.305 ± 0.003
DED 950	0.233 ± 0.006

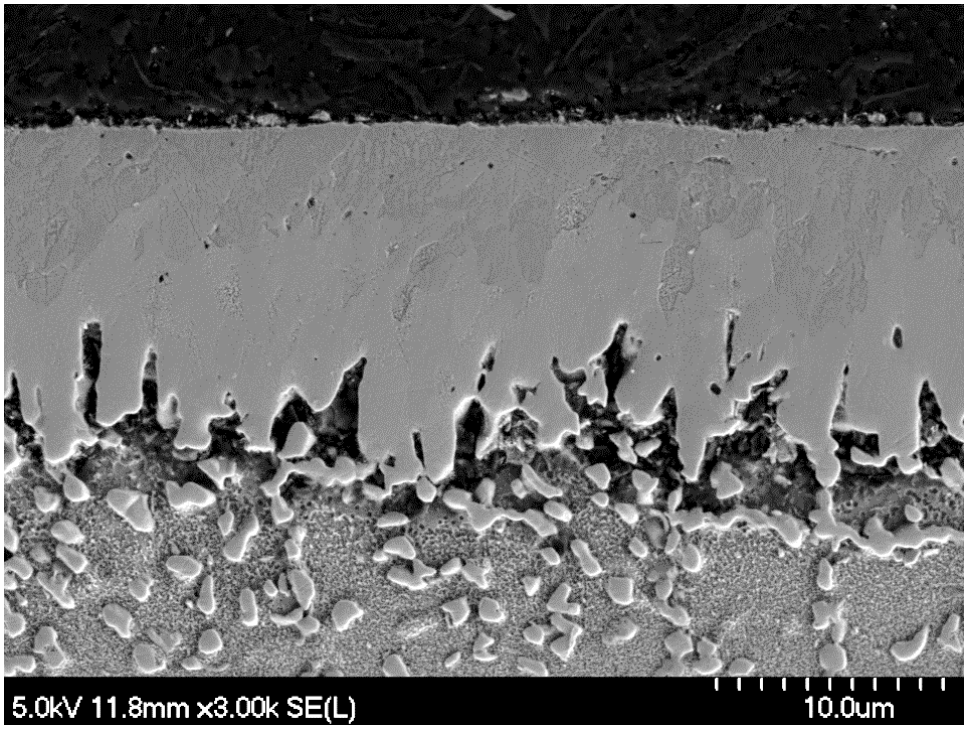

(a)

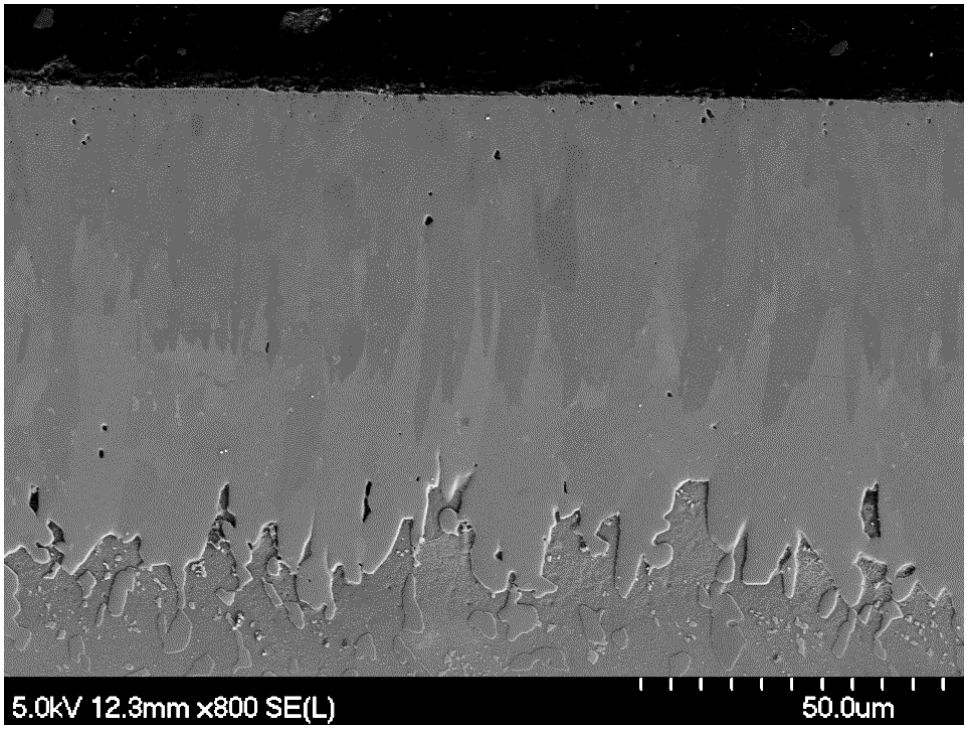

(b)

Figure 6.2: FE-SEM micrographs of the cross-sectional view of DED 800 (a) and DED 950 (b) highlighting the dual-phase boride layer after a hold time of 4 hours. The outer most layer (darker) is comprised of FeB and the layer below (light) is the Fe_2B.

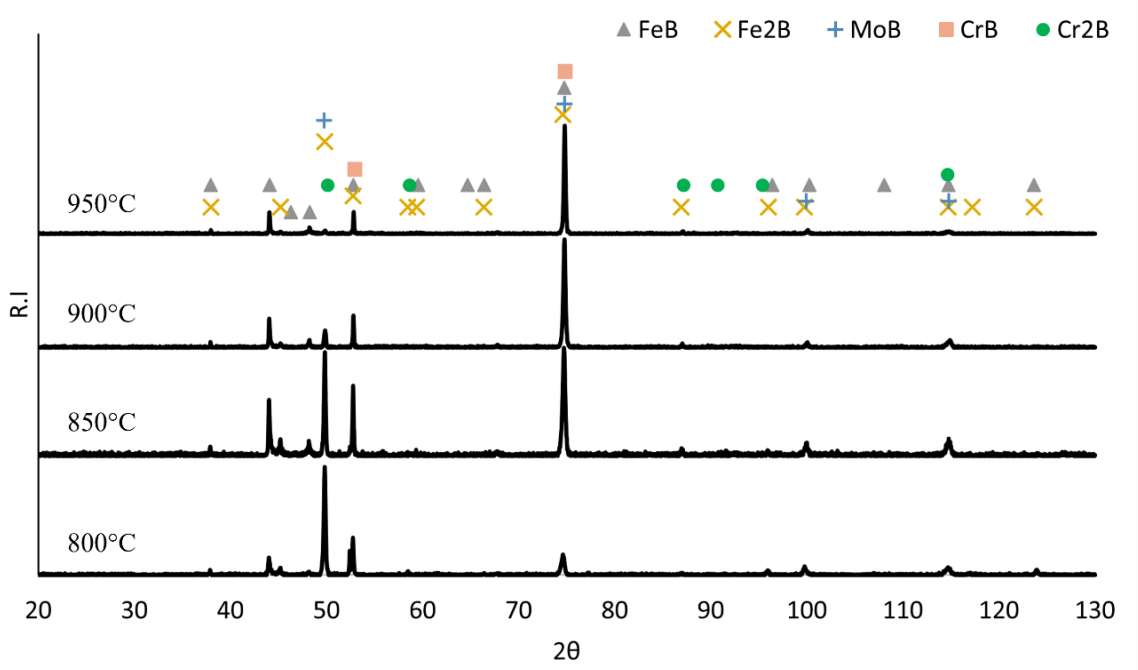

Figure 6.3: XRD traces of wrought borided samples processed at 800°C, 850°C, 900°C, and 950°C after a hold time of 4 hours.

The values of the FeB, Fe_2B, and total layer thicknesses are listed in Table 6.4. It is evident that the higher temperatures resulted in a thicker boride layer due to accelerated diffusion at elevated temperatures. The DED-processed material has comparable FeB, Fe_2B, and total layer thickness values. This should be expected as this is a thermochemical process, and the chemical composition of the printed material is of similar values to the wrought. Therefore, the diffusion behavior and formation of the boride layer appears to be analogous. However, WDS analysis showed that the distribution of alloying is not consistent for the DED-processed samples compared to the wrought equivalent. Furthermore, since the examined surface was that of the top layers (*i.e.,* last printed layers) the formation of boride layer may be slightly altered near the substrate where the lower layers experienced a tempering effect. Plotting the WDS results

for boron of samples processed at 800°C and 850°C, and 900°C and 950°C, Figure 6.4(a) and Figure 6.4(b) respectively. It indicates the boron distribution in the DED sample is comparable to the wrought equivalent. The boron content is initially higher at the surface, then decreases until it reaches a negligible amount into the matrix. There may be some deviations in the formation of the boride layer in the laser DED-processed samples, as the top surface encounters less thermal cycling compared to the lower layers which have been re-heated several times during the DED 'build'. This cyclic heating prior to the boriding treatment, may have an impact on the formation of the boride layer but this study only focused on the top layer (i.e. last printed layer) of the sample.

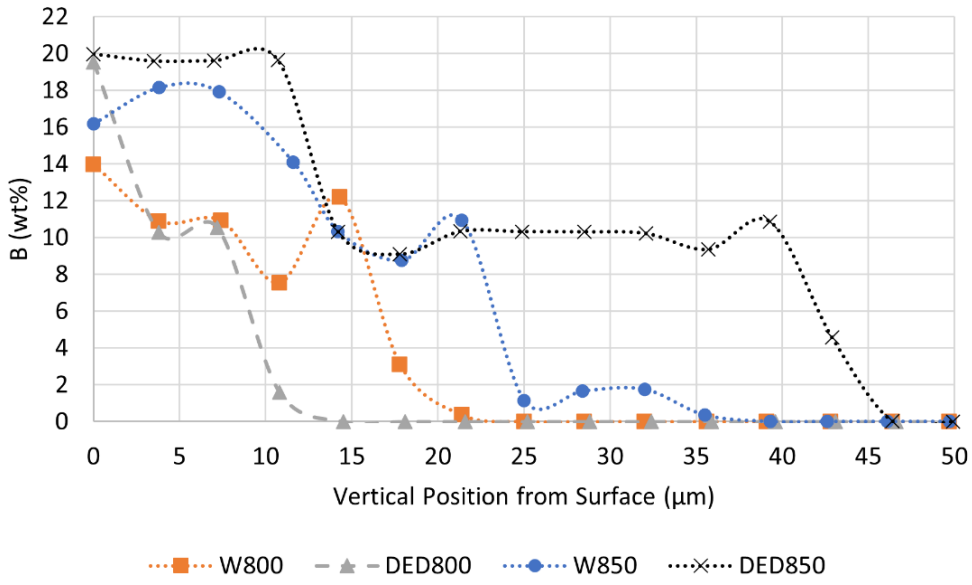

(a)

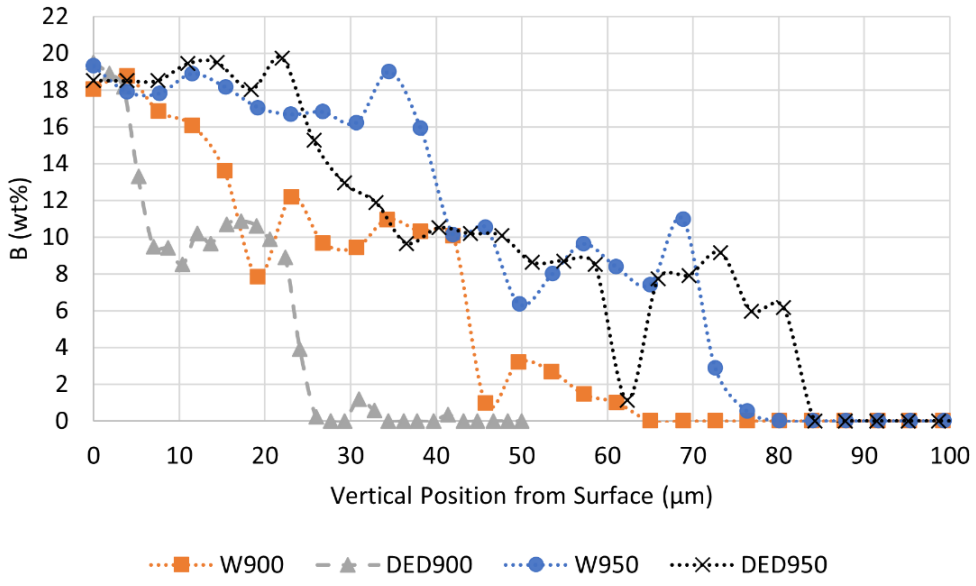

(b)

Figure 6.4: WDS analysis of the Boron content (wt%) measured vertically from the surface (0 µm) of samples processed at 800°C and 850°C (a) and for temperatures 900°C and 950°C (b) after a hold time of 4 hours.

Alloying additions of Si, Cr, V, and Mo will reduce the thickness of the overall boride layer [197], [204], but the Cr content has a greater influence on the boride layer morphology. As the Cr content increases, it forms chromium-boron phases and flattens the boride layer [196], [197]. If the Si content exceeds 0.8 wt%, it promotes the formation of brittle structures and soft ferrite situated under the layer, which has a lower loading capacity [195], [197]. EDS mapping of the cross-section suggests that mainly Si and smaller amounts of Cr are displaced by the boride layer, with Si accumulating in the transition zone as illustrated in Figure 6.5. Cr is also known to accumulate in the transition region, but this redistribution may be due to Cr-C reactions that are forming alloy carbides [205], [206]. Another study found that the Cr is depleted from the matrix

and enters the boride layer [207]. Chromium is capable of dissolving into the FeB and Fe_2B phases [201], [208]. These results agree with this study, as the EDS mapping of Cr suggests the transition zone is depleted.

Table 6.4: FeB, Fe_2B, and total boride layer thicknesses processed at temperatures of 800°C, 850°C, 900°C, and 950°C after a hold time of 4 hours.

Sample	**FeB Thickness (µm)**	**Fe_2B Thickness (µm)**	**Total Thickness (µm)**
W800	5.61 ± 1.14	6.67 ± 1.74	12.28 ± 2.08
DED800	5.90 ± 1.53	7.28 ± 1.90	13.19 ± 2.44
W850	11.98 ± 1.22	9.89 ± 2.07	21.87 ± 2.40
DED850	13.05 ± 2.26	10.76 ± 2.20	23.81 ± 3.16
W900	23.92 ± 3.29	19.39 ± 4.74	43.28 ± 5.77
DED900	21.38 ± 2.29	20.28 ± 4.12	41.66 ± 4.72
W950	44.23 ± 4.42	33.01 ± 8.02	77.23 ± 9.16
DED950	44.52 ± 4.85	34.25 ± 3.28	78.78 ± 5.86

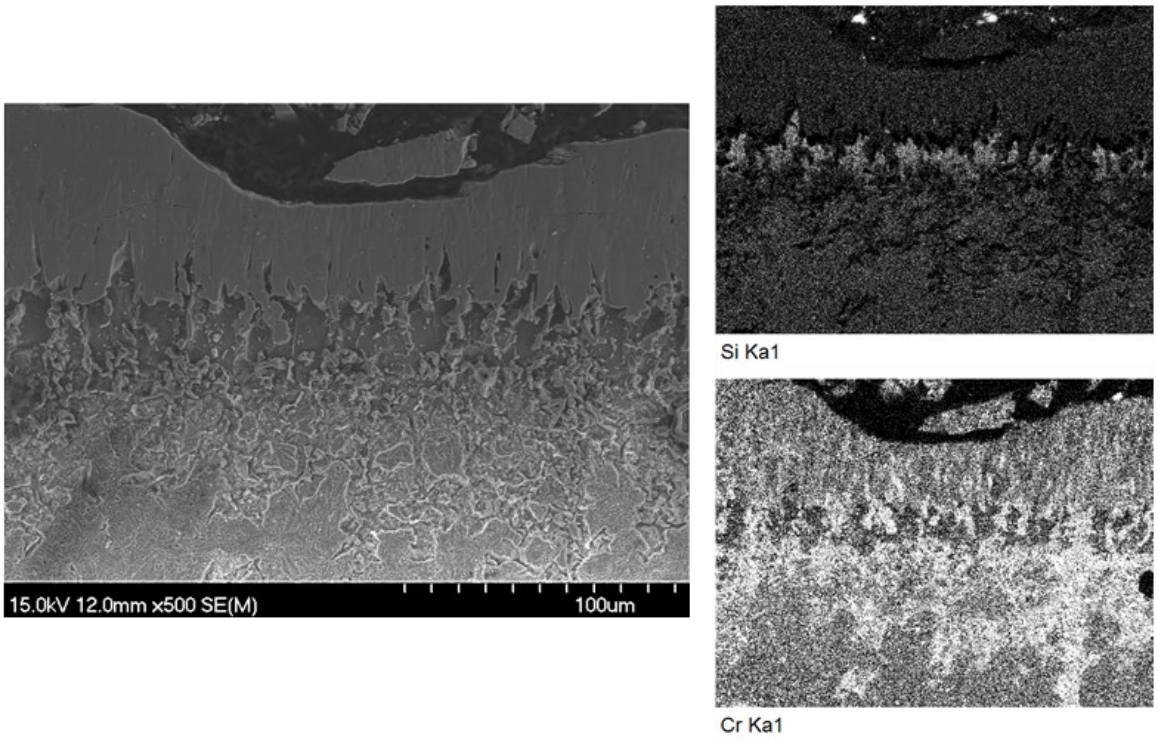

Figure 6.5: EDS mapping of W950 highlighting the displacement of Si and Cr to the transition region with a hold time of 4 hours.

Cr also promotes the formation of boron-rich formations and will reduce the thickness of the boride layer [209]. Plotting the WDS results for the samples processed at 800°C and 850°C shown in Figure 6.6(a), the displacement of the Cr from the surface remains stable in the DED samples but for the wrought samples there is slight increase below the surface with large variation in measurements. Increasing the boriding temperatures to 900°C and 950°C, the WDS results plotted in Figure 6.6(b) show no clear trend for either the wrought or DED samples. Cr is a ferrite stabilizing element; therefore, it raises the transformation temperature [45], [210].

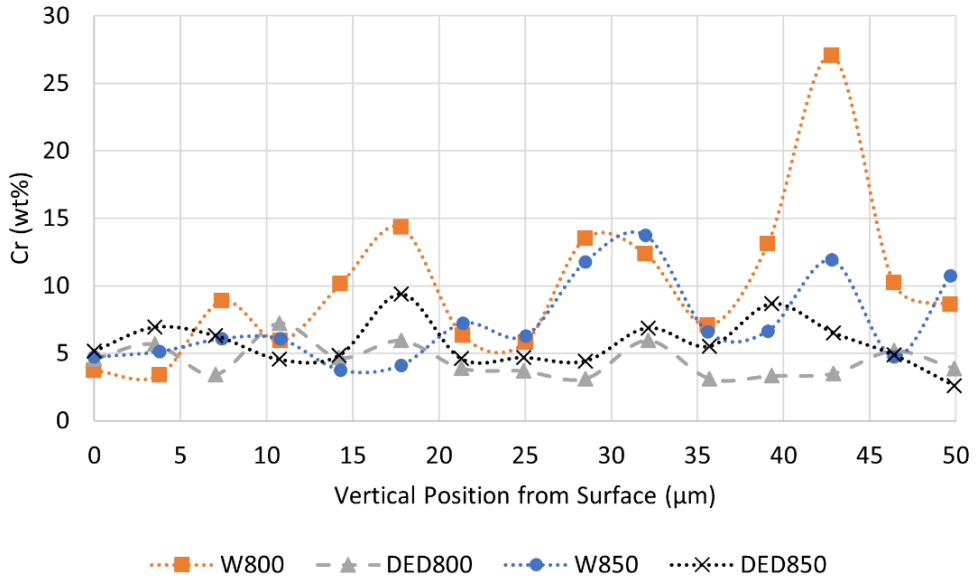

(a)

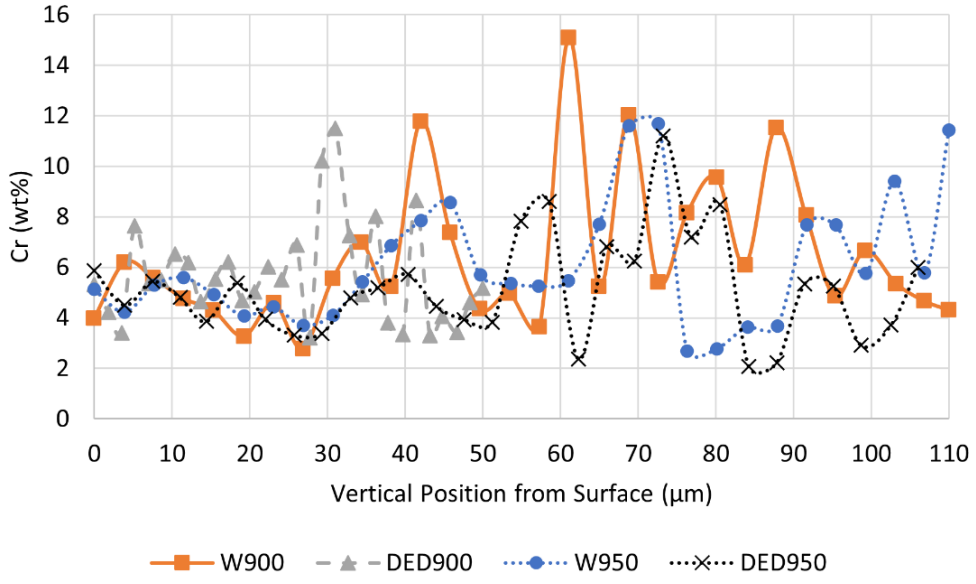

(b)

Figure 6.6: WDS analysis of the Chromium content (wt%) measured vertically from the surface (0 µm) of samples processed at 800°C and 850°C (a) and for temperatures 900°C and 950°C (b) after a hold time of 4 hours.

The Si has been displaced ahead of the boride layer because it is insoluble in this phase. From the WDS analysis of the samples processed at 800°C and 850°C, shown in Figure 6.7(a), the Si content in sample DED800 was not displaced as far from the surface compared to the wrought equivalent processed at 800°C. Whereas, from the analysis it is appears that Si was pushed further ahead in the DED sample processed at 850°C than the wrought equivalent. Plotting the Si concentration at a boriding temperature of 900°C and 950°C shown in Figure 6.7(b), the DED sample processed at 900°C has a Si concentration located closer to the surface. Whereas the DED and wrought samples processed at 950°C have comparable displacement of Si from the surface. The displacement of Si ahead of the boride layer is not ideal because Si is a ferrite stabilizer which reduces the wear resistance, with failure caused by the 'eggshell effect' [45]. A higher Si concentration at the transition layer makes it difficult to fully austenitize this region, potentially resulting in issues when an additional heat treatment is required [210], [211]. The remaining alloying elements, Mo and V, known to influence the boride layer, remain consistent from the surface over the varying temperatures compared to the wrought, as shown in Figure 6.8(a,b) and Figure 6.9(a,b) respectively. Mo and V will form intermetallic phases with boron [44], but it requires higher concentrations of these elements. *Habig* and *Chatterjee-Fisher* noted adhesive wear was shown to decrease when Cr and Mo was in solution of the boride layer, as well as reduction in abrasive wear when Cr, Mo, and V are in solution [212].

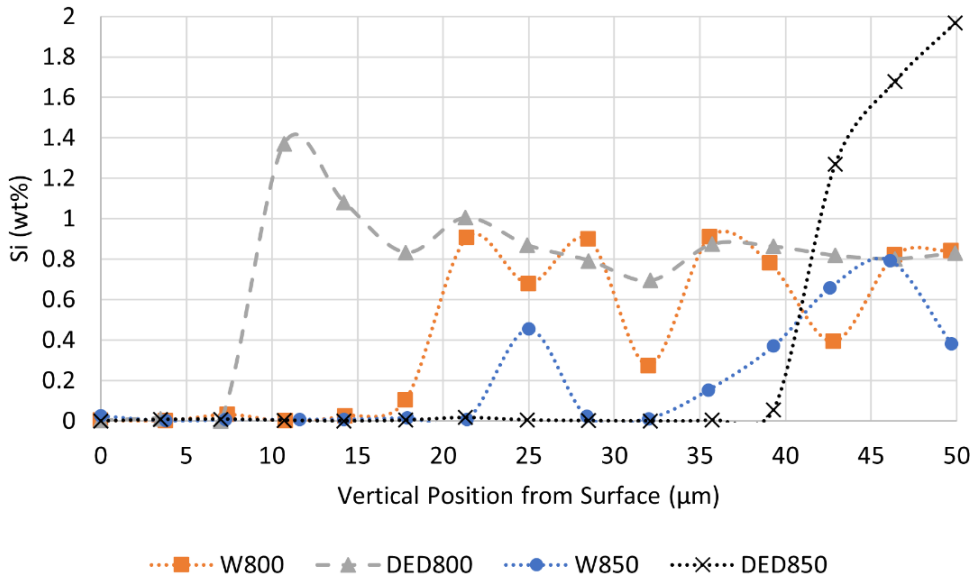

(a)

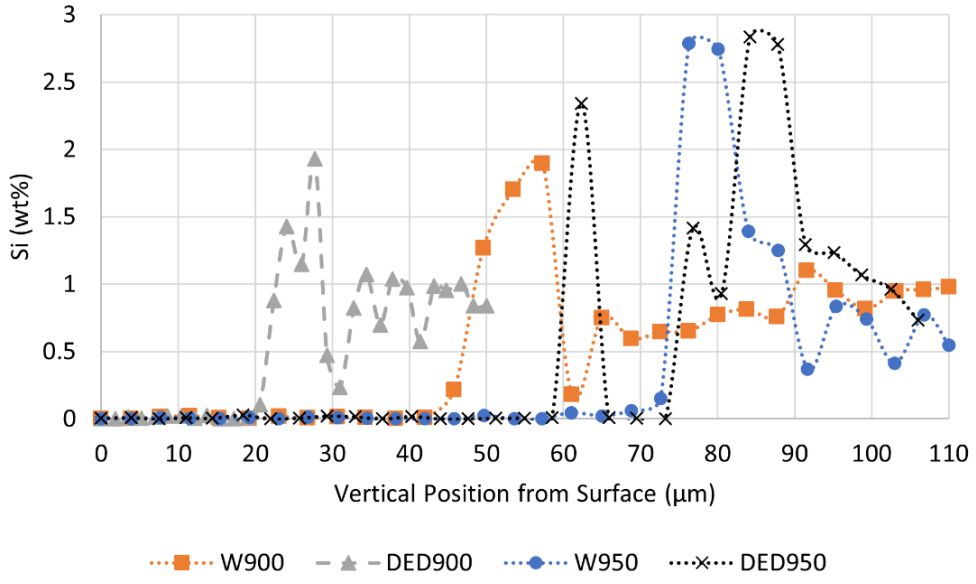

(b)

Figure 6.7: WDS analysis of the Silicon content (wt%) measured vertically from the surface (0 µm) of samples processed at 800°C and 850°C (a) and for temperatures 900°C and 950°C (b) after a hold time of 4 hours.

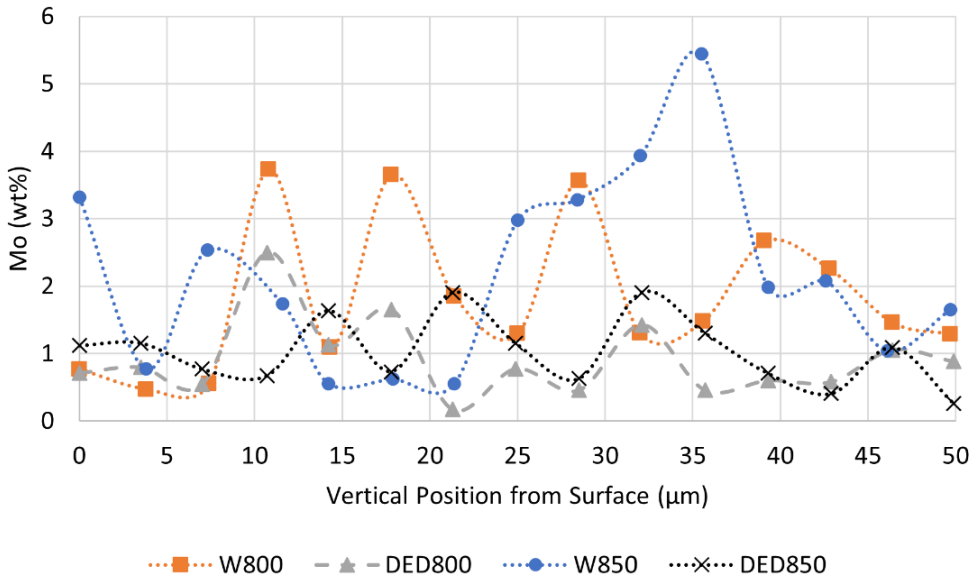

(a)

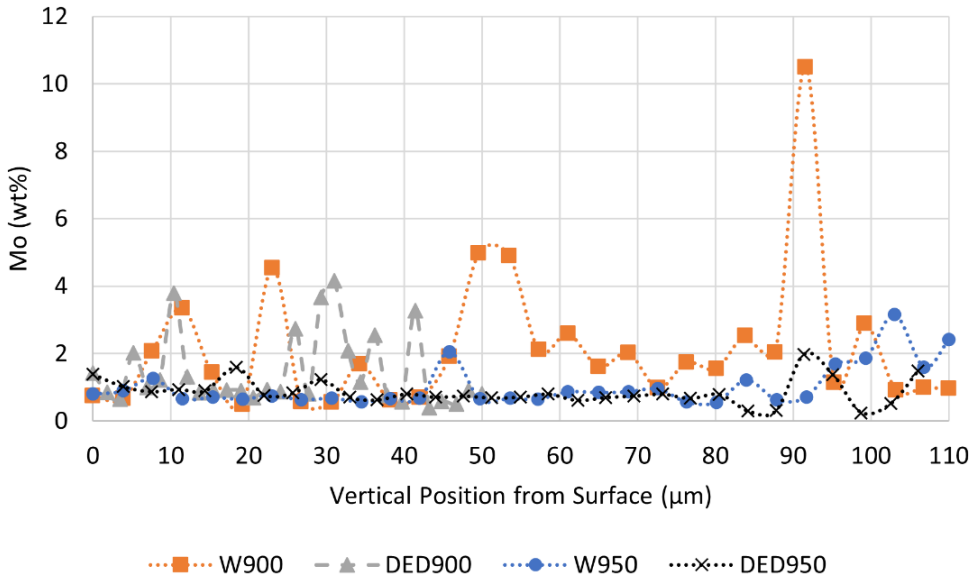

(b)

Figure 6.8: WDS analysis of the Molybdenum content (wt%) measured vertically from the surface (0 µm) of samples processed at 800°C and 850°C (a) and for temperatures 900°C and 950°C (b) after a hold time of 4 hours.

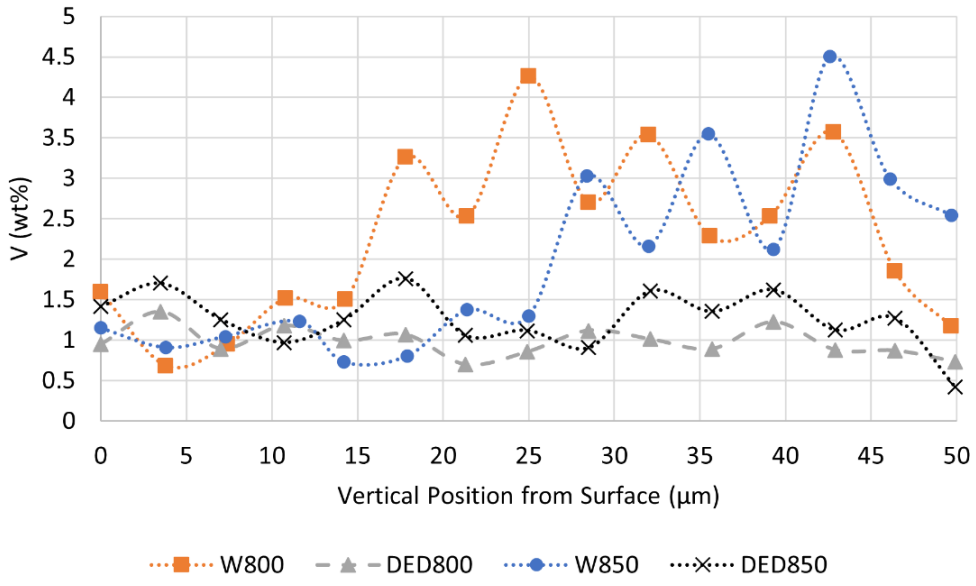

(a)

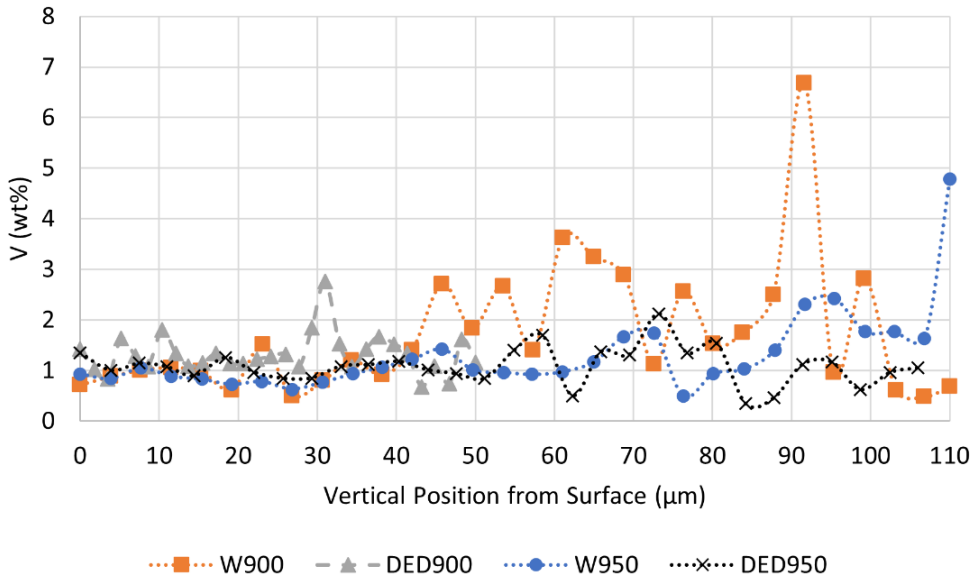

(b)

Figure 6.9: WDS analysis of the Vanadium content (wt%) measured vertically from the surface (0 µm) of samples processed at 800°C and 850°C (a) and for temperatures 900°C and 950°C (b) after a hold time of 4 hours.

6.4 Summary of Pack Borided DED H13

From the present study the following conclusions have be made about pack boriding of wrought and DED-processed H13 tool steel:

- The surface of the borided samples appear porous with surface cracking seen in the samples processed at 950°C, due to significant FeB formation. However, there is not a significant increase in surface roughness.

  The borided structure consists of two layers; the outer layer composed of FeB and the inner layer comprised of Fe_2B. This layer has a "saw-tooth" morphology. Higher heat treatment temperatures of 900°C and 950°C resulted in a thicker boride layer. There seems to be no significant differences in the thickness of the dual-phase boride layer between wrought H13 and DED-processed H13 tool steel. The main findings from this research are as listed:

- Insoluble alloying additions such as Si are pushed ahead of the boride layer and accumulate in the transition region. The addition of Cr is slightly depleted from the matrix and is distributed in the boride layer.

- The alloying additions of Cr, Mo, Si, and V remain stable in the DED-processed samples moving away from the surface compared to the wrought which shows greater deviation and displacement.

- To see if the distribution of alloying in the boride layer impacts wear resistance, reciprocating wear conditions are recommended.

7 CONCLUSIONS AND SUGGESTIONS FOR FUTURE WORK

7.1 Research Goals

This research aimed to determine system printing parameters for an FGM of H13-Cu. The second objective was to print an FGM of H13-Cu onto a C110 Cu substrate, starting with development of baseline conditions for printing H13 onto a like substrate. Based on the quantitative and qualitative analysis of this study, it can be concluded that a defect free FGM of H13-Cu is not feasible using the DED technology with changing composition in the build direction. The results of this study agreed with the initial expectations where the miscibility gap of H13 tool steel and Cu compounded by the reflectivity issues of Cu having low absorptivity at near-infrared wavelengths limited the successful printing of an FGM using DED. The addition of the Ni buffer layer was not explored in this study due to time constraints but is proposed as a future solution to the issue. To determine starting printing parameters, characterization of pure DED H13 was investigated, beginning with:

- The geometrical and surface characterization of as-printed H13 when the scanning speed and powder feed rates are varied (Section 4.9.2 and Section 4.9.3).
- Microstructural characterization of DED H13 in the as-printed and heat-treated condition when the scanning speed and powder feed rates are varied (Section 4.11).

- Initial scratch wear response of DED H13 in the as-printed and heat-treated condition when the scanning speed, powder feed rate, and number of printed layers varying (Section 4.13).

Successful printing parameters were obtained for printing pure H13 over three different DED systems. Printing of pure H13 was conducted at Centre de Métallurgie du Québec (CMQ) and Dalhousie University. This provides useful information in that system parameters are transferrable with relative ease with only minor adjustments needed. Based on this, a user should be able to have reproducible results using the selected system parameters and PSD for printing H13.

The system parameters for printing pure H13 were used as reference to find parameters for an FGM of H13-Cu. FGM samples were printed at the Navajo Technical University (NTU) in the Center for Advanced Manufacturing in New Mexico. The FGM investigation began with:

- DSC analysis of varying H13-Cu blends to understand the thermodynamic behavior of the material system to help relate it to the DED-processed samples (Section 5.5)
- Microstructural characterization of single and 3-layered clads of varying H13-Cu compositions, with varying laser powers, printed on an annealed wrought H13 substrate (Section 5.6.2). 3-dimensional FGM samples were printed on the annealed wrought H13 at two different laser powers (Section 5.6.3).
- Initial printing on a C110 substrate of single and 3-layer clads of varying H13-Cu compositions with varying laser powers and scanning speeds (Section 5.6.4).

7.2 Conclusions

7.2.1 Surface and Geometrical Characterization of DED H13

A range of scanning speeds and powder feed rates were examined to determine if the surface roughness of the as-printed 3-dimensional sample could be minimized while also maintaining geometrical accuracy. From the results, a slower scanning speed of 400 mm/min caused over-building in the build direction (+z), with increasing speed (700 mm/min) resulting in under-building. From the tested system parameters, a combination of dimensional accuracy and reduction of surface roughness is desired. Setting B2 is recommended; with a scanning speed of 600 mm/min and powder feed rate of 7 g/min, resulting in a top surface roughness of 32.91 μm and a side surface roughness of 17.69 μm. Adding a shallow draft angle of 10 - 25° to the build direction would help improve the side surface roughness. Since the powder requirements for DED are relatively coarse, slight over-building is acceptable and a rough surface finish of the consolidated part will require final machining. The single-track and multi-track clad samples showed a clear trend of increasing surface roughness with decreasing scanning speed, with the scanning speed being more significant in both sets than the feed rate. Finally, changing the layer thickness using A3 settings did not have a clear impact on the top surface roughness and side surface roughness.

7.2.2 Microstructural Characterization of DED H13

When the scanning speeds and powder feed rates were varied, H13 tool steel single and 3-layer clads, and 3-dimensional samples were successfully deposited onto an annealed wrought H13 substrate. The shape of the as-printed clad influenced the density, with a higher wetting angle causing it to decrease.

The microstructure of the clad samples resulted in a cellular dendritic structure, with lath martensite, retained austenite, and fine metal carbides (MC and M_7C_3), as a result of rapid solidification. In the 3-dimensional samples, cyclic heating indicative of the DED process will temper previously deposited layers, resulting in a cellular tempered martensite and the precipitation of fine alloy carbides in the lower layers, and a very fine lath martensite and retained austenite structure in the top layers. Applying a quench and double temper heat treatment to the as-printed material results in a homogenous matrix consisting of alloy carbides dispersed in tempered martensite.

Hardness varied in the build direction due to the cyclic heating creating an inhomogeneous microstructure. Heat treating reduced the hardness, and its variation, due to the homogenous matrix.

7.2.3 Initial Wear Response of DED H13

Initial scratch testing at loads of 5 N and 10 N showed no obvious trend in the scratch hardness, cross-sectional area of the track, or surface roughness of the scratch track when the scanning speed, powder feed rates, or number of printed layers is varied. Samples showed excellent bonding to the substrate, with scratch testing revealing internal defects such as gas porosity. The as-printed DED material consisted of a martensitic structure and fine alloy carbides leading to a higher scratch hardness than the quench and double-tempered DED samples. Increasing the load to 10N, the as-printed condition reaches a comparable scratch hardness to the wrought quenched sample. This comparable scratch hardness is due to martensite having a low work hardenability in the wrought quenched sample, whereas the as-printed martensitic matrix would be slightly tougher due to a small tempering effect from the cyclic heating.

The heat treatment decreased the overall scratch resistance of the DED samples but they had similar scratch hardness over the loading conditions due to the tougher tempered martensite and alloy carbide dispersion supporting the load.

7.2.4 Characterization of FGM H13-Cu Processed Using DED

DSC traces of the fully melted trials indicated that as the Cu-content increased the H13-rich peaks diminished in area which was also observed in the interrupted DSC analysis. Upon immediate cooling from a full melt, the area and melting point of the H13-peak decreases with increasing Cu-content. The melting point of the Cu-peak is slightly higher than the pure Cu sample as it has alloyed with the H13. The H13-Cu system appears to follow the Fe-Cu phase diagram, with similar solid solubilities suggested by EDS. Microstructures of the fully melted DSC samples showed a clear separation of the Fe-rich and Cu-liquids associated with the miscibility gap.

From the examined DED samples, cross-sections of single layer and 3-layer tracks of varying mixtures of H13-Cu resulted in the detrimental vertical cracking characteristic of solidification cracking. Porosity and micro-porosity were prevalent, with EDS suggesting that Cu was situated adjacent to these locations. Due to the rapid solidification sub-micron circular ε-Cu precipitates formed in the dendrites of the clad samples when processed at a lower laser power. It is recommended to avoid cladding large concentrations of Cu onto wrought H13.

Finally, 3-dimensional FGM samples were printed with six compositional changes in the build direction (+z), however these experienced major cracking and porosity concerns. This is attributed to the tendency for Cu to promote solidification cracking when in large concentrations, Fe-Cu displaying a miscibility gap, and the residual stresses from CTE

differences. Distinct microstructures were observed in the FGMs as the Cu concentration increased, with multiple different microstructures observed in the same composition zone.

7.2.5 Initial DED Printing on a C110 Substrate with Varying H13-Cu Blends

Printing on a C110 substrate proved to be challenging, with no metallurgical bond being achieved. The poor results are credited to the high thermal conductivity and reflectivity issues of copper, making bonding an issue. Printing pure Cu was the least successful, with no clad being produced under laser powers of 400 – 500W. However, minimal bonding was achieved as the H13 content increased. Higher laser powers (800 – 950W) showed no improvement to the bonding issues with major 'balling' of the deposited powders and inconsistent beads. Laser preheating of a reduced substrate size did not improve the metallurgical bonding even with high laser powers (700 – 950W).

7.2.6 Surface Treatment of DED H13 using Pack Boriding

Results from this study showed that the formation of the dual phase boride layer using the pack boriding method showed similar behavior between DED-processed H13 and more conventional wrought H13. This is to be expected as the boriding process is thermochemically based, with the starting chemistries of the two materials having comparable values. The dual phase boride layer consists of an outer layer of FeB and an inner layer of Fe_2B. WDS analysis showed that the wrought material had a greater fluctuation in the distribution of the alloying additions Cr, Mo, Si, and V moving away from the surface.

7.3 Suggestions for Future Work

7.3.1 FGM of H13-Cu Using DED Technology

Significant research has been conducted into the characterization of H13 processed using DED technology with plenty of supporting literature. Further research is recommended into the fabrication of an FGM of H13-Cu using DED to find successful printing system parameters with suggestions that would include:

- The addition of buffer layer that would have solubility in H13 and Cu. A suitable candidate for this buffer layer would be Ni, as it commonly added to steel (*i.e.,* stainless steel) and has solubility in Cu. Initial residual stresses should be investigated as the buffer layer should help mitigate residual stresses in a 3-dimensional build. In addition, Ni has an absorption wavelength near that of Fe. The addition of Ni-based alloys and stainless steels have been studied but a pure Ni layer has not been attempted at this time. This would require finding printing parameters for printing an FGM of H13-Ni.
- Thermal conductivity testing at varying elevated temperatures. Since H13 is intended for elevated temperature tooling applications, it will experience thermal cycling. The FGM must make a significant increase in thermal transfer while maintaining high wear resistance. Furthermore, this may be in conjunction with the addition of conformal cooling channels to aid in improving the heat transfer which is already a commercially viable technique as AM technology allows for greater design freedom.
- Exploring the response from a quench and temper heat treatment should be investigated. It is unlikely that pure DED H13 would be applied in the as-printed

condition, nor would an FGM of H13-Cu. Heat treatments could include tempering directly from the as-printed state or could involve a traditional quench and temper. This would be combined with mechanical testing, specifically reciprocating wear testing compared to pure DED H13 and wrought H13.

7.3.2 FGM of H13-Cu Printed on a Copper Substrate

Further study into printing on a highly pure Cu substrate appears to be possible and previous studies have shown that this is the case. A major issue with using a laser as the power source on a Cu substrate is the problem of reflection. Changing the laser source to a smaller wavelength will enhance the absorption. To help improve printing on the current DED style system, pre-heating the substrate, or maintaining the substrate at a temperature above room temperature should be explored. By heating the Cu substrate, it will help reduce the heat transfer and hopefully improve the melt pool characteristics to avoid balling of the clad track. Surface alteration to reduce reflection or depositing a thin Ni layer may be explored as an alternative solution to pre-heating or combination of these could be used.

8 REFERENCES

[1] European Powder Metallurgy Association (EPMA), “Introduction To Additive Manufacturing Technology,” p. 56, 2017.

[2] ASTM F3187, “Standard Guide for Directed Energy Deposition of Metals,” 2016. doi: 10.1520/F3187.

[3] I. M. Jyotsna Dutta Majumdar, Ed., *Laser-Assisted Fabrication of Materials*, vol. 161. Springer Berlin, Heidelberg, 2013.

[4] J. G. Eden, “Laser technology: theory and operating principles,” *IEEE Potentials*, vol. 4, no. 2, pp. 7–12, 1985.

[5] H. Lee, C. H. J. Lim, M. J. Low, N. Tham, V. M. Murukeshan, and Y. J. Kim, “Lasers in Additive: A Review,” *Int. J. Precis. Eng. Manuf. - Green Technol.*, vol. 4, no. 3, pp. 307–322, 2017, doi: 10.1007/s40684-017-0037-7.

[6] H. Hügel, “New solid-state lasers and their application potentials,” *Opt. Lasers Eng.*, vol. 34, no. 4–6, pp. 213–229, 2000, doi: 10.1016/S0143-8166(00)00065-8.

[7] W. M. Steen and J. Mazumder, *Laser Material Processing*, 4th ed. Springer London, 2010.

[8] M. K. Imran, S. H. Masood, and M. Brandt, “Direct Metal Deposition of H13 Tool Steel on Copper Alloy Substrate: Parametric Investigation,” *Lasers Manuf. Mater. Process.*, vol. 2, no. 4, pp. 242–260, 2015, doi: 10.1007/s40516-015-0018-z.

[9] R. P. Gu, Dongdong, W. Meiners, K. Wissenbach, “Laser additive manufacturing of metallic components: materials, processes, and mechanisms,” *Int. Mater. Rev.*,

vol. 657, no. 133–164, pp. 163–180, 2012, doi: 10.1179/1743280411Y.0000000014.

[10] D. Gu, *Laser Additive Manufacturing (AM): Classification, Processing Philosophy, and Metallurgical Mechanisms*. 2015.

[11] I. Gibson, D. Rosen, and B. Stucker, *Additive Manufacturing Technologies*, 2nd ed. Springer, 2015.

[12] M. Miedzinski, "Materials for Additive Manufacturing by Direct Energy Deposition," Chalmers University of Technology, 2017.

[13] D. Singh and S. Dangwal, "Effects of process parameters on surface morphology of metal powders produced by free fall gas atomization," *J. Mater. Sci.*, vol. 41, no. 12, pp. 3853–3860, 2006, doi: 10.1007/s10853-006-6652-2.

[14] R. M. German, *Powder Metallurgy Science*, 2nd ed. Princeton, New Jersey: Powder Metal Industries, 1997.

[15] T. Duda and L. V. Raghavan, "3D metal printing technology: the need to re-invent design practice," *AI Soc.*, vol. 33, no. 2, pp. 241–252, 2018, doi: 10.1007/s00146-018-0809-9.

[16] L. Taimisto, "Process parameters in laser sintering process," Lappeenranta University of Technology, 2009.

[17] D. Zhang *et al.*, "Metal Alloys for Fusion-Based Additive Manufacturing," *Adv. Eng. Mater.*, vol. 20, no. 5, pp. 1–20, 2018, doi: 10.1002/adem.201700952.

[18] T. T. Laura Cordova, Mónica Campos, "Powder Characterization and

Optimization for Additive Manufacturing," *56th Annu. Conf. Metall.*, p. 926872, 2017.

[19] B. Dutta and F. H. (Sam. Froes, "The Additive Manufacturing (AM) of titanium alloys," *Met. Powder Rep.*, vol. 72, no. 2, pp. 96–106, 2017, doi: 10.1016/j.mprp.2016.12.062.

[20] R. P. Martukanitz, "Directed-Energy Deposition Processes," in *Additive Manufacturing Processes*, vol. 24, M. S. David L. Bourell, William Frazier, Howard Kuhn, Ed. ASM International, 2020, pp. 220–238.

[21] D. G. Ahn, "Applications of laser assisted metal rapid tooling process to manufacture of molding & forming tools - state of the art," *Int. J. Precis. Eng. Manuf.*, vol. 12, no. 5, pp. 925–938, 2011, doi: 10.1007/s12541-011-0125-5.

[22] Y. Hu and W. Cong, "A review on laser deposition-additive manufacturing of ceramics and ceramic reinforced metal matrix composites," *Ceram. Int.*, vol. 44, no. 17, pp. 20599–20612, 2018, doi: 10.1016/j.ceramint.2018.08.083.

[23] S. Y. Wen, Y. C. Shin, J. Y. Murthy, and P. E. Sojka, "Modeling of coaxial powder flow for the laser direct deposition process," *Int. J. Heat Mass Transf.*, vol. 52, no. 25–26, pp. 5867–5877, 2009, doi: 10.1016/j.ijheatmasstransfer.2009.07.018.

[24] Z. Y. Chua, I. H. Ahn, and S. K. Moon, "Process monitoring and inspection systems in metal additive manufacturing: Status and applications," *Int. J. Precis. Eng. Manuf. - Green Technol.*, vol. 4, no. 2, pp. 235–245, 2017, doi: 10.1007/s40684-017-0029-7.

[25] M. Hirsch *et al.*, “Assessing the capability of in-situ nondestructive analysis during layer based additive manufacture,” *Addit. Manuf.*, vol. 13, pp. 135–142, 2017, doi: 10.1016/j.addma.2016.10.004.

[26] S. K. Everton, M. Hirsch, P. I. Stavroulakis, R. K. Leach, and A. T. Clare, “Review of in-situ process monitoring and in-situ metrology for metal additive manufacturing,” *Mater. Des.*, vol. 95, pp. 431–445, 2016, doi: 10.1016/j.matdes.2016.01.099.

[27] K. Wang, H. Wang, F. Liu, and H. Zhai, “Modeling rapid solidification of multi-component concentrated alloys,” *Acta Mater.*, vol. 61, no. 4, pp. 1359–1372, 2013, doi: 10.1016/j.actamat.2012.11.013.

[28] B. Zheng, Y. Zhou, J. E. Smugeresky, J. M. Schoenung, and E. J. Lavernia, “Thermal behavior and microstructure evolution during laser deposition with laser-engineered net shaping: Part II. Experimental investigation and discussion,” *Metall. Mater. Trans. A Phys. Metall. Mater. Sci.*, vol. 39, no. 9, pp. 2237–2245, 2008, doi: 10.1007/s11661-008-9566-6.

[29] M. M. Kirka, P. Nandwana, Y. Lee, and R. R. Dehoff, “Solidification and solid-state transformation sciences in metals additive manufacturing,” *Scr. Mater.*, vol. 135, pp. 130–134, 2017, doi: 10.1016/j.scriptamat.2017.01.005.

[30] D. Gu, C. Ma, M. Xia, D. Dai, and Q. Shi, “A Multiscale Understanding of the Thermodynamic and Kinetic Mechanisms of Laser Additive Manufacturing,” *Engineering*, vol. 3, no. 5, pp. 675–684, 2017, doi: 10.1016/J.ENG.2017.05.011.

[31] H. Fayazfar *et al.*, “A critical review of powder-based additive manufacturing of

ferrous alloys: Process parameters, microstructure and mechanical properties," *Mater. Des.*, vol. 144, pp. 98–128, 2018, doi: 10.1016/j.matdes.2018.02.018.

[32] G. Telasang, J. Dutta Majumdar, G. Padmanabham, M. Tak, and I. Manna, "Effect of laser parameters on microstructure and hardness of laser clad and tempered AISI H13 tool steel," *Surf. Coatings Technol.*, vol. 258, no. 258, pp. 1108–1118, 2014, doi: 10.1016/j.surfcoat.2014.07.023.

[33] M. Y. S. David A. Porter, Kenneth E. Easterling, *Phase Transformation in Metals and Alloys*, 3rd ed. Boca Raton, Florida: CRC Press, 2009.

[34] M. Policelli, "Development of a New Method to Fabricate Titanium Metal Matrix Composutes via LENS with Improved Material Properties," 2011.

[35] S. Singh, S. Ramakrishna, and R. Singh, "Material issues in additive manufacturing: A review," *J. Manuf. Process.*, vol. 25, pp. 185–200, 2017, doi: 10.1016/j.jmapro.2016.11.006.

[36] A. J. Pinkerton and L. Li, "Multiple-layer laser deposition of steel components using gas- and water-atomised powders: The differences and the mechanisms leading to them," *Appl. Surf. Sci.*, vol. 247, no. 1–4, pp. 175–181, 2005, doi: 10.1016/j.apsusc.2005.01.083.

[37] A. J. Pinkerton and L. Li, "Direct additive laser manufacturing using gas- and water-atomised H13 tool steel powders," *Int. J. Adv. Manuf. Technol.*, vol. 25, no. 5–6, pp. 471–479, 2005, doi: 10.1007/s00170-003-1844-2.

[38] G. Y. Baek, K. Y. Lee, S. H. Park, and D. S. Shim, "Effects of substrate preheating

during direct energy deposition on microstructure, hardness, tensile strength, and notch toughness," *Met. Mater. Int.*, vol. 23, no. 6, pp. 1204–1215, 2017, doi: 10.1007/s12540-017-7049-2.

[39] C. Leyens and E. Beyer, *Innovations in laser cladding and direct laser metal deposition*. Elsevier Ltd., 2014.

[40] O. Hentschel *et al.*, "Processing of AISI H11 Tool Steel Powder Modified with Carbon Black Nanoparticles for the Additive Manufacturing of Forging Tools with Tailored Mechanical Properties by Means of Laser Metal Deposition (LMD)," *Metals (Basel).*, vol. 8, no. 9, p. 659, 2018, doi: 10.3390/met8090659.

[41] D. S. Shim, G. Y. Baek, and E. M. Lee, "Effect of substrate preheating by induction heater on direct energy deposition of AISI M4 powder," *Mater. Sci. Eng. A*, vol. 682, no. November 2016, pp. 550–562, 2017, doi: 10.1016/j.msea.2016.11.029.

[42] J. Walker, J. R. Middendorf, C. C. C. Lesko, and J. Gockel, "Multi-material laser powder bed fusion additive manufacturing in 3-dimensions," *Manuf. Lett.*, vol. 31, pp. 74–77, 2022, doi: 10.1016/j.mfglet.2021.07.011.

[43] G. Roberts, G. Krauss, and R. Kennedy, *Tool Steels*, 5th ed. Materials Park, OH: ASM International, 1998.

[44] ASM, *Alloy Phase Diagram, vol. 3*. ASM International, 1992.

[45] W. F. Smith, *Structure and Properties of Engineering Alloys*, 1st ed. New York: McGraw-Hill Inc., 1981.

[46] ASM International, *ASM Handbook, Vol. 4. Heat-treating.* ASM International, 1991.

[47] D. G. R. William D. Callister, Jr., *Materials Science and Engineering: An Introduction - 7th Edition*, 9th ed. Hoboken, New Jersey: John Wiley & Sons, Inc., 2013.

[48] ASM, *Properties and Selection: Irons, Steels, and High-Performance Alloys, vol. 1*. ASM International, 1990.

[49] J. R. Davis, Ed., *Metals Handbook - Desk Edition*, 2nd ed. Boca Raton, Florida: CRC Press, 1998.

[50] J. Choi and Y. Chang, "Characteristics of laser aided direct metal/material deposition process for tool steel," *Int. J. Mach. Tools Manuf.*, vol. 45, no. 4–5, pp. 597–607, 2005, doi: 10.1016/j.ijmachtools.2004.08.014.

[51] J. Chen and L. Xue, "Laser cladding of wear resistant CPM 9V tool steel on hardened H13 substrate for potential automotive tooling Applications," *Mater. Sci. Technol. Conf. Exhib. 2010, MS T'10*, vol. 4, 2010.

[52] L. X. Jianyin Chen, "Comparison study of H13 tool steel microstructure produced by laser cladding and laser consolidation," 2010.

[53] B. Ule, F. Vodopivec, M. Pristavec, and F. Gresovnik, "Temper embrittlement of hot work die steel," vol. 6, no. December, pp. 1181–1186, 1990.

[54] G. Telasang, J. Dutta Majumdar, N. Wasekar, G. Padmanabham, and I. Manna, "Microstructure and Mechanical Properties of Laser Clad and Post-cladding

Tempered AISI H13 Tool Steel," *Metall. Mater. Trans. A Phys. Metall. Mater. Sci.*, vol. 46, no. 5, pp. 2309–2321, 2015, doi: 10.1007/s11661-015-2757-z.

[55] F. Klocke, K. Arntz, M. Teli, K. Winands, M. Wegener, and S. Oliari, "State-of-the-art Laser Additive Manufacturing for Hot-work Tool Steels," *Procedia CIRP*, vol. 63, pp. 58–63, 2017, doi: 10.1016/j.procir.2017.03.073.

[56] G. K. A. R Marder, "The Morphology of Martensite in Iron-Carbon Alloys," *Trans. Am. Soc. Met.*, vol. 60, pp. 651–660, 1967.

[57] H. G. Nanesa, M. Jahazi, and R. Naraghi, "Martensitic transformation in AISI D2 tool steel during continuous cooling to 173 K," *J. Mater. Sci.*, vol. 50, no. 17, pp. 5758–5768, 2015, doi: 10.1007/s10853-015-9123-9.

[58] ASM, *Welding brazing and soldering, vol. 6*. ASM International, 1993.

[59] H. K. D. H. Bhadeshia and R. W. K. Honeycombe, *Steels: Microstructure and Properties*, 4th ed. Oxford: Butterworth-Heinemann, 2017.

[60] J. Cech, D. Canelo-yubero, and N. Ganev, "Microstructure and Mechanical Properties of Laser Additive Manufactured H13 Tool Steel," *Metals (Basel).*, vol. 12, no. 2, pp. 1–21, 2022, doi: https://doi.org/10.3390/met12020243.

[61] A. Medvedeva, J. Bergström, S. Gunnarsson, and J. Andersson, "High-temperature properties and microstructural stability of hot-work tool steels," *Mater. Sci. Eng. A*, vol. 523, no. 1–2, pp. 39–46, 2009, doi: 10.1016/j.msea.2009.06.010.

[62] A. Ning, W. Mao, X. Chen, H. Guo, and J. Guo, "Precipitation Behavior of Carbides in H13 Hot Work Die Steel and Its Strengthening during Tempering,"

Metals (Basel)., vol. 7, no. 3, p. 70, 2017, doi: 10.3390/met7030070.

[63] C. S. Smith and E. W. Palmer, "Alloys of copper and iron," *Jom*, vol. 2, no. 12, pp. 1486–1499, 1950, doi: 10.1007/bf03399177.

[64] I. Yamauchi, T. Irie, and H. Sakaguchi, "Metastable liquid separation in undercooled Fe-Cu and Fe-Cu-Si melts containing a small B concentration and their solidification structure," *J. Alloys Compd.*, vol. 403, no. 1–2, pp. 211–216, 2005, doi: 10.1016/j.jallcom.2005.05.031.

[65] M. K. Imran, S. H. Masood, M. Brandt, S. Bhattacharya, and J. Mazumder, "Direct metal deposition (DMD) of H13 tool steel on copper alloy substrate: Evaluation of mechanical properties," *Mater. Sci. Eng. A*, vol. 528, no. 9, pp. 3342–3349, 2011, doi: 10.1016/j.msea.2010.12.099.

[66] M. Shen and M. B. Bever, "Gradients in polymeric materials," *J. Mater. Sci.*, vol. 7, no. 7, pp. 741–746, 1972, doi: 10.1007/BF00549902.

[67] M. Koizumi, "FGM activities in Japan," *Compos. Part B Eng.*, vol. 28, no. 1–2, pp. 1–4, 1997, doi: https://doi.org/10.1016/S1359-8368(96)00016-9.

[68] R. Singh, V. Bhavar, P. Kattire, S. Thakare, S. Patil, and R. K. P. Singh, "x," *IOP Conf. Ser. Mater. Sci. Eng.*, vol. 229, no. 1, 2017, doi: 10.1088/1757-899X/229/1/012021.

[69] R. M. Mahamood, E. T. Akinlabi, M. Shukla, and S. Pityana, "Functionally graded material: An overview," *Lect. Notes Eng. Comput. Sci.*, vol. 3, pp. 1593–1597, 2012.

[70] J. Song, Y. Yu, Z. Zhuang, Y. Lian, X. Liu, and Y. Qi, “Preparation of W-Cu functionally graded material coated with CVD-W for plasma-facing components,” *J. Nucl. Mater.*, vol. 442, no. 1-3 SUPPL.1, pp. S208–S213, 2013, doi: 10.1016/j.jnucmat.2013.01.326.

[71] E. Askari, M. Mehrali, I. H. S. C. Metselaar, N. A. Kadri, and M. M. Rahman, “Fabrication and mechanical properties of Al2O3/SiC/ZrO2 functionally graded material by electrophoretic deposition,” *J. Mech. Behav. Biomed. Mater.*, vol. 12, pp. 144–150, 2012, doi: 10.1016/j.jmbbm.2012.02.029.

[72] J. Rodriguez, K. Hoefer, A. Haelsig, and P. Mayr, “Functionally graded SS 316l to ni-based structures produced by 3D plasma metal deposition,” *Metals (Basel).*, vol. 9, no. 6, 2019, doi: 10.3390/met9060620.

[73] I. M. El-Galy, B. I. Saleh, and M. H. Ahmed, “Functionally graded materials classifications and development trends from industrial point of view,” *SN Appl. Sci.*, vol. 1, no. 11, pp. 1–23, 2019, doi: 10.1007/s42452-019-1413-4.

[74] R. S. Parihar, S. Gangi Setti, and R. K. Sahu, “Preliminary investigation on development of functionally graded cemented tungsten carbide with solid lubricant via ball milling and spark plasma sintering,” *J. Compos. Mater.*, vol. 52, no. 10, pp. 1363–1377, 2018, doi: 10.1177/0021998317724217.

[75] J. J. Sobczak and L. Drenchev, “Metallic Functionally Graded Materials: A Specific Class of Advanced Composites,” *J. Mater. Sci. Technol.*, vol. 29, no. 4, pp. 297–316, 2013, doi: 10.1016/j.jmst.2013.02.006.

[76] R. Singh, V. Bhavar, P. Kattire, S. Thakare, S. Patil, and R. K. P. Singh, “A

Review on Functionally Gradient Materials (FGMs) and Their Applications," *IOP Conf. Ser. Mater. Sci. Eng.*, vol. 229, no. 1, 2017, doi: 10.1088/1757-899X/229/1/012021.

[77] E. W. Spisz, A. J. Weigund, R. L. Bowmun, and J. R. Juck, "Solar absorptances and spectral reflectances of 12 metals for temperatures ranging from 300 to 500 K.," *Nasa, Tn D-5353*, no. August 1969, 1969, [Online]. Available: https://ntrs.nasa.gov/archive/nasa/casi.ntrs.nasa.gov/19690022517.pdf.

[78] M. Naeem, "Laser Processing of Reflective Materials," *Laser Tech. J.*, vol. 10, no. 1, pp. 18–20, 2013, doi: 10.1002/latj.201390001.

[79] H. Siva Prasad, F. Brueckner, J. Volpp, and A. F. H. Kaplan, "Laser metal deposition of copper on diverse metals using green laser sources," *Int. J. Adv. Manuf. Technol.*, vol. 107, no. 3–4, pp. 1559–1568, 2020, doi: 10.1007/s00170-020-05117-z.

[80] K. Asano *et al.*, "Laser metal deposition of pure copper on stainless steel with blue and IR diode lasers," *Opt. Laser Technol.*, vol. 107, pp. 291–296, 2018, doi: 10.1016/j.optlastec.2018.06.012.

[81] F. F. Noecker and J. N. DuPont, "Microstructural development and solidification cracking susceptibility of Cu deposits on steel: Part I," *J. Mater. Sci.*, vol. 42, no. 2, pp. 495–509, 2007, doi: 10.1007/s10853-006-1258-2.

[82] Y. S. Touloukian, R. W. Powell, C. Y. Ho, and P. G. Klemens, "Thermal Conductivity of Metallic Elements and Alloys," vol. 1, 1970.

[83] K. C. Apacki, “Copper-alloy molds provide cycle time and quality advantages for injection molding and resin transfer molding,” *SAE Tech. Pap.*, vol. 104, no. 1995, pp. 470–480, 1995, doi: 10.4271/950566.

[84] M. Naebe and K. Shirvanimoghaddam, “Functionally graded materials: A review of fabrication and properties,” *Appl. Mater. Today*, vol. 5, pp. 223–245, 2016, doi: 10.1016/j.apmt.2016.10.001.

[85] Z. Zeng *et al.*, “Wire and arc additive manufacturing of a Ni-rich NiTi shape memory alloy: Microstructure and mechanical properties,” *Addit. Manuf.*, vol. 32, no. January, 2020, doi: 10.1016/j.addma.2020.101051.

[86] T. A. Rodrigues *et al.*, “In-situ strengthening of a high strength low alloy steel during Wire and Arc Additive Manufacturing (WAAM),” *Addit. Manuf.*, vol. 34, no. March, 2020, doi: 10.1016/j.addma.2020.101200.

[87] A. Angelastro and S. L. Campanelli, “Direct laser metal deposition of WC / Co / Cr powder by means of the functionally graded materials strategy Direct laser metal deposition of WC / Co / Cr powder by means of the functionally graded materials strategy,” *Surf. Topogr. Metrol. Prop.*, vol. 5, 2017.

[88] W. Li, J. Zhang, X. Zhang, and F. Liou, “Effect of optimizing particle size on directed energy deposition of Functionally Graded Material with blown Pre-Mixed Multi-Powder,” *Manuf. Lett.*, vol. 13, pp. 39–43, 2017, doi: 10.1016/j.mfglet.2017.07.001.

[89] K. Arnold, R. Fletcher, D. Daniels, “Layered Fabrication of Tool Steel and Functionally Graded Materials with a Nd: YAG Pulsed Laser,” *Scandanavian J.*

Med. Sci. Sport., vol. 26, no. 3, pp. 348–358, 2016, doi: 10.3390/buildings5020405.

[90] R. M. Mahamood and E. T. Akinlabi, "Laser metal deposition of functionally graded Ti6Al4V / TiC," *Jmade*, vol. 84. pp. 402–410, 2015, doi: 10.1016/j.matdes.2015.06.135.

[91] Y. Sato *et al.*, "Fabrication of Pure Copper Rod by Multi-beam Laser Metal Deposition with Blue Diode Lasers," *J. Laser Micro Nanoeng.*, vol. 16, no. 3, pp. 189–193, 2021, doi: 10.2961/JLMN.2021.03.2007.

[92] M. A. Lodes, R. Guschlbauer, and C. Körner, "Process development for the manufacturing of 99.94% pure copper via selective electron beam melting," *Mater. Lett.*, vol. 143, pp. 298–301, 2015, doi: 10.1016/j.matlet.2014.12.105.

[93] V. E. Beal, P. Erasenthiran, C. H. Ahrens, and P. Dickens, "Evaluating the use of functionally graded materials inserts produced by selective laser melting on the injection moulding of plastics parts," *Proc. Inst. Mech. Eng. Part B J. Eng. Manuf.*, vol. 221, no. 6, pp. 945–954, 2007, doi: 10.1243/09544054JEM764.

[94] I. Sciences and M. K. Imran, "Copper Based Bi-Metallic Tooling for High Pressure Die Casting Using Direct Metal Deposition," Swinburne University of Technology, 2012.

[95] M. K. Imran, S. H. Masood, W. Q. Song, and M. Brandt, "Study of Bond Strength for Laser Direct Metal Deposition of Tool Steel on Copper Alloy Substrate," *Adv. Mater. Res.*, vol. 230–232, pp. 945–948, 2011, doi: 10.4028/www.scientific.net/AMR.230-232.945.

[96] X. Zhang *et al.*, “Additive manufacturing of copper – H13 tool steel bi-metallic structures via Ni-based multi-interlayer,” *Addit. Manuf.*, vol. 36, p. 101474, 2020, doi: 10.1016/j.addma.2020.101474.

[97] U. Artiček, “Razvoj mikrostrukture pri izdelavi gradientnega materiala H13-Cu,” 2014.

[98] K. S. Osipovich *et al.*, “Gradient transition zone structure in ‘steel–copper’ sample produced by double wire-feed electron beam additive manufacturing,” *J. Mater. Sci.*, vol. 55, no. 22, pp. 9258–9272, 2020, doi: 10.1007/s10853-020-04549-y.

[99] V. E. Beal, P. Erasenthiran, N. Hopkinson, P. Dickens, and C. H. Ahrens, “The effect of scanning strategy on laser fusion of functionally graded H13/Cu materials,” *Int. J. Adv. Manuf. Technol.*, vol. 30, no. 9–10, pp. 844–852, 2006, doi: 10.1007/s00170-005-0130-x.

[100] A. Popovich, V. Sufiiarov, I. Polozov, E. Borisov, D. Masaylo, and A. Orlov, “Microstructure and mechanical properties of additive manufactured copper alloy,” *Mater. Lett.*, vol. 179, pp. 38–41, 2016, doi: 10.1016/j.matlet.2016.05.064.

[101] L. Constantin *et al.*, “Additive manufacturing of copper/diamond composites for thermal management applications,” *Manuf. Lett.*, vol. 24, pp. 61–66, 2020, doi: 10.1016/j.mfglet.2020.03.014.

[102] J. A. Williams, “Analytical models of scratch hardness,” *Tribol. Int.*, vol. 29, no. 8, pp. 675–694, 1996, doi: 10.1016/0301-679X(96)00014-X.

[103] X. Xu, S. van der Zwaag, and W. Xu, “The effect of martensite volume fraction on

the scratch and abrasion resistance of a ferrite-martensite dual phase steel," *Wear*, vol. 348–349, pp. 80–88, 2016, doi: 10.1016/j.wear.2015.11.017.

[104] A. Bahrami, S. H. M. Anijdan, M. A. Golozar, M. Shamanian, and N. Varahram, "Effects of conventional heat treatment on wear resistance of AISI H13 tool steel," *Wear*, vol. 258, no. 5–6, pp. 846–851, 2005, doi: 10.1016/j.wear.2004.09.008.

[105] S. D. Barbara Illowsky, *Introductory Statistics*. Houston: OpenStax, Rice University, 2013.

[106] ASTM E975, "X-Ray Determination of Retained Austenite in Steel with Near Random Crystallographic Orientation." doi: 10.1520/E0975-13.necessary.

[107] L.Markusson, "Powder characterization for additive manufacturing processes," Luleå University of Technology, 2017.

[108] R. J. S. C. Y. Kong, P. A. Carroll, P. Brown, "The Effect of Average Powder Particle Size on Deposition Efficiency, Deposit Height and Surface Roughness in the Direct Metal Laser Deposition Process," in *14th International Conference on Joining Materials*, 2007, [Online]. Available: https://www.twi-global.com/technical-knowledge/published-papers/the-effect-of-average-powder-particle-size-on-deposition-efficiency-deposit-height-and-surface-roughness-in-the-direct-metal-las.

[109] R. M. Mahamood and E. T. Akinlabi, "Scanning speed and powder flow rate influence on the properties of laser metal deposition of titanium alloy," *Int. J. Adv. Manuf. Technol.*, vol. 91, no. 5–8, pp. 2419–2426, 2017, doi: 10.1007/s00170-016-9954-9.

[110] R. M. Mahamood, E. T. Akinlabi, M. Shukla, and S. Pityana, "Characterizing the effect of laser power density on microstructure, microhardness, and surface finish of laser deposited titanium alloy," *J. Manuf. Sci. Eng. Trans. ASME*, vol. 135, no. 6, pp. 2013–2016, 2013, doi: 10.1115/1.4025737.

[111] R. M. Mahamood and E. T. Akinlabi, "Effect of Powder Flow Rate on Surface Finish in Laser Additive Manufacturing Process," *IOP Conf. Ser. Mater. Sci. Eng.*, vol. 391, no. 1, 2018, doi: 10.1088/1757-899X/391/1/012005.

[112] J. P. Oliveira, T. G. Santos, and R. M. Miranda, "Revisiting fundamental welding concepts to improve additive manufacturing: From theory to practice," *Prog. Mater. Sci.*, vol. 107, p. 100590, 2020, doi: 10.1016/j.pmatsci.2019.100590.

[113] F. Caiazzo and V. Alfieri, "Laser-aided directed energy deposition of steel powder over flat surfaces and edges," *Materials (Basel).*, vol. 11, no. 3, 2018, doi: 10.3390/ma11030435.

[114] F. Caiazzo, V. Alfieri, P. Argenio, and V. Sergi, "Additive manufacturing by means of laser-aided directed metal deposition of 2024 aluminium powder: Investigation and optimization," *Adv. Mech. Eng.*, vol. 9, no. 8, pp. 1–12, 2017, doi: 10.1177/1687814017714982.

[115] A. Saboori *et al.*, "Production of single tracks of Ti-6Al-4V by directed energy deposition to determine the layer thickness for multilayer deposition," *J. Vis. Exp.*, vol. 2018, no. 133, pp. 1–10, 2018, doi: 10.3791/56966.

[116] J. H. Jang, B. D. Joo, S. M. Mun, M. Y. Sung, and Y. H. Moon, "Application of direct laser melting to restore damaged steel dies," *Met. Mater. Int.*, vol. 17, no. 1,

pp. 167–174, 2011, doi: 10.1007/s12540-011-0223-z.

[117] E. M. Lee, G. Y. Shin, H. S. Yoon, and D. S. Shim, “Study of the effects of process parameters on deposited single track of M4 powder based direct energy deposition,” *J. Mech. Sci. Technol.*, vol. 31, no. 7, pp. 3411–3418, 2017, doi: 10.1007/s12206-017-0239-5.

[118] C. Zhong, T. Biermann, A. Gasser, and R. Poprawe, “Experimental study of effects of main process parameters on porosity, track geometry, deposition rate, and powder efficiency for high deposition rate laser metal deposition,” *J. Laser Appl.*, vol. 27, no. 4, p. 042003, 2015, doi: 10.2351/1.4923335.

[119] J. S. Park, J. H. Park, M. G. Lee, J. H. Sung, K. J. Cha, and D. H. Kim, “Effect of Energy Input on the Characteristic of AISI H13 and D2 Tool Steels Deposited by a Directed Energy Deposition Process,” *Metall. Mater. Trans. A Phys. Metall. Mater. Sci.*, vol. 47, no. 5, pp. 2529–2535, 2016, doi: 10.1007/s11661-016-3427-5.

[120] P. A. Kobryn, E. H. Moore, and S. L. Semiatin, “Effect of laser power and traverse speed on microstructure, porosity, and build height in laser-deposited Ti-6Al-4V,” *Scr. Mater.*, vol. 43, no. 4, pp. 299–305, 2000, doi: 10.1016/S1359-6462(00)00408-5.

[121] G. Zhu, D. Li, A. Zhang, G. Pi, and Y. Tang, “The influence of laser and powder defocusing characteristics on the surface quality in laser direct metal deposition,” *Opt. Laser Technol.*, vol. 44, no. 2, pp. 349–356, 2012, doi: 10.1016/j.optlastec.2011.07.013.

[122] D. S. Shim, G. Y. Baek, J. S. Seo, G. Y. Shin, K. P. Kim, and K. Y. Lee, “Effect of

layer thickness setting on deposition characteristics in direct energy deposition (DED) process," *Opt. Laser Technol.*, vol. 86, pp. 69–78, 2016, doi: 10.1016/j.optlastec.2016.07.001.

[123] M. Marya, V. Singh, J. Y. Hascoet, and S. Marya, "A Metallurgical Investigation of the Direct Energy Deposition Surface Repair of Ferrous Alloys," *J. Mater. Eng. Perform.*, vol. 27, no. 2, pp. 813–824, 2018, doi: 10.1007/s11665-017-3117-5.

[124] A. J. Pinkerton and L. Li, "Effects of powder geometry and composition in coaxial laser deposition of 316L steel for rapid prototyping," *CIRP Ann. - Manuf. Technol.*, vol. 52, no. 1, pp. 181–184, 2003, doi: 10.1016/S0007-8506(07)60560-5.

[125] S. Nam, H. Cho, C. Kim, and Y.-M. Kim, "Effect of Process Parameters on Deposition Properties of Functionally Graded STS 316/Fe Manufactured by Laser Direct Metal Deposition," *Metals (Basel).*, vol. 8, no. 8, p. 607, 2018, doi: 10.1099/0022-1317-77-11-2819.

[126] H. Qi, J. Mazumder, and H. Ki, "Numerical simulation of heat transfer and fluid flow in coaxial laser cladding process for direct metal deposition," *J. Appl. Phys.*, vol. 100, no. 2, 2006, doi: 10.1063/1.2209807.

[127] M. Gharbi *et al.*, "Influence of various process conditions on surface finishes induced by the direct metal deposition laser technique on a Ti-6Al-4V alloy," *J. Mater. Process. Technol.*, vol. 213, no. 5, pp. 791–800, 2013, doi: 10.1016/j.jmatprotec.2012.11.015.

[128] A. J. Pinkerton and L. Li, "Rapid prototyping using direct laser deposition - The effect of powder atomization type and flowrate," *Proc. Inst. Mech. Eng. Part B J.*

Eng. Manuf., vol. 217, no. 6, pp. 741–752, 2003, doi: 10.1243/09544050360673134.

[129] R. M. Mahamood and E. T. Akinlabi, "Effect of laser power on surface finish during Laser Metal Deposition process," *Lect. Notes Eng. Comput. Sci.*, vol. 2, pp. 965–969, 2014.

[130] M. Rombouts, G. Maes, W. Hendrix, E. Delarbre, and F. Motmans, "Surface finish after laser metal deposition," *Phys. Procedia*, vol. 41, pp. 810–814, 2013, doi: 10.1016/j.phpro.2013.03.152.

[131] D. Wang, S. Mai, D. Xiao, and Y. Yang, "Surface quality of the curved overhanging structure manufactured from 316-L stainless steel by SLM," *Int. J. Adv. Manuf. Technol.*, vol. 86, no. 1–4, pp. 781–792, 2016, doi: 10.1007/s00170-015-8216-6.

[132] D. F. Susan, J. D. Puskar, J. A. Brooks, and C. V. Robino, "Quantitative characterization of porosity in stainless steel LENS powders and deposits," *Mater. Charact.*, vol. 57, no. 1, pp. 36–43, 2006, doi: 10.1016/j.matchar.2005.12.005.

[133] Y. Hua and J. Choi, "Feedback control effects on dimensions and defects of H13 tool steel by direct metal deposition process," *J. Laser Appl.*, vol. 17, no. 2, pp. 118–126, 2005, doi: 10.2351/1.1848530.

[134] F. Sciammarella and B. Salehi Najafabadi, "Processing Parameter DOE for 316L Using Directed Energy Deposition," *J. Manuf. Mater. Process.*, vol. 2, no. 3, p. 61, 2018, doi: 10.3390/jmmp2030061.

[135] N. A. Kistler, D. J. Corbin, A. R. Nassar, E. W. Reutzel, and A. M. Beese, "Effect of processing conditions on the microstructure, porosity, and mechanical properties of Ti-6Al-4V repair fabricated by directed energy deposition," *J. Mater. Process. Technol.*, vol. 264, pp. 172–181, 2019, doi: 10.1016/j.jmatprotec.2018.08.041.

[136] R. Besler, M. Bauer, K. P. Furlan, A. N. Klein, and R. Janssen, "Effect of processing route on the microstructure and mechanical properties of hot work tool steel," *Mater. Res.*, vol. 20, no. 6, pp. 11–19, 2017, doi: 10.1590/1980-5373-MR-2016-0726.

[137] F. Pöhl, C. Hardes, F. Scholz, and J. Frenzel, "Orientation-Dependent Deformation Behavior of 316L Steel Manufactured by Laser Metal Deposition and Casting under Local Scratch and Indentation Load," *Materials (Basel).*, vol. 13, no. 7, p. 1765, 2020, doi: 10.3390/ma13071765.

[138] J. Mazumder, A. Schifferer, and J. Choi, "Direct materials deposition: Designed macro and microstructure," *Mater. Res. Innov.*, vol. 3, no. 3, pp. 118–131, 1999, doi: 10.1007/s100190050137.

[139] W. Kurz and D. J. Fisher, *Fundamentals Of Solidification*, Third. Enfield, 1992.

[140] C. Böhm, M. Werz, and S. Weihe, "Dilution ratio and the resulting composition profile in dissimilar laser powder bed fusion of alsi10mg and al99.8," *Metals (Basel).*, vol. 10, no. 9, pp. 1–12, 2020, doi: 10.3390/met10091222.

[141] A. Fathi, E. Toyserkani, A. Khajepour, and M. Durali, "Prediction of melt pool depth and dilution in laser powder deposition," *J. Phys. D. Appl. Phys.*, vol. 39, no.

12, pp. 2613–2623, 2006, doi: 10.1088/0022-3727/39/12/022.

[142] K. Zhang, X. Zhang, and W. Liu, “Influences of processing parameters on dilution ratio of laser cladding layer during laser metal deposition shaping,” *Adv. Mater. Res.*, vol. 549, pp. 785–789, 2012, doi: 10.4028/www.scientific.net/AMR.549.785.

[143] Y. Chen, Y. Guo, B. Lu, M. Xu, and J. Xu, “Microstructure and properties of the interface area in the laser cladded ni based coatings on the 1Cr10Mo1NiWVNbN steel,” *Metals (Basel).*, vol. 7, no. 5, pp. 1–9, 2017, doi: 10.3390/met7050175.

[144] G. Y. Baek *et al.*, “Mechanical characteristics of a tool steel layer deposited by using direct energy deposition,” *Met. Mater. Int.*, vol. 23, no. 4, pp. 770–777, 2017, doi: 10.1007/s12540-017-6442-1.

[145] J. Leunda, V. G. Navas, C. Soriano, and C. Sanz, “Improvement of Laser Deposited High Alloyed Powder Metallurgical Tool Steel by a Post-tempering Treatment,” *Phys. Procedia*, vol. 39, pp. 392–400, 2012, doi: 10.1016/j.phpro.2012.10.053.

[146] L. Xue, J. Chen, and S. H. Wang, “Freeform Laser Consolidated H13 and CPM 9V Tool Steels,” *Metallogr. Microstruct. Anal.*, vol. 2, no. 2, pp. 67–78, 2013, doi: 10.1007/s13632-013-0061-0.

[147] M. T. Coll Ferrari, “Effect of austenitising temperature and cooling rate on microstructures of hot-work tool steels,” University West, 2015.

[148] H. Wang, S. Zhang, C. Zhang, C. Wu, J. Zhang, and A. O. Abdullah, “Effects of V and Cr on laser cladded Fe-based coatings,” *Coatings*, vol. 8, no. 3, 2018, doi:

10.3390/coatings8030107.

[149] F. Deirmina, N. Peghini, B. Almangour, D. Grzesiak, and M. Pellizzari, “Heat treatment and properties of a hot work tool steel fabricated by additive manufacturing,” *Mater. Sci. Eng. A*, vol. 753, no. January, pp. 109–121, 2019, doi: 10.1016/j.msea.2019.03.027.

[150] K. M. McHugh, Y. Lin, Y. Zhou, and E. J. Lavernia, “Influence of cooling rate on phase formation in spray-formed H13 tool steel,” *Mater. Sci. Eng. A*, vol. 477, no. 1–2, pp. 50–57, 2008, doi: 10.1016/j.msea.2007.05.121.

[151] M. J. Holzweissig, A. Taube, F. Brenne, M. Schaper, and T. Niendorf, “Microstructural Characterization and Mechanical Performance of Hot Work Tool Steel Processed by Selective Laser Melting,” *Metall. Mater. Trans. B Process Metall. Mater. Process. Sci.*, vol. 46, no. 2, pp. 545–549, 2015, doi: 10.1007/s11663-014-0267-9.

[152] J. Speer, D. K. Matlock, B. C. De Cooman, and J. G. Schroth, “Carbon partitioning into austenite after martensite transformation,” *Acta Mater.*, vol. 51, no. 9, pp. 2611–2622, 2003, doi: 10.1016/S1359-6454(03)00059-4.

[153] D. V. Edmonds, K. He, F. C. Rizzo, B. C. De Cooman, D. K. Matlock, and J. G. Speer, “Quenching and partitioning martensite-A novel steel heat treatment,” *Mater. Sci. Eng. A*, vol. 438–440, no. SPEC. ISS., pp. 25–34, 2006, doi: 10.1016/j.msea.2006.02.133.

[154] L. Wang and J. G. Speer, “Quenching and Partitioning Steel Heat Treatment,” *Metallogr. Microstruct. Anal.*, vol. 2, no. 4, pp. 268–281, 2013, doi:

10.1007/s13632-013-0082-8.

[155] J. S. Park *et al.*, “Effect of heat treatment on the characteristics of tool steel deposited by the directed energy deposition process,” *Met. Mater. Int.*, vol. 22, no. 1, pp. 143–147, 2016, doi: 10.1007/s12540-016-5372-7.

[156] C. Chen *et al.*, “Effect of Heat Treatment on Microstructure and Mechanical Properties of Laser Additively Manufactured AISI H13 Tool Steel,” *J. Mater. Eng. Perform.*, vol. 26, no. 11, pp. 5577–5589, 2017, doi: 10.1007/s11665-017-2992-0.

[157] N. Ur Rahman, M. B. de Rooij, D. T. A. Matthews, G. Walmag, M. Sinnaeve, and G. R. B. E. Römer, “Wear characterization of multilayer laser cladded high speed steels,” *Tribol. Int.*, vol. 130, no. August 2018, pp. 52–62, 2019, doi: 10.1016/j.triboint.2018.08.019.

[158] S. H. Riza, “Mechanical Characterisation of High Strength Alloys Produced by Laser Assisted Direct Metal Deposition,” Swinburne, 2015.

[159] R. Cottam, J. Wang, and V. Luzin, “Characterization of microstructure and residual stress in a 3D H13 tool steel component produced by additive manufacturing,” *J. Mater. Res.*, vol. 29, no. 17, pp. 1978–1986, 2014, doi: 10.1557/jmr.2014.190.

[160] R. Colaço and R. Vilar, “Effect of Laser Surface Melting on the Tempering Behaviour of Din X42Cr13 Stainless Tool Steel,” *Scr. Mater.*, vol. 38, no. 1, pp. 107–113, 1997, doi: 10.1016/s1359-6462(97)00441-7.

[161] J. Leunda, C. Soriano, C. Sanz, and V. G. Navas, “Laser cladding of vanadium-

carbide tool steels for die repair," *Phys. Procedia*, vol. 12, pp. 345–352, 2011, doi: 10.1016/j.phpro.2011.03.044.

[162] J. Guo, L. Ai, T. Wang, Y. Feng, D. Wan, and Q. Yang, "Microstructure evolution and micro-mechanical behavior of secondary carbides at grain boundary in a Fe–Cr–W–Mo–V–C alloy," *Mater. Sci. Eng. A*, vol. 715, no. August 2017, pp. 359–369, 2018, doi: 10.1016/j.msea.2018.01.024.

[163] Attaullah Arain, "Heat Treatment and Toughness Behavior of Tool Steels (D2 and H13) for Cutting Blades," University of Toronto, 1999.

[164] J. Zeisig *et al.*, "Microstructure and abrasive wear behavior of a novel FeCrMoVC laser cladding alloy for high-performance tool steels," *Wear*, vol. 382–383, no. February, pp. 107–112, 2017, doi: 10.1016/j.wear.2017.04.021.

[165] S. H. Wang, J. Y. Chen, and L. Xue, "A study of the abrasive wear behaviour of laser-clad tool steel coatings," *Surf. Coatings Technol.*, vol. 200, no. 11, pp. 3446–3458, 2006, doi: 10.1016/j.surfcoat.2004.10.125.

[166] N. Hashemi *et al.*, "Oxidative wear behaviour of laser clad High Speed Steel thick deposits: Influence of sliding speed, carbide type and morphology," *Surf. Coatings Technol.*, vol. 315, pp. 519–529, 2017, doi: 10.1016/j.surfcoat.2017.02.071.

[167] M. Roy, *Surface engineering for enhanced performance against wear*, vol. 9783709101. 2013.

[168] B212, "Standard Test Method for Apparent Density of Free-Flowing Metal Powders Using the Hall Flowmeter Funnel," *ASTM Stand.*, vol. 02, no. August, pp.

89–91, 2017, doi: 10.1520/B0212-17.2.

[169] ASTM, “B213-17: Standard Test Methods for Flow Rate of Metal Powders Using the Hall Flowmeter,” *ASTM Stand.*, pp. 1–4, 2017, doi: 10.1520/B0213-17.2.

[170] T. Ishida, “The interaction of molten copper with solid iron,” *J. Mater. Sci.*, vol. 21, no. 4, pp. 1171–1179, 1986, doi: 10.1007/BF00553249.

[171] R. N. Grugel and A. H. Well, “Alloy solidification in systems containing a liquid miscibility gap,” *Metall. Trans. A*, vol. 12, no. 4, pp. 669–681, 1981, doi: 10.1007/BF02649742.

[172] D. Varanasi and P. Baumli, “Grain boundary behavior of copper with C45 medium carbon steel,” *Resolut. Discov.*, vol. 3, no. 2, pp. 24–28, 2018, doi: 10.1556/2051.2018.00059.

[173] H. Terasaki, Y. Komizo, and S. Member, “Solidification cracking susceptibility of alloy tool steel,” pp. 126–129, 2009.

[174] H. B. D. L. Aucott, J. Li, A. Rack, “Solidification cracking during welding of steel : In situ X-ray observation Solidification cracking during welding of steel : In situ X-ray observation,” in *IOP Conf. Series: Materials Science and Engineering 529*, 2019, p. 6, doi: 10.1088/1757-899X/529/1/012026.

[175] T. Hashimoto, H. Terasaki, and Y. Komizo, “Effect of tip velocity on weld solidification process of hot-work tool steel,” *Weld. Int.*, vol. 23, no. 6, pp. 431–438, 2009, doi: 10.1080/09507110802542932.

[176] G. Agarwal, A. Kumar, I. M. Richardson, and M. J. M. Hermans, “Evaluation of

solidification cracking susceptibility during laser welding in advanced high strength automotive steels," *Mater. Des.*, vol. 183, p. 108104, 2019, doi: 10.1016/j.matdes.2019.108104.

[177] V. E. Beal, P. Erasenthiran, N. Hopkinson, P. Dickens, and C. H. Ahrens, "Optimisation of processing parameters in laser fused H13/Cu materials using response surface method (RSM)," *J. Mater. Process. Technol.*, vol. 174, no. 1–3, pp. 145–154, 2006, doi: 10.1016/j.jmatprotec.2005.04.101.

[178] W. D. Callister Jr and D. G. Rethwisch, *Materials Science and Engineering - An Introduction 10th Edition*. 2018.

[179] I. Magnabosco, P. Ferro, F. Bonollo, and L. Arnberg, "An investigation of fusion zone microstructures in electron beam welding of copper-stainless steel," *Mater. Sci. Eng. A*, vol. 424, no. 1–2, pp. 163–173, 2006, doi: 10.1016/j.msea.2006.03.096.

[180] J. N. DuPont, C. V. Robino, J. R. Michael, M. R. Nous, and A. R. Marder, "Solidification of Nb-bearing superalloys: Part I. Reaction sequences," *Metall. Mater. Trans. A Phys. Metall. Mater. Sci.*, vol. 29, no. 11, pp. 2785–2796, 1998, doi: 10.1007/s11661-998-0319-3.

[181] S. Kou, "Solidification and liquation cracking issues in welding," *Jom*, vol. 55, no. 6, pp. 37–42, 2003, doi: 10.1007/s11837-003-0137-4.

[182] Y. Sato *et al.*, "In situ X-ray observations of pure-copper layer formation with blue direct diode lasers," *Appl. Surf. Sci.*, vol. 480, no. October 2018, pp. 861–867, 2019, doi: 10.1016/j.apsusc.2019.03.057.

[183] A. Munitz, “Liquid separation effects in Fe-Cu alloys solidified under different cooling rates,” *Metall. Trans. B*, vol. 18, no. 3, pp. 565–575, 1987, doi: 10.1007/BF02654269.

[184] Y. Kimura and S. Takaki, “Phase transformation mechanism of Fe-Cu alloys,” *ISIJ Int.*, vol. 37, no. 3, pp. 290–295, 1997, doi: 10.2355/isijinternational.37.290.

[185] Q. Chen and Z. Jin, “The Fe-Cu system: A thermodynamic evaluation,” *Metall. Mater. Trans. A*, vol. 26, no. 2, pp. 417–426, 1995, doi: 10.1007/BF02664678.

[186] C. Yao, B. Xu, X. Zhang, J. Huang, J. Fu, and Y. Wu, “Interface microstructure and mechanical properties of laser welding copper-steel dissimilar joint,” *Opt. Lasers Eng.*, vol. 47, no. 7–8, pp. 807–814, 2009, doi: 10.1016/j.optlaseng.2009.02.004.

[187] S. Chen, J. Huang, J. Xia, H. Zhang, and X. Zhao, “Microstructural characteristics of a stainless steel/copper dissimilar joint made by laser welding,” *Metall. Mater. Trans. A Phys. Metall. Mater. Sci.*, vol. 44, no. 8, pp. 3690–3696, 2013, doi: 10.1007/s11661-013-1693-z.

[188] Z. H. Liu, D. Q. Zhang, S. L. Sing, C. K. Chua, and L. E. Loh, “Interfacial characterization of SLM parts in multi-material processing: Metallurgical diffusion between 316L stainless steel and C18400 copper alloy,” *Mater. Charact.*, vol. 94, pp. 116–125, 2014, doi: 10.1016/j.matchar.2014.05.001.

[189] C. G. Lee, S. J. Kim, T. H. Lee, and C. S. Oh, “Effects of tramp elements on formability of low-carbon TRIP-aided multiphase cold-rolled steel sheets,” *ISIJ Int.*, vol. 44, no. 4, pp. 737–743, 2004, doi: 10.2355/isijinternational.44.737.

[190] E. Diagram, “The Cr-Cu (Chromium-Copper) System,” vol. 5, no. 1, pp. 59–68, 1984.

[191] H. Okamoto, “Cu-V (Copper-Vanadium),” *J. Phase Equilibria Diffus.*, vol. 31, no. 1, pp. 83–84, 2010, doi: 10.1007/s11669-009-9631-x.

[192] Subramanian P.R. and Laughlin DE, “The Cu-Mo (Copper-Molybdenum) System,” *Bull. Alloy Phase Diagrams*, vol. 11, no. 2, pp. 169–172, 1990.

[193] D. Gu *et al.*, “Densification behavior, microstructure evolution, and wear performance of selective laser melting processed commercially pure titanium,” *Acta Mater.*, vol. 60, no. 9, pp. 3849–3860, 2012, doi: 10.1016/j.actamat.2012.04.006.

[194] W. R. Kim *et al.*, “Microstructural study on a Fe-10Cu alloy fabricated by selective laser melting for defect-free process optimization based on the energy density,” *J. Mater. Res. Technol.*, vol. 9, no. 6, pp. 12834–12839, 2020, doi: 10.1016/j.jmrt.2020.09.051.

[195] L. C. Casteletti, A. N. Lombardi, and G. E. Totten, “Encyclopedia of Tribology,” *Encyclopedia of Tribology*. Springer Boston, Boston, 2013, doi: 10.1007/978-0-387-92897-5.

[196] I. Hutchings and P. Shipway, *Tribology: Friction and wear of engineering materials: Second Edition*. 2017.

[197] J. R. Davis, *Surface Hardening of Steels*, vol. 1, no. 1. ASM International: ASM International, 2002.

[198] W. Muhammad, “Boriding of high carbon high chromium cold work tool steel,” *IOP Conf. Ser. Mater. Sci. Eng.*, vol. 60, no. 1, 2014, doi: 10.1088/1757-899X/60/1/012062.

[199] N. Manthani, A. Joshi, V. Pawar, and R. Singh, “Improvement in Wear Resistance of AISI H13 Steel by Pack-Boronizing Method,” *J. Nanosci. Nanotechnol. Res.*, vol. 2, no. 2, pp. 2–4, 2018, [Online]. Available: http://www.imedpub.com/journal-nanoscience-nanotechnology-research/.

[200] A. Erdoğan, “Investigation of high temperature dry sliding behavior of borided H13 hot work tool steel with nanoboron powder,” *Surf. Coatings Technol.*, vol. 357, no. September 2018, pp. 886–895, 2019, doi: 10.1016/j.surfcoat.2018.10.066.

[201] E. E. V. Cárdenas *et al.*, “Characterization and wear performance of boride phases over tool steel substrates,” *Adv. Mech. Eng.*, vol. 8, no. 2, pp. 1–10, 2016, doi: 10.1177/1687814016630257.

[202] A. Günen *et al.*, “Properties and Corrosion Resistance of AISI H13 Hot-Work Tool Steel with Borided B4C Powders,” *Met. Mater. Int.*, pp. 1329–1340, 2019, doi: 10.1007/s12540-019-00421-0.

[203] S. Şahin, “Effects of boronizing process on the surface roughness and dimensions of AISI 1020, AISI 1040 and AISI 2714,” *J. Mater. Process. Technol.*, vol. 209, no. 4, pp. 1736–1741, 2009, doi: 10.1016/j.jmatprotec.2008.04.040.

[204] M. Carbucicchio and G. Palombarini, “Effects of alloying elements on the growth of iron boride coatings,” *J. Mater. Sci. Lett.*, vol. 6, no. 10, pp. 1147–1149, 1987, doi: 10.1007/BF01729165.

[205] G. Palombarini and M. Carbucicchio, “Influence of carbon on the chromium redistribution when boriding iron alloys,” *J. Mater. Sci. Lett.*, vol. 12, no. 11, pp. 797–798, 1993, doi: 10.1007/BF00277975.

[206] K. Matiašovský, M. Chrenková-Paučírová, P. Fellner, and M. Makyta, “Electrochemical and thermochemical boriding in molten salts,” *Surf. Coatings Technol.*, vol. 35, no. 1–2, pp. 133–149, 1988, doi: 10.1016/0257-8972(88)90064-3.

[207] C. Badini, C. Gianoglio, and G. Pradelli, “Preferential distribution of chromium and nickel in the borided layer obtained on synthetic Fe-Cr-Ni alloys,” *J. Mater. Sci.*, vol. 21, no. 5, pp. 1721–1729, 1986, doi: 10.1007/BF01114731.

[208] V. I. Dybkov, “Boride Coatings of Fe-Cr Alloys and Chromium Steels,” *Int. J. Mater. Chem. Phys.*, vol. 1, no. 1, pp. 43–66, 2015.

[209] M. Carbucicchio and G. Sambogna, “Influence of chromium on boride coatings produced on iron alloys,” *Thin Solid Films*, vol. 126, no. 3–4, pp. 299–305, 1985, doi: 10.1016/0040-6090(85)90324-4.

[210] H. C. Fiedler and W. J. Hayes, “The formation of a solf layer in borided hot work die steels,” *Metall. Trans.*, vol. 1, no. 4, pp. 1071–1073, 1970, doi: 10.1007/BF02811810.

[211] H. Yang, X. Wu, G. Cao, and Z. Yang, “Enhanced boronizing kinetics and high temperature wear resistance of H13 steel with boriding treatment assisted by air blast shot peening,” *Surf. Coatings Technol.*, vol. 307, pp. 506–516, 2016, doi: 10.1016/j.surfcoat.2016.09.029.

[212] K. H. Habig and R. Chatterjee-Fischer, “Wear behaviour of boride layers on alloyed steels.,” *in: Eurotrib ’81, 3Rd Int. Tribology Congress on Tribological Processes in Solid Body Contact Areas, (Warsaw, Poland: Sep. 21*, vol. 1, Radom,. 1981.

APPENDIX

A1. Research Dissemination

The NSERC HI-AM network required semi-annual internal progress reports that included completion of goals and examples of findings. Pack boriding heat treatments of DED-processed H13 and wrought H13 were conducted by Riley Roache co-supervised by the thesis author. Mr. Roache characterized the as-borided surface roughness using confocal laser-scanning microscopy and FE-SEM, conducted XRD analyses on the wrought borided samples, and imaged the cross-sections of samples using FE-SEM. The remaining characterization of EDS and WDS was completed by the author with assistance from the relevant technicians. Published material from these studies are listed below with the contributing authors:

- Owen Craig, Kevin Plucknett, Joshua Toddy, Scott Halliday, Nylana Murphy. "Microstructure Characterization of Functionally Graded H13 Tool Steel and Copper Using Directed Energy Deposition." 5th HI-AM Conference 2022.
- • Owen Craig, Riley Roache, Kevin Plucknett. "Microstructural Characterization of Pack Borided H13 Tool Steel Processed Using DED." 61st Conference of Metallurgists 2022.
- Owen Craig, Samer Omar, Kevin Plucknett "Material Characterization Comparison of D2 and H13 Tools Steels Manufactured Using DED." 60th Conference of Metallurgists 2021.
- Owen Craig, Alexandre Bois-Brochu, Kevin Plucknett. "Geometry and surface characteristics of H13 hot-work tool steel manufactured using laser-directed

energy deposition.” The International Journal of Advanced Manufacturing Technology (2021) 116:699–718.

- Owen Craig, Alexandre Bois-Brochu, Kevin Plucknett. “Microstructure Characterization of Directed Energy Deposition of H13 Tool Steel.” 4 th HI-AM Conference 2021.
- Owen Craig, Kevin Plucknett. “Scratch Hardness and Wear Response of Additively Manufactured H13 Tool Steel Using DED with Post Heat Treatments.” 23rd International Conference on Wear of Materials 2021.
- Owen Craig, Alexandre Bois-Brochu, Kevin Plucknett. “Geometry and Surface Characterization of Additively Manufactured H13 Hot-Work Tool Steel Using Directed Energy Deposition.” 3rd HI-AM Conference 2020.
- Owen Craig, Kevin Plucknett. “Laser DED Cladding of H13 Tool Steel and Elemental Equivalents.” 2nd HI-AM Conference 2019.